



UNIVERSIDAD NACIONAL AUTÓNOMA DE MÉXICO

Maestría y Doctorado en Ciencias Bioquímicas

Caracterización de los cambios conformacionales del canal iónico permeable a protones H_v1 durante su activación

TESIS

QUE PARA OPTAR POR EL GRADO DE:

Doctor en Ciencias

PRESENTA:

M. en C. Esteban Suárez Delgado

TUTOR PRINCIPAL

Dr. León David Islas Suárez
Facultad de Medicina, UNAM

MIEMBROS DEL COMITÉ TUTOR

Dr. Froylán Miguel Gómez Lagunas
Facultad de Medicina, UNAM
Dr. Takuya Nishigaki Shimizu
Instituto de Biotecnología, UNAM

Ciudad de México. Enero, 2024



Universidad Nacional
Autónoma de México

Dirección General de Bibliotecas de la UNAM

Biblioteca Central



UNAM – Dirección General de Bibliotecas
Tesis Digitales
Restricciones de uso

DERECHOS RESERVADOS ©
PROHIBIDA SU REPRODUCCIÓN TOTAL O PARCIAL

Todo el material contenido en esta tesis esta protegido por la Ley Federal del Derecho de Autor (LFDA) de los Estados Unidos Mexicanos (México).

El uso de imágenes, fragmentos de videos, y demás material que sea objeto de protección de los derechos de autor, será exclusivamente para fines educativos e informativos y deberá citar la fuente donde la obtuvo mencionando el autor o autores. Cualquier uso distinto como el lucro, reproducción, edición o modificación, será perseguido y sancionado por el respectivo titular de los Derechos de Autor.



**PROTESTA UNIVERSITARIA DE INTEGRIDAD Y
HONESTIDAD ACADÉMICA Y PROFESIONAL
(Graduación con trabajo escrito)**

De conformidad con lo dispuesto en los artículos 87, fracción V, del Estatuto General, 68, primer párrafo, del Reglamento General de Estudios Universitarios y 26, fracción I, y 35 del Reglamento General de Exámenes, me comprometo en todo tiempo a honrar a la Institución y a cumplir con los principios establecidos en el Código de Ética de la Universidad Nacional Autónoma de México, especialmente con los de integridad y honestidad académica.

De acuerdo con lo anterior, manifiesto que el trabajo escrito titulado:

Caracterización de los cambios conformacionales del canal iónico permeable a protones H_v1 durante su activación

que presenté para obtener el grado de ----Doctorado ---- es original, de mi autoría y lo realicé con el rigor metodológico exigido por mi programa de posgrado, citando las fuentes de ideas, textos, imágenes, gráficos u otro tipo de obras empleadas para su desarrollo.

En consecuencia, acepto que la falta de cumplimiento de las disposiciones reglamentarias y normativas de la Universidad, en particular las ya referidas en el Código de Ética, llevará a la nulidad de los actos de carácter académico administrativo del proceso de graduación.

Atentamente

M. en C. Esteban Suárez Delgado
Número de cuenta: 306296392

Reconocimientos Académicos

Al Dr. León David Islas Suárez por recibirme en su laboratorio y proporcionar su enseñanza y guía durante todo el proyecto.

A los Doctores de mi comité tutor, Dr. Takuya Nishigaki Shimizu y Dr. Froylan Miguel Gómez Lagunas por sus valiosas aportaciones e ideas en lo referente al uso de sondas fluorescentes y el estudio de los canales iónicos.

A los Doctores de mi jurado de grado, Dra. Claudia Lydia Treviño Santa Cruz, Dr. Arturo Hernández Cruz, Dra. Myrian Velasco Torres, Dr. Alberto Darszón Israel y Dr. Carlos Muñoz Garay, por su revisión a esta tesis y sus oportunos comentarios.

A la Dra. Gisela Rangel Yescas por todos los trabajos de biología molecular de las construcciones realizadas en este trabajo.

A la Lic. María Eugenia Orozco Contreras por su participación en los experimentos control de la figura 16.

Este trabajo contó con el apoyo de una beca de tesis doctoral del CONACyT No. 463819 (CVU 659182), así como también del Programa de Apoyo a los Estudiantes de Posgrado (PAEP) que permitió presentar este trabajo en formato póster bajo el nombre *Characterization of Gating of the Voltage-Gated Proton Channel (Hv1) During Activation Using Non-Canonical Amino Acids* en la *63rd Annual Meeting of the Biophysical Society* realizada en el 2019 en Baltimore, EUA.

Además, este trabajo fue apoyado por la subvención DGAPA-PAPIIT-UNAM No. IN215621 otorgada al Dr. León David Islas Suárez.

Agradecimientos personales

En el transcurso de casi toda una década en un laboratorio, afortunadamente toca agradecer a muchas personas que tocaron mi existencia. Todos ellos permitieron y ayudaron que haya podido terminar este proyecto conservando la cantidad adecuada de sanidad mental.

Agradezco al Dr. León Islas por abrirme las puertas de su laboratorio donde caí en blandito y darle la oportunidad a un médico de conocer realmente lo que implica el estudio de los canales iónicos. También por enseñarme a ser un científico con rigor pero con soltura, por su inagotable paciencia y por siempre considerarme en los proyectos. Nunca entendí por que no usó el Suárez de su nombre. Sin duda se le oye bien.

A la Dra. Gisela Rangel Yescas por su amistad, guía, confianza y enseñarme mis primeros pasos de salsa.

A todos mis compañeros y amigos del laboratorio con quienes compartí el día a día y pudimos tener una gran dinámica de trabajo y una red de apoyo y chimes. A Victor por guiarme en mis primeros pasos dentro de la electrofisiología. A Gema quien tiene la virtud de convertir una tarde pesada en risas. A Miriam, compañera de aventuras, la hermanita siniestra que nunca tuve y siempre quise. A Andrea por sus comentarios ultrapragmáticos y honestos. Así como a Ricardo, Javier, Ceci, Aymé y en especial a Maru quien con carácter inquisitivo y su fuerte amor al debate me enseñó la invaluable lección de conocer profundamente un tema si se quiere explicar a un nuevo estudiante.

A Alexis Méndez Coteró, por su gran amistad y su invaluable mecenazgo hacia alguien lo suficientemente necio para dedicarse a la ciencia.

A Mimí Moreno por su cariño y apoyo en todos los momentos en donde necesité un respiro, y por ser alguien con quien descubrir la realidad siempre es estimulante.

A J.P. Jonhson y Sam Goodchild por darle la oportunidad a un millenial de trabajar de lo que estudió, oportunidad en un millón. Además de su paciencia, apoyo y confianza a lo largo de estos últimos dos años.

Y por último a mi pilar, mi familia. A mi hemano Bruno, a mi padre Ricardo Suárez quien me dio el ejemplo para ser un buen hombre, a mi madre Leticia Delgado cuya fuerza y tenacidad me sigue inspirando.

A todos ustedes: Gracias infinitas y totales.

Índice General

Reconocimientos Académicos.....	3
Índice de figuras.....	8
Índice de tablas.....	10
Índice de abreviaturas.....	11
Resumen.....	12
Abstract.....	13
Introducción.....	14
Canales iónicos activados por voltaje y el dominio sensor de voltaje: una semblanza.....	14
Canal iónico activado por voltaje permeable a protones Hv1.....	22
Planteamiento del problema.....	28
Hipótesis.....	31
Objetivo General.....	31
Objetivos Particulares.....	31
Metodología.....	32
Sistema de Incorporación del aminoácido no canónico Anap.....	32
Biología Molecular.....	33
Expresión en células HEK 293.....	39
Electrofisiología.....	41
Adquisición de datos electrofisiológicos.....	44
Adquisición de fluorimetría y espectrometría.....	46
Modelo cinético.....	50
Resultados.....	52
Incorporación de la sonda Anap en el canal Hv1.....	52
La fluorescencia de Anap incorporado es insensible a los cambios de acidez.....	62
La sonda Anap presentó cambios de fluorescencia voltaje-dependientes.....	65
La fluorescencia de Anap en la posición 197 es apagada por una fenilalanina en S2.....	69
La incorporación del Anap en el sitio L201 permitió detectar una nueva transición durante la activación.....	75
El valor del pH absoluto a un lado de la membrana puede cambiar la respuesta al voltaje.....	82
Discusión.....	86

El sistema de incorporación del aminoácido Anap fue eficiente para el estudio Hv1	86
Los cambios conformacionales del S4 de Hv1 y su modulación por el Δ pH revelados por la incorporación de Anap.	89
F150 como molécula apagadora de la fluorescencia de Anap.....	94
Conclusiones	97
Bibliografía	98
Anexos.....	109

Índice de figuras

Figura 1. Alineamiento de secuencia de los cuatro STM del VSD de la superfamilia de proteínas que presentan VSD.	20
Figura 2. Esquema de activación de un VSD y su participación en la apertura del canal.	21
Figura 3. Esquema de la arquitectura de los dominios sensores de voltaje en diferentes proteínas moduladas por voltaje.	24
Figura 4. El gradiente de protones es un potente modulador de la activación del canal.	27
Figura 5. Propiedades fluorescentes de Anap en diferentes solventes.	32
Figura 6. Esquema de sistema de incorporación de Anap a través de la supresión del codón ámbar adaptado para el canal H _v 1.	34
Figura 7. Esquema de construcción del plásmido codificante de la proteína de fusión H _v 1-mCherry.	37
Figura 8. Esquema de sitios en donde se incorporó Anap en H _v 1. A y B.	38
Figura 9. Esquema simplificado de un circuito durante un experimento típico de Patch-clamp en la configuración célula completa.	42
Figura 10. Técnica de Patch-clamp y sus configuraciones.	43
Figura 11. Esquema de un set de microscopía de fluorescencia.	47
Figura 12. Procedimiento para la medición del espectro de Anap.	48
Figura 13. La adición de la proteína fluorescente mCherry en el C-terminal de H _v 1 no cambió las propiedades electrofisiológicas de H _v 1.	53
Figura 14. La fluorescencia de Anap se superpone a la de mCherry en la región membranal.	54
Figura 15. La incorporación de Anap en la proteína de fusión H _v 1-mCherry produjo canales iónicos funcionales.	55
Figura 16. La presencia de los tres componentes del sistema de incorporación Anap son necesarios para producir canales funcionales.	56
Figura 17. El sistema de incorporación de Anap suprime el codón ámbar insertado en la secuencia de H _v 1.	57

Figura 18. La introducción de Anap en el S4 del canal H _v 1 no cambia su comportamiento con respecto al voltaje en la mayoría de las mutantes.....	59
Figura 19. La fluorescencia de Anap unida a diferentes posiciones dentro del S4 de H _v 1.....	60
Figura 20. La fluorescencia de Anap disminuye conforme es incorporado en residuos cercanos a la región central del segmento S4.....	62
Figura 21. La fluorescencia de Anap incorporado al canal H _v 1 es estable a los cambios de acidez.....	63
Figura 22. La fluorescencia de Anap incorporado al canal H _v 1-V62Anap fue estable a la presencia de corrientes de protones.....	64
Figura 23. La fluorescencia de Anap en la mutante H _v 1-A197Anap reveló el movimiento de S4 en respuesta de pulsos de voltaje.....	66
Figura 24. Anap en la mutante H _v 1-A197Anap reveló el movimiento de S4 responde a la modulación por Δ pH.....	67
Figura 25. Los cambios de fluorescencia en la mutante H _v 1-A197Anap no son provocados por desplazamientos del pico de emisión de fluorescencia de Anap.....	69
Figura 26. El residuo de fenilalanina en el sitio 150 es un apagador de Anap.....	71
Figura 27. La doble mutante presenta cambios de fluorescencia en respuesta a pulsos de voltaje.....	73
Figura 28. Los cambios de fluorescencia de la doble mutante H _v 1-F150A-A197Anap también responden a la modulación de pH.....	74
Figura 29. La cinética de la señal fluorescente de H _v 1-L201Anap durante la desactivación está fuertemente modulada por el pH.....	76
Figura 30. La señal de Anap en el sitio L201 también responde a la modulación por diferencias de acidez a ambos lados de la membrana.....	77
Figura 31. La cinética del componente rápido de la fluorescencia durante la desactivación en H _v 1-L201Anap demuestra una relación estrecha con el cierre de la conductancia.....	79
Figura 32. Modelo cinético secuencial simple.....	81
Figura 33. Modelo alostérico de activación de H _v 1 por voltaje.....	83
Figura 34. Los valores de pH absolutos son determinantes en la activación en H _v 1-L201Anap.....	84

Índice de tablas

Tabla 1. Secuencias de los diferentes oligonucleótidos utilizados para la mutagénesis puntual en la construcción Hv1-cherry.....	39
Tabla 2. Soluciones utilizadas en los experimentos de Patch-clamp Fluorometry.....	45
Tabla 3. Arreglos de filtros de excitación y emisión junto con el espejo dicroico que se usaron para cada proteína fluorescente.....	46
Tabla 4. Parámetros de ajuste a la ecuación de Boltzmann de las mutantes simples.....	59
Tabla 5. Parámetros de ajuste del modelo cinético simple.	85
Tabla 6. Parámetros de ajuste del modelo alostérico.....	85

Índice de abreviaturas

ATP	Trifosfato de adenosina
Anap	ácido 3-[6-acetilnaftalen-2-ilamino]-2-aminopropan
Anap-OMe	Anap éster metílico
Ca ²⁺	Ion calcio
Cs ⁺	Ion cesio
E _H ⁺	Potencial de equilibrio de protones
F	Constante de Faraday
F-V	Curva de fluorescencia en función de voltaje
G-V	Curva de conductancia en función del voltaje
HCN	Canales activados por hiperpolarización y nucleótidos cíclicos
H _V 1	Canal iónico activado por voltaje permeable a protones
hH _V 1	Canal iónico activado por voltaje permeable a protones humano
CiH _V 1	Canal iónico activado por voltaje permeable a protones de <i>Ciona intestinalis</i>
K ⁺	Ion potasio
K _B	Contante de Boltzmann
K _v	Canal de potasio activado por voltaje
Na ⁺	Ion sodio
Na _v	Canal de sodio activado por voltaje
PCF	Patch-Clamp Fluorometry
pH _e	pH extracelular
pH _i	pH intracelular
Q-V	Curva carga en función del voltaje
R	Residuo de Arginina
STM	Segmento transmembranal
TVEC	Fijación de voltaje con dos electrodos
V _{0.5}	Potencial medio de activación
VCF	Voltage-clamp Fluorometry
V _f	Potencial de fijación
VGIC	Canales iónicos activados por voltaje
V _{mem}	Potencial de membrana
V _{rev}	Potencial de reversión de un ion
V _{test}	Pulso prueba
VSD	Dominio sensor de voltaje
ΔpH	Gradiente de protones (pH _{externo} – pH _{interno})

Resumen

El canal iónico permeable a protones activado por voltaje (H_V1) es una proteína de membrana encontrada en diferentes organismos y que cumple una variada gama de actividades fisiológicas dentro de estos, destacando el control del potencial de membrana y los cambios de pH. En los humanos se produce por el gen *HVCN1* y se ha mostrado evidencia de su función en diferentes linajes celulares, por ejemplo en distintas variedades de leucocitos, espermatozoides, y células astrocitarias.

La activación dependiente del voltaje de los canales H_V1 sigue siendo poco conocida, en parte debido a la dificultad de obtener mediciones directas del movimiento del sensor de voltaje en forma de corrientes de activación. Para evitar este problema, en este trabajo se implementó la técnica de Patch-clamp Fluorometry en combinación con la incorporación del aminoácido fluorescente no canónico Anap para monitorear simultáneamente la apertura del canal y el movimiento del segmento S4. El registro simultáneo de corrientes y señales de fluorescencia permitió la correlación directa de estos parámetros con el movimiento del S4 y la investigación de su dependencia en el voltaje y el gradiente de pH (ΔpH). También se encontraron datos que indican que la fluorescencia de Anap incorporado en la hélice S4 se apaga mediante un residuo aromático de fenilalanina ubicado en la hélice S2 y que el movimiento del S4 en relación con este apagador es responsable del aumento de la fluorescencia tras la despolarización. La cinética de la señal de fluorescencia reveló la existencia de una transición muy lenta en la vía de desactivación, que parece estar ampliamente regulada por el ΔpH . Además, los resultados también sugieren que el sensor de voltaje puede moverse después de la apertura del canal y que el valor absoluto del pH puede influir en la apertura del canal. Estos resultados arrojan luz sobre las complejidades de la apertura dependiente del voltaje de los canales H_V1 humanos.

Abstract

The voltage-gated proton channel H_V1 is a membrane protein found in different organisms that fulfills a wide range of physiological activities, highlighting the control of membrane potential and pH changes. In humans, it is produced by the HVCN1 gene, and evidence has been shown of its function in different cell lineages, such as several classes of leukocytes, sperm, and astrocyte cells.

The voltage-dependent activation of H_V1 remains poorly understood, partly due to the difficulty of obtaining direct measurements of voltage sensor motion in the form of gating currents. To avoid this problem, we used the Patch-clamp fluorometry technique in combination with the incorporation of the non-canonical fluorescent amino acid Anap to monitor the opening of the channel and the movement of the S4 segment simultaneously. The simultaneous recording of currents and fluorescence signals allowed the direct correlation of these parameters with the movement of S4 and the investigation of their dependence on voltage and pH gradient (ΔpH). Moreover, data suggest that Anap incorporated into helix S4 is quenched by an aromatic phenylalanine residue located in helix S2 and that the motion of S4 relative to this quencher is responsible for the increase in fluorescence upon depolarization. The kinetics of the fluorescence signal revealed the existence of a very slow transition in the deactivation pathway, which appears to be largely regulated by ΔpH . Furthermore, the results suggest that the voltage sensor can move after the channel opening, and the absolute pH value can influence the opening step. These results shed light on the complexities of voltage-dependent opening of human H_V1 channels.

Introducción

Canales iónicos activados por voltaje y el dominio sensor de voltaje: una semblanza

Si bien conocer el momento en el cual la vida inició resulta un ejercicio de amplia teorización científica, no queda lugar a dudas que la creación de un límite representado por la membrana celular fue un asunto esencial y definitivo. Con la existencia de un espacio interno, los nutrientes necesarios para los procesos bioquímicos quedan accesibles y cercanos a la maquinaria celular que sostiene la vida. Además, crear compartimentos permite organizar mejor las tareas y los recursos e incrementa la probabilidad de ocurrencia de las interacciones moleculares claves para que la vida se mantenga (Hille, 2001; Walter, 2007).

Sin embargo, la delimitación involucra un principio que se puede convertir en un problema para la subsistencia impidiendo el desalojo de catabolitos residuales que no pueden ser reincorporados a la vía metabólica y dificultando la obtención de nuevos nutrientes. Por tanto, junto con la aparición de una membrana, la evolución de diferentes mecanismos que permitan el transporte a través de esta parece una transición igualmente necesaria para mantener el dinamismo de reacciones que permiten la vida tal y como la conocemos (Vereb et al., 2003).

Estos mecanismos de transporte celular involucraron la presencia de proteínas integrales relacionadas estrechamente con la membrana y que se diversificaron con el paso de la evolución. Esta diversificación permitió que, además de que los sustratos se movieran a través de la membrana para integrarse a las vías metabólicas, el movimiento de sustratos y la fluctuación en su concentración se aprovechara como una señal a la que las células fueran capaz de responder y adaptarse. Permitiendo así desarrollar estrategias de manejo de información y

agregando un nuevo nivel de complejidad a los organismos (Moran et al., 2015; Nair et al., 2019).

Una de estas estrategias es el movimientos de iones a través de la membrana que caracteriza a los tejidos excitables, como el muscular y el nervioso, por citar los ejemplos más reconocibles (Grant, 2009; Hille, 1970). En las células de estos tejidos, los iones utilizados típicamente para la comunicación celular son el Na^+ , K^+ , Cl^- , y Ca^{2+} (Hille, 2001; X. C. Zhang et al., 2018).

Dada la naturaleza propia de la membrana celular y de las proteínas embebidas en ella, en el estado de reposo los diferentes iones no se disponen de forma simétrica a ambos lados de la membrana. La distribución asimétrica de los iones forma gradientes electroquímicos para cada ión que derivan tanto de su concentración química a cada lado de la membrana como de la carga eléctrica que poseen los iones cuando están en disolución. La distribución de dichas cargas eléctricas alrededor de la membrana lipídica, que actúa como un capacitor, forma un campo eléctrico con un potencial entre dos compartimentos, el intracelular y el extracelular. Este potencial eléctrico recibe el nombre de potencial de membrana y, dado a su acumulación de cargas eléctricas negativas, la región intracelular suele tener valores más negativos con respecto a la región extracelular, alrededor de -70 mV. (Bezanilla, 2007; Cardozo, 2016; Sperelakis, 1995).

En el potencial de membrana, los múltiples gradientes electroquímicos de cada uno de los iones se combinan ponderados por su permeabilidad a la membrana en reposo. Entonces, el gradiente electroquímico de cada ion se traduce en un potencial eléctrico que se denomina potencial de equilibrio (E_{ion}) o potencial de reversión (V_{rev}) específico de cada ión, y es el valor de potencial al cual la fuerza electroquímica a ambos lados de la membrana se equilibra y flujo neto de iones es nulo (Hille, 2001; Nimigean, 2023). En consecuencia, cualquier diferencia del

potencial de membrana respecto al potencial de reversión de cualquier ión determinará el flujo de este hacia afuera o adentro de la célula, siempre en función de su gradiente electroquímico. Por lo tanto, este potencial de membrana constituye la piedra angular de la señalización bioeléctrica en las células, ya que, al modificar este potencial eléctrico mediante el control de los flujos de iones a través de la membrana, las células han forjado un sistema que les permite comunicarse o responder al ambiente en escala de milisegundos (Bezanilla, 2007; Hille, 1970).

El control de estos flujos de iones que atraviesan la membrana se basa en la acción de diversos tipos de proteínas que se relacionan estrechamente con esta estructura celular. Estas proteínas transmembranales permiten detectar estímulos del entorno, discriminar entre los múltiples sustratos y transportarlos dependiendo de las necesidades de la célula y las condiciones donde se desarrollan (Alberts, 2002; Kulbacka et al., 2017).

Estas proteínas membranales que controlan el flujo de los iones son clasificadas en dos grandes tipos, los transportadores y los canales iónicos. Los primeros, transportan los iones en contra del gradiente de concentración, es decir, permiten aumentar el gradiente gracias a la inversión de energía a través de la hidrólisis del ATP o mediante el acoplamiento del transporte de otro sustrato que esté siguiendo la dirección de su gradiente (Alberts, 2002). Por su parte, los canales iónicos son proteínas transmembranales que tienen la función de formar un poro por el cual los iones se moverán siguiendo la dirección que reduzca el gradiente electroquímico del ion que lo atraviesa. Los canales permiten el flujo de varios millones de iones por segundo en función de su propio gradiente electroquímico. Este movimiento de iones a alta velocidad a través de la membrana crea corrientes eléctricas que modifican el potencial eléctrico de la membrana y estos cambios rápidos en el potencial pueden propagarse a lo largo de la membrana, sirviendo

como una señal para el resto de las proteínas membranales o para las células cercanas (Bezanilla, 2007; Catterall, 1995).

En términos generales, estos cambios rápidos en el potencial de membrana se producen mayoritariamente por la acción de canales iónicos activados por voltaje permeables a sodio (Na_v), calcio (Ca_v) y potasio (K_v) que responden a su vez a los cambios de potencial. A través de una activación secuencial de estos canales en su membrana, las células usan el gradiente electroquímico de los iones para producir una respuesta en la membrana celular, que en estos tejidos se conoce como potencial de acción, mientras que las bombas restauran la situación previa de los gradientes para que la capacidad de producir el potencial de acción se mantenga (Debanne et al., 2011; Grant, 2009).

Los canales iónicos se han diversificado a través del tiempo para poder activarse a diferentes tipos de estímulos físicos y químicos. Para facilitar su estudio, se pueden clasificar según el principal estímulo activador en 3 categorías generales: Los canales iónicos activados por ligando, que son sensibles a diferentes moléculas que pueden interactuar en sus múltiples sitios de unión que pueden localizarse tanto en el lado extracelular del canal como en el intracelular (Zagotta, 2023). Otro tipo de canal son los mecanosensibles, que se activan por deformaciones en la membrana que los aloja o por fuerzas ejercidas directamente en su estructura (Cox et al., 2019). Por último y quizá los más estudiados están los canales iónicos activados por voltaje (VGIC). Estos presentan dentro de su estructura residuos de aminoácidos eléctricamente cargados que se disponen dentro del campo eléctrico de la membrana. Gracias a la interacción de estas cargas con dicho campo a los VGIC les es posible detectar y responder a los cambios de potencial de la membrana (Hoshi, 2023). Es importante señalar que la naturaleza es más compleja y esta es una forma simple de catalogar a los canales iónicos, es decir, se ha observado que estas proteínas pueden ser reguladas por más de un mecanismo y su apertura puede

depender de diversos estímulos o efectos físicos. Por ejemplo, en los canales iónicos activados por voltaje, también se han descrito que la presión osmótica (Macdonald, 2002), la temperatura (García-Ávila & Islas, 2019), la concentración de otros iones (Horrigan & Aldrich, 2002), la acción de otras proteínas membranales (Salvage et al., 2020) o la fluidez de la membrana (Zakany et al., 2020) pueden alterar la sensibilidad al voltaje o la velocidad de activación del canal.

Dentro de la amplia diversidad de VGIC, se puede describir la existencia de diversos dominios en sus estructuras que presentan una actividad específica. En general, es correcto pensar que los VGIC son proteínas multimodulares conformadas por múltiples subunidades (en los K_v) o dominios (en los Na_v y Ca_v) que se disponen radial y simétricamente alrededor de un poro de conducción iónica que se encuentra al centro (Wisedchaisri & Gamal El-Din, 2022; X. C. Zhang et al., 2018). Cada subunidad o dominio presentan a su vez dominios sensores de voltaje (VSD), un dominio de poro (PD) que a su vez contienen un filtro de selectividad, y una compuerta de activación que se encuentra en la región intracelular del canal. Estos dominios se relacionan actúan coordinadamente para permitir la traducción de estímulos eléctricos en flujos de corrientes a través de la membrana (Chowdhury, 2023). Al proceso que sucede entre la detección de un estímulo y el mecanismo de la apertura y cierre del canal se le llama *gating* (Bezanilla, 2018).

Gracias a las técnicas de control y fijación del voltaje desarrolladas en el siglo pasado, como la fijación de voltaje con dos electrodos (*Two-electrode voltage clamp* o TEVC en inglés) o la fijación de voltaje en microáreas de membrana (*Patch-clamp* en inglés), se han podido disecar las corrientes iónicas y analizar las propiedades biofísicas de los distintos VGIC. Midiendo las corrientes iónicas que atraviesan los VGIC en respuesta a cambios de voltaje, se ha podido describir las cinéticas de sus transiciones de apertura y cierre, así como estimar la fracción de canales que se encuentran abiertos a un determinado potencial de membrana. Esto último permite

cuantificar la conductancia en función del voltaje (curva G-V), es decir, como el voltaje cambia la probabilidad de que los canales transiten de un estado cerrado a un estado abierto o conductivo (Hille, 2001; Hoshi, 2023). Un parámetro clásico de la cuantificación de estas propiedades es el voltaje medio de activación o $V_{0.5}$. Este valor se define como el voltaje en donde la mitad de la población de canales se encuentran en un estado abierto o conductivo y se utiliza frecuentemente como un punto de referencia en el potencial de membrana en donde el canal tenderá a cambiar de un estado cerrado a un estado abierto (Chanda, 2015).

En los VGIC, los VSD son las estructuras que les permiten a los canales iónicos activados por voltaje interactuar con el campo eléctrico de la membrana y responder a su potencial eléctrico. Estos dominios están agrupados en una superfamilia estructuralmente conservada dentro de las distintas proteínas de membrana reguladas por voltaje, como fosfatasas activadas por voltaje y los canales iónicos activados por voltaje. Los VSD están compuestos de 4 segmentos transmembranales nombrados S1 a S4. Su último segmento, S4, presenta múltiples cargas positivas a lo largo de su estructura constituidas por los residuos de aminoácidos arginina (R) o lisina (K). Por ejemplo, en los canales Na_v y K_v , el número de residuos con carga en el S4 es entre 4 y 7, separadas entre sí por dos aminoácidos (figura 1) (Bezanilla, 2008; Chowdhury, 2023; Moreau et al., 2014).

Estos residuos cargados positivamente se atraen electrostáticamente hacia la cara interior de la membrana celular cuando el potencial de membrana está en reposo, lo que mantiene al VSD ya al canal en una conformación de reposo. Al ocurrir una despolarización, el aumento de cargas positivas en el interior de la membrana repele las cargas del VSD hacia el lado extracelular de la membrana. Este movimiento producido en el VSD lo conduce a una conformación activada y el movimiento producido se transfiere, por un acoplamiento electromecánico mediado por el asa entre S4 y S5, a la región del poro, lo que lleva a un cambio estructural

del canal predisponiéndolo a transitar a un estado abierto conductivo. Si los cuatro VSD dentro del canal pasan a un estado activado de forma concertada, el poro pasará a una conformación abierta y permitirá el flujo de iones (figura 2) (Bezanilla, 2018; Chowdhury, 2023).

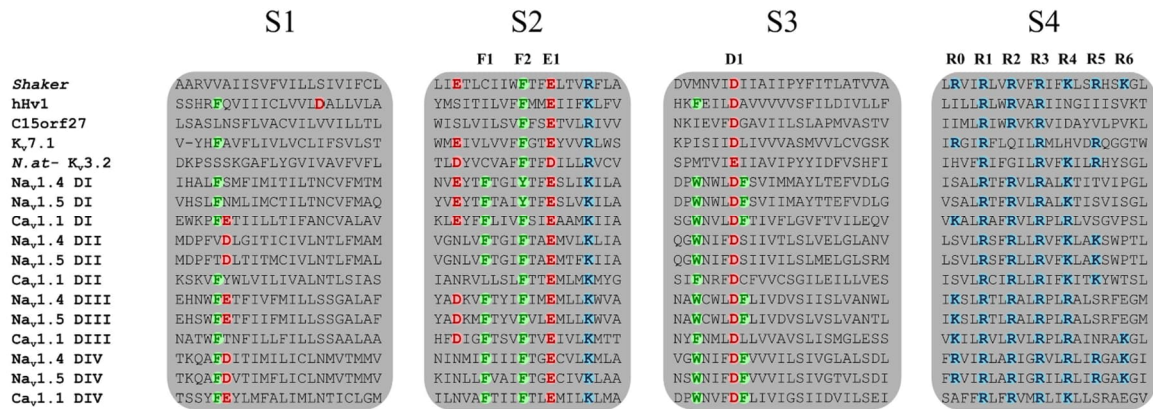


Figura 1. Alineamiento de secuencia de los cuatro STM del VSD de la superfamilia de proteínas que presentan VSD. Se muestran ejemplos de canales de sodio (Na_v1.4, Na_v1.5), calcio (Ca_v1.1) y potasio (K_v7.1). También se muestran los miembros de la superfamilia de proteínas que presentan VSD, como H_v1 y C15orf27 (un dominio sensor de voltaje sin aparente función biológica). Los segmentos S1, S2 y S3 contienen residuos altamente conservados aromáticos (en verde, fenilalanina, triptófano o tirosina) y cargados negativamente (en rojo, aspartato o glutamato), mientras que el segmento S4 contiene al menos tres residuos cargados positivamente (en azul, arginina y lisina). Los residuos implicados en el centro de transferencia de carga están anotados como F1, F2, E1, D1 y R0 a R6. Nótese el residuo D112 en S1 en el H_v1. Modificado de (Moreau et al., 2014).

Una forma efectiva de cuantificar los cambios de posición de los VSD es midiendo cómo se mueven sus cargas con respecto al campo eléctrico de la membrana. Al moverse dentro de este espacio finito en respuesta de pulsos de voltaje, los VSD producen corrientes transitorias que se aceleran en respuesta al voltaje (Catacuzzeno et al., 2023). Estas corrientes comúnmente conocidas como gating currents o corrientes “de compuerta” o “de activación” al graficarse sus integrales en función del voltaje (curvas Q-V) permite cuantificar la voltaje-dependencia de la activación de VSD. En los VGIC canónicos, la V0.5 de estas curvas suele ser de 20 a 40 mV más negativa de la V0.5 de la apertura del canal. Lo que implica que el VSD se debe de activar antes de que el poro se abra.

Sin embargo, cabe señalar que estas corrientes suelen ser miles de veces más pequeñas en comparación a las corrientes iónicas que pueden atravesar el canal. Por lo tanto, el estudio de los movimientos de los VSD de los canales necesita del bloqueo del poro o la reducción de la corriente iónica mediante el reemplazo del ión permeante por iones impermeables, lo que dificulta el estudio de las corrientes de compuerta en todos los canales (Bezanilla, 2018).

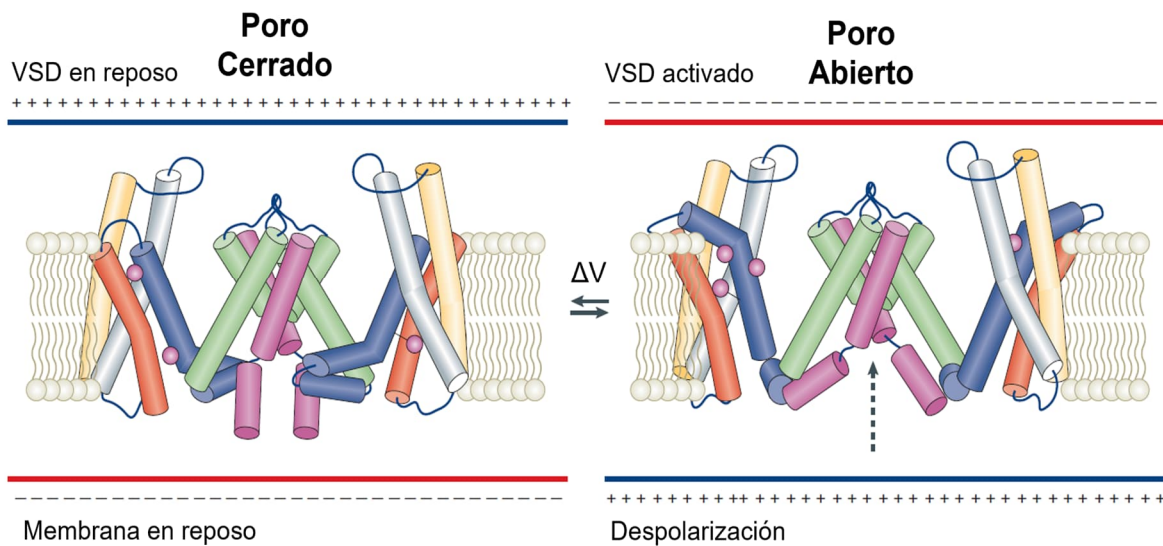


Figura 2. Esquema de activación de un VSD y su participación en la apertura del canal. Se muestra una perspectiva lateral de dos subunidades del tetrámero de K_v tipo Shaker encontradas en el poro del canal y respondiendo a dos situaciones extremas. Las otras dos subunidades necesarias para la formación del canal se retiraron por motivos ilustrativos. Cada subunidad tiene los segmentos transmembranales bajo el siguiente código de color: S1 en gris, S2 en amarillo, S3 en naranja, S4 en azul, S5 y filtro de selectividad en verde, S6 en magenta. Las argininas del S4 se esquematizan como círculos magentas. En respuesta a la polarización de la membrana estas cargas se ven atraídas por el interior negativo de la célula (panel izquierdo, línea roja), mientras que la despolarización aumenta vuelve más positivo la región intracelular (panel derecho línea azul), repeliendo las cargas y moviendo el S4 hacia regiones extracelulares. Este movimiento se acopla electromecánicamente a través del linker S4-S5 perturbando la arquitectura del S6 y facilitando que este adopte la configuración abierta, que permite el flujo de iones a favor de su gradiente electroquímico (flecha discontinua). Modificado de (Bezanilla, 2008).

Canal iónico activado por voltaje permeable a protones H_v1

El canal iónico permeable a protones H_v1 comprende la única familia de canales iónicos activados por voltaje que transportan protones (Chaves et al., 2023; Decoursey, 2003). Si bien las primeras evidencias de su existencia datan desde las décadas de los 1970 y 1980 (Fogel & Hastings, 1972; R. C. Thomas & Meech, 1982), el estudio específico de las corrientes de protones activadas por voltaje en células de mamíferos fueron descritas y estudiadas en la década de 1990 (Cherny et al., 1995; DeCoursey & Cherny, 1994, 1996). Después, el descubrimiento de la secuencia genética de las VSP a principios del presente siglo permitió encontrar la secuencia de los primeros homólogos de H_v1 y expresarla heterológamente en modelos biológicos (Ramsey et al., 2006; Sasaki et al., 2006).

A partir de ese punto se han encontrado homólogos de la proteína ampliamente distribuidos en la naturaleza, desde organismos unicelulares (diatomeas, algas, dinoflagelados) hasta en especies más complejas como peces, anfibios, aves y mamíferos (Chaves et al., 2023). Esta amplia distribución se ve reflejada en la versatilidad de funciones que puede abarcar en los diferentes organismos. Por ejemplo, se han estudiado sus repercusiones directas en la capacitación de los espermatozoides (Lishko & Kirichok, 2010; Zhao et al., 2018), en la regulación del pH de la superficie de las vías aéreas en roedores (Cherny et al., 1995), en la maduración de ovocitos en anfibios (Baud & Barish, 1984) en la bioluminiscencia en dinoflagelados (Smith et al., 2011), en la secreción de histamina en los basófilos (Musset et al., 2008), en la secreción de insulina en las células pancreáticas (Pang et al., 2020), en el proceso de malignización de linfocitos B y células mamarias (Alvear-Arias et al., 2023) y en el estallido respiratorio de la fagocitosis en eosinófilos y neutrófilos (El Chemaly et al., 2010, 2014; Ramsey et al., 2009; Zhao et al., 2018).

Como representante de la superfamilia de VSD, estructuralmente el canal H_v1 se compone de 4 segmentos transmembranales (STM) con sus dominios N- y C-terminales dirigidos hacia el citosol (figura 3) (DeCoursey et al., 2016; Geragotelis et al., 2020; Takeshita et al., 2014). Sin embargo, el canal H_v1 carece de los 2 STM que conforman la región de poro en los demás canales iónicos canónicos (S5 y S6), confiriéndole la característica que el VSD del H_v1 presente doble función, se encarga tanto de responder al potencial eléctrico a través de membrana como de formar el poro por donde se moverán los protones una vez se active el canal (figura 2).

Además, existe evidencia que apoya la conclusión que el dominio C-terminal tiene una participación importante en la función. En los vertebrados y algunos invertebrados (*Ciona intestinalis*, por ejemplo), la región C-terminal puede formar estructuras helicoidales superenrolladas, conocidas como *coiled-coil* que relacionan estrechamente dos monómeros H_v1 entre sí, formando dímeros (Fujiwara et al., 2012; Smith & DeCoursey, 2013). Las repercusiones funcionales de esta capacidad de dimerización conllevan la presencia de un mecanismo de cooperatividad entre los dos VSD que coordina los estados abierto y cerrado de ambos monómeros a pesar de que cada uno mantiene su capacidad de conducir a los protones (Tombola et al., 2008, 2010). Aún no se ha encontrado alguna razón específica para la formación de dichos dímeros, se estima que estos son dos veces más dependientes al voltaje en comparación con el canal sin C-terminal y que se piensa es de expresión monomérica en la membrana (DeCoursey, 2015; Gonzalez et al., 2010; S.-Y. Lee et al., 2008; Mony et al., 2020). Por su parte, la región del N-terminal no parece presentar una función estructural en particular, sin embargo, estudios han informado que posee un sitio de fosforilación que le permite entrar a un estado de activación facilitada (Hondares et al., 2014; Musset et al., 2010).

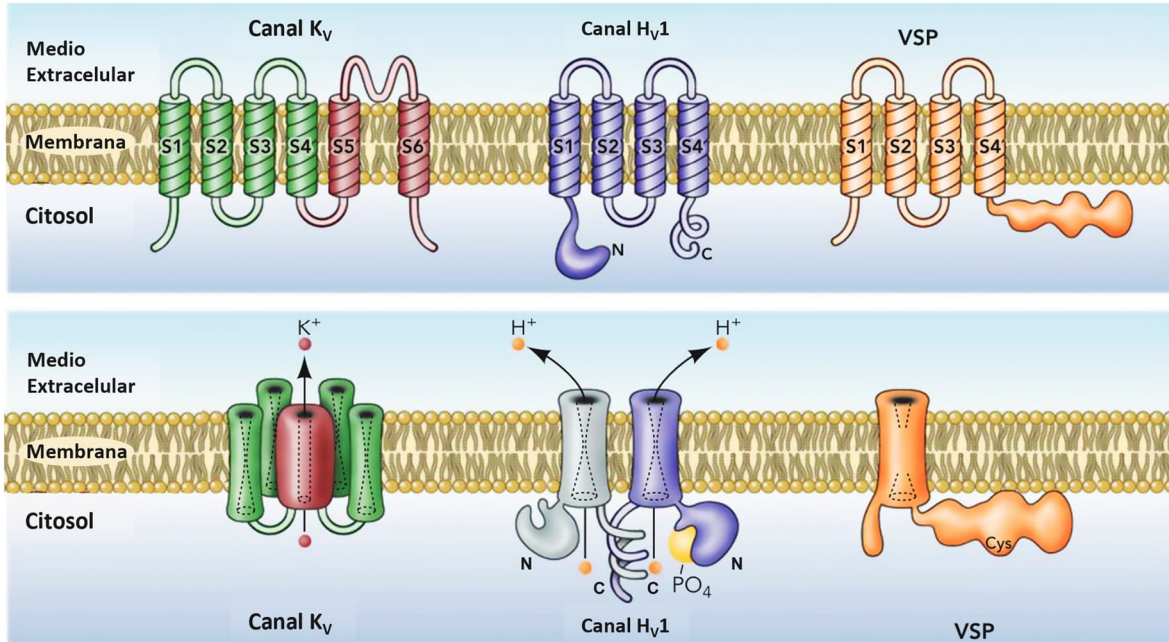


Figura 3. Esquema de la arquitectura de los dominios sensores de voltaje en diferentes proteínas moduladas por voltaje. En el panel superior se ilustran los segmentos transmembranales de las subunidades que forman a los VGIC activados por voltaje (en este ejemplo un K_v), H_v1 y la fosfatasa sensor de voltaje (VSP). Se puede observar cómo cada VSD (en verde para los VGIC, azul para H_v1 y naranja para las VSP) está formado por 4 segmentos transmembranales. En el panel inferior se muestra una representación de las proteínas en su forma oligomérica funcional. Mientras el KV es un tetrámero con cuatro VSD rodeando un dominio del poro formado por la unión de los 4 pares de segmentos S5-S6, el canal de protones se presenta como un dímero de VSD unidos por el C-terminal y sin PD. Nótese la presencia de una vía de conducción propia de cada monómero para los protones. También se muestra la región en N-terminal que se puede presentar fosforilación y potenciar la función del canal. El VSP es un monómero cuyo VSD detecta el potencial de la membrana y, en consecuencia, regula la actividad de la fosfatasa intracelular unida. Modificado de (DeCoursey, 2013).

A través de su estudio experimental en los últimos 50 años, se han encontrado características electrofisiológicas del canal H_v1 que lo vuelven único en su tipo. Posiblemente la más importante es su selectividad considerada perfecta hacia los protones (Chaves et al., 2023). Esta selectividad se comprobó en varias ocasiones a través de experimentos de intercambio iónico en donde la selectividad resulta alrededor de 1 millón de veces más preferente a los protones que a otros iones monovalentes como Na⁺, Cl⁻ y K⁺ (Q. Li et al., 2015; Musset et al., 2011). Se piensa que esta característica puede deberse a que las concentraciones de protones libres en el medio intracelular son tres órdenes de magnitud más reducidas que el resto de los iones capaces de permear la membrana (aproximadamente 0.1 μM a pH 7),

haciendo necesario que el canal sea varios órdenes de magnitud más selectivo (DeCoursey & Hosler, 2014; Musset & DeCoursey, 2012).

Los mecanismos involucrados en la formación de la vía de conductancia y del filtro de selectividad aún son materia de estudio y amplio debate. Se han propuesto dos mecanismos mediante los cuales los protones atraviesan el sensor del voltaje cuando el canal se activa en respuesta al movimiento del S4. El primero involucra la creación de una cadena de moléculas de agua en el interior del VSD que comunicará las dos cavidades (interna y externa). Cuando el canal realiza un cambio conformacional en el momento de su activación, la barrera hidrofóbica constituida por el centro de transferencia de carga (formado por un residuo de fenilalanina en la posición 150 en el canal H_v1 humano) es reemplazado por dicha cadena molecular de agua y el flujo de los átomos de hidrógeno se realiza de forma saltatoria desde una molécula donadora de hidronio (H₃O⁺) hasta una molécula aceptora de agua (H₂O), lo que se conoce como mecanismo de Grotthuss (Boytssov et al., 2023; DeCoursey, 2003; Ramsey et al., 2010). El segundo mecanismo se parece al primero, sin embargo, en este se involucran residuos de los aminoácidos que conforman el canal iónico. Estos residuos forman una senda de transferencia de protones por donde el protón se transporta, aunque no excluye la participación de moléculas de agua en el movimiento de los protones (Chamberlin et al., 2015; Dudev et al., 2015; Musset & DeCoursey, 2012).

Con base en estos dos modelos se ha tratado de establecer alguna conexión entre el cambio conformacional que induce la activación con la formación del filtro de selectividad y el poro en respuesta al movimiento del S4 (Kulleperuma et al., 2013; Randolph et al., 2016). Gracias a los experimentos que se han realizado a partir de dichos modelos, se ha descrito que el residuo de aspartato localizado en el sitio 112 (S1) es muy importante para el filtro de selectividad y la formación del poro, dada a su estrecha relación con los residuos de arginina y triptófano que se

encuentran en el S4 (R205, W207 y R208) (Cherny et al., 2015; Morgan et al., 2013; Musset et al., 2011). Al mutar dicho aminoácido por otros aminoácidos con diferente carga o ausencia de ésta, se pudo modificar la selectividad y la permeabilidad del canal. Así mismo, a través de mutaciones en residuos que presentan carga eléctrica en los STM S1, S2 y S3, se ha podido identificar más interacciones electrostáticas entre los diferentes residuos de aminoácidos cargados que se encuentran distribuidos en la proteína. Estas interacciones permiten la estabilización de los estados del canal, tanto el cerrado (interacciones entre E153 y D174 con R211) como el abierto (interacciones entre D123 y E119 con R205 y R208) (DeCoursey et al., 2016; Geragotelis et al., 2020). A pesar de estos descubrimientos, no se ha elucidado completamente cuales son los cambios conformacionales que conllevan a la estructuración del poro y del filtro de selectividad, ni las relaciones moleculares específicas de dicho filtro.

Otra característica esencial del canal iónico H_v1 , y tal vez la más definitoria e intrigante, ya que hasta el momento no se ha encontrado una evidencia directa relacionada a la estructura del canal, es que la concentración del ion permeante a ambos lados de la membrana modula el voltaje de activación del canal, es decir, que el gradiente de acidez a través de la membrana está estrechamente relacionado con el voltaje de activación. Dicho gradiente, nombrado ΔpH , se obtiene mediante la resta del pH intracelular al pH extracelular ($pH_e - pH_i = \Delta pH$) (Cherny et al., 1995). Los resultados experimentales en las diferentes estirpes celulares que expresan H_v1 , han arrojado una relación de corrimiento promedio aproximadamente de 40 mV en el voltaje medio de activación ($V_{0.5}$) por cada unidad de ΔpH que se modifique (figura 4) (Chaves et al., 2023). Entonces, entre más positivo el valor de ΔpH , es decir, entre más ácido sea el interior de la célula o más alcalino el medio extracelular, el voltaje de activación tenderá a ser más negativo, y viceversa, entre más pequeña sea la diferencia entre los compartimientos intra y extracelular, el voltaje de activación tenderá hacia voltajes más positivos.

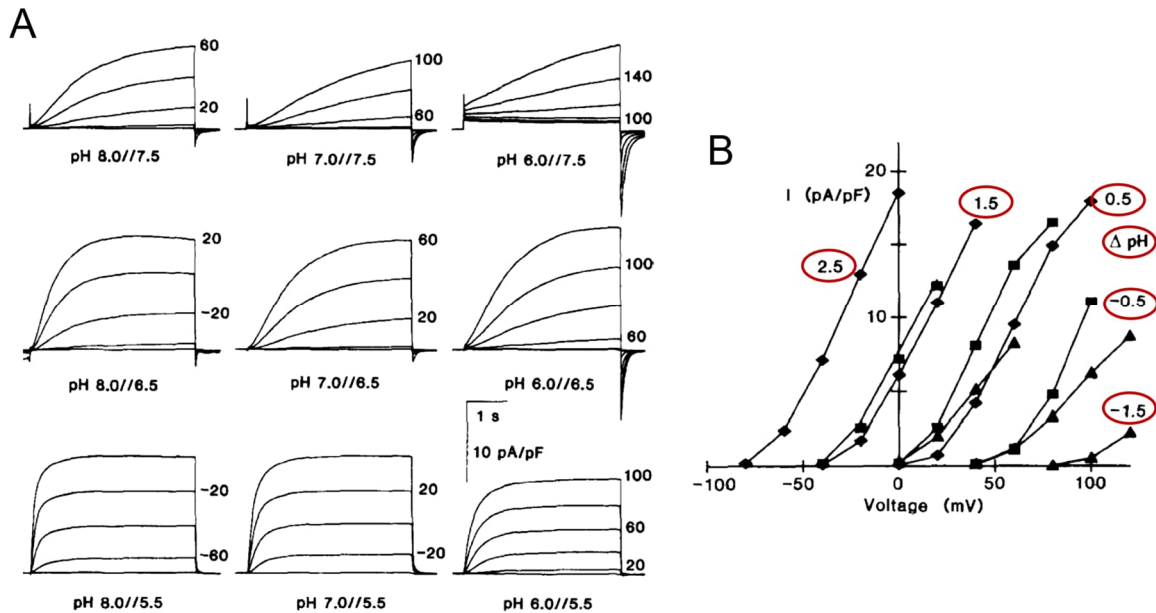


Figura 4. El gradiente de protones es un potente modulador de la activación del canal. A. familias de corrientes de protones obtenidas en epitelio alveolar a diferentes pHs indicados como pH externo//pH interno. Pulsos en aumentos de 20 mV y duración de 4 s. Las corrientes máximas de estas familias se grafican en B, con diamantes para pHi = 5.5, cuadrados para pHi = 6.5 y triángulos para pHi = 7.5. Los números a un lado de las gráficas dentro del óvalo rojo muestran el valor del Δ pH. Nótese como la voltaje-dependencia apertura del canal es determinada por este gradiente. Modificado de (Cherny et al., 1995).

Aún se desconocen los mecanismos moleculares que controlan este tipo de modulación en la función del canal, sin embargo, se ha teorizado que esta constante modificación de la $V_{0.5}$ de activación tiene por función que siempre se encuentre en valores de potencial más positivos que el V_{rev} de los protones (E_{H^+}) y, por tanto, cada vez que se active el canal la corriente de protones se dirija hacia el espacio extracelular (DeCoursey, 2015). Por lo que se ha propuesto que esta vía de eflujo de protones ayuda a evitar la acumulación de ácido que se produce por el metabolismo celular. Solamente se ha descrito una excepción a esta regla, que es el caso de las especies de dinoflagelados, en donde se ha observado que el canal produce una corriente entrante de protones que puede servir para algunas funciones en estos organismos, especialmente en la bioluminiscencia (Smith et al., 2011).

Planteamiento del problema

Como se ha descrito previamente, a pesar de que los estudios sobre el canal H_v1 en los años recientes han logrado describir ciertas particularidades de su comportamiento, como su función en diferentes linajes celulares (He et al., 2021; Pang et al., 2020; Zhao et al., 2018), su dimerización y cooperatividad (Mony et al., 2020; Smith & DeCoursey, 2013) o los aminoácidos importantes para la selectividad a protones (Morgan et al., 2013; Musset et al., 2011), existen características como su estructura y los mecanismos que rigen su activación que siguen sin dilucidar por completo. Recientemente se ha investigado el movimiento del S4 con mutantes de los canales de CiH_v1 y hH_v1 que bloquean parcialmente el poro gracias al atrapamiento de un residuo de arginina mutado en el S4 (Carmona et al., 2018; De La Rosa & Ramsey, 2018). Sin embargo, al contener en el mismo dominio VSD la detección del potencial y la formación del poro, resulta difícil estimar las propiedades biofísicas de una propiedad sin afectar a la otra. En H_v1 , bloquear el poro con alguna molécula podría afectar el movimiento del S4 y su respuesta al voltaje. Por esta razón, se vuelve necesario enfocar el estudio de este canal desde otras perspectivas metodológicas.

A mediados de la década de 1990 se desarrolló un enfoque en el estudio de los canales donde se fusionaron técnicas de fluorometría con los registros electrofisiológicos de TEVC, creando así la técnica de fluorometría de fijación de voltaje (*Voltage-Clamp Fluorometry* o VCF en inglés) (Cha & Bezanilla, 1997; Mannuzzu et al., 1996; Talwar & Lynch, 2015). Esta técnica se ha utilizado para estimar tanto la estequiometría de las diferentes subunidades, así como los cambios conformacionales de los canales durante su ciclo de activación a través de mediciones de fluorescencia de sondas unidas a estos canales. La aplicación de estas técnicas de fluorescencia pasó en pocos años a aplicarse también para los registros de Patch-clamp, dando lugar a la técnica nombrada *Patch-clamp*

Fluorometry en inglés (PCF) (Kusch & Zifarelli, 2014). Esta técnica otorga la posibilidad de evaluar los cambios conformacionales y revelar estados transitorios del canal que pueden ser eléctricamente silenciosos (estados cerrados, inactivados o desensibilizados). Debido a tales ventajas el PCF se ha utilizado en el estudio de un amplio número de canales iónicos utilizando múltiples tipos de herramientas fluorescentes, como sondas sintéticas unidas al canal a través de sus residuos de cisteína, proteínas fluorescentes incorporadas a la estructura del canal mediante modificaciones genéticas, ligandos fluorescentes específicos para la proteína, o la introducción de aminoácidos no canónicos fluorescentes incorporados a la secuencia del canal (Suárez-Delgado & Islas, 2020; Taraska & Zagotta, 2010).

Este último es uno de los métodos recientes que dependen del uso de sondas fluorescentes que se pueden colocar en la secuencia de las proteínas en forma de aminoácidos no canónicos (Coddington & Trudeau, 2020; Kalstrup & Blunck, 2013; M. Li et al., 2022; Zagotta et al., 2021). Gracias a sus características fluorescentes, estas sondas pueden presentar cambios en la intensidad de su brillo relacionados a cambios conformacionales de la proteína a la cual está unida y revelar información sobre dichos cambios de manera dinámica. También, gracias a su tamaño relativamente pequeño, se utilizan para experimentos de FRET de una mayor resolución espacial en comparación a la que ofrecen las sondas sintéticas y proteínas fluorescentes usadas tradicionalmente.

Cuando se planteó este proyecto con el hHv1 se esperó poder utilizar este sistema de incorporación de aminoácidos no canónicos para introducir la sonda Anap (ácido 3-[6-acetilnaftalen-2-ilamino]-2-aminopropanoico) en diferentes sitios de su estructura. Se eligieron diversos lugares en los que se esperaba que el movimiento producido por la activación cambie la polaridad del ambiente en donde se encuentra la sonda y, en consecuencia, se puedan medir cambios en la fluorescencia durante la aplicación de protocolos electrofisiológicos. Los sitios

donde se planeó hacer un escaneo de sustitución de aminoácidos, fueron: el segmento proximal del S4, el segmento distal del S4, el asa entre S3 y S4, el segmento proximal de S1 y el segmento distal de S1. Cabe hacer notar que las sondas tradicionales no han sido incorporadas en el S4, por lo que el uso de Anap en nuestros experimentos representó la primera vez que se mide fluorescencia de estos sitios.

Hipótesis

Si se pueden introducir sondas fluorescentes en forma de aminoácidos no canónicos dentro de la secuencia del canal H_V1 sin afectar su función, dichas sondas servirán para detectar y caracterizar los cambios conformacionales del sensor de voltaje del canal H_V1 y al momento de su activación, así como su modulación a diversos valores de ΔpH .

Objetivo General

Determinar los cambios conformacionales de los STM y su movimiento perpendicular con respecto a la membrana celular relacionados con la activación del canal H_V1 a través de espectroscopia de fluorescencia en función de diferentes voltajes y valores de ΔpH .

Objetivos Particulares

- Realizar la construcción del canal H_V1 con el aminoácido Anap incorporado en sitios específicos de su secuencia.
- Determinar los movimientos relativos de los segmentos transmembranales del canal H_V1, principalmente S4, relacionados con su activación a partir del monitoreo de cambios en la fluorescencia.

Metodología

Sistema de Incorporación del aminoácido no canónico Anap

Con el objetivo de investigar las transiciones voltaje-dependientes del STM 4 del VSD de H_v1 mediante la técnica PCF, se planteó la introducción de la sonda fluorescente Anap en la estructura del canal (figura 5). Esta sonda se desarrolló por el grupo de trabajo del Dr. Peter G. Schultz a partir del fluoróforo “Prodan”, ampliamente utilizado en el estudio de la biología celular (Chatterjee et al., 2013; H. S. Lee et al., 2009; M. C. Puljung, 2021).

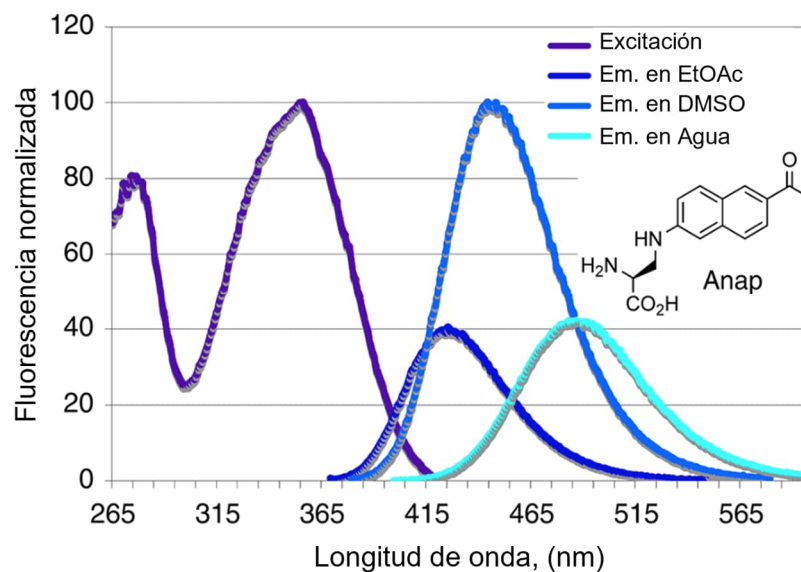


Figura 5. Propiedades fluorescentes de Anap en diferentes solventes. Estructura molecular y espectros normalizados de excitación (púrpura) y emisión en solventes con diferentes polaridades: Acetato de etilo (EtOAc) en azul oscuro; Dimetilsulfóxido (DMSO) en azul claro; agua en cian. Nótese el corrimiento de cerca de 90 nm entre el solvente polar y el apolar. Modificado de (Chatterjee et al., 2013).

Este aminoácido no canónico ya se ha utilizado como sonda para el estudio del movimiento y la estequiometría otras proteínas de membrana porque su fluorescencia es muy sensible a los cambios de polaridad del ambiente en el que se encuentra (Dai & Zagotta, 2017; Kalstrup & Blunck, 2013; Mizutani et al., 2022;

Zagotta et al., 2016). Por ejemplo, mientras que su pico de excitación máxima se encuentra y mantiene a los 360 nm, su espectro de emisión en medios apolares como el acetato de etilo, presenta un pico de emisión máxima alrededor de los 420 nm. Por otro lado, en ambientes polares su pico de emisión se recorre hacia longitudes de onda más rojas, llegando hasta los 490 nm. Además de estas características fotofísicas, posee un coeficiente de extinción molar de $17,500 \text{ cm}^{-1} \text{ M}^{-1}$ y un rendimiento cuántico de 0.48 (Chatterjee et al., 2013).

Para incorporar este aminoácido no canónico al canal Hv1, se usó el plásmido pAnap (gentilmente donado por la Dra. Sharona Gordon, University of Washington, Seattle, Washington, EUA) que contiene la información genética de un tRNA modificado y una tRNA-aminoacil sintetasa que une específicamente el Anap al tRNA modificado; ambos evolucionados a partir del par tRNA/tRNA-aminoacil sintetasa de leucina de la bacteria *Escherichia coli* (Chatterjee et al., 2013; Gordon et al., 2018; H. S. Lee et al., 2009). El tRNA de este par reconoce la secuencia del codón “ámbar” (TAG), una secuencia que de manera natural constituye un codón de paro muy poco frecuente en mamíferos (Belinky et al., 2018). Por lo tanto, se puede sustituir la secuencia genética de un aminoácido en la proteína de interés por el codón ámbar mediante biología molecular y, al coexpresar la proteína mutante con el plásmido pAnap e incubar con Anap en el medio, la maquinaria molecular representada por el par tRNA/tRNA-aminoacil sintetasa introducirá el Anap dentro de la secuencia de aminoácidos de la proteína en el sitio con el codón ámbar (figura 6) (Gordon et al., 2018).

Biología Molecular

El uso de aminoácidos no canónicos en la investigación de proteínas membranales a menudo requiere proteínas reporteras, como las proteínas fluorescentes (PF), que no afecten la función de la proteína en estudio y confirmen

la incorporación exitosa de estos aminoácidos en el sitio deseado. Entonces, si la célula presenta la fluorescencia tanto de PF como de Anap, se infiere con cierta seguridad que se tiene incorporado el Anap a la secuencia de la proteína de fusión. Esto además de facilitar la detección de células que hayan incorporado el aminoácido no canónico, reduce la presencia de falsos positivos, ya que la distribución del aminoácido es uniforme en el cultivo celular y puede producir niveles de fluorescencia basal que dificulten la visualización de las células que hayan rescatado dicho aminoácido (M. C. Puljung, 2021).

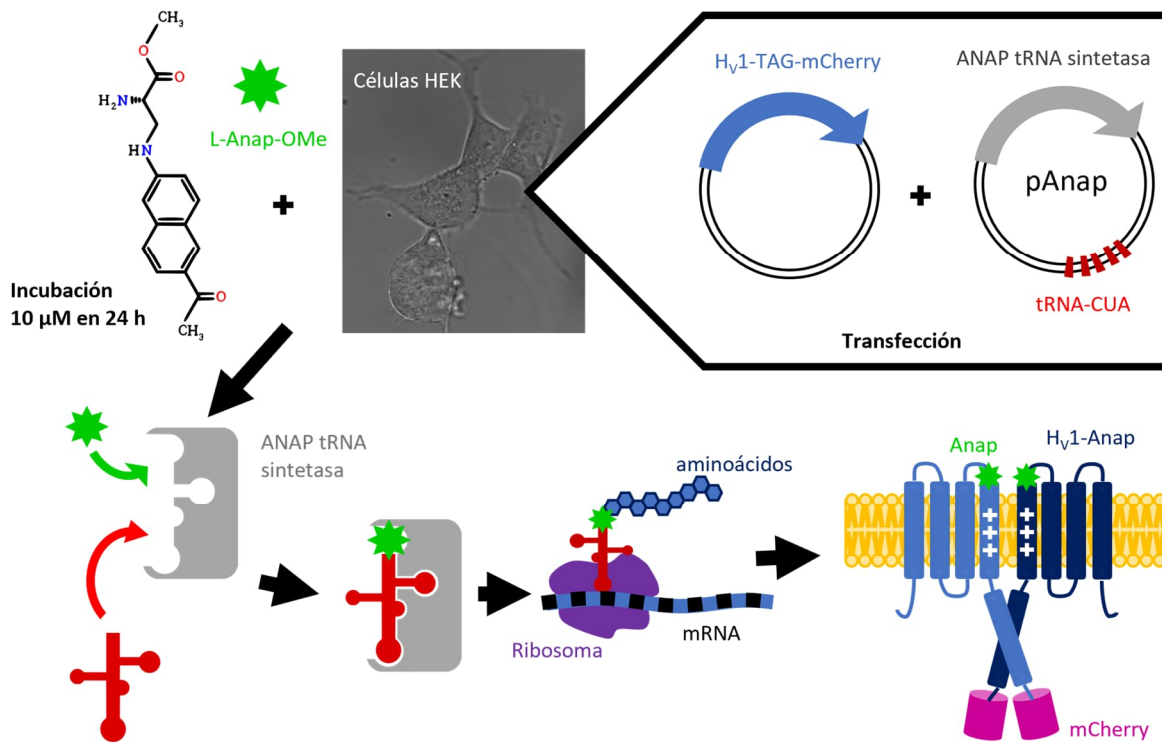


Figura 6. Esquema de sistema de incorporación de Anap a través de la supresión del codón ámbar adaptado para el canal Hv1. En la transfección se combinan los plásmidos de la proteína diana HV1-TAG-mCherry y el pAnap que contiene la información genética para sintetizar la enzima ANAP tRNA sintetasa (marcas grises) y el tRNA-CUA (marcas rojas) capaz de leer el codón ámbar. Post-transfección, se incubaron las células con 10 µM de L-Anap-OMe (marcas verdes). La presencia del aminoácido, junto con la expresión simultánea del par ANAP tRNA sintetasa/TRNA-CUA permitió que la sonda se incorpore dentro de la secuencia del canal.

En este proyecto, se eligió la proteína fluorescente mCherry como proteína reportera debido a que sus espectros de excitación (con pico en 587 nm) y emisión (con pico en 610 nm) se encuentran alejados del láser de 405 nm que se utilizó para excitar la sonda fluorescente Anap (Shu et al., 2006). Otra razón importante para la elección de mCherry fue que la constante de acidez (pKa) de su fluoróforo es de alrededor de 4.5. La acidez del entorno puede llevar a la protonación de los fluoróforos, cambiando su ambiente electrónico y, por ende, afectando la intensidad de su brillo en valores cercanos al pKa (Merzlyak et al., 2007; Shu et al., 2006). El pKa de mCherry se encuentra al menos a un orden de magnitud por debajo del pH intracelular más ácido con el que se trabajó durante los experimentos de PCF (pH de 5.5 a 7.5). En estos valores de pH más básicos que el pKa del fluoróforo de mCherry, este se encuentra desprotonado, lo que propicia que sus valores de fluorescencia sean estables en presencia de corrientes salientes de protones y cambios locales de acidez que pueden ser provocados por la función de H_v1.

Teniendo en cuenta estos factores, se diseñó una proteína de fusión con el canal hH_v1 (que es una amable donación del Dr. Scott Ramsey, Virginia Commonwealth University, Richmond, Virginia, EUA) y la proteína fluorescente (PF) mCherry en el extremo C-terminal del canal, unidos por un linker de 9 aminoácidos (GGSGGSGGS). Esta proteína hH_v1-GGSGGSGGS-mCherry (H_v1-Cherry de ahora en adelante) fue utilizada como construcción de fondo para la incorporación de Anap dentro de la secuencia de hH_v1, que por simplicidad en adelante solo se mencionará como H_v1.

El plásmido codificante de la proteína de fusión recién mencionada, H_v1-mCherry, se sintetizó a través de una variante de la técnica de reacción en cadena de la polimerasa (PCR) llamada PCR-Overlap (Nelson & Fitch, 2011). En esta técnica se usan dos pares de oligonucleótidos que reconocen la secuencia genética de los extremos de cada una de las dos proteínas de interés, en este caso H_v1 y mCherry

(figura 7). Además de reconocer estos extremos, los oligonucleótidos contienen la secuencia del linker de 9 aminoácidos que se localizó entre las dos proteínas y de sitios de restricción enzimática a los extremos de la secuencia de la nueva proteína de fusión para su integración a un vector de expresión. Así, con una primera reacción de PCR se obtienen dos productos que pertenecen al H_v1+linker y al linker+mCherry. En una subsecuente PCR, se colocan los dos productos previos junto con los oligonucleótidos de los extremos, que contienen los sitios de restricción que se utilizaron para la clonación dentro de un plásmido, en este caso pcDNA 3.1. La integridad del producto de esta segunda PCR y la subclonación al plásmido se verificaron por análisis de restricción del plásmido mientras que la secuencia genética se confirmó a través de reacciones de secuenciación realizadas en la unidad de biología molecular del Instituto de Fisiología Celular.

Como se mencionó anteriormente, la proteína resultante H_v1-mCherry se utilizó como fondo para la introducción de mutaciones puntuales usando la secuencia del codón ámbar (TAG) dentro de sitios específicos del canal iónico H_v1 ya que el sistema de incorporación de este aminoácido requiere la presencia de un codón ámbar dentro de la secuencia genética de la proteína diana, en el lugar del codón del aminoácido que se desea reemplazar. Los aminoácidos más relevantes se encuentran en la región extracelular del segmento transmembranal S4 (figura 8). Se seleccionó este enfoque debido a la evidencia que sugiere que dicho segmento dentro de los VSD es el que contiene los residuos con carga eléctrica positiva que hacen que los dominios sean sensibles al campo eléctrico de la membrana. Esta sensibilidad se traduce en un movimiento voltaje-dependiente en dirección extracelular en respuesta a la despolarización, lo que lleva a la activación del VSD ya la apertura del canal en la mayoría de los canales iónicos dependientes del voltaje (Bezanilla, 2018; Catacuzzeno et al., 2023; Talwar & Lynch, 2015).

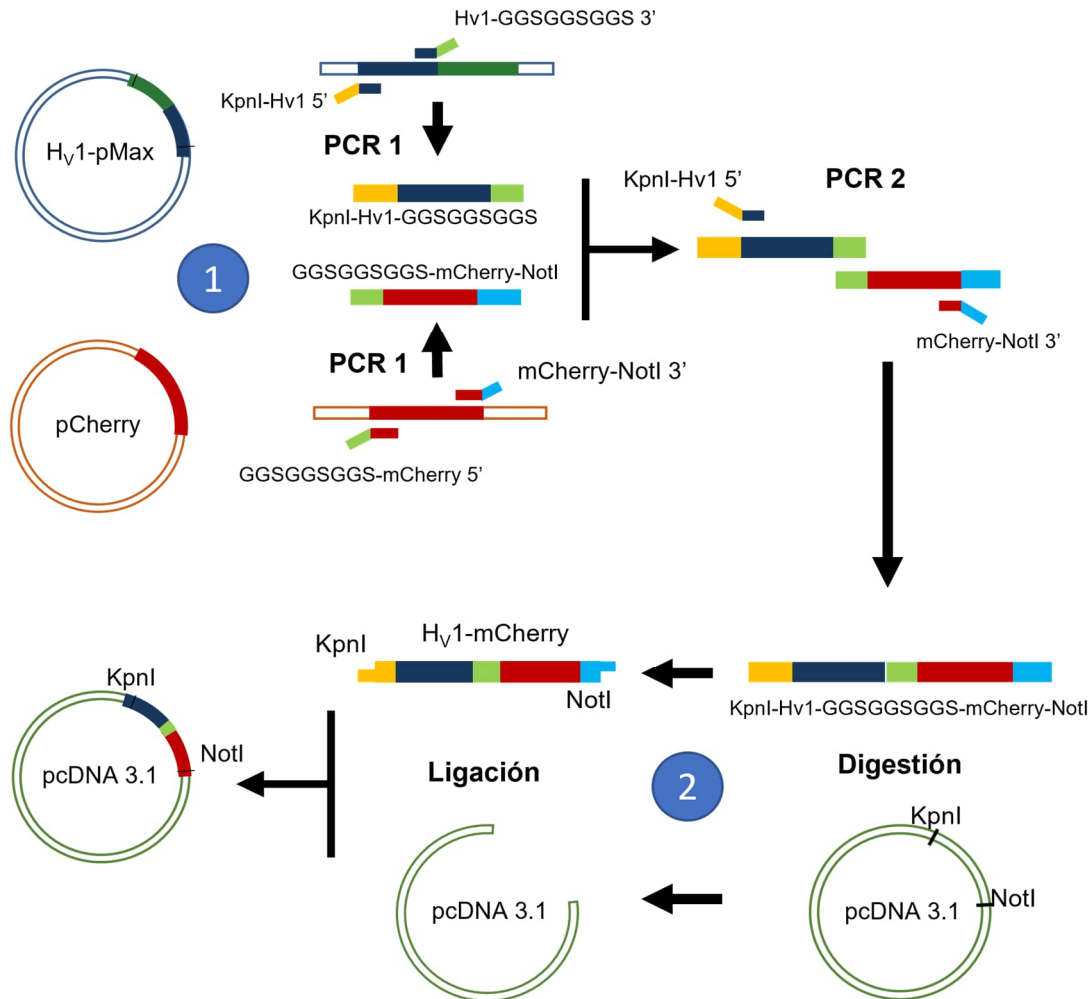


Figura 7. Esquema de construcción del plásmido codificante de la proteína de fusión Hv1-mCherry. En un primer paso (1) se realizan las PCR para obtener la secuencia del canal iónico (azul marino) y de la mCherry (rojo) de sus respectivos vectores unidos a las secuencias de restricción KpnI (amarillo) y NotI (azul claro). En una segunda PCR, se usan los productos del primer paso junto con los oligonucleótidos KpnI-Hv1-linker y linker-mCherry-NotI para obtener la secuencia de la proteína fluorescente unida al C-terminal del canal iónico con un linker de 9 residuos (verde claro) que se subclonó (2) a pcDNA3.1 usando de nueva cuenta los sitios de restricción KpnI y NotI.

Los sitios seleccionados inicialmente para incorporar la sonda fluorescente se encuentran: A197, L198, G199, L200, L201 e I202. Además, se eligió el sitio Q191, que se encuentra en el asa que une al STM 3 con el STM 4 una región común de incorporación de sondas fluorescentes en los canales iónicos; y en el sitio V62 que se encuentra en el dominio citoplasmático N-terminal, para la evaluar la fluorescencia en un sitio donde en principio la polaridad del solvente no cambia.

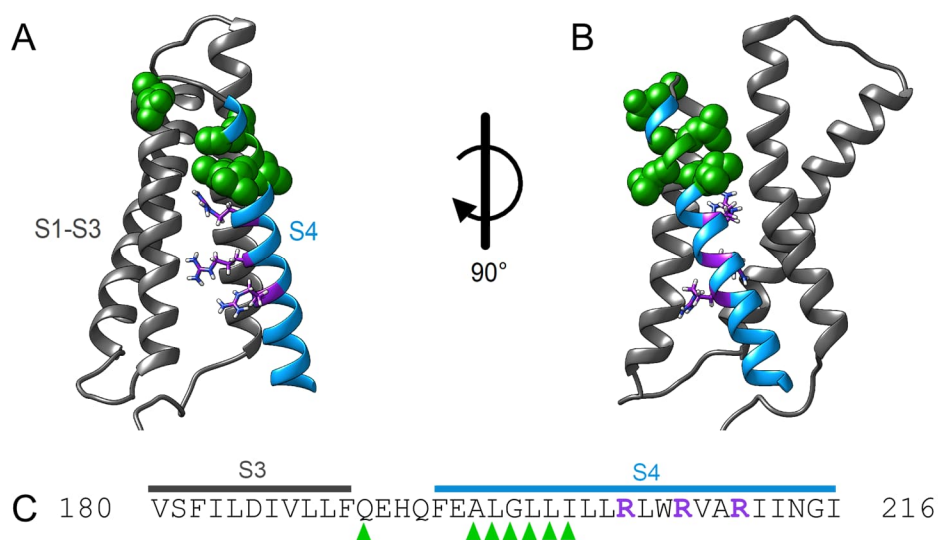


Figura 8. Esquema de sitios en donde se incorporó Anap en Hv1. A y B. Visión lateral de los segmentos transmembrana S1-S4 del VSD Hv1 en estado desactivado basado en el modelo de Geragotelis et. al. 2020. La región extracelular se localiza en la parte superior del modelo, S1-S3 están en gris mientras que S4 está en azul claro. Los residuos de arginina con carga positiva de S4 se muestran en púrpura y los residuos en los que se incorporó individualmente Anap están resaltados en esferas verdes y con puntas de flecha verdes en la secuencia de la región S3-S4 del canal en C.

Para realizar las mutaciones en los sitios mencionados se empleó la técnica de mutagénesis puntual a través de una DNA polimerasa de alta fidelidad nombrada KOD (Novagen). En este método, se diseñaron los oligonucleótidos reemplazando el triplete de nucleótidos que corresponde al del aminoácido que se sustituirá por el Anap con la secuencia TAG. En la tabla 1 se muestran los diferentes oligonucleótidos diseñados para la incorporación de Anap en los sitios escogidos. Con estos oligonucleótidos se realizó una PCR de plásmido completo (Munteanu et al., 2012) del pcDNA 3.1 donde se encuentra la proteína de fusión Hv1-Cherry. El producto de esta PCR se trató con la enzima de restricción DpnI, que degradó al plásmido original que se encuentra metilado debido a su síntesis bacteriana. Los plásmidos nuevos, sintetizados *in-vitro*, contienen ahora el codón ámbar en el sitio elegido para la introducción del Anap.

Se realizó la transformación de bacterias competentes DH5 α con el plásmido pcDNA 3.1/Hv1-TAG-Cherry resistente a penicilina. Las bacterias se cultivan en LB-

agar con penicilina para la selección de clonas positivas. Se extrajo el plásmido de diversas colonias de bacterias a través de un protocolo Midi-Prep (QIAGEN) siguiendo las instrucciones del fabricante. Se eligió un plásmido que haya contenido exitosamente la construcción Hv1-TAG-Cherry para realizar una reacción de secuenciación y así verificar la integridad de dicha construcción. Las construcciones que presentaron la mutación de manera exitosa se utilizaron para la expresión heteróloga y los experimentos de fluorescencia y electrofisiología en células HEK293. Aquellas colonias con la construcción correcta se guardaron en criotubos con glicerol y se almacenaron a -75 °C.

Sitio	Oligonucleótido	Secuencia
Q191	Hv1-Q191TAG 5'	GACATTGTCCTCCTGTTCTAGGAGCACCAGTTTGAGGCT
	Hv1-Q191TAG 3'	AGCCTCAAACCTGGTGCTCCTAGAACAGGAGGACAATGTC
A197	Hv1-A197TAG 5'	CAGGAGCACCAGTTTGAGTAGCTGGGCCTGCTGATTCTG
	Hv1-A197TAG 3'	CAGAATCAGCAGGCCAGCTACTCAAACCTGGTGCTCCTG
L198	Hv1-L198TAG 5'	GAGCACCAGTTTGAGGCTTAGGGCCTGCTGATTCTGCTC
	Hv1-L198TAG 3'	GAGCAGAATCAGCAGGCCCTAAGCCTCAAACCTGGTGCTC
G199	Hv1-G199TAG 5'	CACCAGTTTGAGGCTCTGTAGCTGCTGATTCTGCTCCGG
	Hv1-G199TAG 3'	CCGGAGCAGAATCAGCAGCTACAGAGCCTCAAACCTGGTG
L200	Hv1-L200TAG 5'	CAGTTTGAGGCTCTGGGCTAGCTGATTCTGCTCCGGCTG
	Hv1-L200TAG 3'	CAGCCGGAGCAGAATCAGCTAGCCCAGAGCCTCAAACCTG
L201	Hv1-L201TAG 5'	TTTGAGGCTCTGGGCCTGTAGATTCTGCTCCGGCTGTGG
	Hv1-L201TAG 3'	CCACAGCCGGAGCAGAATCTACAGGCCAGAGCCTCAAAA
I202	Hv1-I202TAG 5'	GAGGCTCTGGGCCTGCTGTAGCTGCTCCGGCTGTGGCGG
	Hv1-I202TAG 3'	CCGCCACAGCCGGAGCAGCTACAGCAGGCCAGAGCCTC

Tabla 1. Secuencias de los diferentes oligonucleótidos utilizados para la mutagénesis puntual en la construcción Hv1-cherry. En rojo se resalta la inserción de la secuencia del codón ámbar para los experimentos de incorporación de Anap.

Expresión en células HEK 293

Para los experimentos de electrofisiología y fluorescencia se usó la línea celular adherente proveniente de células de riñón embrionario humano, HEK293 (Human Embryonic Kidney 293). Estas células se cultivaron y mantuvieron en medio

DMEM (ThermoFisher) suplementado con suero bovino fetal (5 %) y penicilina-estreptomicina (1 %) a 37°C en una atmósfera controlada de 95% de aire y 5 % de CO₂. Para su uso experimental, las células se disociaron usando tripsina-EDTA (ThermoFisher) y colocaron en cajas de Petri de 35 mm con fondo de vidrio (World Precision Instruments) y medio DMEM fresco. Después de 24 horas, las células se transfectaron usando el agente jetPei (Polyplus) bajo las especificaciones del fabricante. En el protocolo de transfección, los plásmidos elegidos se mezclaron con el agente jetPei (5 µl) en 200 µl de solución 150 mM NaCl y se incubaron durante media hora previa a su aplicación en las células HEK 293.

Para los experimentos de incorporación de Anap, se cotransfectó 750 ng del plásmido pAnap (que contiene el par AnapRS) junto con 500 ng del plásmido de las diferentes mutantes H_v1-TAG-Cherry. Previo a la transfección, a las células transfectadas se les cambió el medio y posteriormente se les agregó la solución del agente de transfección junto con el plásmido. Al final, se colocó la versión éster metílico del aminoácido Anap (L-Anap-OMe, AsisChem Inc., ASIS-0146, stock a 10mM en DMSO) al medio a una concentración final de 10 µM (figura 6). Esta forma esterificada permite al aminoácido cruzar la membrana celular, y ya en el citoplasma es hidrolizado por las esterasas nativas no específicas en la versión final L-Anap que podrá ser empleado en la síntesis del canal (M. C. Puljung, 2021; Zagotta et al., 2016). Después de la aplicación del Anap, las células se incubaron a 37 °C en una atmósfera controlada de 95 % de aire y 5 % de CO₂.

Los registros de corriente y fluorescencia de las células se realizaron entre 12 y 24 horas después de la transfección. Cuatro horas previas al registro, las células se sometieron a un protocolo en el cual se sustituyó el medio de cultivo por 300 µl de un medio al que se adicionado con tripsina a una concentración de 0.25 % durante 4 o 5 minutos. Después, se colocó de nueva cuenta 2 ml de medio DMEM fresco, que inactivó a la tripsina y permitió que las células comenzaran a adherirse

al vidrio de la cámara de registro. Esto permitió tener células redondeadas para el experimento, lo que facilita la formación del sello y el control del voltaje.

Electrofisiología

Para la medición de las corrientes de protones a través de los canales H_v1 en las membranas de células HEK se usó la técnica de patch-clamp en su modalidad de célula completa o *whole-cell*. Esta poderosa técnica creada hace cerca de 50 años permite fijar el potencial eléctrico de la membrana celular con una alta resolución temporal y así inducir los diferentes estados por los que transitan los canales iónicos activados por voltaje, así como las corrientes iónicas que fluyen por ellos (Cahalan & Neher, 1992; Hille, 2001; Neher & Sakmann, 1976).

Para realizar esta técnica, es necesario el uso de un amplificador que contiene un circuito especializado para medir corrientes eléctricas de magnitudes dentro del rango de nanoamperios (10^{-9}) a picoamperios (10^{-12}), además de tener la capacidad de mantener fijo el potencial de la membrana celular a los valores con los cuales se decida experimentar. Una versión simple del circuito utilizado donde se muestran sus componentes más esenciales se expone en la figura 9. En este esquema se puede observar que el circuito del amplificador se conecta a la célula a través de una pipeta de borosilicato llena de solución fisiológica en donde se coloca el electrodo de registro. Durante el estímulo, el flujo de iones que atraviesa los canales produce una corriente que pasa por este electrodo (I_p) que cambia el voltaje de la pipeta (V_p). El voltaje de la pipeta es comparado de forma continua con el voltaje comando (V_{com}) aplicado por el experimentador a través de un amplificador operacional (op-amp). La diferencia entre estos dos voltajes, V_p y V_{com} , se reingresa automáticamente de vuelta a la pipeta mediante un asa de retroalimentación que contiene un resistor (R_f). Esto resulta en una inyección de corriente que retorna el voltaje V_p a valores idénticos de V_{com} , fijando así el potencial eléctrico de la

membrana. Entonces, la corriente inyectada tiene la misma magnitud que la corriente iónica disipada a través de los canales iónicos que se hayan abierto durante el estímulo y se calcula con un amplificador diferencial que obtiene el voltaje de salida (V_{out}) = $I_p R_r$. Es decir, el V_{out} es la diferencia entre el voltaje del amplificador operacional y V_{com} y es igual al producto de la corriente que fluye por los canales (I_p) y la resistencia R_r . Además, entre más grande sea R_r mayor será la sensibilidad del circuito para el registro electrofisiológico dado que los cambios de V_{out} serán más grandes aún con corrientes muy pequeñas (Sigworth, 1995).

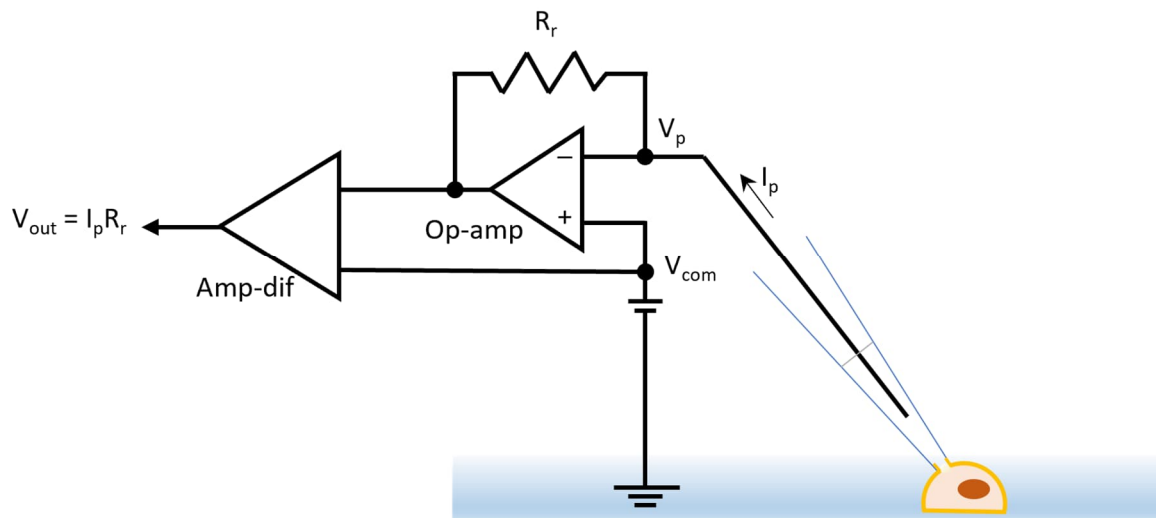


Figura 9. Esquema simplificado de un circuito durante un experimento típico de Patch-clamp en la configuración célula completa. Al momento de romper la membrana celular al interior de la pipeta sin dañar la integridad del sello, el potencial a través de la membrana es sostenido o fijado mediante la inyección de corriente a través de una resistencia de retroalimentación (R_r). Dicha corriente es el resultado de la función de un amplificador operacional (Op-Amp) que compara constantemente el potencial de la pipeta (V_p) y el potencial comando (V_{com}) que elige el experimentador.

Como se mencionó en el párrafo anterior, la forma de conectar la célula al circuito del amplificador, garantizando la fijación del potencial eléctrico de la membrana, es a través de la formación de sellos de esta con una pipeta de borosilicato cuya punta tenga de 1 a 2 micras de diámetro interno. La membrana lipídica que entra en contacto con la pipeta obstruye la corriente eléctrica que fluye hacia el electrodo de registro dentro de la pipeta de borosilicato, creando un sello y por lo tanto una resistencia dentro del circuito. Si la resistencia del sello es mayor a

un gigaohm ($G\Omega$), técnicamente se considera que se ha logrado exitosamente el sello bajo la configuración de célula unida o *cell-attached* u *on-cell* (figura 10). Con esta configuración se puede controlar el voltaje a través de la porción de la membrana que se encuentra dentro de la pipeta manteniendo intacta la composición intracelular. A partir de esta configuración se pueden alcanzar las demás configuraciones que otorgan un poderoso arsenal para el estudio de los canales iónicos a diferentes niveles. Por un lado, si se decide retirar la pipeta de la célula manteniendo la integridad del sello, se puede escindir una porción de la membrana originando la modalidad *inside-out*, donde se expone al baño la porción citoplasmática de los canales.

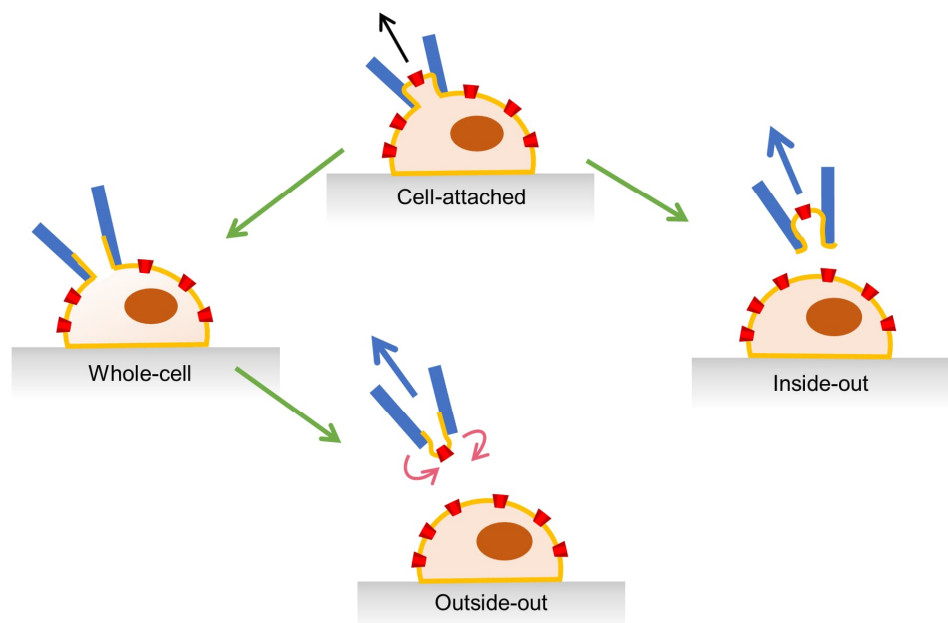


Figura 10. Técnica de Patch-clamp y sus configuraciones. Se esquematiza la punta de una pipeta de vidrio haciendo contacto con la membrana celular (líneas azules) haciendo contacto y presión negativa (flecha negra) con la membrana celular (figuras amarillas). Además, se muestra la secuencia de obtención para las demás configuraciones (flechas verdes) según los movimientos de la pipeta después de alcanzar las configuraciones previas (flechas azules) y la respuesta de la membrana celular a este movimiento (flechas rosas). Los canales iónicos son esquematizados en forma de conos rojos truncados. Nótese como la disposición del canal cambia de dirección entre las configuraciones outside-out e inside-out.

Si más bien se decide romper la membrana dentro de la pipeta manteniendo la resistencia del sello, se accede a la configuración *whole-cell* o célula completa. Como su nombre lo indica, esta modalidad permite tener registro de todos los canales iónicos que se expresan en la totalidad de la membrana, además de controlar el contenido citoplasmático mediante la solución de la pipeta.

Por último, si después de alcanzar la modalidad de célula completa, se decide alejar la pipeta de la célula cuidadosamente, se puede separar una parte de la membrana que tenderá a reorganizarse en un parche más pequeño en donde la cara extracelular de los canales se dirige hacia el baño, alcanzando la modalidad *outside-out*, útil para investigación de ligandos extracelulares que modulen la actividad del canal (Cahalan & Neher, 1992).

Adquisición de datos electrofisiológicos

En este proyecto se recurrió a la modalidad de *whole-cell* para poder cuantificar la mayor señal posible, tanto de fluorescencia como de la corriente de protones. Se forjaron pipetas con capilares de borosilicato (Sutter Instruments) que tenían una punta con diámetro de 2-3 μm y una resistencia de 2-5 $\text{M}\Omega$. Los experimentos se realizaron a una temperatura ambiente de 23-25 $^{\circ}\text{C}$. Las soluciones empleadas para el registro se resumen en la tabla 2. Como se puede apreciar en la tabla, se mantuvo un $\Delta\text{pH} = 0, 1$ o 2 dependiendo de la necesidad de los experimentos. Al momento de obtener el gigasello en la configuración *cell-attached*, se dejó estabilizar el sello durante 2 minutos antes de realizar la modalidad *whole-cell*. Después de obtener dicha modalidad, se dejó reposar durante 7 minutos para permitir que el citoplasma se dializará por la solución de la pipeta y que el sello se estabilizara.

Solución intracelular	Solución extracelular
80 mM TMA OH ⁻	80 mM TMA OH ⁻
80 mM MeSO ₃ H ⁺	80 mM MeSO ₃ H ⁺
10 mM EGTA	2 mM CaCl ₂
10 mM MgCl ₂	2 mM MgCl ₂
8 mM HCl	4 mM HCl
100 mM Buffer (MES o HEPES)	100 mM Buffer (MES o HEPES)
pH 5.5, 6, 6.5 o 7 (titulado con TMA OH ⁻ o MeSO ₃ H ⁺)	pH 5.5 6, 6.5 o 7 (titulado con TMA OH ⁻ o MeSO ₃ H ⁺)

Tabla 2. Soluciones utilizadas en los experimentos de Patch-clamp Fluorometry

TMA OH⁻: Hidróxido de Tetrametilamonio

MeSO₃ H⁺: Ácido Metanosulfónico

El registro de las corrientes se realizó con un amplificador Axopatch 200b (Axon), las corrientes macroscópicas se obtuvieron a 20 kHz y se filtraron a 5kHz. Los datos se adquirieron con el software PATCHMASTER (HEKA Elektronik GMBH). Las corrientes obtenidas se analizaron con el programa IGOR Pro (Wavemetrics Inc).

El cálculo de la conductancia en las corrientes de protones que se obtuvieron en whole-cell (G_H) se realizó a través de la ecuación de Ohm:

$$G(V) = \frac{I(V)}{V - V_{rev}} \quad \text{Ecuación 1}$$

Donde V es el voltaje al pulso prueba, $I(V)$ es la corriente de protones a dicho pulso prueba y V_{rev} es el potencial de reversión que se obtuvo a través de la ecuación de Nernst para el ion H⁺. Estos datos de conductancia se ajustaron a la ecuación de Boltzmann para obtener el voltaje medio de activación del canal y el movimiento de carga aparente asociada a la apertura del canal:

$$\frac{G}{G_{max}} = \frac{1}{1 + \exp\left(-\frac{z(V - V_{0.5})}{k_B T}\right)}$$

Donde z es la carga aparente asociada a la apertura del canal (en unidades de e_0); G_{max} es la conductancia máxima; $V_{0.5}$ es el voltaje medio de activación (el valor de potencial en donde se registra la activación del 50% de los canales), k_B es la constante de Boltzmann y T es la temperatura en grados Kelvin.

Adquisición de fluorimetría y espectrometría

Los valores de fluorescencia de la proteína fluorescente y la sonda Anap utilizadas en los experimentos de *whole-cell* se obtuvieron mediante un set conformado por un microscopio de epifluorescencia (Nikon TE-200U) que utiliza un Láser Ar-Ion (Spectra-Physics) para la excitación de Cherry y un láser de estado sólido con emisión de 390 a 410 nm (Compas 405-50 CW-COHERENT) para la excitación de Anap. Ambos láseres están acoplados al puerto de iluminación del microscopio mediante un riel de componentes ópticos diseñados y fabricados en el laboratorio. Los componentes son: lente bola 3 mm, filtros de densidad neutra (ND), lente colimador de 50 mm de distancia focal y un lente de 300 mm que enfoca al haz de luz al objetivo. Dentro del microscopio se tienen acoplados en cubos preensamblados los filtros de excitación, espejos dicróicos y filtros de emisión que son específicos para cada uno de los fluoróforos a utilizar. Los que se usaron para los experimentos con Anap y Cherry se resumen en la siguiente tabla:

Proteína Fluorescente	Filtro de excitación	Espejo dicróico	Filtro de emisión
Anap	405/20x	z405rdc	ET 425 lp
mCherry	514/10x	z514rdc	HQ 530 lp

Tabla 3. Arreglos de filtros de excitación y emisión junto con el espejo dicróico que se usaron para cada proteína fluorescente.

El tiempo de exposición al láser se controló por un obturador Uniblitz VMM-D1 (Vincent Associates) colocado a la salida del láser y controlado por el software Micromanager (versión 1.4). Las muestras se observaron en el microscopio de epifluorescencia con un objetivo de inmersión en aceite Nikon x60, con una apertura numérica de 1.4. La luz se captó mediante una cámara EMCCD (iXon Ultra, Andor) controlada por Micromanager (figura 11). Las imágenes de la fluorescencia obtenida en los experimentos se analizaron con los programas Image J e Igor Pro (Wavemetrics).

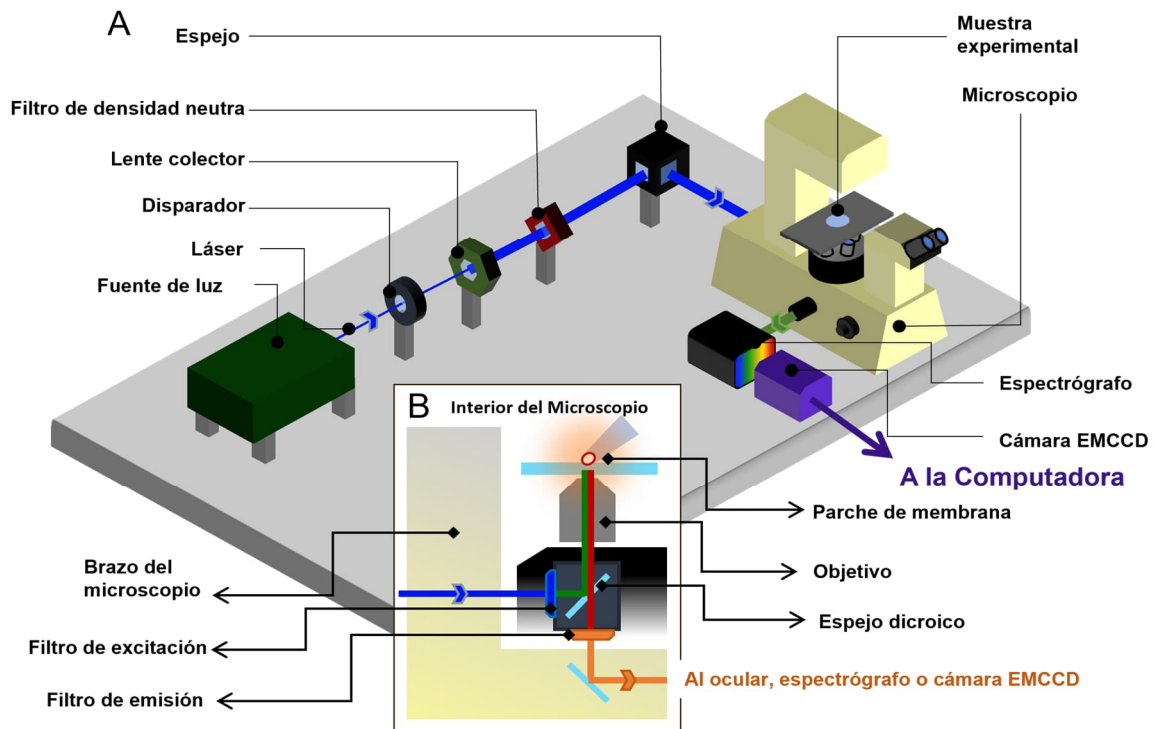


Figura 11. Esquema de un set de microscopía de fluorescencia. En azul se muestra el láser y su dirección con puntas de flecha azules. **A.** Recorrido del láser fuera del microscopio y el equipamiento con el que se controlan sus propiedades. **B.** Recorrido del láser dentro del microscopio. Nótese que el láser cambia de longitud de onda gracias a los filtros de emisión y excitación. Modificado de (Suárez-Delgado & Islas, 2020).

Para las mediciones espectrales, la luz del microscopio se dirigió a través de un espectrógrafo de gradilla SpectraPro 2150i (Princeton Instruments, EE. UU.) montado entre el microscopio y la cámara EMCCD. La fluorescencia de mCherry se

utilizó como indicador de los canales asociados a la membrana. Se selecciona una pequeña área de la fluorescencia mCherry asociada a la membrana usando la rendija del espectrógrafo, y los espectros mCherry y Anap se registraron midiendo un escaneo lineal de 10 píxeles de ancho desde la imagen espectral de la membrana celular (figura 12). El espectro de fluorescencia de fondo se registró a partir de una región de la imagen sin células y se restó de la fluorescencia de Anap y mCherry. A menos que se indique lo contrario, todos los espectros se obtuvieron a potencial de reposo en células no parcheadas (P. Thomas & Smart, 2005) y un $\Delta\text{pH} \sim -0,2$.

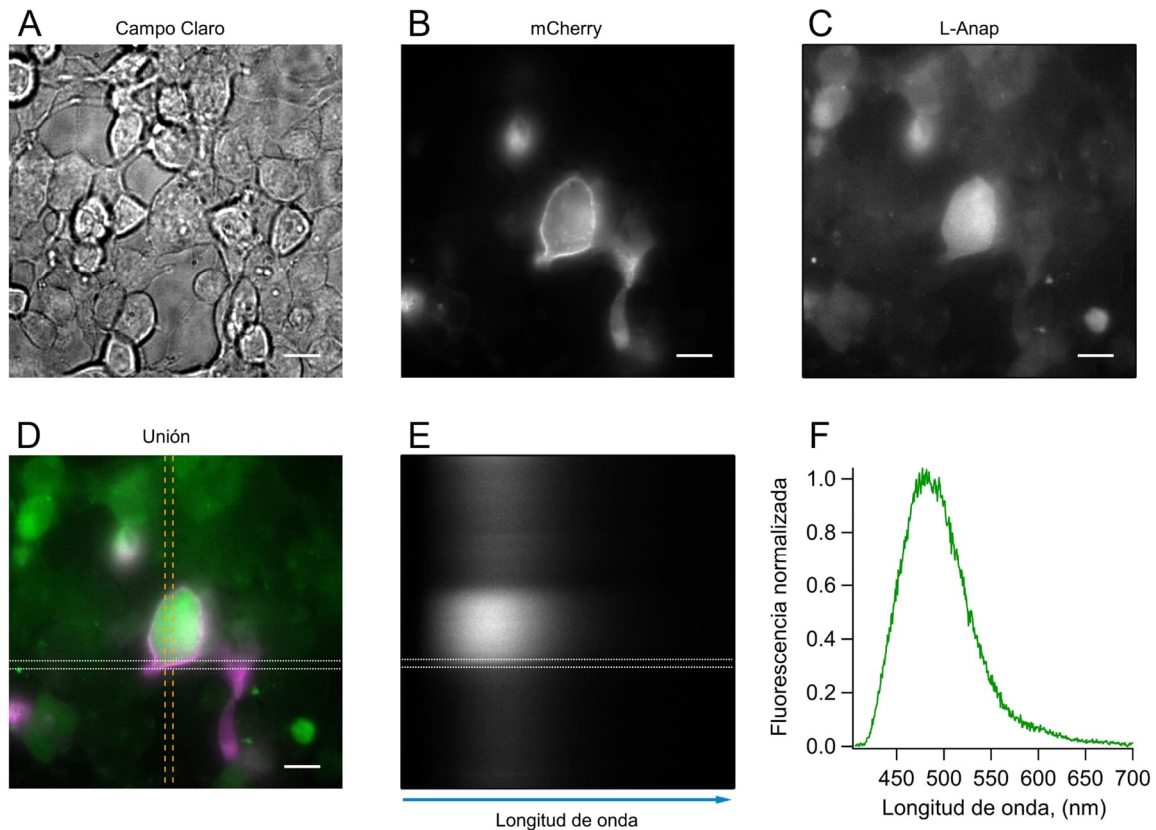


Figura 12. Procedimiento para la medición del espectro de Anap. La célula HEK293 que se va a registrar se elige en el campo claro (A) y se excita la señal fluorescente de mCherry (B) a 514 nm. Cuando se confirma la fluorescencia de Anap, excitando la célula a 405 nm (C), se aísla una porción de la membrana celular con la rendija del espectrógrafo (D), líneas amarillas verticales discontinuas; señal de mCherry en magenta; señal de Anap en verde). El espectrógrafo dispersa la luz Anap que pasa por esta rendija (E), produciendo una imagen espectral, y se realiza un escaneo lineal (líneas horizontales discontinuas blancas en E y D) de la membrana identificada por la fluorescencia de mCherry. La intensidad de fluorescencia medida en este escaneo se presenta en F. Barra de escala = 10 μm .

Los protocolos de adquisición de fluorescencia durante los experimentos de Patch-Clamp Fluorometry estuvieron bajo la dirección del software PatchMaster (HEKA) mediante el uso de un arduino UNO (Arduino) que acopló y convirtió una señal inicial analógica proveniente del amplificador en forma de pulso TTL en un pulso digital que Micromanager reconocía para activar la cámara y el disparador. Con estas herramientas se logró sincronizar el registro electrofisiológico con el de fluorescencia. La frecuencia de adquisición de cada pila de imágenes fluorescentes correspondientes a cada paso del protocolo de voltaje fue de 10-25 Hz (100 a 40 ms de tiempo de exposición). Para mejorar la captación de luz y la velocidad de adquisición, se utilizó una modalidad llamada *binning* que consiste en sumar la luz colectada de varios píxeles adyacentes, sacrificando la resolución espacial de la imagen. Entre las diferentes modalidades se usaron: BIN 8 (64 píxeles) BIN 4 (16 píxeles) y BIN 2 (4 píxeles) en la adquisición de la cámara.

La fluorescencia de las imágenes obtenidas se evaluó con la creación de un ROI (*region of interest* en inglés) que tomaba toda la extensión de la membrana celular. A estos datos se le restó la fluorescencia basal del campo óptico (*background*) para conseguir la fluorescencia absoluta de la célula. Después, los cambios de fluorescencia se normalizaron bajo la siguiente fórmula:

$$\% \text{ de cambio de fluorescencia} = \frac{F_i - F_0}{F_0} \times 100 = \frac{\Delta F}{F_0} \times 100$$

Ecuación 3

Donde ΔF es el valor de la fluorescencia absoluta de cada imagen de la pila (F_i) menos el valor de la fluorescencia absoluta al inicio del protocolo (F_0).

Asimismo, a los valores de fluorescencia de cada paso se les corrige el fotoblanqueo, que es el fenómeno de la destrucción fotoquímica de un fluoróforo debido a su exposición continua a la luz que lo excita. Para dicha corrección, se ajusta una doble exponencial al segundo o tercer paso del protocolo. Después, la

tendencia obtenida del ajuste se sustrae matemáticamente en cada registro de fluorescencia del protocolo.

Seguidamente, para la construcción de las curvas de cambios de fluorescencia en función del voltaje (curvas F-V), los valores de fluorescencia obtenidos al final de cada pulso prueba se normalizaron respecto al valor de fluorescencia del paso con voltaje más positivo del protocolo. A las curvas resultantes se les ajusta la siguiente ecuación de Boltzmann:

$$\frac{F}{F_{max}} = \frac{1}{1 + \left(-\frac{z(V - V_{0.5})}{k_B T} \right)} \quad \text{Ecuación 4}$$

Donde F es el valor de fluorescencia al final del pulso prueba V y F_{max} es el máximo valor de cambio de fluorescencia, mientras que las demás variables tienen el mismo significado que en la ecuación 2.

Modelo cinético

La reproducción de las señales de corriente fluorescencia correspondientes a los modelos cinéticos en los esquemas I y II se calcularon usando programas escritos dentro del software IgorPro. La probabilidad de ocupar cada estado discreto en los modelos se calculó mediante la resolución numérica de las ecuaciones diferenciales que describen las transiciones entre dichos estados. Por lo tanto, P_i es la probabilidad de residir cada estado discreto i y se calculó a través de la ecuación:

$$\frac{dP_i}{dx} = \sum_{i \neq j} (P_j k_{ji} - P_i k_{ij}) \quad \text{Ecuación 5}$$

Las constantes de velocidad k_{ij} o k_{ji} entre los diferentes estados i y j son dadas por:

$$k_{ij} = k_{ij}(0) \cdot \exp(-z_{ij}V/k_B T) \quad \text{Ecuación 6}$$

Donde $k_{ij}(0)$ es el valor de la constante de velocidad a 0 mV, z_{ij} es la carga parcial asociada con dicha transición, mientras que k_B y T tienen el mismo significado que en la ecuación 2.

Para simular la corriente iónica en función del tiempo t y los valores de voltaje prueba V , se utilizó la siguiente ecuación:

$$I(t, V) = \gamma_{ch} \cdot N \cdot (V - V_{rev}) \cdot P_o(t, V) + \gamma_{leak} \cdot (V - V_{rev}^{leak}) \quad \text{Ecuación 7}$$

Donde γ_{ch} es la conductancia unitaria del canal de protones, N es el número de canales, V_{rev} es el potencial de equilibrio de los protones y P_o es la probabilidad de residencia del canal en el estado abierto, también conocida como probabilidad de apertura. Mientras tanto γ_{leak} es la conductancia de la corriente de fuga y V_{rev}^{leak} es el potencial de reversión de las corrientes de fuga.

Por último, la señal de fluorescencia fue modelada con la ecuación:

$$F(t, V) = \sum_{i=0}^n P_i(t, V) \cdot f_i \quad \text{Ecuación 8}$$

Donde f_i es la fluorescencia del estado i en unidades arbitrarias.

Resultados

Incorporación de la sonda Anap en el canal H_V1

Para validar el sistema de incorporación, fue necesario evaluar la competencia de la proteína de fusión H_V1-mCherry como canal iónico ya que esta construcción serviría como fondo para las mutantes usadas en la incorporación del Anap en la estructura del canal. En la figura 13 A se muestran familias de corrientes tanto del canal WT como de la nueva construcción H_V1-mCherry obtenidas a un $\Delta pH = 1$, usando la técnica de patch-clamp en la modalidad de célula completa (whole-cell). Se puede observar que ambas construcciones responden a cambios de voltaje, produciendo corrientes salientes con una cinética de activación en el rango de segundos y cualitativamente sigmoidea.

Al analizar el comportamiento de ambas construcciones en función del voltaje (figura 13 B), se observa que el voltaje medio de activación ($V_{0.5}$) es similar en ambas construcciones (34.1 ± 1.5 mV en WT vs. 33.8 ± 2.5 mV en H_V1-mCherry), así como también el movimiento de carga aparente durante la activación ($1.5 \pm 0.1 e_0$ vs. $1.3 \pm 0.1 e_0$, WT vs. H_V1-mCherry, respectivamente). Estas similitudes indican que la adición de la proteína fluorescente mCherry en el C-Terminal del canal H_V1 no afectó sus propiedades electrofisiológicas, lo que lo convierte en una proteína reportera útil para la incorporación de Anap en el canal.

Teniendo establecida la validez de la proteína de fusión como fondo, se utilizó este plásmido para producir las mutantes en donde se incorporó la sonda. Utilizando la técnica de mutación puntual del plásmido completo, se logró sustituir la secuencia de diferentes codones dentro del canal H_V1 de manera individual por el codón ámbar (ver metodología, figura 8, tabla 1). Los sitios mutados al codón ámbar dentro de la porción extracelular S4 fueron A197, L198, G199, L200, L201 e I202. Mientras que

se eligieron otros dos sitios fuera del S4: Q191, que se encuentra en el asa extracelular S3-S4, una región común de incorporación de sondas fluorescentes en otros canales iónicos dependientes de voltaje; y en V62 que se encuentra en la porción N-Terminal de H_v1 .

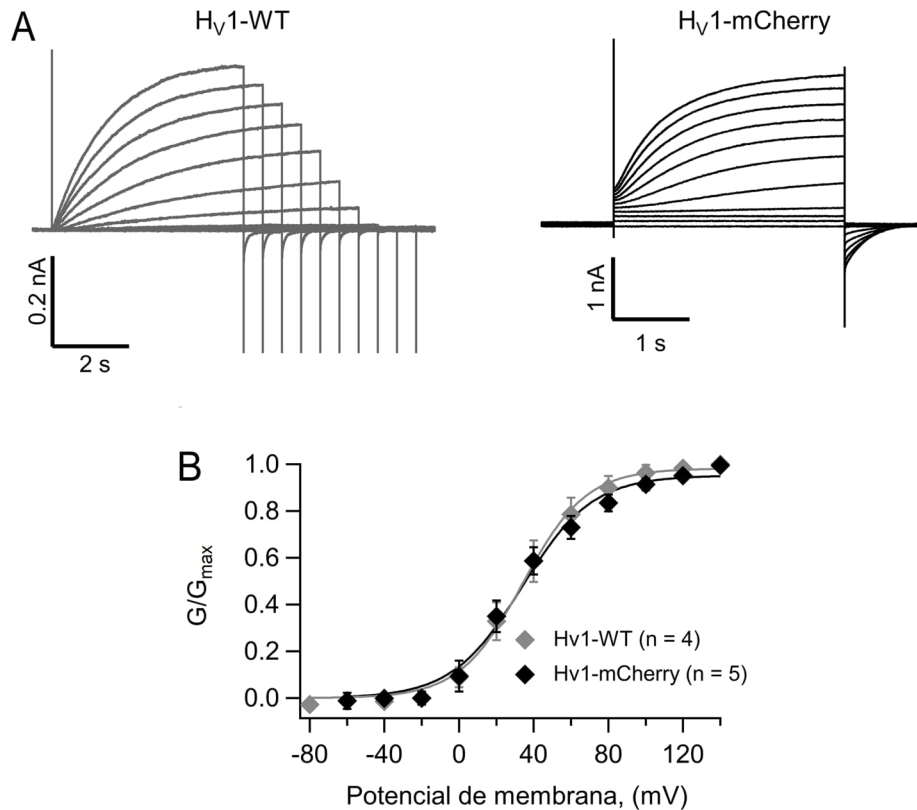


Figura 13. La adición de la proteína fluorescente mCherry en el C-terminal de H_v1 no cambió las propiedades electrofisiológicas de H_v1 . **A.** Familias de corriente obtenidas por células HEK293 transfectadas con H_v1 -WT (trazos grises) y la proteína de fusión H_v1 -mCherry (trazos negros) a $\Delta pH = 1$. Los trazos para H_v1 -WT se obtuvieron a través un protocolo de voltaje con un potencial de fijación de -80 mV y pulsos pruebas -80 mV a +140 mV en pasos de +20 mV con duración variable para reducir la aparición del fenómeno de depleción de protones. Los trazos para la proteína de fusión H_v1 -mCherry se obtuvieron con un protocolo de voltaje de pulsos prueba de 4 s de duración de -60 mV a +140 mV a partir de un voltaje de fijación de -60 mV. Con los datos de corriente al final del pulso prueba en ambas construcciones, se calcularon las relaciones conductancia-voltaje (**B**) de acuerdo con la ecuación 2, donde se puede observar que tienen un comportamiento similar.

Una vez que se tuvieron las nuevas mutantes listas para expresar, se transfectaron los plásmidos H_v1 -TAG-mCherry y el plásmido pAnap en células HEK293 y se incubaron con Anap en el medio. Entre 24 y 48 horas después de la transfección, se observó la presencia de células con integración de Anap mediante

tres observaciones en conjunto: 1) la señal de fluorescencia de Anap fue mayor en aquellas donde el rescate se realizó en comparación al resto de las células, lo que indica una mayor concentración del aminoácido no canónico en las células donde se incorporó; 2) se presentó la fluorescencia de la proteína reportera m-Cherry en la región membranal de las células transfectadas, sugiriendo que Anap rescató la traducción completa de los canales y la proteína fluorescente unida al C-Terminal (figura 14); y 3) se detectaron corrientes de protones en respuesta a voltaje, lo que demuestra la presencia de canales funcionales (figura 15).

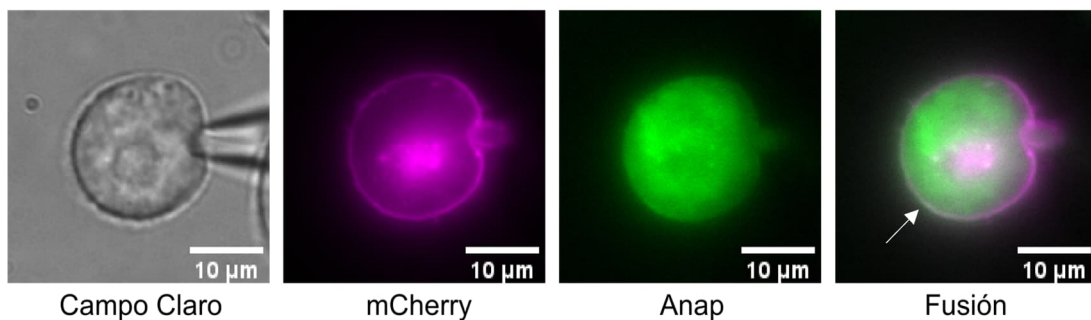


Figura 14. La fluorescencia de Anap se sobrepone a la de mCherry en la región membranal. Experimento representativo de Patch-clamp Fluorometry (PCF) que muestra una célula que ha incorporado a la sonda fluorescente en el sitio Q191 del H_v1 a través del sistema de supresión del codón ámbar. Nótese que la fluorescencia de mCherry (magenta) y Anap (verde) se sobrepone en la región membranal (flecha blanca).

Sin embargo, una posible interpretación de estos experimentos es que los canales pudieron haber incorporado otro aminoácido de forma inespecífica, compitiendo con la presencia de Anap. Para descartar esta posibilidad, se decidió investigar la especificidad del rescate evaluando la presencia de corrientes de protones y fluorescencia de Anap y mCherry en experimentos que mantuvieran la cotransfección de ambos plásmidos pero en ausencia de Anap (figura 16). Respecto a la formación de canales, estos experimentos revelaron que la falta del aminoácido no canónico evitó la formación de canales funcionales más allá de los expresados de forma endógena por células HEK sin transfectar, con una densidad de corriente de protones alrededor de 2-3 pA/pF, mientras las células sometidas a las

condiciones completas para la incorporación presentaron una densidad en el rango de 100 a 150 pA/pF, es decir, una expresión de 50 veces más.

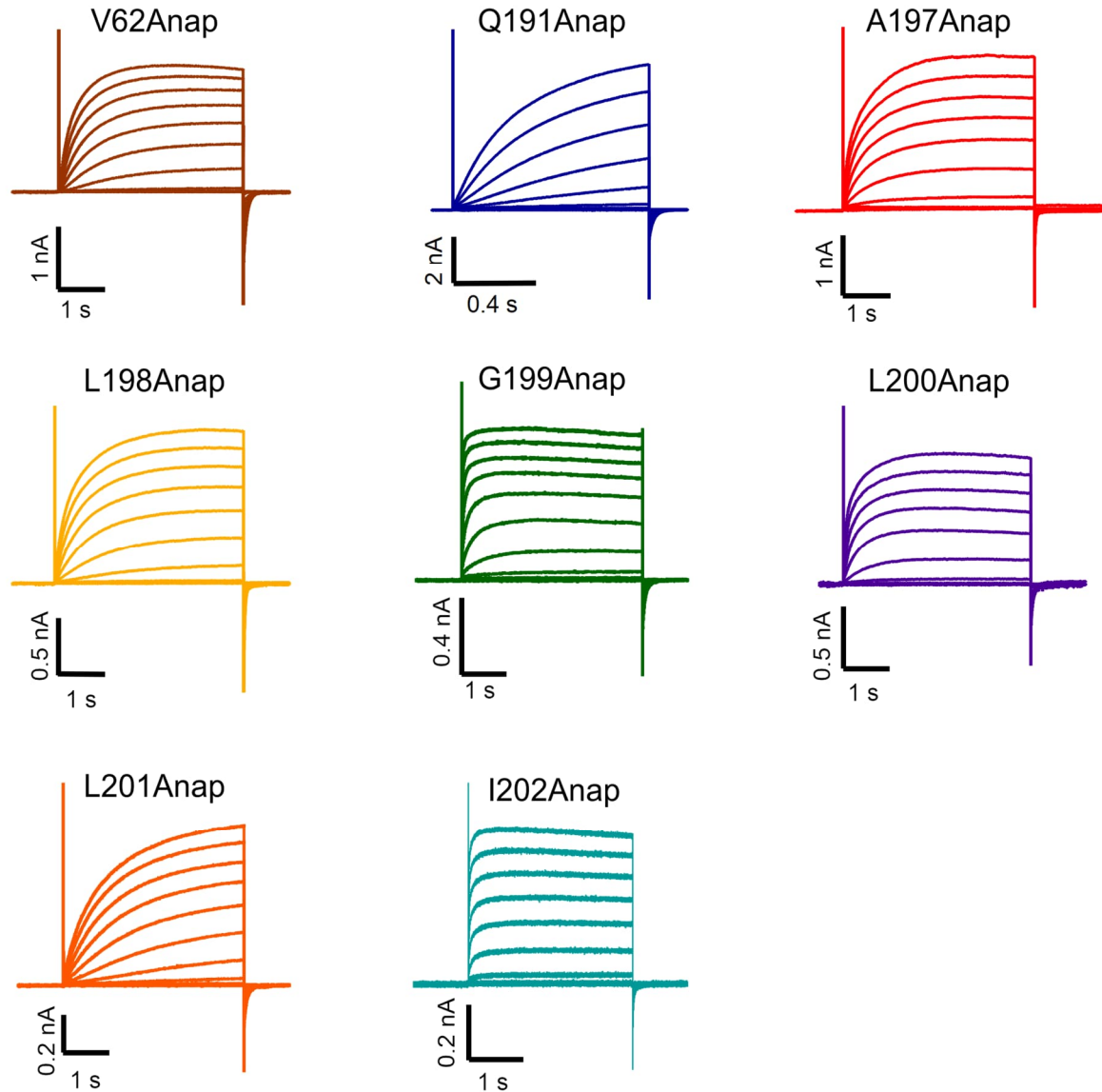


Figura 15. La incorporación de Anap en la proteína de fusión Hv1-mCherry produjo canales iónicos funcionales. Familias de corriente de canales en donde se realizó el experimento de incorporación de Anap en las diferentes posiciones indicadas del canal. Las familias de corriente se obtuvieron a $\Delta\text{pH} = 1$ a través de un protocolo de pulsos de voltaje de -100 mV a $+140$ mV desde un potencial de fijación de -100 mV. Los datos de corriente se usaron para calcular las relaciones conductancia-voltaje de cada construcción (ecuación 2) mostradas en la figura 18. Los valores de ajuste a la ecuación de Boltzmann y la n experimental para cada mutante son recopilados en la tabla 4.

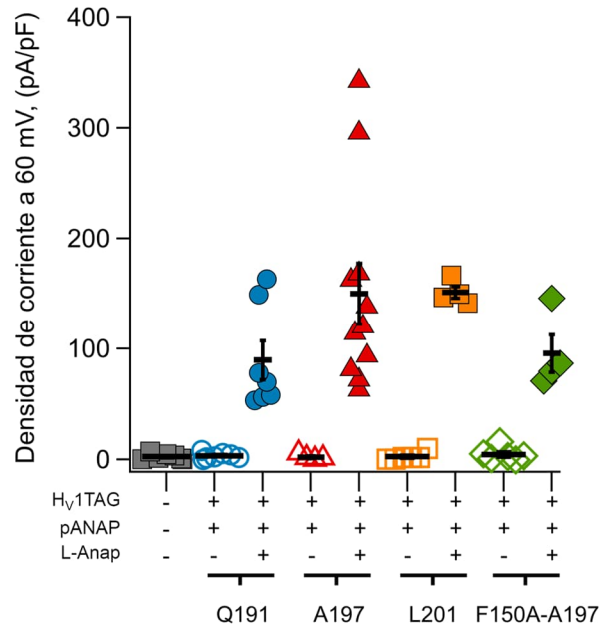


Figura 16. La presencia de los tres componentes del sistema de incorporación Anap son necesarios para producir canales funcionales. Cuantificación de la densidad de corriente al pulso prueba de 60 mV en células HEK293 cotransfectadas con el plásmido H_v1-TAG para diferentes posiciones (Q191, círculos azules; A197, triángulos rojos; L201, cuadrados naranjas; F150A-A197, diamantes verdes) y el plásmido pAnap con (+, marcas llenas) o sin (-, marcas vacías) la presencia de Anap en el medio de incubación. Destaca que los experimentos que no se incubaron con Anap presentaron una densidad de corriente similar a las células no transfectadas (marcas grises), indicando una baja probabilidad de incorporación inespecífica de aminoácidos dentro de las mutantes. Las marcas muestran experimentos individuales mientras que las barras horizontales y las barras de error muestran el promedio \pm el error estándar, respectivamente. Los valores de estos promedios son los siguiente: **células no transfectadas** 2.6 ± 0.98 pA/pF, $n = 7$. **H_v1-Q191TAG + pAnap:** 3.4 ± 1.04 pA/pF ($n = 7$). **H_v1-Q191TAG + pAnap + Anap:** 89.7 ± 17.53 pA/pF ($n = 7$). **H_v1-A197TAG + pAnap:** 2.1 ± 1.2 pA/pF ($n = 4$). **H_v1-A197TAG + pAnap + Anap:** 149.9 ± 27.42 pA/pF ($n = 11$). **H_v1-L201TAG + pAnap:** 2.6 ± 1.47 pA/pF ($n = 6$). **H_v1-L201TAG + pAnap + Anap:** 151.1 ± 5.4 pA/pF ($n = 4$). **H_v1-F150A-A197TAG + pAnap:** 4.6 ± 2.4 pA/pF ($n = 6$). **H_v1-F150A-A197TAG + pAnap + Anap:** 95.7 ± 16.98 pA/pF ($n = 4$).

Por otro lado, en experimentos de microscopía confocal, la señal de mCherry fue más intensa en células que se cultivaron en las condiciones completas para la incorporación de Anap (figura 17 panel derecho), en comparación con lo que se observó en células que solo se sometieron a la transfección del plásmido H_v1-TAG o en combinación con el plásmido pAnap, pero en ausencia de la incubación con Anap (figura 17, paneles izquierdo y medio). Además, es notable observar que en el panel inferior derecho de la figura 17 la señal fluorescente de Anap es mayor en las células que rescataron la expresión de la proteína mCherry en comparación con las

células que no lo lograron, sugiriendo nuevamente que hubo una mayor retención de Anap del medio en las células donde la incorporación fue exitosa. La combinación de estos resultados con los experimentos electrofisiológicos indica que la incorporación de la sonda fluorescente a la proteína del canal fue específica para las diferentes mutantes probadas en el trabajo.

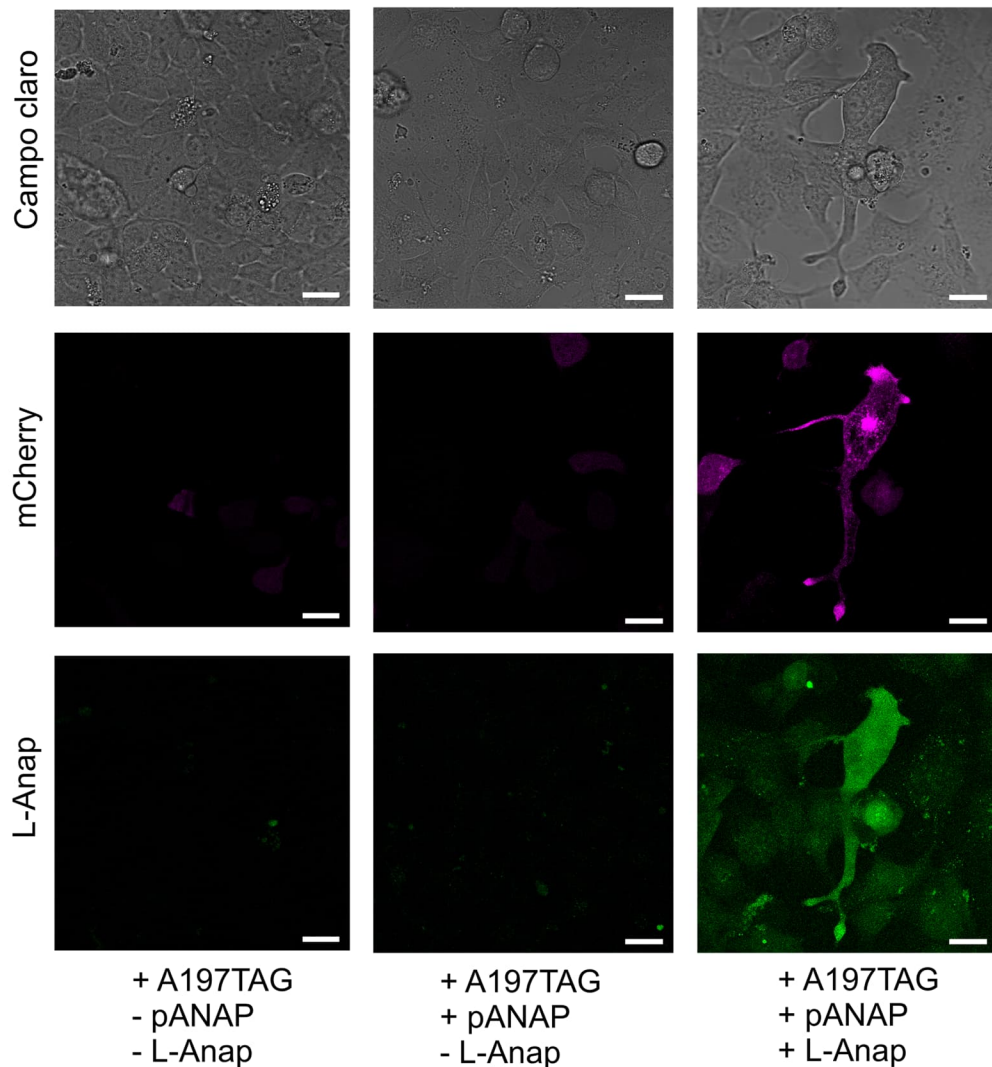


Figura 17. El sistema de incorporación de Anap suprime el codón ámbar insertado en la secuencia de H_v1. Imágenes de microscopía confocal de células HEK 293 en campo claro (panel superior), fluorescencia de mCherry (panel intermedio) y fluorescencia de Anap (panel inferior). Cada columna muestra el mismo campo de visión y las etiquetas inferiores resumen las condiciones experimentales, indicando la transfección del plásmido H_v1-A197TAG en solitario (columna de la izquierda) o en conjunto a pANap en ausencia de Anap (columna media) y finalmente bajo la presencia de Anap en el medio de cultivo (columna de la derecha). Barras de escala = 10µm.

Al analizar las corrientes de protones de las nuevas mutantes, se encontró que estas construcciones tenían una $V_{0.5}$ similar al canal WT encontrado en la proteína de fondo H_v1-mCherry, dentro de un rango de entre +20 y -20 mV, con la excepción clara de la mutante que introdujo la sonda en el sitio I202 (figura 18). Este canal mutante presentó un desplazamiento de su $V_{0.5}$ de activación de alrededor de 60 mV hacia potenciales más negativos (tabla 4). Además, en esta mutante la cinética de activación de las corrientes macroscópicas parece haber perdido su sigmoidicidad y ser cualitativamente más rápida (figura 15, trazos cian). Esta característica también se encontró en la mutante H_v1-G199Anap (figura 15, trazos verdes). Sin embargo, el movimiento de carga aparente, es decir, la pendiente de la curva de la relación conductancia-voltaje (curva G-V), es similar al resto de las mutantes y al fondo WT, que se encontraron en un rango de valores entre 1 y 2 cargas elementales (tabla 4). Esto sugiere que la incorporación de Anap en estos sitios propicia cambios estructurales que, para H_v1-I202Anap, permiten la apertura del canal con una menor inversión de energía al correr la activación a potenciales más negativos, y en ambas construcciones, promueven una transición más rápida del canal al estado abierto. Sin embargo, esta propiedad no se investigó con profundidad porque se buscó estudiar al canal con la menor perturbación de las propiedades electrofisiológicas respecto al canal silvestre.

El siguiente paso consistió en evaluar el espectro de Anap como sonda fluorescente en el sistema de epifluorescencia. Se tomaron los espectros de ambas sondas fluorescentes en la región de la membrana celular, identificada con facilidad gracias a la fluorescencia de mCherry (figura en la sección de Métodos). En todas las mutantes probadas, el espectro de emisión de la proteína reportera mCherry presentó una morfología equivalente a la reportada en la literatura, con un pico de emisión alrededor de los 610 nm (Shu et al., 2006). Esto permitió asegurar que la producción de la proteína reportera se realizó sin alteraciones significativas a su estructura.

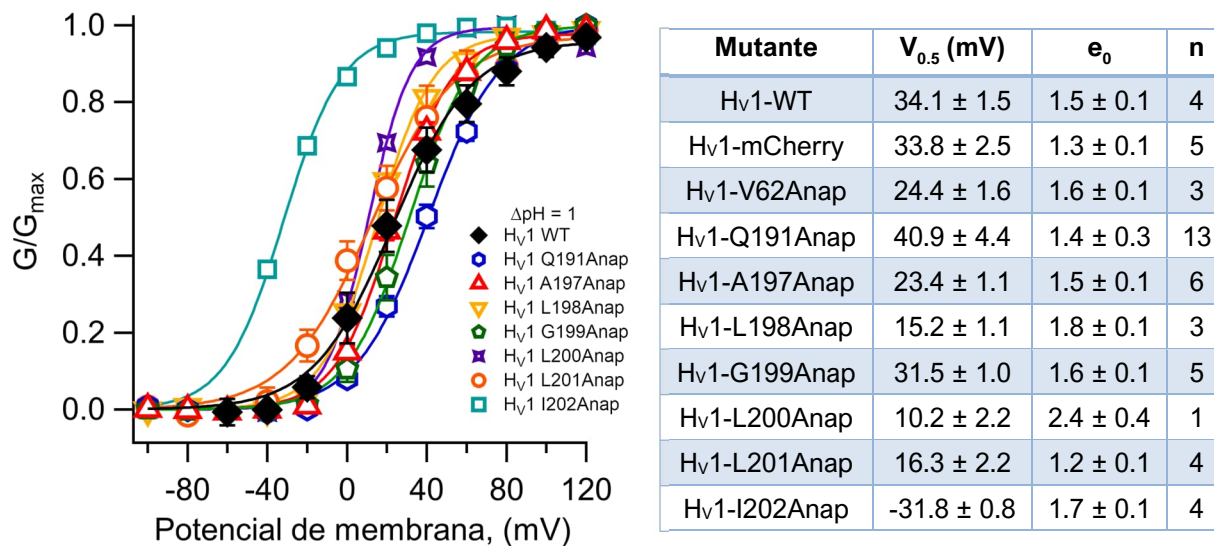


Figura 18. La introducción de Anap en el S4 del canal Hv1 no cambia su comportamiento con respecto al voltaje en la mayoría de las mutantes. Curvas G-V obtenidas de las familias corrientes producidas por las mutantes de Hv1 que incorporaron a Anap dentro del S4 y el asa extracelular S3-S4. Nótese cómo hay un corrimiento hacia potenciales negativos del voltaje medio de activación en la construcción Hv1-I202Anap. A cada serie de datos se le ajustó una ecuación de Boltzmann (ecuación 2) y sus parámetros de ajuste se resumen en la tabla 4.

Tabla 4. Parámetros de ajuste a la ecuación de Boltzmann de las mutantes simples. Se muestran la n experimental junto con el promedio \pm SEM de $V_{0.5}$ y las cargas aparentes (e_0) de cada construcción.

Por otro lado, el espectro de emisión de Anap incorporado a los canales no mostró cambios drásticos en el pico de emisión entre la mayoría de las mutantes (figura 19). La longitud de onda correspondiente al pico de emisión máxima se mantuvo alrededor de 486 nm (con un rango de ± 3 nm) y la forma del espectro obtenido fue similar para las diferentes construcciones dentro de S4, con excepción de la mutante Hv1-I202Anap (figura 19B). En este canal mutante, el pico se desplazó a los 477 nm de longitud de onda. Estos resultados sugieren que el Anap incorporado en el asa S3-S4 y la región extracelular de S4, con excepción de I202, se encontró en un ambiente mayoritariamente polar, ya que la longitud de onda de máxima emisión de Anap es de aproximadamente 486 nm en solución acuosa (Chatterjee et al., 2013; M. C. Puljung, 2021).

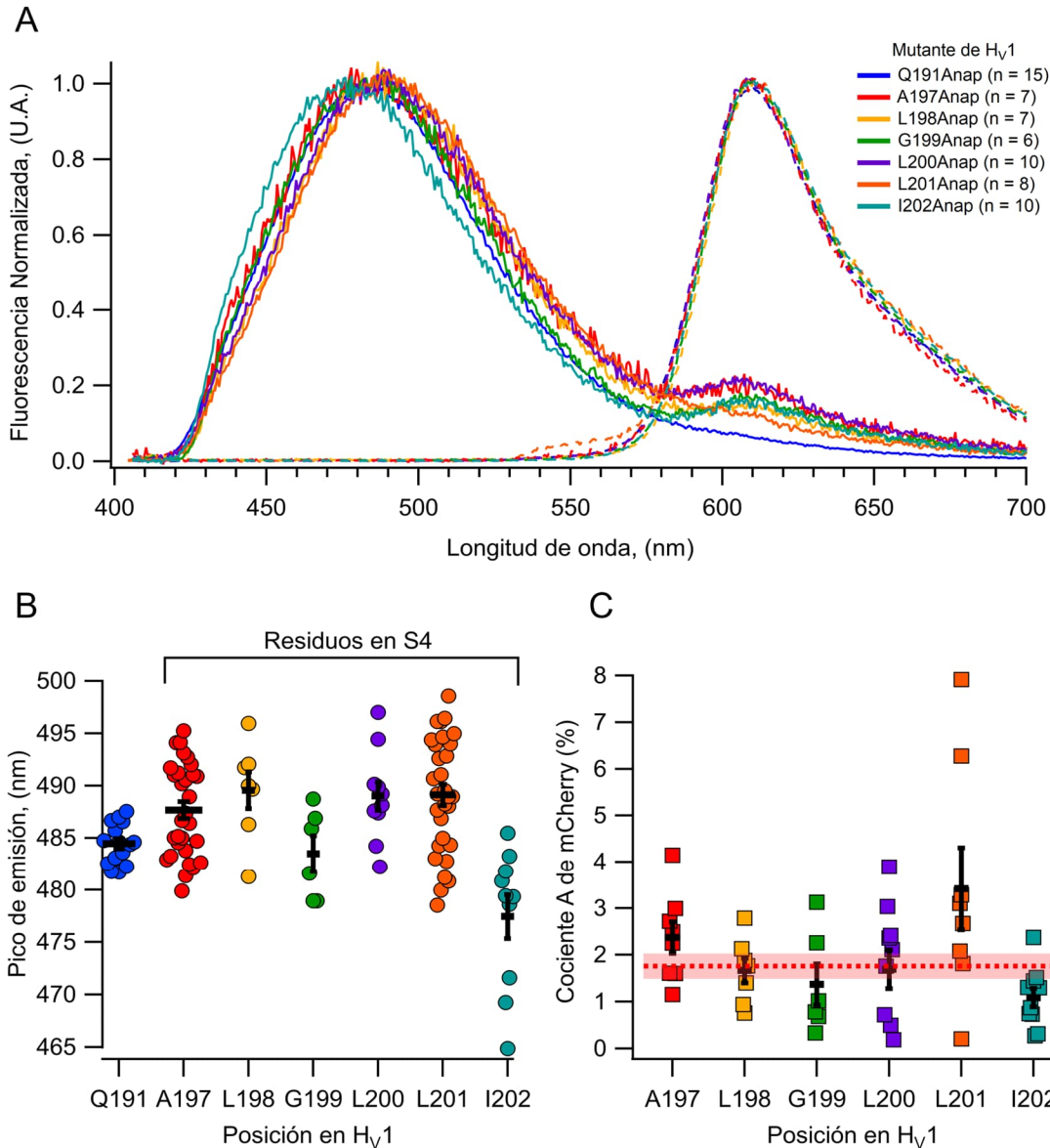


Figura 19. La fluorescencia de Anap unida a diferentes posiciones dentro del S4 de H_v1. **A.** Espectros promedios normalizados de Anap (líneas continuas) y mCherry (líneas discontinuas) obtenidos en los experimentos de incorporación de Anap para cada una de las construcciones. En los espectros de Anap con las mutantes en S4 se puede observar un segundo pico de emisión localizado alrededor de los 610 nm, que coincide con el pico de emisión de mCherry. **B.** Mediciones del pico del espectro de emisión de Anap incorporado en el asa extracelular (Q191: 484.4 ± 0.5 nm, $n = 15$) y sitios en la region extracelular de S4 (A197: 487.7 ± 0.8 nm, $n = 30$; L198: 489.6 ± 1.8 nm, $n = 7$; G199: 483.5 ± 1.7 nm, $n = 6$; L200: 489 ± 1.4 nm, $n = 10$; L201: 489.1 ± 1 nm, $n = 30$; I202: 477.4 ± 2.1 nm, $n = 10$). Nótese que el pico de emisión suele estar dentro del rango entre 484-490 nm a excepción de I202 en el cual el pico de emisión en promedio se encuentra en 477 nm. **C.** Cuantificación de la excitación directa (cociente A) de mCherry a través de su pico de emisión (610 nm) excitando con el láser de 405 nm. La línea roja horizontal discontinua es el cociente A para la construcción H_v1-WT-mCherry (1.87%) y el área sombreada representa su error estándar. Los valores de cociente por mutante fueron: A197: $2.4 \pm 0.3\%$, $n = 8$; L198: $1.7 \pm 0.3\%$, $n = 7$; G199: $1.4 \pm 0.4\%$, $n = 6$; L200: $1.7 \pm 0.4\%$, $n = 10$; L201: $3.4 \pm 0.9\%$, $n = 8$; I202: $1.1 \pm 0.3\%$, $n = 10$. En B y C, los marcadores representan experimentos individuales y las barras negras representan el promedio \pm el error estándar.

Cabe destacar que los espectros de las mutantes que introdujeron Anap en el S4 presentaron un segundo pico de emisión de menor intensidad en la longitud de onda de 610 nm. Este segundo pico es idéntico en posición al pico de mCherry (figura 19A). Esto podría explicarse porque el láser utilizado para la excitación de Anap también puede excitar en cierta proporción a mCherry. Para evaluar la procedencia de este segundo pico, se realizaron experimentos de excitación cruzada de la proteína H_V1-WT-mCherry expresada en células HEK293 con el láser de 405 nm. Estos experimentos consisten en excitar al fluoróforo con dos fuentes de luz distintas: una para evaluar el valor máximo de fluorescencia que se puede obtener en el sistema, en este caso el láser a 514 nm, y otra con el láser de 405 nm para conocer el porcentaje de excitación cruzada (De-la-Rosa et al., 2013). Al obtener un cociente con estos dos espectros resultantes de cada medición (cociente A), se observa que hay alrededor de un 2% de excitación cruzada de mCherry con el láser de 405 nm. Este valor es muy cercano al porcentaje obtenido en las mediciones de este segundo pico de Anap en las mutantes, lo que sugiere que dicho segundo pico en el espectro de emisión puede ser explicado como excitación por el láser de 405 nm de la fluorescencia de la proteína reportera, mCherry.

Bajo la suposición de que la expresión de mCherry se lograría por la incorporación de Anap durante la síntesis de los canales H_V1-Anap-Cherry, el cociente de la fluorescencia de Anap con respecto a el brillo de mCherry sería un indicador de la eficiencia cuántica de Anap. Se observó que este cociente varió en cada una de las posiciones dentro del S4 en donde se incorporó Anap (figura 20 A). Esta variación estuvo dentro del 10 y 40% del brillo de mCherry en todas las mutantes, con una tendencia decreciente conforme el Anap se colocaba en sitios más profundos del S4 (figura 20 B). Este análisis sugiere que, si bien el pico de emisión de Anap permanece relativamente estable independientemente de su colocación dentro del S4, su profundidad en la membrana celular podría influir en

su brillo, lo que sugiere la existencia de algún grupo molecular que interactúa con el Anap y funciona como un apagador de su fluorescencia.

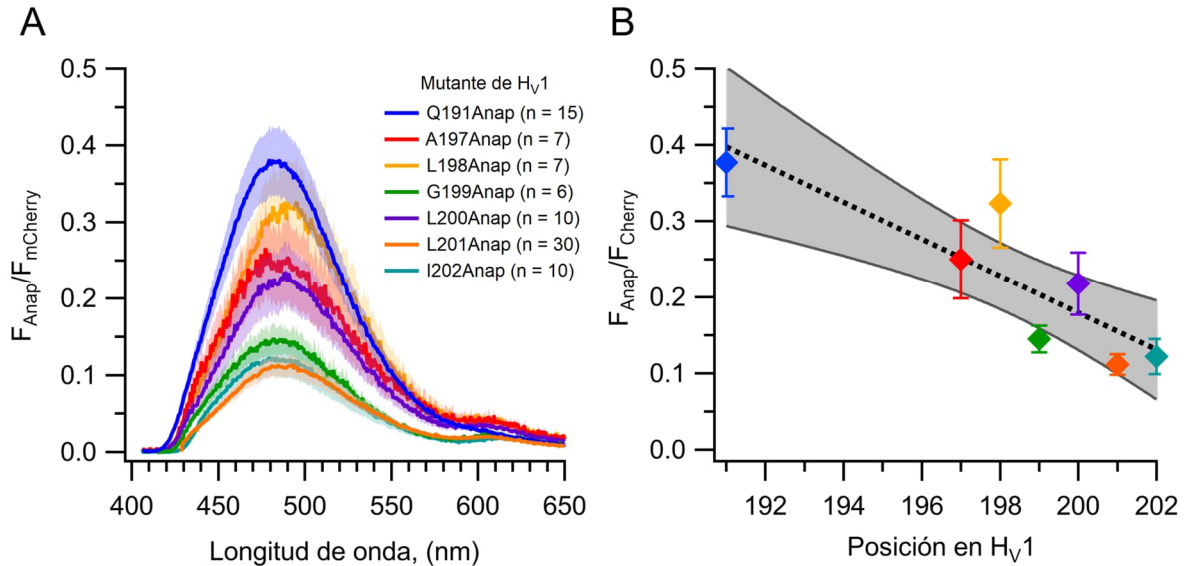


Figura 20. La fluorescencia de Anap disminuye conforme es incorporado en residuos cercanos a la región central del segmento S4. A. Fracción de la fluorescencia de Anap con respecto a la de mCherry determinada por el espectro de emisión. El trazo representa el promedio del espectro mientras que el área sombreada representa \pm el error estándar. **B.** Representación del cociente de fluorescencia Anap/mCherry medido a la longitud de onda del pico de emisión para cada mutante en función a la posición de incorporación dentro del canal H_V1. Las marcas representan los promedios y las barras de error representan el error estándar, mientras que la línea punteada en gris corresponde a un ajuste lineal y el área sombreada corresponde a los intervalos de confianza del 90%. Se puede observar una tendencia en la reducción del cociente de la fluorescencia del 2.4% por posición dentro del S4.

La fluorescencia de Anap incorporado es insensible a los cambios de acidez

Para validar la idoneidad del Anap para medir los cambios conformacionales del canal de protones, es crucial que sea insensible a los cambios locales de pH generados por el canal H_V1 durante su actividad. El Anap sin incorporar contiene grupos funcionales amino y carboxilo que podrían protonarse y alterar las propiedades fluorescentes de la sonda (figura 5, recuadro), por lo que estimar los efectos de la protonación en el aminoácido libre no es un control correcto. Entonces, se decidió medir la fluorescencia en respuesta a los cambios de acidez del Anap ya

incorporado al canal, donde los enlaces peptídicos que unen al Anap a la proteína reducen los sitios de protonación que podrían influir en los cambios de fluorescencia.

Con este fin, se midió la intensidad del pico del espectro de emisión de Anap en la región de la membrana de células transfectadas con la construcción Hv1-Q191Anap, que incorpora la sonda en el asa extracelular S3-S4, mientras se variaba el pH en la solución extracelular en un rango de valores de 3 a 9. En esta posición, el Anap se encuentra expuesto a la solución extracelular tanto en estado cerrado como en el abierto. Los resultados obtenidos en la intensidad de la fluorescencia no mostraron cambios significativos dentro del rango de acidez evaluado en comparación con el pH 7 (figura 21 A). Además, se constató que no hubo modificaciones significativas en la forma del espectro de emisión en los diferentes valores de pH extracelular (figura 21 B).

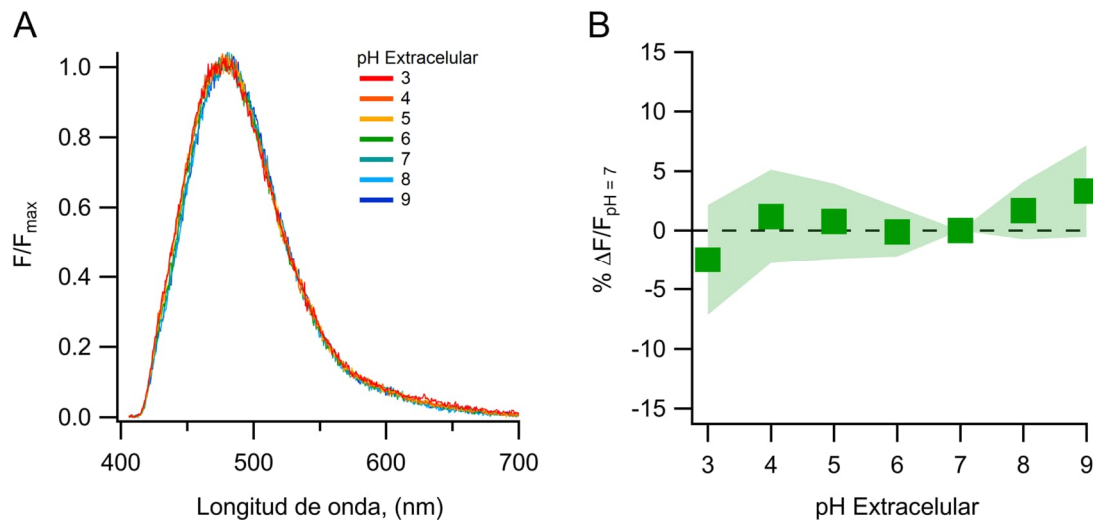


Figura 21. La fluorescencia de Anap incorporado al canal Hv1 es estable a los cambios de acidez. A. Espectros de emisión promedios de la fluorescencia de Anap incorporado en el sitio Q191Anap, localizado en el asa extracelular S3-S4, en respuesta a cambios del pH extracelular. El pico de emisión se encontró alrededor de los 477 a 480 nm. B. Cambios de intensidad de fluorescencia a diferentes valores de pH extracelular con respecto a pH 7 (n = 13). La intensidad fue medida del pico de emisión y no fue estadísticamente diferente al ser analizado con una prueba ANOVA de dos vías (F-estadística = 0.09, grados de libertad = 6 y p = 0.99). Cada marca representa el promedio y la sombra el error estándar.

Para proporcionar más evidencia de la insensibilidad de la fluorescencia de Anap a los posibles cambios de pH durante la activación del canal, se utilizó la mutante H_V1-V62Anap. Esto coloca al Anap en la región intracelular del canal, pero sin excluir el efecto del cambio de pH local provocado por el transporte de protones (De-la-Rosa et al., 2016; Gordienko et al., 1996). Los experimentos de registro simultáneo de fluorescencia y corriente con la mutante H_V1-V62Anap a $\Delta\text{pH} = 1$ demostraron que no hubo cambios en la intensidad de fluorescencia a pesar de la existencia de corrientes de protones en respuesta al voltaje. Lo que indica que el brillo del aminoácido es resistente a los cambios de acidez durante la activación de H_V1 (Figura 22). En consecuencia, estos hallazgos aunados con los del experimento anterior indican que la sonda Anap es insensible a los cambios locales de pH que pueden ocurrir durante el funcionamiento de H_V1, lo que la hace una sonda adecuada para medir los cambios conformacionales del canal de protones.

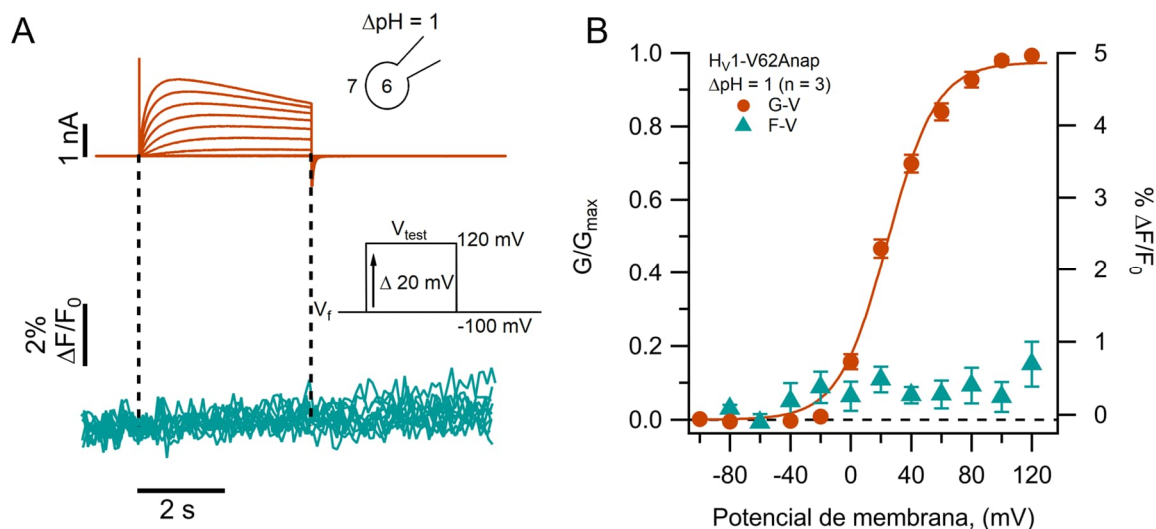


Figura 22. La fluorescencia de Anap incorporado al canal H_V1-V62Anap fue estable a la presencia de corrientes de protones. A. Experimento representativo de Patch-clamp Fluorometry con la mutante H_V1-V62Anap. Las corrientes (trazos naranjas, panel superior) junto con la señal de fluorescencia (líneas turquesas) se obtuvieron con un protocolo de pulsos de voltaje (V_{test}) de -100 mV a +120 mV en pasos de 20 mV desde un voltaje de fijación (V_f) de -100mV y a $\Delta\text{pH} = 1$. B. Curvas de conductancia (G-V) y fluorescencia relativa (F-V) en función del potencial de membrana de los experimentos mostrados en A. Los cambios de la fluorescencia no sobrepasan el 1%, mientras que los datos de conductancia (círculos naranjas) pudieron ser ajustados a una ecuación de Boltzmann (ec, línea naranja continua). Los parámetros de ajuste fueron: $V_{0.5} = 24.4 \pm 1.6$ mV; $q = 1.5 \pm 0.1$ e_0 . Los datos mostrados en B representan los promedios y error estándar.

La sonda Anap presentó cambios de fluorescencia voltaje-dependientes

Tras haber validado la estabilidad de la fluorescencia Anap en un amplio rango de pH, el siguiente paso fue evaluar si existían cambios de fluorescencia en función del voltaje, lo que daría información sobre los cambios conformacionales del canal durante su activación. Para ello, se expresó la mutante H_v1-A197Anap, que incorpora el Anap en la porción extracelular de S4 del canal de protones. Con las células que expresan este canal exitosamente, se realizaron experimentos de PCF bajo condiciones de pH simétricas a ambos lados de la membrana ($\Delta\text{pH} = 0$), en donde se registró simultáneamente la señal de fluorescencia de Anap y las corrientes de protones en respuesta a los protocolos de voltaje.

Bajo estas condiciones, se observó un aumento en la señal de fluorescencia de Anap a partir de los 20 mV, el cual se correlacionó con la presencia de corrientes salientes en los registros electrofisiológicos (figura 23). Además, la intensidad de la señal de Anap aumentó con las subsecuentes despolarizaciones, alcanzando una amplitud máxima a voltajes más positivos (a partir de 100 mV). Estos resultados son consistentes con la idea de que los cambios en la fluorescencia de Anap registrados reflejan un proceso saturable en función del voltaje. Este fenómeno de saturación suele observarse en los registros de corriente de compuerta en los VSD de los canales activados por voltaje y se relaciona con el movimiento del S4 durante la activación (Catacuzzeno et al., 2023; Kalstrup & Blunck, 2013; Villalba-Galea et al., 2009).

Al experimentar con otros gradientes de acidez ($\Delta\text{pH} = 1$ y 2), la fluorescencia también aumentó en respuesta del voltaje (figura 24 A). Entonces, estos cambios de fluorescencia se manifestaron hacia la misma dirección que $\Delta\text{pH} = 0$, lo que sugiere

que se está midiendo el mismo proceso o cambio conformacional. No obstante, estos cambios de fluorescencia se presentaron a diferentes rangos de voltaje

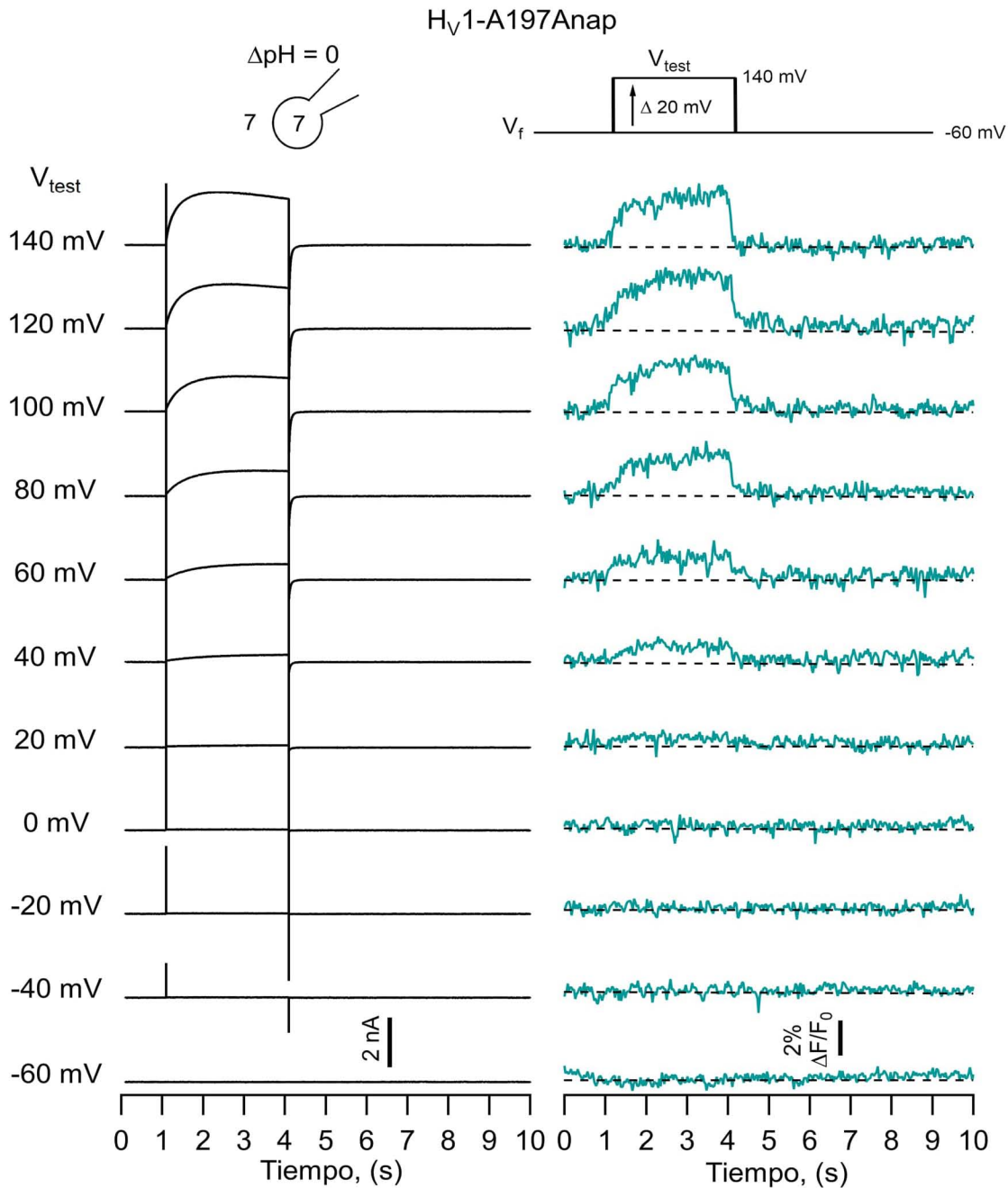


Figura 23. La fluorescencia de Anap en la mutante H_v1-A197Anap reveló el movimiento de S4 en respuesta de pulsos de voltaje. Se muestra el registro de corriente (trazos negros) y fluorescencia (trazos turquesa) obtenidos de forma simultánea en un experimento representativo de Patch-clamp Fluorometry con la sonda incorporada en el sitio A197 a $\Delta\text{pH} = 0$. Ambas señales se registraron en respuesta de un protocolo de voltaje con un pulso prueba (V_{test}) de -60 mV hasta 140 mV en pasos de +20 mV desde un potencial de mantenimiento (V_i) de -60 mV. Los trazos se desplazaron verticalmente entre sí con

fines ilustrativos siguiendo el valor del pulso prueba y se colocó una línea punteada para denotar la fluorescencia basal.

dependiendo del gradiente de acidez, siguiendo la modulación por pH que tiene la conductancia del canal H_v1 (figura 24 B). Así, al normalizar la fluorescencia y compararla con la conductancia, se observó en la curva F-V y G-V un corrimiento de la $V_{0.5}$ ~31 mV desde ΔpH 2 a 1 y ~46 mV desde ΔpH 1 a 0. Este corrimiento de la $V_{0.5}$ en las curvas concuerda con lo reportado previamente del corrimiento de 40 mV por unidad de ΔpH (Chaves et al., 2023). Por otra parte, se encontró una superposición de las curvas F-V con las G-V. Esta superposición indica que el desplazamiento de S4 revelado por la fluorescencia es simultáneo con la activación del canal.

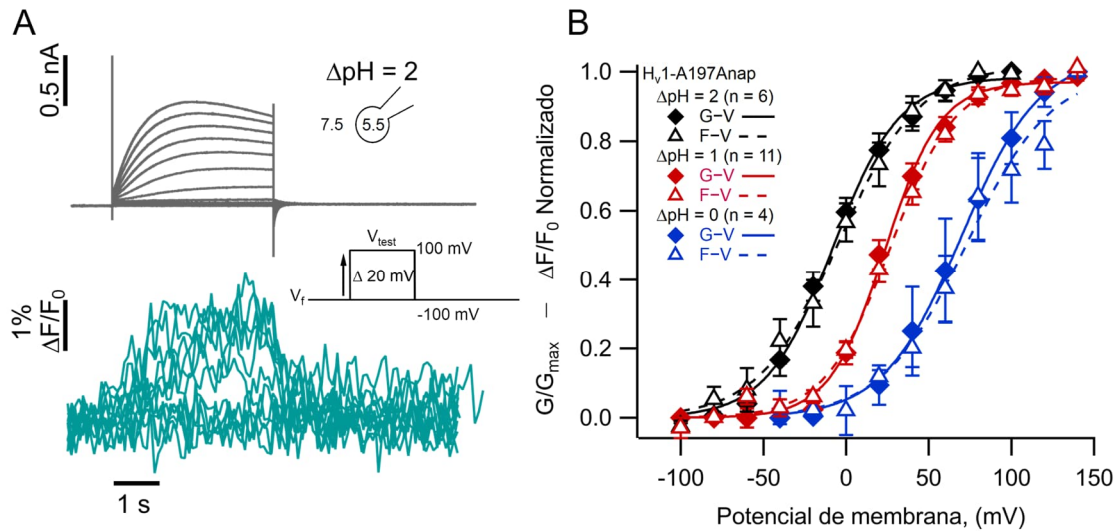


Figura 24. Anap en la mutante H_v1 -A197Anap reveló el movimiento de S4 responde a la modulación por ΔpH . **A.** Experimento representativo de Patch-clamp Fluorometry registro de corriente (trazos grises, panel superior) y fluorescencia (trazos turquesa, panel inferior) obtenidos de forma simultánea con la sonda incorporada en el sitio A197 a $\Delta\text{pH} = 2$. Ambas señales fueron registradas en respuesta de un protocolo de voltaje con un pulso prueba (V_{test}) de -100 mV hasta 100 mV en pasos de +20mV desde un potencial de mantenimiento de -100 mV (V_i). **B.** Curvas F-V (triángulos vacíos) y G-V (rombos) a diferentes valores de ΔpH ($\Delta\text{pH} = 0$ en azul, $n = 4$; $\Delta\text{pH} = 1$ en rojo, $n = 11$; $\Delta\text{pH} = 2$ en negro, $n = 6$). Los datos se ajustaron a la ecuación de Boltzmann (G-V, curvas continuas; F-V, curvas discontinuas) con los siguientes parámetros: $\Delta\text{pH} = 0$; **F-V:** $V_{0.5} = 72.7 \pm 6$ mV; $q = 1.0 \pm 0.1 e_0$. **G-V:** $V_{0.5} = 69.6 \pm 1.5$ mV; $q = 1.1 \pm 0.1 e_0$. $\Delta\text{pH} = 1$; **F-V:** $V_{0.5} = 26.6 \pm 1.5$ mV; $q = 1.3 \pm 0.1 e_0$. **G-V:** $V_{0.5} = 23.4 \pm 1.3$ mV; $q = 1.5 \pm 0.1 e_0$. $\Delta\text{pH} = 2$; **F-V:** $V_{0.5} = -4.5 \pm 1.7$ mV; $q = 1.0 \pm 0.1 e_0$. **G-V:** $V_{0.5} = -8.1 \pm 2.6$ mV; $q = 1.2 \pm 0.1 e_0$.

Con esta información se puede considerar que la incorporación de Anap en el sitio A197 del canal permite cuantificar los cambios conformacionales del S4 de Hv1 y que la incorporación de Anap no afectó la modulación por pH del canal. Además, que el rearrreglo de S4 es simultáneo a la formación de la conductancia del canal y que este movimiento en respuesta al voltaje es efectivamente modulado por la diferencia de concentración de protones.

Es interesante observar que en la mutante Hv1-A197Anap, a diferencia de los experimentos con sondas sintéticas, la intensidad de la señal de fluorescencia aumenta en lugar de disminuir con la aplicación de potenciales positivos. Este comportamiento en respuesta al voltaje implica que la fluorescencia transite de un estado de bajo rendimiento a otro de mayor brillo. Una explicación posible es que la activación del S4 involucre un cambio en el ambiente de solvatación del Anap, lo que se traduzca en un corrimiento hacia el rojo de su espectro de emisión, aumentando así la fluorescencia efectiva que puede captar el sistema (figura 5).

Para investigar esta posibilidad, se realizó un experimento en el que se registraron los espectros de emisión en los experimentos de PCF durante los últimos 300 ms del voltaje de fijación y del pulso prueba de cada paso de voltaje, de -100 a 140 mV. Los resultados de este experimento muestran que la intensidad del espectro de Anap aumenta a potenciales positivos con la misma voltaje-dependencia observada en los experimentos previos de PCF (figura 25). Sin embargo, no se observaron cambios en el pico de emisión de Anap, que se encontró nuevamente alrededor de los 485 nm; ni en la morfología general de los espectros. Esto indica que el Anap en el sitio 197, ubicado en la porción extracelular del S4, permanece en un ambiente polar durante todos los voltajes y que los cambios de fluorescencia son únicamente relativos a una reducción del rendimiento cuántico del fluoróforo, pero no del espectro de emisión.

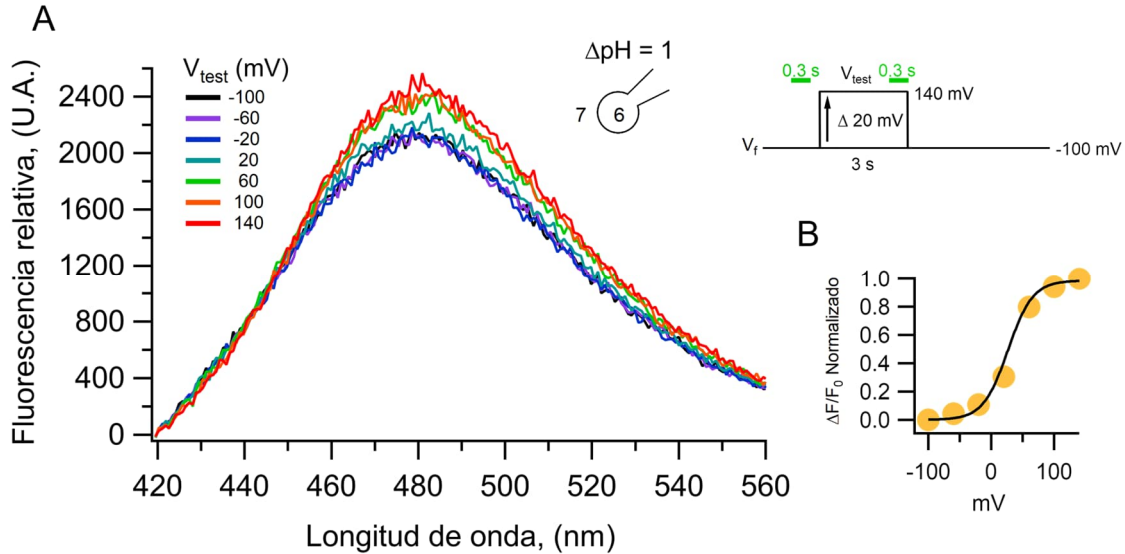


Figura 25. Los cambios de fluorescencia en la mutante H_V1-A197Anap no son provocados por desplazamientos del pico de emisión de fluorescencia de Anap. A. Espectro de emisión de Anap en el sitio A197 obtenidos durante los últimos 300 ms del pulso prueba en respuesta a diferentes pulsos de voltaje (segunda barra verde en el esquema del protocolo de voltaje) en un protocolo de -100 mV a 140 mV (V_{test}) con pasos de +20 mV desde un potencial de mantenimiento (V_i) de +20 mV. El pico de emisión en todos los voltajes se encontró a una longitud de onda alrededor de los 480 nm. A la intensidad de fluorescencia del pico de este espectro se le restó la intensidad del pico obtenido en los 300 ms previos al pulso prueba durante el potencial de mantenimiento en cada paso de voltaje (primera barra verde en el esquema del protocolo de voltaje). La diferencia normalizada se muestra en B en función del potencial del pulso prueba. La curva negra es el ajuste de los datos de fluorescencia a $\Delta pH = 1$ mostrada en la figura 24.

La fluorescencia de Anap en la posición 197 es apagada por una fenilalanina en S2

Recapitulando, se observó que la incorporación del aminoácido no canónico Anap permitió registrar cambios en la fluorescencia durante la activación y desactivación del canal, sugiriendo el registro del movimiento de S4. Al investigar la causa de estos cambios, se demostró que no son provocados por fluctuaciones en el pH local ni por modificaciones en el espectro durante la activación, como se creía inicialmente (figuras 21 y 25). Además, se ha observado que el espectro no experimenta cambios significativos en su forma o en la longitud de onda del pico de emisión en relación con el sitio de incorporación, excepto en el sitio I202, indicando

que la sonda no experimenta cambios drásticos en su entorno al ser incorporada en la región extracelular de S4 (figura 19 A y B). Sin embargo, al examinar la relación de la fluorescencia de Anap y mCherry en los canales en función de su posición a lo largo del S4, la evidencia sugiere que la intensidad de la fluorescencia de Anap puede modificarse debido al sitio de incorporación. En concreto, la intensidad de la fluorescencia de Anap tiende a disminuir a medida que se coloca más profundamente en S4 (Figura 20). Una posible explicación para esta observación es que el Anap incorporado interactúa con una molécula cercana que reduce su fluorescencia mediante interacciones estrechas, como la transferencia de electrones fotoinducida o la interacción catión- π (Lakowicz, 2006). Esta molécula apagadora de la fluorescencia (comúnmente conocida como *quencher* en inglés) estaría próxima al Anap en la posición de reposo del sensor de voltaje del canal. Por lo tanto, el posterior aumento en la fluorescencia observado durante la activación del canal podría ser consecuencia del distanciamiento de la sonda respecto al apagador, gracias al movimiento de S4 hacia la región extracelular.

Los residuos aromáticos de los aminoácidos son grupos funcionales que frecuentemente interactúan con fluoróforos y pueden funcionar como apagadores (Islas & Zagotta, 2006; Klymchenko, 2017; Mizutani et al., 2022; Young & Artigas, 2021). Por lo tanto, es posible proponer que la molécula apagadora en nuestros experimentos sea un residuo aromático cercano al Anap durante el reposo del canal. Para evaluar la presencia de residuos aromáticos cercanos al sitio A197 (figura 26 A), se utilizó un modelo computacional del VSD desactivado del H_v1 previamente publicado (Randolph et al., 2016). De esta manera, se localizó a los aminoácidos con cadenas aromáticas más cercanos espacialmente al sitio A197. Estos residuos son la fenilalanina en la posición 195, el triptófano en la posición 207 (ambos en S4) y la fenilalanina en la posición 150 (S2). Los dos primeros resultan ser candidatos difíciles ya que podrían moverse junto con el Anap gracias a que también se encuentran en el S4. En cambio, F150 difiere de los anteriores al encontrarse en S2,

en una condición presumiblemente inmóvil, siendo más factible que la distancia cambie entre el Anap y este residuo. Además, se ha descrito que este residuo ha sido identificado como centro de transferencia de carga por su posición y la dirección de su anillo hacia la cavidad interna del VSD (Tao et al., 2010; Wu et al., 2022).

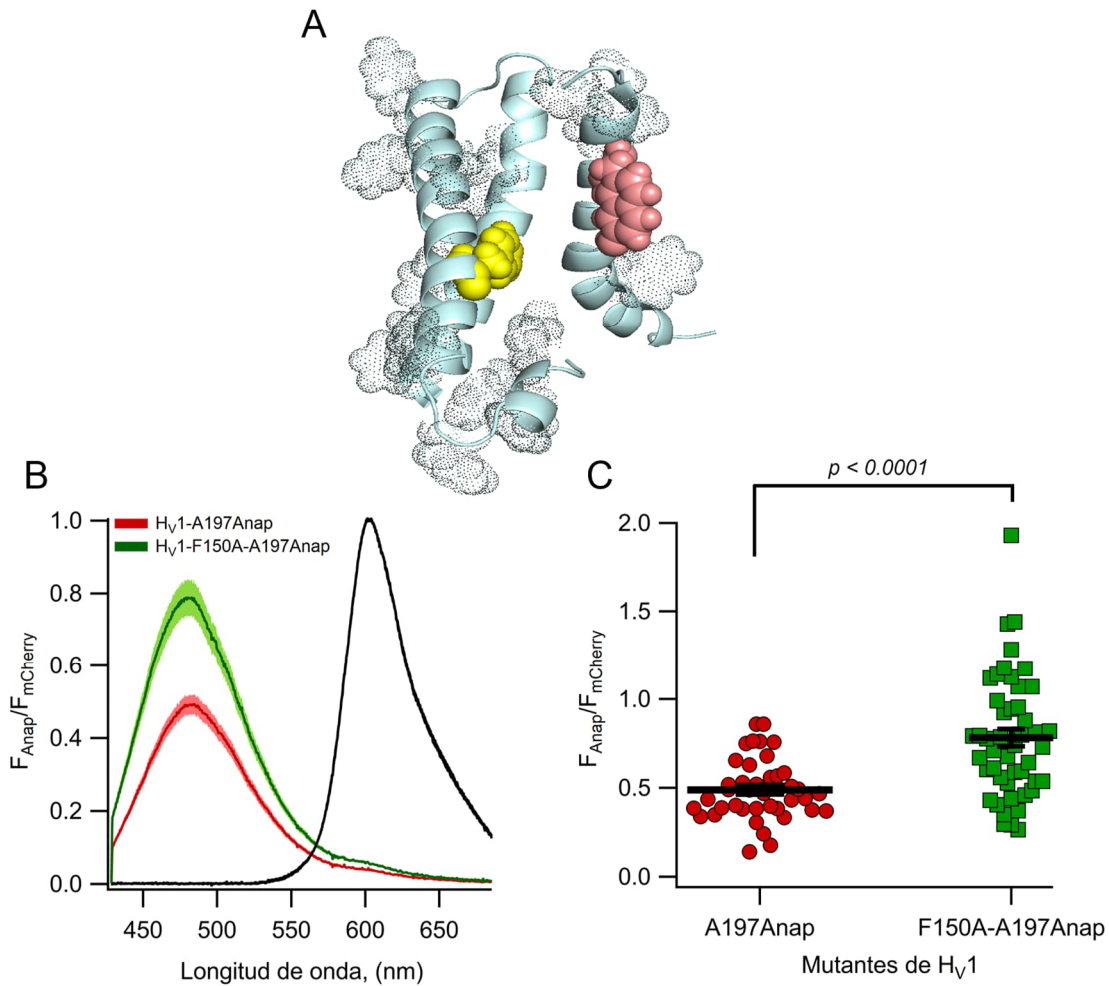


Figura 26. El residuo de fenilalanina en el sitio 150 es un apagador de Anap. **A.** Modelo computacional de Hv1 en estado cerrado que muestra la distribución de los diferentes residuos aromáticos en la estructura del canal (mostrados con redes de puntos mientras que cadena principal de aminoácidos en celeste) resaltando al Anap en rosa y F150 en amarillo. Observe cómo este último es el residuo aromático fuera de S4 más cercano al Anap. Una porción de S3 que no contiene residuos aromáticos se removió por motivos ilustrativos. **B.** Espectros de Anap promediados en ambas mutantes (Hv1-A197Anap, rojo; Hv1-F150A-A197Anap, verde) normalizados a la fluorescencia de mCherry unida al final de cada construcción (trazo negro). Los espectros se obtuvieron en células en reposo sin fijación de voltaje a $\Delta pH \approx -0.2$. Las líneas indican el promedio y las sombras el error estándar. **C.** Normalización del pico de emisión de Anap a la fluorescencia de mCherry entre la mutante simple Hv1-A197Anap-Cherry ($0,49 \pm 0,03$; $n = 41$) y la doble mutante Hv1-F150A-A197Anap-Cherry ($0,79 \pm 0,05$; $n = 49$) 48 horas post-transfección. Cada punto indica una célula individual y las líneas horizontales señalan la media \pm el error

estándar. Se realizó una prueba T de Welch para datos no pareados encontrando una t-estadística = 5.2, grados de libertad = 71.18 y un valor de p de 1.6×10^{-6} .

Para probar si la cadena aromática del aminoácido fenilalanina 150 pudiera estar actuando como una molécula apagadora de Anap durante el estado de reposo, se construyó la mutante F150A mediante mutagénesis puntual usando como fondo la mutante H_v1-A197tag-Cherry. Esta doble mutante H_v1-F150A-A197Anap se expresó en células HEK y se midió en la región membranal la intensidad del espectro de Anap en correspondencia del espectro de mCherry usando un $pH_e = 7$ ($\Delta pH \sim -0.2$). Bajo estas condiciones de acidez, los canales se encuentran presumiblemente en un estado cerrado debido a que el potencial de reposo en las células HEK es alrededor de -20 a -40 mV, que es suficientemente negativo para reducir al mínimo la probabilidad de apertura del canal. Al cuantificar los espectros en la región membranal, se encontró que la emisión de fluorescencia de Anap del canal H_v1-F150A-A197Anap era aproximadamente 60% más brillante que la mutante simple H_v1-A197Anap después de 48 horas de incubación post-transfección (figura 26 B y C). No obstante, el pico de emisión del espectro de Anap no presentó corrimientos en su longitud de onda por la ausencia de fenilalanina. Estos resultados sugieren que el anillo aromático de la fenilalanina es capaz de apagar el Anap en el sitio 197 durante el estado cerrado.

Asimismo, se realizaron experimentos de PCF en esta doble mutante a $\Delta pH = 1$ para evaluar si había cambios de fluorescencia durante la activación del canal a pesar de la ausencia de la molécula apagadora (figura 27 A). En estos experimentos fue posible registrar aumentos de fluorescencia en respuesta a potenciales positivos a pesar de la ausencia del grupo aromático. La señal de fluorescencia durante la activación también se saturó a potenciales positivos, indicando que, como en la mutante simple H_v1-A197Anap, se está registrando el movimiento de S4 de H_v1 con el Anap incorporado. También, la presencia de estos aumentos de fluorescencia en ausencia de fenilalanina propone la existencia de posibles apagadores adicionales

que también afecten al Anap o que este haya podido demostrar su sensibilidad al medio.

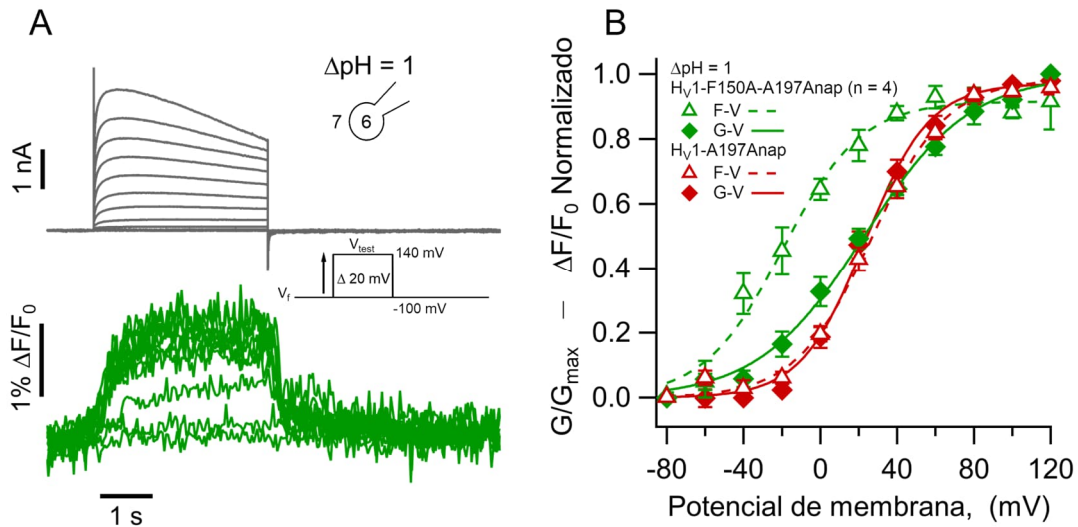


Figura 27. La doble mutante presenta cambios de fluorescencia en respuesta a pulsos de voltaje. A. Corrientes (trazos grises) y señal de fluorescencia (trazos verdes) de un experimento representativo de PCF en la doble mutante $H_V1-F150A-A197Anap$ a $\Delta pH = 1$ en respuesta de un protocolo de pulsos de voltaje (V_{test}) de 4 s desde -100 mV a 100 mV en pasos de $+20$ mV. **B.** Comparación de las curvas G-V (diamantes) y F-V (triángulos vacíos) entre la mutante sencilla $H_V1-A197Anap$ (marcadores rojos, tomados de la figura 24B, $n=11$) y la doble mutantes $H_V1-F150A-A197Anap$ (marcadores verdes, $n=4$). Se observa como la señal de fluorescencia de la doble mutante se satura a potenciales más negativos que su conductancia y que está última tiene valores parecidos a la mutante sencilla $H_V1-A197Anap$. Los datos del ajuste a la ecuación de Boltzmann para la construcción $H_V1-F150A-A197Anap$ fueron: **F-V**: $V_{0.5} = -19.8 \pm 2.7$ mV; $q = 1.2 \pm 0.1 e_0$; **G-V**: $V_{0.5} = 22.7 \pm 2.3$ mV; $q = 0.9 \pm 0.1 e_0$. Los marcadores presentados en B son el promedio \pm error estándar.

Sin embargo, al comparar las curvas F-V y G-V, se encontraron diferencias entre la mutante de fondo y la doble mutante $H_V1-F150A-A197Anap$. En los experimentos a $\Delta pH = 1$, se pudo observar que las $V_{0.5}$ de activación de las conductancias no fueron diferentes entre ambas construcciones (23.4 mV en $H_V1-A197Anap$ vs 23.3 mV en la doble mutante) aunque la pendiente en la doble mutante se encuentra relativamente disminuida. Por su parte, las curvas F-V presentaron una diferencia en el voltaje medio de activación de 40 mV, siendo la curva de la doble mutante más negativa (figura 27 B).

Subsecuentemente, se registró bajo la condición experimental de $\Delta\text{pH} = 0$ (figura 28). La señal de fluorescencia también presentó un aumento de su magnitud durante la activación del canal y se saturó a potenciales positivos. La reducción del gradiente de protones produjo un corrimiento hacia potenciales más positivos de ambas curvas, G-V y F-V, aunque no en la misma magnitud. Entre $\Delta\text{pH} = 0$ y $\Delta\text{pH} = 1$ el corrimiento entre las curvas G-V es cercano a 42 mV, mientras que en las curvas F-V se separan alrededor de 60 mV.

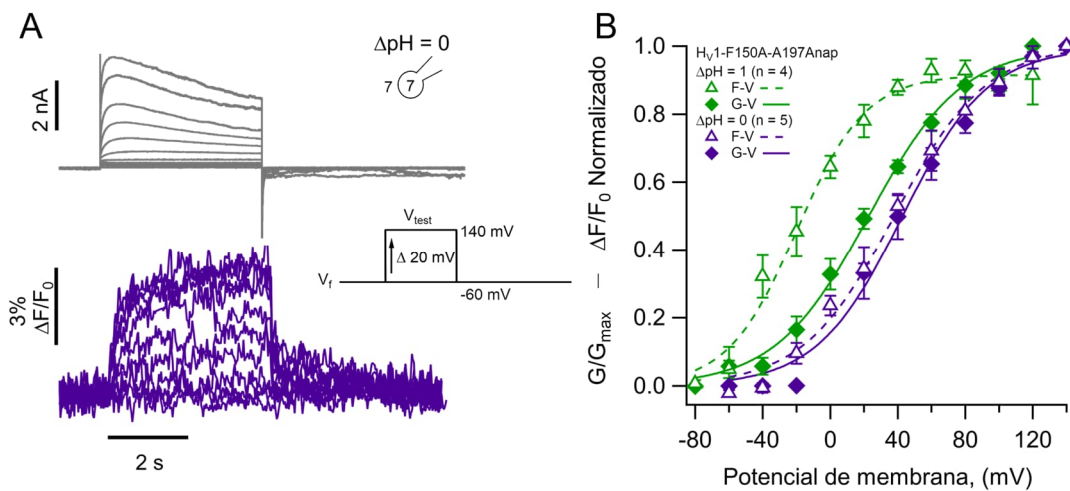


Figura 28. Los cambios de fluorescencia de la doble mutante $H_V1-F150A-A197Anap$ también responden a la modulación de pH. **A.** Corrientes (trazos grises) y señal de fluorescencia (trazos morados) de un experimento representativo de PCF en la doble mutante $H_V1-F150A-A197Anap$ a $\Delta\text{pH} = 0$ en respuesta de un protocolo de pulsos de voltaje (V_{test}) de 4 s desde -100 mV a 100 mV en pasos de +20 mV. Nótese como la señal de la fluorescencia al final del pulso prueba no regresa completamente a la línea basal, describiendo dos cinéticas durante el cierre del canal **B.** Comparación de las curvas G-V (diamantes) y F-V (triángulos vacíos) entre las condiciones $\Delta\text{pH} = 0$ (marcadores morados) y $\Delta\text{pH} = 1$ (marcadores verdes) en la doble mutante $H_V1-F150A-A197Anap$. Se puede observar como la curva F-V a $\Delta\text{pH} = 0$ está corrida 58 mV a potenciales más positivos en comparación de lo observado a $\Delta\text{pH} = 1$. Los datos del ajuste a la ecuación de Boltzmann en las condiciones de $\Delta\text{pH} = 0$ fueron: **F-V:** $V_{0.5} = 38.0 \pm 3.0$ mV; $q = 0.9 \pm 0.1 e_0$; **G-V:** $V_{0.5} = 42.6 \pm 3.8$ mV; $q = 1.0 \pm 0.1 e_0$. Los marcadores presentados en B son el promedio \pm error estándar.

Entonces, si bien en esta doble mutante los efectos del ΔpH presentan la misma tendencia del canal WT, es decir, ante la reducción de la diferencia de la concentración de protones a ambos lados de la membrana el voltaje de activación del canal se desplaza hacia potenciales más positivos, el comportamiento dispar que

tienen las relaciones de ambas curvas F-V con su respectiva G-V, en ambas condiciones de ΔpH , muestra que el residuo aromático presenta un rol muy importante para el establecimiento de la conductancia, el movimiento del S4 y su modulación por pH.

Por otra parte, cabe destacar que el curso temporal de la señal de fluorescencia durante la desactivación del canal en los experimentos a $\Delta\text{pH} = 0$, que representa el regreso del S4 a sus estados basales, presentó un comportamiento bifásico. Este comportamiento en la cinética de la señal sugiere que el movimiento que hace el VSD de regreso a su estado su posición de reposo puede tener distintas velocidades. Además, que aparezca a un ΔpH específico, apuntó que esa tasa cinética puede ser pH dependiente.

La incorporación del Anap en el sitio L201 permitió detectar una nueva transición durante la activación

Para continuar la exploración de la cinética de las señales de fluorescencia durante la activación del canal, se decidió retomar el uso de las mutantes simples, eligiendo la construcción $\text{H}_{\text{V}1}\text{-L201Anap}$. Esta mutante fue la construcción que rescató al Anap en la posición más cercana a las cargas en el S4 que no modificó significativamente la electrofisiología del canal en los experimentos iniciales a $\Delta\text{pH} = 1$. Además, se razonó que $\text{H}_{\text{V}1}\text{-L201Anap}$, al tener al aminoácido fluorescente en una posición más profunda en S4 y estar presumiblemente más cerca de F150 en el estado cerrado, podría producir una señal más intensa al moverse a regiones extracelulares y por lo tanto podría ser un mejor indicador de la cinética del movimiento S4 durante la función el canal.

Teniendo esto en consideración, se llevaron a cabo experimentos de PCF con esta construcción bajo tres diferentes condiciones de ΔpH : 0, 1 y 2 (figura 29). En

todas estas condiciones de gradiente de acidez, se observaron incrementos en la señal de fluorescencia que son saturables en respuesta a pulsos de potenciales positivos. Estas señales mostraron una modulación por el gradiente de protones en dos principales aspectos: la voltaje-dependencia de activación y la cinética de la señal fluorescente.

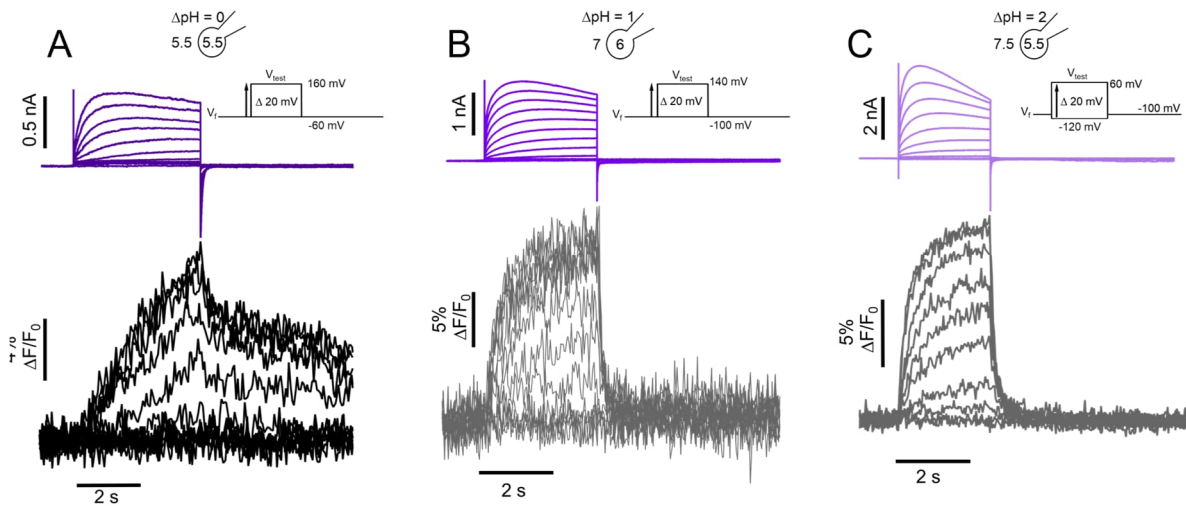


Figura 29. La cinética de la señal fluorescente de $H_V1-L201Anap$ durante la desactivación está fuertemente modulada por el pH. Experimentos representativos de PCF con la mutante $H_V1-L201Anap$ con 3 diferentes condiciones de acidez transmembranal: $\Delta pH = 0$ (A), $\Delta pH = 1$ (B) y $\Delta pH = 2$ (C). Las familias de corrientes se muestran en el panel superior (trazos morados) junto con su respectivo protocolo de voltaje (pulso prueba = V_{test} , voltaje de mantenimiento = V_i), mientras que las señales fluorescentes se observan en los paneles inferiores (trazos negros y grises). Es notable como en la condición de $\Delta pH = 0$ la señal de fluorescencia durante la desactivación presenta dos componentes, siendo el segundo de ellos lo suficientemente lento que la señal no vuelve al nivel de la línea basal.

Tanto la modulación como la saturación de la señal a potenciales positivos se pueden apreciar mejor al examinar las relaciones entre las curvas G-V y F-V, las cuales parecen ser estrechas en estas tres condiciones de acidez (figura 30). La diferencia más amplia entre la $V_{0.5}$ de activación de ambas señales se encontró a $\Delta pH = 2$, con una diferencia de alrededor de 10 mV, siendo más negativa la G-V. Este estrecho margen de diferencia solo en una condición refuerza el hallazgo de que el movimiento del S4 revelado por la incorporación de Anap está estrechamente coordinado con el establecimiento de la conductancia a protones.

Por otra parte, un aspecto relevante de esta mutante fue su respuesta a los cambios de ΔpH . A diferencia del corrimiento esperado de entre 30 y 40 mV observado entre las condiciones $\Delta\text{pH} = 1$ y $\Delta\text{pH} = 2$, el desplazamiento de la $V_{0.5}$ entre $\Delta\text{pH} = 1$ y $\Delta\text{pH} = 0$ es de alrededor de 80 mV en la G-V y de 76 mV en la F-V. Este corrimiento respeta la tendencia de ir hacia potenciales positivos cuando el gradiente de protones disminuye, sin embargo, es cerca del doble de magnitud a comparación del observado en otras mutantes estudiadas y en WT, sugiriendo que esta relación gradiente de acidez y voltaje de activación fue alterada y que L201 puede ser un sitio importante para esta relación.

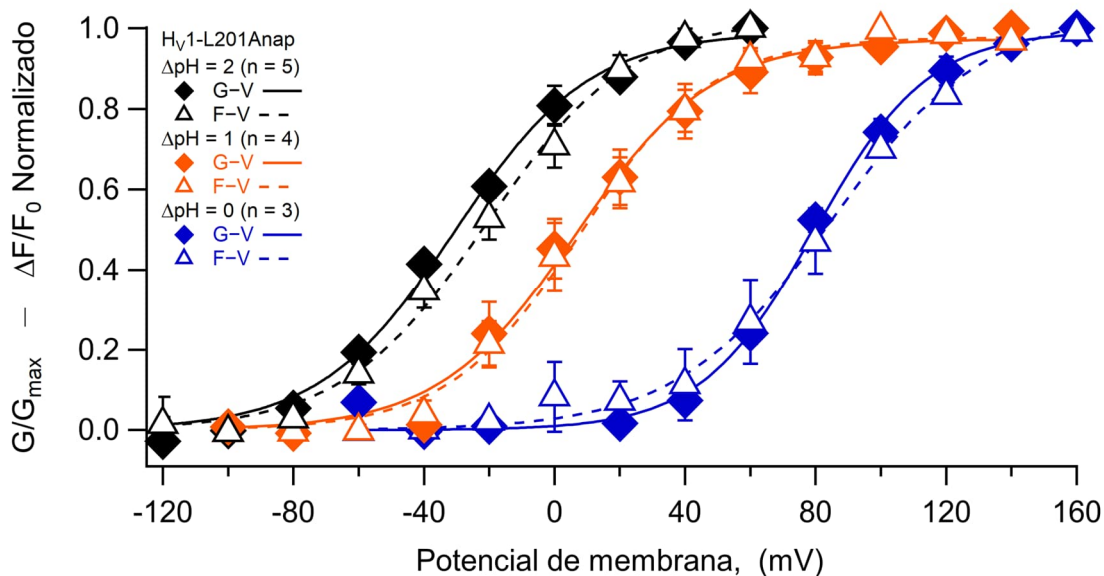


Figura 30. La señal de Anap en el sitio L201 también responde a la modulación por diferencias de acidez a ambos lados de la membrana. Relaciones G-V (rombos) y F-V (triángulos vacíos) en las diferentes condiciones de acidez probadas: $\Delta\text{pH} = 0$ (marcadores azules, $n = 3$), $\Delta\text{pH} = 1$ (marcadores naranjas, $n = 4$) y $\Delta\text{pH} = 2$ (marcadores negros, $n = 5$) del mutante $H_{V1}\text{-L201Anap}$. Los datos son la media \pm SEM. Se observa que la diferencia entre la activación en $\Delta\text{pH} = 1$ y $\Delta\text{pH} = 0$ es de alrededor de 77 mV/unidad ΔpH . Parámetros de ajuste de Boltzmann para cada condición fueron: **$\Delta\text{pH} = 0$, F-V:** $V_{0.5} = 84.6 \pm 2.1$ mV, $q = 1.0 e_0 \pm 0.1$; **G-V:** $V_{0.5} = 79.7 \pm 1.8$ mV, $q = 1.4 \pm 0.1 e_0$. **$\Delta\text{pH} = 1$, F-V:** $V_{0.5} = 7.7 \pm 1.6$ mV, $q = 1.2 \pm 0.1 e_0$. **G-V:** $V_{0.5} = 6.3 \pm 2.2$ mV; $q = 1.2 \pm 0.1 e_0$. **$\Delta\text{pH} = 2$, F-V:** $V_{0.5} = -21.1 \pm 2.3$ mV; $q = 1.1 \pm 0.1 e_0$. **G-V:** $V_{0.5} = -30.6 \pm 2.1$ mV; $q = 1.2 \pm 0.1 e_0$.

Respecto a la cinética de los trazos de fluorescencia en respuesta al voltaje, esta resultó ser sensible a la concentración de protones a ambos lados de la membrana. Bajo las condiciones de $\Delta\text{pH} = 1$ y 2, la fluorescencia aumentó de

manera exponencial durante la activación del canal, alcanzando un estado estacionario al final del pulso de prueba de 4 segundos. Mientras que para $\Delta\text{pH} = 0$, la cinética fue relativamente más lenta y no alcanzó dicho estado estacionario, mostrando un cambio de cinética menos pronunciado (figura 29 A). Estos resultados proporcionan una mayor evidencia de cómo el gradiente de protones puede modular la constante de tiempo del movimiento del S4, sugiriendo que la reducción del gradiente de protones disminuye la velocidad en los cambios conformacionales de este segmento transmembranal durante la activación.

Uno de los hallazgos más importantes fue que, como se observó en los experimentos con la doble mutante, la señal fluorescente durante la desactivación reveló dos componentes con diferentes cinéticas, uno rápido y otro lento. Al comparar la cinética de cierre a -60 mV, partiendo desde el pulso de prueba a +160 mV, se observó que el componente rápido de la señal fluorescente presenta una constante de tiempo aproximadamente 130 ms, muy similar a los 140 ms de las corrientes de desactivación o corrientes de cola (figura 31). Mientras tanto, el componente lento de la desactivación tuvo una constante de tiempo aproximadamente 60 veces más lenta (8.6 ± 0.75 s). Esta observación sugiere que el retorno del segmento S4 al estado de reposo puede sucederse a diferentes tasas de velocidad y que esa tasa podría ser pH-dependiente. Entonces, el primer componente de la señal de fluorescencia estaría estrechamente relacionado con la transición del estado abierto a un estado cerrado cercano al estado abierto, mientras que el segundo componente de fluorescencia, el componente lento, podría estar indicando la presencia de al menos una segunda transición del S4 de varios segundos de duración hacia estados cerrados más profundos.

Sin embargo, la estimación de la cinética de los trazos de corriente se alteró por una reducción de su magnitud durante el final de los pulsos prueba. Esta reducción se debe al rápido cambio de la concentración de protones que se

encuentran en la vecindad de canal (De-la-Rosa et al., 2016). Este efecto de depleción de protones es promovido por la combinación de dos factores, el primero a resaltar es lo eficientes que son los protones para moverse tanto en los medios acuosos como a través del canal, mientras que la otra condición es la baja concentración de protones en los valores de pH utilizados durante los experimentos. A pesar de encontrarse entre uno o dos órdenes de magnitud más concentrados que en condiciones fisiológicas, la concentración se encuentra en los rangos de μM (para pH 5 y 6) a nM (para pH 7). Estas concentraciones son de 3 a 4 órdenes de magnitud más pequeñas que las observadas fisiológicamente para sodio o potasio, iones usualmente asociados con los canales iónicos y las señales bioeléctricas. La combinación de estas condiciones promueve la aparición de pseudoinactivación que caracteriza a las corrientes de estos canales y en consecuencia a estas alteraciones en la cinética de la corriente, una estimación directa de la misma no fue posible en la mayoría de los experimentos.

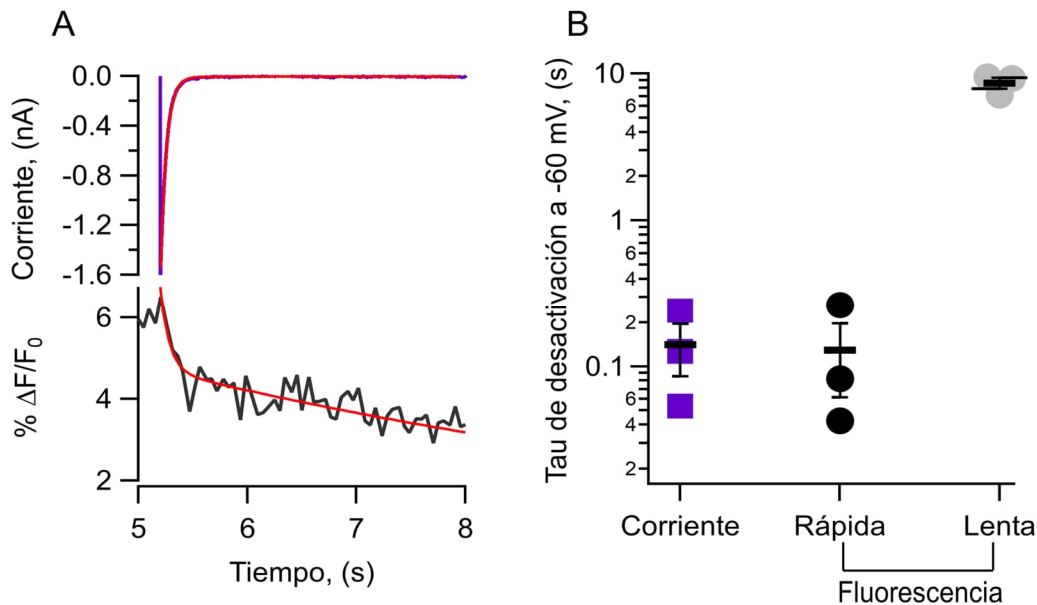


Figura 31. La cinética del componente rápido de la fluorescencia durante la desactivación en Hv1-L201Anap demuestra una relación estrecha con el cierre de la conductancia. A. Corriente de cola (trazo morado, panel superior) con un ajuste exponencial superpuesto (rojo). Señal de decaimiento de fluorescencia registrado de forma simultánea (trazo negro) con un ajuste exponencial doble (rojo). Ambos registros se obtuvieron a -60 mV tras un pulso de prueba a 160 mV y un $\Delta\text{pH} = 0$ ($\text{pH}_{\text{ext}} = 5,5/\text{pH}_i = 5,5$). B. Constantes de tiempo obtenidas de los ajustes realizados como se muestra en A. Las barras horizontales y las barras de error representan valores medios \pm SEM, y los marcadores son experimentos individuales. Para las colas de corriente (cuadros morados) la constante de tiempo fue de 140.6 ± 54.9

ms. Mientras que, para la señal de fluorescencia, el componente rápido (círculos negros) tuvo una constante de tiempo de 129.4 ± 68.1 ms y el lento de 8.61 ± 0.75 s. Se observa como la constante de tiempo del componente rápido de la fluorescencia presenta un valor similar que el cierre de la conductancia del canal.

Tratando de explorar la cinética de ambas señales en términos cualitativos, se buscó ajustar un modelo cinético enfocándose en los trazos de corriente que presentaron el menor efecto de depleción de protones y la cinética de sus trazos de fluorescencia. Para la realización de modelos cinéticos es preferible partir desde la configuración mínima necesaria, es decir, con la cantidad de estados mínimos indispensables para explicar el fenómeno de activación. Por lo tanto, se consideró la característica sigmoidicidad de los trazos de corriente en este canal, que se puede observar con mejor definición en los pulsos de voltaje donde la probabilidad de apertura del canal ronda el 20%. Este retraso está asociado a las transiciones entre múltiples estados cerrados previos al estado abierto (Gonzalez et al., 2010; Villalba-Galea, 2014). En el canal H_{V1} , al considerarse un dímero de VSD, se puede pensar en un estado inicial donde ambos VSD se encuentran en una posición de reposo y con una transición hacia el estado activado de cada dominio previo a la transición hacia el estado abierto. Esto daría por resultado un modelo cinético simplificado de 4 estados y 3 transiciones (Figura 32 A). Este modelo se asemeja al descrito previamente para el canal H_{V1} expresado en ovocitos (Villalba-Galea, 2014). Para poder estimar la fluorescencia, si tenemos en cuenta los resultados en donde la activación de H_{V1} aumenta la cantidad de fluorescencia, se añadió al modelo la condición de que cada estado presenta un valor de fluorescencia que aumenta cuando el VSD transita hacia el estado activado.

Bajo este modelo, las constantes de tiempo se modularon por el gradiente de protones, en general acelerando las transiciones hacia el estado activado bajo la condición $\Delta pH = 2$ (tabla 5). Asimismo, a $\Delta pH = 0$, una de las transiciones entre estados cerrados (k_{21}) se configuró para que fuera mucho más lenta que la transición de estado abierto a cerrado (k_{32}), que define el cese de la conductancia de protones durante la desactivación. La diferencia entre las cinéticas de estas dos transiciones

permite recrear la diferencia entre los trazos de fluorescencia y corriente durante el cierre y el comportamiento bifásico de la fluorescencia revelados en los experimentos. Con estos ajustes, el modelo puede predecir que, cuando el pH intracelular es más ácido (como en $\Delta\text{pH} = 2$), la transición lenta es largamente afectada, indicando que ese cambio conformacional es especialmente sensible a la modulación por pH (figura 32 B).

A

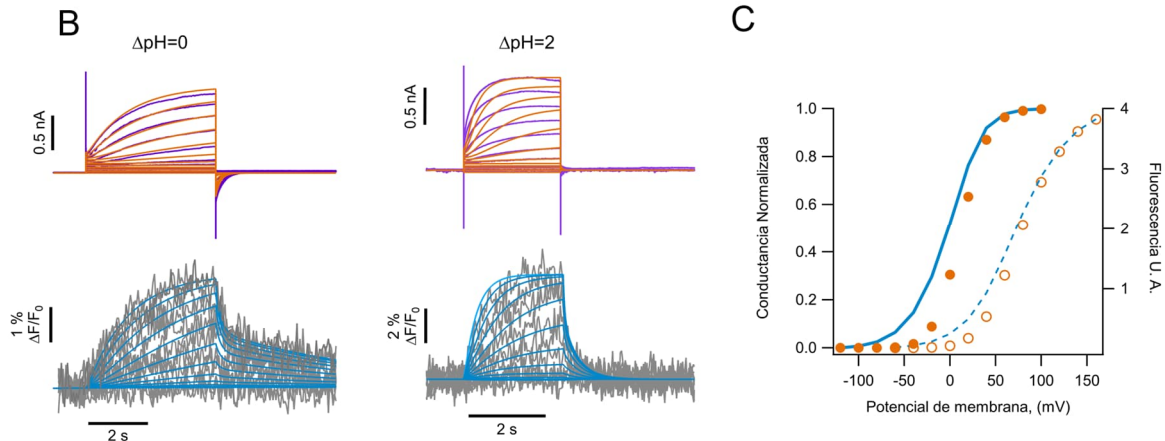
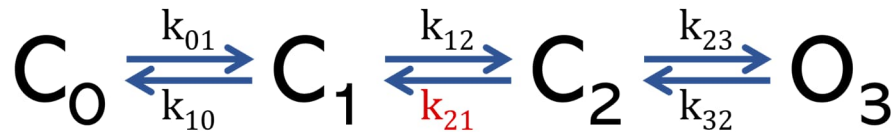


Figura 32. Modelo cinético secuencial simple. **A.** Esquema 1 del modelo de activación secuencial. C = cerrado, O = Abierto. Los k_i son constantes de velocidad. En rojo se presenta la constante de velocidad de cierre indicada en rojo es responsable del lento retorno de la señal de fluorescencia tras la repolarización y tiene un valor 10 veces menor que la transición de cierre de la conductancia. **B.** Comparación de la corriente y la fluorescencia en dos valores de ΔpH (0 y 2) con las predicciones del modelo de activación secuencial en el Esquema 1. Las trazas experimentales de corriente (trazos violetas) y fluorescencia (trazos grises) se muestran al fondo. Los rastros de corriente simulados son de color mostaza y los rastros de fluorescencia son de color naranja. Los parámetros de simulación se pueden encontrar en la tabla 5 **C.** Simulación que compara la conductancia en estado estacionario (marcas naranjas) y la fluorescencia (trazos azules) en función del voltaje y del ΔpH (marcas llenas y línea continua para $\Delta\text{pH} = 2$; marcas vacías y línea discontinua). Nótese como la señal de fluorescencia precede a la activación de la conductancia a potenciales negativos.

Si bien este modelo puede reproducir cualitativamente los resultados cinéticos, se encuentra limitado para reproducir la relación de las curvas F-V con

sus respectivas G-V y su modulación por el gradiente de protones (figura 32 C). En este modelo, las curvas F-V preceden a las G-V a potenciales negativos, pero como se describió anteriormente, las relaciones observadas en estas curvas pueden variar según el ΔpH . Mientras se superponen a $\Delta\text{pH} = 0$ y 1, la curva F-V se encuentra corrida $\sim 10\text{mV}$ a potenciales positivos con respecto de la G-V a $\Delta\text{pH} = 2$. Esto sugiere considerar la existencia de múltiples estados abiertos que se pueden presentar sin la necesidad de una total activación de los VSD (Stefani et al., 1997). Dicha observación sugiere que los canales $\text{H}_\text{v}1$ podrían operar a través de un mecanismo más complicado que el secuencial mostrado en el esquema 1 y el cuál considere la existencia de varios estados abiertos. Entonces, se desarrolló un modelo alostérico que contempla, además de la transición de desactivación lenta, un factor que permite incorporar la modulación pH-dependencia de las constantes de activación y la presencia de estados abiertos. Este modelo puede dar cuenta, de forma cualitativa, tanto de las cinéticas de las señales de fluorescencia y de corriente como de las relaciones entre las curvas F-V y G-V a diferentes ΔpH (figura 33, tabla 6).

El valor del pH absoluto a un lado de la membrana puede cambiar la respuesta al voltaje

Como se ha descrito anteriormente en la literatura y se ha observado a lo largo de este trabajo, una de las características más especiales de este canal es la modulación que el gradiente de pH ejerce sobre el voltaje de activación (Chaves et al., 2023). Sin embargo, en experimentos recientes también se ha observado que el valor absoluto de pH puede ser también un determinante de la apertura del canal (Carmona et al., 2021).

Para explorar la posibilidad de que el pH absoluto podría modificar la activación del canal, se realizaron experimentos que sometieron a la mutante $\text{H}_\text{v}1$ -

L201Anap a $\Delta\text{pH} = 0$ con un mayor valor de pH intra y extracelular ($\text{pH} = 7$). Si el valor absoluto no resultaba más importante para la modulación que la diferencia neta (ΔpH), se esperaría que los cambios en la señal de fluorescencia presenten esencialmente las mismas cualidades que las observadas previamente a valores de pH intra y extracelular más concentrados ($\text{pH} = 5.5$, figura 34).

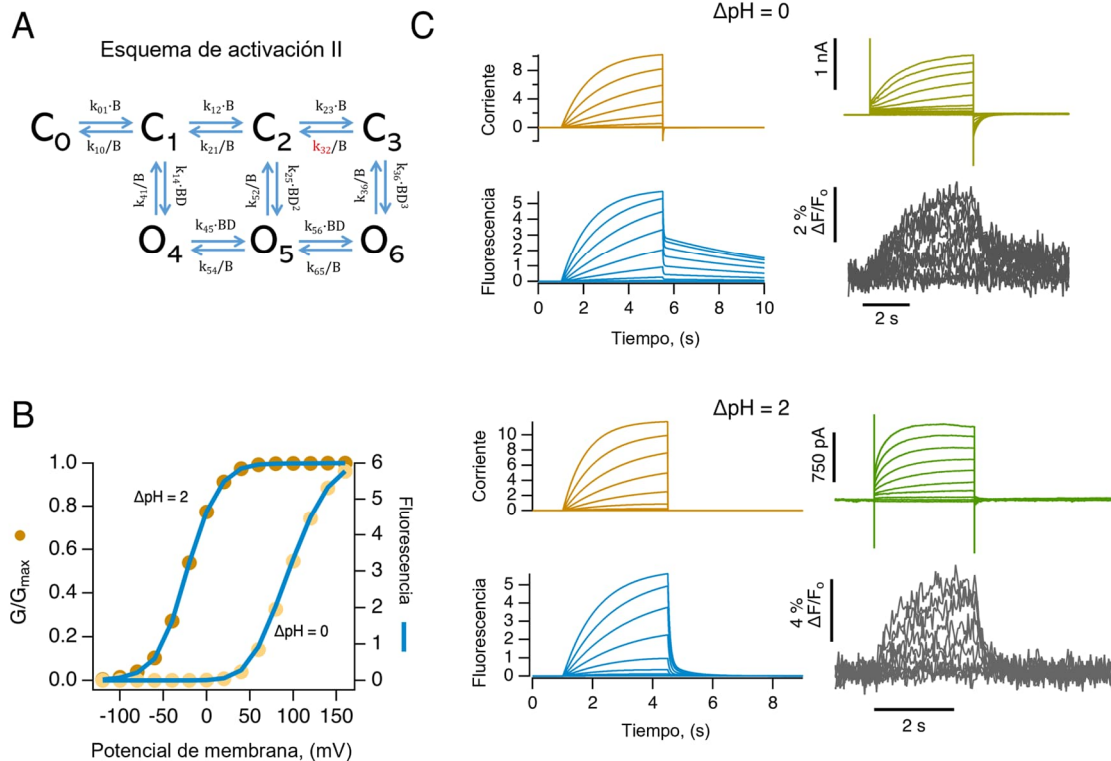


Figura 33. Modelo alostérico de activación de Hv1 por voltaje. **A.** Esquema del modelo alostérico. C = cerrado, O = Abierto. Los k_{ij} son constantes de velocidad y D es un factor de acoplamiento alostérico para la apertura del canal, mientras que B es un factor empírico que explica la dependencia del pH de las constantes de velocidad. Nótese que, en este modelo, la apertura del canal puede ocurrir sin el movimiento total del sensor de voltaje. La constante de velocidad de cierre indicada en rojo tiene un valor mucho menor que todos los demás (a 0 mV) y es responsable del lento retorno de la señal de fluorescencia tras la repolarización. **B.** Simulación que compara la conductancia en estado estacionario y la fluorescencia en función del voltaje. En este mecanismo, la fluorescencia aparece con los mismos voltajes que la conductancia, ya que la apertura del canal puede ocurrir desde estados cerrados tempranos y las corrientes pueden fluir sin la activación del sensor de voltaje completo. **C.** Comparación de corrientes simuladas (líneas naranjas) y señales de fluorescencia (trazos azules) con corrientes registradas experimentalmente (trazos verdes) y fluorescencia (registros en gris) en los dos valores indicados de ΔpH , utilizando los parámetros proporcionados en tabla 6.

Los experimentos de PCF revelaron diferencias importantes tanto en la señal de fluorescencia como en la modulación de la conductancia a protones. En lo

referente de la señal de fluorescencia, los experimentos con pH simétrico de 7 mostraron un crecimiento continuo sin llegar a un estado estacionario y mostrando una menor tendencia a la saturación. Además, durante la desactivación el retorno de la señal mostró una reducción en la amplitud del componente lento. Interesantemente, la respuesta de la conductancia en función del voltaje se desacopló de la curva de fluorescencia, ocurriendo alrededor de 36 mV a potenciales más negativos. Esto demuestra que los valores absolutos de pH a ambos lados de la membrana pueden afectar al VSD de forma diferenciada.

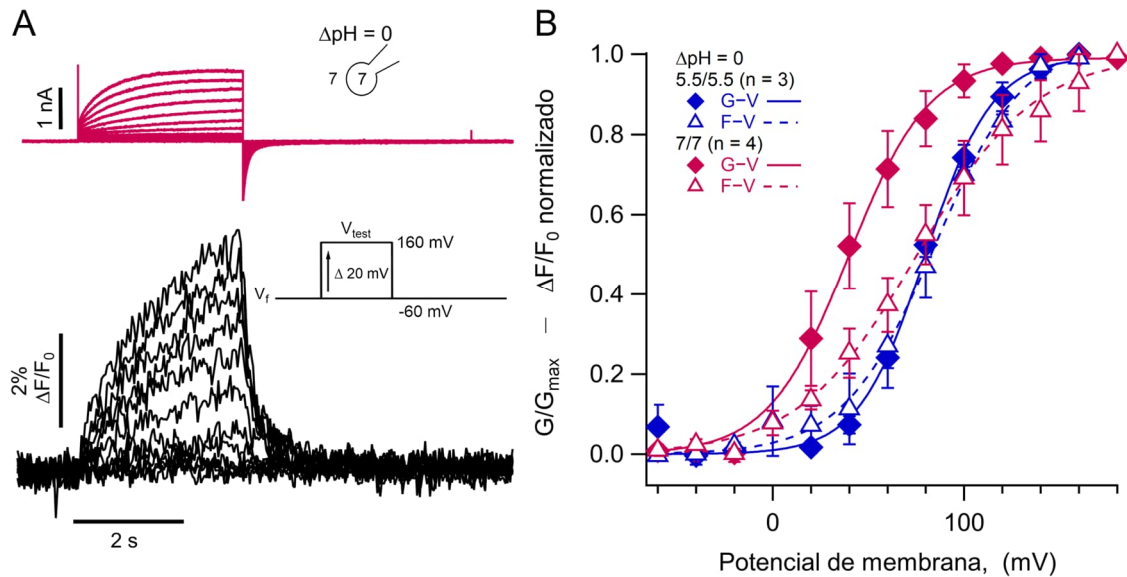


Figura 34. Los valores de pH absolutos son determinantes en la activación en Hv1-L201Anap. A. Experimento representativo de PCF a $\Delta\text{pH} = 0$ ($7_{\text{ext}}-7_{\text{int}}$). Las corrientes se muestran en magentas y la señal de fluorescencia en trazos negros. Se nota en estos últimos una pérdida del componente lento durante el regreso al potencial de mantenimiento, a diferencia de lo encontrado en los experimentos de la figura 29 A que tiene las mismas condiciones de $\Delta\text{pH} = 0$, pero con pH 5.5 en ambos lados de la membrana. **B.** Curvas G-V (rombos rellenos) y F-V (triángulos vacíos) a $\Delta\text{pH} = 0$ pero con diferentes valores absolutos de pH ($\text{pH}_e/\text{pH}_i = 5,5/5,5$ en azul $n = 3$; $\text{pH}_e/\text{pH}_i = 7/7$ en magenta, $n = 4$). Se observa como las curvas F-V en ambas condiciones se presentan en rangos de voltaje similares mientras que la conductancia en los experimentos $7_{\text{ext}}-7_{\text{int}}$ se recorre ~ 40 mV a potenciales más negativos. Los parámetros de ajuste de Boltzmann fueron **pH_e/pH_i = 7/7 F-V:** $V_{0,5} = 75.3 \pm 2.2$ mV; $q = 0.8 \pm 0.04$ e₀. **G-V:** $V_{0,5} = 39.6 \pm 1.3$ mV; $q = 1.2 \pm 0.1$ e₀.

Parámetros de esquema cinético I						
Estado	Fluorescencia	Constante a 0 mV	$\Delta\text{pH} = 0$		$\Delta\text{pH} = 2$	
			velocidad (s^{-1})	z (e_0)	velocidad (s^{-1})	z (e_0)
C0	0	k_{01}	0.12	0.3	1	0.3
C1	1	k_{10}	5	-0.3	5	-0.3
C2	2	k_{12}	2	0.4	16	0.4
O3	4	k_{21}	0.1	-0.3	1	-0.3
		k_{23}	0.11	0.8	0.88	0.8
		k_{32}	1	-0.8	1	-0.8

Tabla 5. Parámetros de ajuste del modelo cinético simple. En rojo se muestra la constante asociada a la transición lenta durante la desactivación de H_v1

Parámetros de esquema cinético II						
Estados	Fluorescencia	Constante a 0 mV	$\Delta\text{pH} = 0$ B = 0.33 D = 2		$\Delta\text{pH} = 2$ B = 12 D = 2	
			velocidad (s^{-1})	z (e_0)	velocidad (s^{-1})	z (e_0)
C0	0	k_{01}	0.1	0.5	0.1	0.5
C1	0	k_{10}	1	-0.3	1	-0.3
C2	0	k_{12}	0.5	1.1	0.5	1.1
C3	3	k_{21}	0.5	-0.4	0.5	-0.4
O4	5	k_{23}	2	0.6	2	0.6
O5	6	k_{32}	0.02	-0.3	200	-0.3
O6	6	k_{14}	1	0.5	1	0.5
		k_{41}	3	-0.6	3	-0.6
		k_{25}	2	0.5	2	0.5
		k_{52}	3	-0.6	3	-0.6
		k_{36}	1	0.5	1	0.5
		k_{63}	3	-0.6	3	-0.6
		k_{45}	1	0.5	1	0.5
		k_{54}	3	-0.6	3	-0.6
		k_{56}	1	0.5	1	0.5
		k_{65}	0.1	-0.6	0.1	-0.6

Tabla 6. Parámetros de ajuste del modelo alostérico. En rojo se muestra la constante asociada a la transición lenta durante la desactivación de H_v1 .

Discusión

El sistema de incorporación del aminoácido Anap fue eficiente para el estudio H_v1

Uno de los aspectos cruciales en el estudio de los canales iónicos es encontrar cómo los diferentes estímulos se traducen en los cambios conformacionales del canal. El uso experimental de sondas fluorescentes ha sido una herramienta que ha ampliado el panorama sobre la naturaleza de esta relación estructura-función en los canales iónicos activados por voltaje, al aportar conocimiento desde la estequiometría de las diferentes subunidades del canal hasta detectar movimientos eléctricamente silenciosos involucrados en la activación (Kusch & Zifarelli, 2014; Suárez-Delgado & Islas, 2020). El Anap ha demostrado ser una herramienta útil en el estudio de la estequiometría y el movimiento de diversas proteínas de membrana y otros canales iónicos (M. C. Puljung, 2021). Debido a su menor tamaño y la posibilidad de incorporación en sitios específicos, se usa frecuentemente como agente donador para estimación de distancias a través de mediciones de transferencia de energía por resonancia (FRET)(Dai, 2022; Dai et al., 2019; Dai & Zagotta, 2017; Gordon et al., 2018; Kawanabe et al., 2018; Zagotta et al., 2016). De igual forma, gracias a la sensibilidad de su fluorescencia a la polaridad del medio, se utiliza para mapear los cambios conformacionales relacionados a la función de canales de potasio tipo *Shaker* (Kalstrup & Blunck, 2013, 2018), canales HCN (Dai et al., 2019) y fosfatasas sensibles a voltaje (Sakata et al., 2016).

En los experimentos realizados en este trabajo, se demostró que se puede incorporar el aminoácido no canónico Anap como sonda fluorescente para estudiar los cambios conformacionales relacionados a la activación dependiente del voltaje en el canal H_v1 humano usando la técnica de PCF. Una ventaja de esta aproximación es que, al ser incorporado genéticamente, permitió colocar el fluoróforo en canales

funcionales en varios sitios a lo largo de S4 y del bucle S3-S4 reduciendo la probabilidad de incorporación inespecífica, como lo muestran las diferencias entre los experimentos electrofisiológicos de expresión en ausencia y presencia del Anap en el medio de incubación (figura 16). Además, para valorar el éxito de esta incorporación se eligió a la proteína fluorescente mCherry como reportera. La presencia de ambas fluorescencias en las células que se sometieron a las condiciones de incorporación y que a su vez presentaron una expresión del canal mayor a los controles en forma de conductancia a los protones, nos permitió afirmar que la incorporación del Anap había sido exitosa.

En este trabajo se buscó evitar perturbaciones relevantes que alteren los cambios conformacionales del canal al incorporar una sonda fluorescente en forma de un aminoácido, lo que podría afectar sus propiedades electrofisiológicas. De esta manera, se podría investigar el movimiento del canal en condiciones similares a las naturales. Los resultados de los experimentos de electrofisiología a $\Delta\text{pH} = 1$ demostraron que las propiedades electrofisiológicas de activación fueron similares a las del canal silvestre tanto en la proteína de fusión con mCherry de reportera en C-terminal, así como en la mayoría de las mutantes donde el aminoácido no canónico ingresó en la estructura del canal $\text{H}_\text{V}1$. Estos resultados demuestran al sistema de incorporación como un sistema robusto para estudiar las propiedades del canal de protones.

Con respecto a la fluorescencia de ambas sondas, los espectros de emisión obtenidos mostraron que ambos fluoróforos presentaron características previamente descritas en la literatura, indicando su integridad al momento de realizar los experimentos. Por otro lado, si bien el láser de 405 nm tuvo la capacidad de excitar a ambas sondas en todas las mutantes probadas, el análisis de porcentaje de excitación cruzada en sus espectros de emisión reveló la ausencia de interacción entre la fluorescencia de ambas sondas, independientemente del sitio de

incorporación. Esto resulta útil porque permite evaluar la intensidad del brillo de forma independiente pero relacionada con el nivel de expresión ya que la presencia de una está ligada a la presencia de la otra y permitiendo a su vez normalizar el brillo de Anap con respecto al de mCherry, una medición que resultó útil para la acumulación de evidencia que señaló a F150 como una molécula apagadora, como se describe en el apartado de los resultados con la doble mutante.

Dado que Anap se diseñó como una sonda sensible al entorno, el hecho de que el espectro de emisión de Anap en estos sitios sea muy similar al de Anap en agua, sugiere que estos residuos están solvatados en el H_v1 nativo. La única posición que muestra un espectro de Anap con desplazamiento hacia el azul es I202, que es el residuo más C-terminal explorado y podría enterrar al grupo R de Anap en un entorno más hidrofóbico. Estos resultados concuerdan con los obtenidos de varios ejercicios de simulación computacional del canal H_v1 donde el VSD presenta en su interior dos cavidades hidratadas, la intracelular y extracelular, distribuidas en un patrón con forma de reloj de arena, separadas por una barrera hidrofóbica durante el estado cerrado (Boytssov et al., 2023; Geragotelis et al., 2020; Ramsey et al., 2010; Randolph et al., 2016). Esto permitiría un ambiente principalmente polar a lo largo de la porción extracelular del S4 de H_v1.

Por otro lado, es bien conocido que la actividad de los canales H_v1 puede cambiar la concentración local de protones cerca del sitio de conducción (Kapus et al., 1993), y las sondas de fluorescencia se han utilizado para detectar estos flujos de protones gracias a que algunos fluoróforos pueden alterar su fluorescencia en función del pH (De-la-Rosa et al., 2016; L. Zhang et al., 2016). Entonces se investigó si el Anap incorporado al canal de protones también cambia su fluorescencia en función del pH. En los experimentos se demostró que el brillo de Anap es altamente insensible al pH en el rango de 4 a 8, además de que no cambia su fluorescencia en condiciones en las que los flujos salientes intensos pueden cambiar el pH intracelular

local. Nuestros experimentos confirman que Anap se puede utilizar sin interferencia por cambios locales en la concentración de protones, agregando mayor evidencia de que este aminoácido es una sonda competente para medir los cambios conformacionales del canal.

Los cambios conformacionales del S4 de H_v1 y su modulación por el ΔpH revelados por la incorporación de Anap.

Cuando se incorporó en la posición 197, la sonda Anap produjo señales de fluorescencia que indican un aumento en la intensidad con la despolarización de la membrana. Además, la magnitud de las señales se saturó en relación con la magnitud en potenciales positivos. Este fenómeno de saturación suele observarse en los registros de corriente de compuerta en los VSD de los canales activados por voltaje y se relaciona con el movimiento del S4 durante la activación (Catacuzzeno et al., 2023). En el caso concreto de H_v1, previamente se han realizado estudios sobre la activación del canal H_v1 de *Ciona intestinalis* con el uso de la sonda fluorescente TMRM unida al bucle S3-S4 a través de puentes disulfuro (Gonzalez et al., 2010; Mony et al., 2015; Qiu et al., 2013; Schladt & Berger, 2020). En estos estudios la señal fluorescente también se saturó a potenciales positivos, pero el movimiento del VSD durante la activación del canal se registró a través del apagamiento de la sonda fluorescente.

Este comportamiento de aumento de fluorescencia en nuestros resultados fue la primera evidencia que indicó que Anap se podría estar alejando de alguna molécula apagadora a medida que los segmentos S4 experimentan un movimiento hacia afuera durante la activación. Comparando con otros estudios en donde Anap se ha incorporado en otras proteínas de membrana, se ha demostrado que los cambios de fluorescencia se presentan dependiendo de la posición donde la sonda se incorpora. Por ejemplo, en el canal de potasio *Shaker*, el Anap se incorporó en el

linker S4-S5, localizándose en el lado intracelular, y mostró una reducción de fluorescencia en respuesta a la despolarización (Kalstrup & Blunck, 2018). También, Anap se incorporó a lo largo del S4 del canal de nucleótidos cíclicos activados por hiperpolarización (Dai et al., 2019), donde la fluorescencia de la sonda se apagó o encendió durante la hiperpolarización de manera dependiente de la posición. Por último, también se ha incorporado Anap en la base del S4 en la fosfatasa dependiente de voltaje de *C. intestinalis* (CiVSP) (Mizutani et al., 2022; Sakata et al., 2016), donde se apaga con la despolarización. Cabe mencionar que, a pesar de esta recopilación de evidencia, la dirección de los cambios de fluorescencia debido al movimiento de S4 es difícil de predecir ya que, se ha descrito que la fluorescencia de Anap es afectada tanto por la polaridad del entorno local como por la interacción con grupos de extinción que forman parte de la secuencia del canal (Chatterjee et al., 2013; Mizutani et al., 2022; M. Puljung et al., 2019).

Los cambios de fluorescencia en función del voltaje que observamos en los canales H_v1-A197Anap (curvas F-V) indican que tienen casi la misma dependencia del voltaje que la formación de la conductancia del canal (curvas G-V) en los tres valores de ΔpH probados. Esto sugiere dos situaciones: 1) que el movimiento de S4 revelado por Anap sigue de cerca la apertura del canal y 2) que el movimiento de S4 y la activación de la conductancia de protones están igualmente afectados por el gradiente de protones. Una conclusión similar se ha alcanzado en estudios que miden los movimientos de S4 de H_v1 mediante fluorescencia (Schladt & Berger, 2020) o en H_v1 de Ciona mediante registros de corriente de compuerta (Carmona et al., 2018; De La Rosa & Ramsey, 2018). En contra de lo que se pensó en un inicio, estos cambios de fluorescencia en función del voltaje no se acompañaron de cambios en el espectro de emisión de Anap, lo que sugiere que la sonda permanece en un entorno solvatado independientemente del estado del canal. Esto también concuerda con el hallazgo de que el dominio del sensor de voltaje (VSD) que forma los canales H_v1 tiene una gran cavidad extracelular capaz de contener muchas

moléculas de agua (Boytsov et al., 2023; Geragotelis et al., 2020; Ramsey et al., 2010).

Incorporar la sonda en un sitio más intracelular dentro del S4, como lo es el sitio L201, mostró hallazgos similares con la mutante H_v1-A197Anap en cuanto a la dirección de los cambios de fluorescencia en respuesta a pulsos de voltaje y su notable modulación por parte del Δ pH. Que los cambios sean en forma de aumento de fluorescencia aporta más evidencia de la existencia de un movimiento en conjunto del S4 durante la activación del canal H_v1 y los VSD en general (Bezanilla, 2018; Carmona et al., 2018; Musset & DeCoursey, 2012). De igual manera, el que la posición del Anap en el sitio 201 fuera más profunda y cercana durante el estado de reposo al residuo apagador F150 permitió una mejor relación señal/ruido en el trazo de fluorescencia.

La construcción H_v1-L201Anap también permitió descubrir un movimiento lento altamente modulado por el efecto del Δ pH en las transiciones de desactivación. La señal de fluorescencia registrada al cerrar el canal a Δ pH = 0 mostró dos componentes, uno con una constante de tiempo de la misma magnitud que el cierre del canal, mientras que el otro fue cerca de 10 veces más lento que el cierre del canal tal como se informa por la corriente de cola. Este dato sugiere que este componente se produce por al menos una transición intermedia lenta. Esto concuerda con los experimentos de VCF reportados en el H_v1 de *C. intestinalis*, donde la señal fluorescente presenta una cinética más lenta durante la desactivación del canal (Qiu et al., 2013; Schladt & Berger, 2020). Curiosamente, los registros de corrientes de compuerta en canales mutantes de H_v1 de *C. intestinalis*, en donde se midió de forma eléctrica el movimiento del S4, muestran que el retorno de la carga después de la despolarización puede ser muy lento, produciendo inmovilización de la carga de compuerta (Carmona et al., 2018). Esta doble transición de una

transición lenta singular en la activación de H_V1 ilustra el valor del registro de fluorescencia con una sonda pequeña como Anap.

Siguiendo los datos de las dos mutantes simples que se estudiaron con diferentes condiciones de ΔpH , H_V1 -A197Anap y H_V1 -L201Anap, la relación estrecha entre las G-V y F-V indican que el movimiento del S4 parece ser simultáneo a la formación de la conductancia, lo que sugiere que el movimiento de S4 puede continuar después de la activación del canal. Esto contrasta con lo usualmente encontrado en los canales activados por voltaje en donde la traducción electromecánica tiene que pasar del VSD al PD (Catacuzzeno et al., 2023). Posiblemente en el H_V1 al ser el mismo dominio VSD el que contiene ambas funciones, ambos sucesos pueden estar más estrechamente relacionados. En los experimentos de cuantificación del movimiento de carga, la comparación de los valores $V_{0.5}$ de las curvas Q-V y G-V en los canales H_V1 (De La Rosa & Ramsey, 2018) indica que la carga se desplaza a valores ligeramente más negativos (aprox. 10 mV) que la conductancia, no en todos los valores de ΔpH . Si bien estos resultados se alinean con los que nosotros encontramos a través de los experimentos de PCF, cabe señalar que la F-V y Q-V se deben considerar observaciones diferentes de un mismo mecanismo. Los cambios de fluorescencia dependen de todos los estados conformacionales en los que el fluoróforo tiene valores distintos de fluorescencia, mientras que las corrientes de compuerta se producen durante las transiciones entre conformaciones con distribuciones de carga dependientes del estado (Cha & Bezanilla, 1997; Mannuzzu et al., 1996). Por estas razones, no se puede esperar que las curvas F-V y Q-V de canales multiconformacionales sean totalmente idénticas.

Integrando los datos de fluorescencia y de electrofisiología fue posible extrapolar cualitativamente estos resultados en un modelo cinético simple secuencial similar a los publicados anteriormente (Qiu et al., 2013; Villalba-Galea, 2014). Este modelo fue capaz de recapitular el comportamiento lento de la

fluorescencia durante la desactivación al asociarlo con una transición tardía entre estados cerrados. Sin embargo, este modelo secuencial señaló la necesidad de implementar un modelo alostérico que contemple los rasgos señalados tanto en este trabajo como en la literatura, como la exquisita modulación por pH, los efectos de cooperatividad en la activación de los VSD y que el movimiento del S4 continuase después de la formación de la conductancia. Este modelo sugiere que todas las transiciones en la vía de activación, incluida una transición lenta característica detectada por fluorescencia, están moduladas por el ΔpH . Por lo tanto, es consistente con experimentos recientes que han demostrado que el efecto característico de regulación del gradiente de protones en los canales de protones dependientes del voltaje se produce mediante un cambio conformacional que afecta al movimiento del sensor de voltaje y no una transición de apertura del canal que ocurre después de la activación del sensor de voltaje (Carmona et al., 2021; Villalba-Galea, 2014). No obstante, el mecanismo de modulación de ΔpH todavía se desconoce. Se ha propuesto que la energía almacenada en el gradiente de pH está directamente acoplada al movimiento de S4 para producir una regulación dependiente de ΔpH (Carmona et al., 2021).

La creación de modelos donde se integren diferentes estímulos que modulan la activación de los canales iónicos es una pieza fundamental para el estudio actual de la función de estos. Por ejemplo, para los canales iónicos de potasio activados por calcio (canales BK), Horrigan y Aldrich integraron un modelo en donde se describe una interacción alostérica entre tres eventos importantes para la apertura del canal: la activación del sensor del voltaje, la unión de los iones Ca^{2+} y la apertura del canal (Horrigan & Aldrich, 2002). En este modelo Horrigan-Aldrich (HA), las constantes de equilibrio de estos tres eventos son afectados a su vez por factores de acoplamiento alostérico entre sí, permitiendo entonces que la apertura de la compuerta del canal y la activación de los VSD sean afectadas de forma diferente por la concentración de calcio y viceversa. Haciendo un acercamiento parecido con

respecto al H_v1 y su modulación por los protones, durante el desarrollo de un trabajo paralelo en el laboratorio con el canal H_v1 de coral de recién descubrimiento, se planteó también un modelo alostérico que recuerda al modelo HA en el que los protones extracelulares e intracelulares pueden afectar a las redes electrostáticas locales y generar una regulación dependiente de ΔpH (De La Rosa & Ramsey, 2018; Rangel-Yescas et al., 2021). Esta clase de modelos predice la existencia de múltiples estados abiertos, lo cual es respaldado por la observación de que el movimiento de S4 puede ocurrir después de la apertura del canal.

Por último, un mecanismo en el que la energía del gradiente de protones se acopla al movimiento de S4 predice que el valor absoluto del pH no debería influir en la regulación. Curiosamente, hemos observado que los valores absolutos de pH utilizados para establecer un $\Delta\text{pH} = 0$ afectan la regulación, lo que concuerda con los resultados observados en las corrientes de activación de la mutante CiH_v1 (Carmona et al., 2021). Cuando $\text{pH}_e = 5.5 / \text{pH}_i = 5.5$, las curvas G-V y F-V están casi superpuestas y la señal de fluorescencia durante el cierre del canal tiene un componente rápido y uno lento; en contraste, cuando $\text{pH}_e = 7 / \text{pH}_i = 7$, la curva F-V tiene casi la misma dependencia del voltaje, pero la conductancia se puede observar a voltajes más negativos y la señal de fluorescencia solo contiene el componente rápido. Estos resultados sugieren que el pH absoluto en el lado extracelular del canal es un determinante de la regulación en estado estacionario, presumiblemente modulando la constante de velocidad lenta en la vía de activación.

F150 como molécula apagadora de la fluorescencia de Anap

Descartada la posibilidad de que los cambios eran producidos por cambios en la polaridad del medio, dado que Anap permanece solvatado en los estados cerrado y abierto, se investigó el origen de los cambios de fluorescencia reportados. Como es común con otras sondas fluorescentes, se planteó la hipótesis de que un

residuo aromático podría actuar como un apagador de Anap a través de mecanismos que requieren una proximidad estrecha como la transferencia de electrones fotoinducida o interacciones catión- π (Islas & Zagotta, 2006; Klymchenko, 2017; Pantazis & Olcese, 2012; Young & Artigas, 2021). Por ejemplo, en la literatura se ha descrito que el residuo aromático del triptófano puede actuar como molécula apagadora de Anap (Mizutani et al., 2022). Se hizo un análisis de la secuencia buscando la presencia de este tipo de residuo y se halló que un residuo aromático fuera de S4 lo suficientemente cercano como para tener esta función apagadora es F150. La mutación F150A en el fondo de Hv1-A197Anap produjo un incremento en la intensidad de fluorescencia de Anap normalizada con la de mCherry en comparación con el mismo cociente Anap/mCherry en la construcción de fondo, lo que indica una reducción del apagamiento de fluorescencia en el estado cerrado por la ausencia de este residuo aromático, revelando su función apagadora de Anap. En conjunto al aumento de las señales de fluorescencia de Hv1-A197Anap en función del voltaje, estos resultados sugieren que el Anap colocado en el sitio 197 se aleja de F150 a medida que el segmento S4 se mueve hacia afuera durante el cambio conformacional de activación del canal. No obstante, cabe señalar que los canales F150A-197Anap todavía producen cambios de fluorescencia con los cambios de potencial de membrana. Esto sugiere que otros residuos de aminoácidos aparte de F150, ya sean aromáticos o que presenten alguna carga que pueda interactuar con el fluoróforo, también participan en apagar la señal de Anap, o que, por otro lado, se sigan produciendo cambios en el rendimiento cuántico de Anap debido a una mayor accesibilidad al solvente dependiente del voltaje.

Se ha demostrado que F150 es un residuo conservado dentro de los canales iónicos activados por voltaje (Moreau et al., 2014; Tao et al., 2010). En Hv1, forma parte de un grupo hidrofóbico a través de la cual las cargas de S4 se deslizan durante la activación del canal, formando parte del centro de transferencia de carga (Banh et al., 2019; Wu et al., 2022). Las mutaciones en esta posición y en W207 en

S4 producen cambios en la compuerta (Cherny et al., 2015; Hong et al., 2013). En los experimentos de este proyecto, F150A-197Anap mostró un comportamiento diferente al encontrado en el canal silvestre. Mientras que en la G-V se presenta un cambio reducido entre ΔpH 0 y 1, de los ~ 40 mV esperados a 22 mV, la curva F-V se desplaza en 58 mV por unidad de ΔpH . Estos cambios podrían explicarse por un movimiento alterado de S4 a través de F150A, lo que lleva a cambios en el acoplamiento entre el movimiento del sensor de voltaje y la activación de la conductancia de protones dado a la ausencia de un componente del centro de transferencia de carga. Al mismo tiempo, esta es la primera vez que se informa que F150 podría tener un papel en el mecanismo de detección y modulación por pH de H_v1.

Conclusiones

- Cuando se encontraron todas las condiciones necesarias para la incorporación del aminoácido, Anap rescató eficientemente la traducción de los canales a juzgar por la fluorescencia de mCherry, fungiendo su papel de reportera en la región membranal de las células transfectadas y la presencia de corrientes de protones en respuesta de voltaje.
- El brillo de Anap es insensible al pH en el rango de 4 a 8, además de no cambiar su fluorescencia en condiciones en las que los flujos salientes intensos pueden cambiar el pH en la vecindad del canal.
- La sonda fluorescente Anap es adecuada para medir los cambios conformacionales del canal de protones, ya que se demostró que es insensible a los cambios locales de pH que pudieran ocurrir durante el funcionamiento del canal H_v1.
- La incorporación de Anap en los sitios A197 y L201 del canal permitió evaluar los cambios conformacionales del S4 de H_v1.
- En el sitio L201, la señal de fluorescencia permitió describir por primera vez la presencia de dos transiciones entre estados cerrados de H_v1, uno acoplado al cierre del canal y otro de cinética lenta entre estados cerrados más profundos.
- El anillo aromático de la fenilalanina en la posición 150 es capaz de fungir como una molécula apagadora del Anap.
- El movimiento del S4 revelado por la incorporación de Anap está estrechamente coordinado con el establecimiento de la conductancia a protones en H_v1, lo que sugiere que el movimiento de S4 puede continuar después de la activación del canal.
- El efecto del gradiente de protones en el canal modula el movimiento del S4 y no solo la apertura de la conductancia de protones, lo que apoya que el VSD es responsable de la modulación por pH.

Bibliografía

- Alberts, B. (2002). Membrane transport of small molecules and the electrical properties of membranes. *Molecular biology of the cell*, 615-658.
<https://cir.nii.ac.jp/crid/1570009751316767232>
- Alvear-Arias, J. J., Pena-Pichicoi, A., Carrillo, C., Fernandez, M., Gonzalez, T., Garate, J. A., & Gonzalez, C. (2023). Role of voltage-gated proton channel (Hv1) in cancer biology. *Frontiers in Pharmacology*, 14.
<https://www.frontiersin.org/articles/10.3389/fphar.2023.1175702>
- Banh, R., Cherny, V. V., Morgan, D., Musset, B., Thomas, S., Kulleperuma, K., Smith, S. M. E., Pomès, R., & DeCoursey, T. E. (2019). Hydrophobic gasket mutation produces gating pore currents in closed human voltage-gated proton channels. *Proceedings of the National Academy of Sciences*, 116(38), 18951-18961.
<https://doi.org/10.1073/pnas.1905462116>
- Baud, C., & Barish, M. E. (1984). Changes in membrane hydrogen and sodium conductances during progesterone-induced maturation of *Ambystoma* oocytes. *Developmental Biology*, 105(2), 423-434. [https://doi.org/10.1016/0012-1606\(84\)90299-9](https://doi.org/10.1016/0012-1606(84)90299-9)
- Belinky, F., Babenko, V. N., Rogozin, I. B., & Koonin, E. V. (2018). Purifying and positive selection in the evolution of stop codons. *Scientific Reports*, 8(1), Article 1.
<https://doi.org/10.1038/s41598-018-27570-3>
- Bezanilla, F. (2007). Voltage-Gated Ion Channels. En S.-H. Chung, O. S. Andersen, & V. Krishnamurthy (Eds.), *Biological Membrane Ion Channels: Dynamics, Structure, and Applications* (pp. 81-118). Springer. https://doi.org/10.1007/0-387-68919-2_3
- Bezanilla, F. (2008). How membrane proteins sense voltage. *Nature Reviews Molecular Cell Biology*, 9(4), Article 4. <https://doi.org/10.1038/nrm2376>
- Bezanilla, F. (2018). Gating currents. *Journal of General Physiology*, 150(7), 911-932.
<https://doi.org/10.1085/jgp.201812090>
- Boytsov, D., Brescia, S., Chaves, G., Koefler, S., Hanneschlaeger, C., Siligan, C., Goessweiner-Mohr, N., Musset, B., & Pohl, P. (2023). Trapped Pore Waters in the Open Proton Channel HV 1. *Small (Weinheim an Der Bergstrasse, Germany)*, 19(16), e2205968. <https://doi.org/10.1002/smll.202205968>
- Cahalan, M., & Neher, E. (1992). [1] Patch clamp techniques: An overview. En *Methods in Enzymology* (Vol. 207, pp. 3-14). Academic Press. [https://doi.org/10.1016/0076-6879\(92\)07003-7](https://doi.org/10.1016/0076-6879(92)07003-7)
- Cardozo, D. (2016). An intuitive approach to understanding the resting membrane potential. *Advances in Physiology Education*, 40(4), 543-547.
<https://doi.org/10.1152/advan.00049.2016>
- Carmona, E. M., Fernandez, M., Alvear-Arias, J. J., Neely, A., Larsson, H. P., Alvarez, O., Garate, J. A., Latorre, R., & Gonzalez, C. (2021). The voltage sensor is responsible

- for Δ pH dependence in Hv1 channels. *Proceedings of the National Academy of Sciences*, 118(19). <https://doi.org/10.1073/pnas.2025556118>
- Carmona, E. M., Larsson, H. P., Neely, A., Alvarez, O., Latorre, R., & Gonzalez, C. (2018). Gating charge displacement in a monomeric voltage-gated proton (Hv1) channel. *Proceedings of the National Academy of Sciences*, 115(37), 9240-9245. <https://doi.org/10.1073/pnas.1809705115>
- Catacuzzeno, L., Conti, F., & Franciolini, F. (2023). Fifty years of gating currents and channel gating. *The Journal of General Physiology*, 155(8), e202313380. <https://doi.org/10.1085/jgp.202313380>
- Catterall, W. A. (1995). Structure and Function of Voltage-Gated Ion Channels. *Annual Review of Biochemistry*, 64(1), 493-531. <https://doi.org/10.1146/annurev.bi.64.070195.002425>
- Cha, A., & Bezanilla, F. (1997). Characterizing Voltage-Dependent Conformational Changes in the ShakerK⁺ Channel with Fluorescence. *Neuron*, 19(5), 1127-1140. [https://doi.org/10.1016/S0896-6273\(00\)80403-1](https://doi.org/10.1016/S0896-6273(00)80403-1)
- Chamberlin, A., Qiu, F., Wang, Y., Noskov, S. Y., & Larsson, H. P. (2015). Mapping the gating and permeation pathways in the voltage-gated proton channel Hv1. *Journal of Molecular Biology*, 427(1), 131-145. <https://doi.org/10.1016/j.jmb.2014.11.018>
- Chanda, S. C., Baron. (2015). Basic Mechanisms of Voltage Sensing. En *Handbook of Ion Channels*. CRC Press.
- Chatterjee, A., Guo, J., Lee, H. S., & Schultz, P. G. (2013). A Genetically Encoded Fluorescent Probe in Mammalian Cells. *Journal of the American Chemical Society*, 135(34), 12540-12543. <https://doi.org/10.1021/ja4059553>
- Chaves, G., Jardin, C., Derst, C., & Musset, B. (2023). Voltage-Gated Proton Channels in the Tree of Life. *Biomolecules*, 13(7), Article 7. <https://doi.org/10.3390/biom13071035>
- Cherny, V. V., Markin, V. S., & DeCoursey, T. E. (1995). The voltage-activated hydrogen ion conductance in rat alveolar epithelial cells is determined by the pH gradient. *The Journal of General Physiology*, 105(6), 861-896. <https://doi.org/10.1085/jgp.105.6.861>
- Cherny, V. V., Morgan, D., Musset, B., Chaves, G., Smith, S. M. E., & DeCoursey, T. E. (2015). Tryptophan 207 is crucial to the unique properties of the human voltage-gated proton channel, hHV1. *Journal of General Physiology*, 146(5), 343-356. <https://doi.org/10.1085/jgp.201511456>
- Chowdhury, B. C., Sandipan. (2023). Voltage-Dependent Gating of Ion Channels. En *Textbook of Ion Channels Volume I*. CRC Press.
- Codding, S. J., & Trudeau, M. C. (2020). Measuring Intrinsic Ligand Dynamics of hERG Potassium Channels using the Unnatural Amino Acid L-ANAP and TM-FRET. *Biophysical Journal*, 118(3), 263a.
- Cox, C. D., Bavi, N., & Martinac, B. (2019). Biophysical Principles of Ion-Channel-Mediated Mechanosensory Transduction. *Cell Reports*, 29(1), 1-12. <https://doi.org/10.1016/j.celrep.2019.08.075>

- Dai, G. (2022). Neuronal KCNQ2/3 channels are recruited to lipid raft microdomains by palmitoylation of BACE1. *Journal of General Physiology*, *154*(4), e202112888. <https://doi.org/10.1085/jgp.202112888>
- Dai, G., Aman, T. K., DiMaio, F., & Zagotta, W. N. (2019). The HCN channel voltage sensor undergoes a large downward motion during hyperpolarization. *Nature Structural & Molecular Biology*, *26*(8), Article 8. <https://doi.org/10.1038/s41594-019-0259-1>
- Dai, G., & Zagotta, W. N. (2017). Molecular mechanism of voltage-dependent potentiation of KCNH potassium channels. *eLife*, *6*, e26355. <https://doi.org/10.7554/eLife.26355>
- De La Rosa, V., & Ramsey, I. S. (2018). Gating Currents in the Hv1 Proton Channel. *Biophysical Journal*, *114*(12), 2844-2854. <https://doi.org/10.1016/j.bpj.2018.04.049>
- Debanne, D., Campanac, E., Bialowas, A., Carlier, E., & Alcaraz, G. (2011). Axon Physiology. *Physiological Reviews*, *91*(2), 555-602. <https://doi.org/10.1152/physrev.00048.2009>
- Decoursey, T. E. (2003). Voltage-gated proton channels and other proton transfer pathways. *Physiological Reviews*, *83*(2), 475-579. <https://doi.org/10.1152/physrev.00028.2002>
- DeCoursey, T. E. (2013). Voltage-gated proton channels: Molecular biology, physiology, and pathophysiology of the H(V) family. *Physiological Reviews*, *93*(2), 599-652. <https://doi.org/10.1152/physrev.00011.2012>
- DeCoursey, T. E. (2015). The Voltage-Gated Proton Channel: A Riddle, Wrapped in a Mystery, inside an Enigma. *Biochemistry*, *54*(21), 3250-3268. <https://doi.org/10.1021/acs.biochem.5b00353>
- DeCoursey, T. E., & Cherny, V. V. (1994). Voltage-activated hydrogen ion currents. *The Journal of Membrane Biology*, *141*(3), 203-223. <https://doi.org/10.1007/BF00235130>
- DeCoursey, T. E., & Cherny, V. V. (1996). II. Voltage-activated Proton Currents in Human THP-1 Monocytes. *The Journal of Membrane Biology*, *152*(2), 131-140. <https://doi.org/10.1007/s002329900092>
- DeCoursey, T. E., & Hosler, J. (2014). Philosophy of voltage-gated proton channels. *Journal of The Royal Society Interface*, *11*(92), 20130799. <https://doi.org/10.1098/rsif.2013.0799>
- DeCoursey, T. E., Morgan, D., Musset, B., & Cherny, V. V. (2016). Insights into the structure and function of HV1 from a meta-analysis of mutation studies. *Journal of General Physiology*, *148*(2), 97-118.
- De-la-Rosa, V., Rangel-Yescas, G. E., Ladrón-de-Guevara, E., Rosenbaum, T., & Islas, L. D. (2013). Coarse Architecture of the Transient Receptor Potential Vanilloid 1 (TRPV1) Ion Channel Determined by Fluorescence Resonance Energy Transfer. *The Journal of Biological Chemistry*, *288*(41), 29506-29517. <https://doi.org/10.1074/jbc.M113.479618>
- De-la-Rosa, V., Suárez-Delgado, E., Rangel-Yescas, G. E., & Islas, L. D. (2016). Currents through Hv1 channels deplete protons in their vicinity. *Journal of General Physiology*, *147*(2), 127-136. <https://doi.org/10.1085/jgp.201511496>

- Dudev, T., Musset, B., Morgan, D., Cherny, V. V., Smith, S. M. E., Mazmanian, K., DeCoursey, T. E., & Lim, C. (2015). Selectivity Mechanism of the Voltage-gated Proton Channel, Hv1. *Scientific Reports*, 5(1), Article 1. <https://doi.org/10.1038/srep10320>
- El Chemaly, A., Nunes, P., Jimaja, W., Castelbou, C., & Demaurex, N. (2014). Hv1 proton channels differentially regulate the pH of neutrophil and macrophage phagosomes by sustaining the production of phagosomal ROS that inhibit the delivery of vacuolar ATPases. *Journal of leukocyte biology*, 95(5), 827-839.
- El Chemaly, A., Okochi, Y., Sasaki, M., Arnaudeau, S., Okamura, Y., & Demaurex, N. (2010). VSOP/Hv1 proton channels sustain calcium entry, neutrophil migration, and superoxide production by limiting cell depolarization and acidification. *Journal of Experimental Medicine*, 207(1), 129-139.
- Fogel, M., & Hastings, J. W. (1972). Bioluminescence: Mechanism and Mode of Control of Scintillon Activity. *Proceedings of the National Academy of Sciences*, 69(3), 690-693. <https://doi.org/10.1073/pnas.69.3.690>
- Fujiwara, Y., Kurokawa, T., Takeshita, K., Kobayashi, M., Okochi, Y., Nakagawa, A., & Okamura, Y. (2012). The cytoplasmic coiled-coil mediates cooperative gating temperature sensitivity in the voltage-gated H⁺ channel Hv1. *Nature Communications*, 3(1), Article 1. <https://doi.org/10.1038/ncomms1823>
- García-Ávila, M., & Islas, L. D. (2019). What is new about mild temperature sensing? A review of recent findings. *Temperature*, 6(2), 132-141. <https://doi.org/10.1080/23328940.2019.1607490>
- Geragotelis, A. D., Wood, M. L., Göddeke, H., Hong, L., Webster, P. D., Wong, E. K., Freites, J. A., Tombola, F., & Tobias, D. J. (2020). Voltage-dependent structural models of the human Hv1 proton channel from long-timescale molecular dynamics simulations. *Proceedings of the National Academy of Sciences*, 117(24), 13490-13498. <https://doi.org/10.1073/pnas.1920943117>
- Gonzalez, C., Koch, H. P., Drum, B. M., & Larsson, H. P. (2010). Strong cooperativity between subunits in voltage-gated proton channels. *Nature Structural & Molecular Biology*, 17(1), Article 1. <https://doi.org/10.1038/nsmb.1739>
- Gordienko, D. V., Tare, M., Parveen, S., Fenech, C. J., Robinson, C., & Bolton, T. B. (1996). Voltage-activated proton current in eosinophils from human blood. *The Journal of Physiology*, 496(2), 299-316. <https://doi.org/10.1113/jphysiol.1996.sp021686>
- Gordon, S. E., Munari, M., & Zagotta, W. N. (2018). Visualizing conformational dynamics of proteins in solution and at the cell membrane. *eLife*, 7, e37248. <https://doi.org/10.7554/eLife.37248>
- Grant, A. O. (2009). Cardiac Ion Channels. *Circulation: Arrhythmia and Electrophysiology*, 2(2), 185-194. <https://doi.org/10.1161/CIRCEP.108.789081>
- He, J., Ritzel, R. M., & Wu, J. (2021). Functions and Mechanisms of the Voltage-Gated Proton Channel Hv1 in Brain and Spinal Cord Injury. *Frontiers in Cellular Neuroscience*, 15. <https://www.frontiersin.org/articles/10.3389/fncel.2021.662971>

- Hille, B. (1970). Ionic channels in nerve membranes. *Progress in Biophysics and Molecular Biology*, 21, 1-32. [https://doi.org/10.1016/0079-6107\(70\)90022-2](https://doi.org/10.1016/0079-6107(70)90022-2)
- Hille, B. (2001). *Ionic Channels of Excitable Membranes*. Sinauer.
- Hondares, E., Brown, M. A., Musset, B., Morgan, D., Cherny, V. V., Taubert, C., Bhamrah, M. K., Coe, D., Marelli-Berg, F., Gribben, J. G., Dyer, M. J. S., DeCoursey, T. E., & Capasso, M. (2014). Enhanced activation of an amino-terminally truncated isoform of the voltage-gated proton channel HVCN1 enriched in malignant B cells. *Proceedings of the National Academy of Sciences*, 111(50), 18078-18083. <https://doi.org/10.1073/pnas.1411390111>
- Hong, L., Pathak, M. M., Kim, I. H., Ta, D., & Tombola, F. (2013). Voltage-sensing domain of voltage-gated proton channel Hv1 shares mechanism of block with pore domains. *Neuron*, 77(2), 274-287.
- Horrigan, F. T., & Aldrich, R. W. (2002). Coupling between Voltage Sensor Activation, Ca²⁺ Binding and Channel Opening in Large Conductance (BK) Potassium Channels. *Journal of General Physiology*, 120(3), 267-305. <https://doi.org/10.1085/jgp.20028605>
- Hoshi, F. T. H., Toshinori. (2023). Models of Ion Channel Gating. En *Textbook of Ion Channels Volume I*. CRC Press.
- Islas, L. D., & Zagotta, W. N. (2006). Short-range Molecular Rearrangements in Ion Channels Detected by Tryptophan Quenching of Bimane Fluorescence. *Journal of General Physiology*, 128(3), 337-346. <https://doi.org/10.1085/jgp.200609556>
- Kalstrup, T., & Blunck, R. (2013). Dynamics of internal pore opening in KV channels probed by a fluorescent unnatural amino acid. *Proceedings of the National Academy of Sciences*, 110(20), 8272-8277. <https://doi.org/10.1073/pnas.1220398110>
- Kalstrup, T., & Blunck, R. (2018). S4–S5 linker movement during activation and inactivation in voltage-gated K⁺ channels. *Proceedings of the National Academy of Sciences*, 115(29), E6751-E6759. <https://doi.org/10.1073/pnas.1719105115>
- Kapus, A., Romanek, R., Qu, A. Y., Rotstein, O. D., & Grinstein, S. (1993). A pH-sensitive and voltage-dependent proton conductance in the plasma membrane of macrophages. *Journal of General Physiology*, 102(4), 729-760. <https://doi.org/10.1085/jgp.102.4.729>
- Kawanabe, A., Hashimoto, M., Nishizawa, M., Nishizawa, K., Narita, H., Yonezawa, T., Jinno, Y., Sakata, S., Nakagawa, A., & Okamura, Y. (2018). The hydrophobic nature of a novel membrane interface regulates the enzyme activity of a voltage-sensing phosphatase. *eLife*, 7, e41653. <https://doi.org/10.7554/eLife.41653>
- Klymchenko, A. S. (2017). Solvatochromic and Fluorogenic Dyes as Environment-Sensitive Probes: Design and Biological Applications. *Accounts of Chemical Research*, 50(2), 366-375. <https://doi.org/10.1021/acs.accounts.6b00517>
- Kulbacka, J., Choromańska, A., Rossowska, J., Weźgowiec, J., Saczko, J., & Rols, M.-P. (2017). Cell Membrane Transport Mechanisms: Ion Channels and Electrical Properties of Cell Membranes. *Advances in Anatomy, Embryology, and Cell Biology*, 227, 39-58. https://doi.org/10.1007/978-3-319-56895-9_3

- Kulleperuma, K., Smith, S. M., Morgan, D., Musset, B., Holyoake, J., Chakrabarti, N., Cherny, V. V., DeCoursey, T. E., & Pomès, R. (2013). Construction and validation of a homology model of the human voltage-gated proton channel hHV1. *Journal of General Physiology*, *141*(4), 445-465.
- Kusch, J., & Zifarelli, G. (2014). Patch-clamp fluorometry: Electrophysiology meets fluorescence. *Biophysical Journal*, *106*(6), 1250-1257.
<https://doi.org/10.1016/j.bpj.2014.02.006>
- Lakowicz, J. R. (Ed.). (2006). Mechanisms and Dynamics of Fluorescence Quenching. En *Principles of Fluorescence Spectroscopy* (pp. 331-351). Springer US.
https://doi.org/10.1007/978-0-387-46312-4_9
- Lee, H. S., Guo, J., Lemke, E. A., Dimla, R. D., & Schultz, P. G. (2009). Genetic Incorporation of a Small, Environmentally Sensitive, Fluorescent Probe into Proteins in *Saccharomyces cerevisiae*. *Journal of the American Chemical Society*, *131*(36), 12921-12923. <https://doi.org/10.1021/ja904896s>
- Lee, S.-Y., Letts, J. A., & MacKinnon, R. (2008). Dimeric subunit stoichiometry of the human voltage-dependent proton channel Hv1. *Proceedings of the National Academy of Sciences*, *105*(22), 7692-7695.
- Li, M., Wang, F., Yan, L., Lu, M., Zhang, Y., & Peng, T. (2022). Genetically encoded fluorescent unnatural amino acids and FRET probes for detecting deubiquitinase activities. *Chemical Communications (Cambridge, England)*, *58*(73), 10186-10189.
<https://doi.org/10.1039/d2cc03623a>
- Li, Q., Shen, R., Treger, J. S., Wanderling, S. S., Milewski, W., Siwowska, K., Bezanilla, F., & Perozo, E. (2015). Resting state of the human proton channel dimer in a lipid bilayer. *Proceedings of the National Academy of Sciences of the United States of America*, *112*(44), E5926-5935. <https://doi.org/10.1073/pnas.1515043112>
- Lishko, P. V., & Kirichok, Y. (2010). The role of Hv1 and CatSper channels in sperm activation. *The Journal of physiology*, *588*(23), 4667-4672.
- Macdonald, A. G. (2002). Ion channels under high pressure. *Comparative Biochemistry and Physiology Part A: Molecular & Integrative Physiology*, *131*(3), 587-593.
[https://doi.org/10.1016/S1095-6433\(01\)00510-4](https://doi.org/10.1016/S1095-6433(01)00510-4)
- Mannuzzu, L. M., Moronne, M. M., & Isacoff, E. Y. (1996). Direct Physical Measure of Conformational Rearrangement Underlying Potassium Channel Gating. *Science*, *271*(5246), 213-216. <https://doi.org/10.1126/science.271.5246.213>
- Merzlyak, E. M., Goedhart, J., Shcherbo, D., Bulina, M. E., Shcheglov, A. S., Fradkov, A. F., Gaintzeva, A., Lukyanov, K. A., Lukyanov, S., Gadella, T. W. J., & Chudakov, D. M. (2007). Bright monomeric red fluorescent protein with an extended fluorescence lifetime. *Nature Methods*, *4*(7), Article 7. <https://doi.org/10.1038/nmeth1062>
- Mizutani, N., Kawanabe, A., Jinno, Y., Narita, H., Yonezawa, T., Nakagawa, A., & Okamura, Y. (2022). Interaction between S4 and the phosphatase domain mediates electrochemical coupling in voltage-sensing phosphatase (VSP). *Proceedings of the National Academy of Sciences*, *119*(26), e2200364119.
<https://doi.org/10.1073/pnas.2200364119>

- Mony, L., Berger, T. K., & Isacoff, E. Y. (2015). A specialized molecular motion opens the Hv1 voltage-gated proton channel. *Nature Structural & Molecular Biology*, 22(4), Article 4. <https://doi.org/10.1038/nsmb.2978>
- Mony, L., Stroebel, D., & Isacoff, E. Y. (2020). Dimer interaction in the Hv1 proton channel. *Proceedings of the National Academy of Sciences*, 117(34), 20898-20907. <https://doi.org/10.1073/pnas.2010032117>
- Moran, Y., Barzilai, M. G., Liebeskind, B. J., & Zakon, H. H. (2015). Evolution of voltage-gated ion channels at the emergence of Metazoa. *Journal of Experimental Biology*, 218(4), 515-525. <https://doi.org/10.1242/jeb.110270>
- Moreau, A., Gosselin-Badaroudine, P., & Chahine, M. (2014). Biophysics, pathophysiology, and pharmacology of ion channel gating pores. *Frontiers in Pharmacology*, 5. <https://www.frontiersin.org/articles/10.3389/fphar.2014.00053>
- Morgan, D., Musset, B., Kulleperuma, K., Smith, S. M. E., Rajan, S., Cherny, V. V., Pomès, R., & DeCoursey, T. E. (2013). Peregrination of the selectivity filter delineates the pore of the human voltage-gated proton channel hHV1. *Journal of General Physiology*, 142(6), 625-640. <https://doi.org/10.1085/jgp.201311045>
- Munteanu, B., Braun, M., & Boonrod, K. (2012). Improvement of PCR reaction conditions for site-directed mutagenesis of big plasmids. *Journal of Zhejiang University SCIENCE B*, 13(4), 244-247. <https://doi.org/10.1631/jzus.B1100180>
- Musset, B., Capasso, M., Cherny, V. V., Morgan, D., Bhamrah, M., Dyer, M. J. S., & DeCoursey, T. E. (2010). Identification of Thr29 as a Critical Phosphorylation Site That Activates the Human Proton Channel Hvcn1 in Leukocytes *. *Journal of Biological Chemistry*, 285(8), 5117-5121. <https://doi.org/10.1074/jbc.C109.082727>
- Musset, B., & DeCoursey, T. (2012). Biophysical properties of the voltage-gated proton channel HV1. *Wiley Interdisciplinary Reviews: Membrane Transport and Signaling*, 1(5), 605-620. <https://doi.org/10.1002/wmts.55>
- Musset, B., Morgan, D., Cherny, V. V., MacGlashan, D. W., Thomas, L. L., Ríos, E., & DeCoursey, T. E. (2008). A pH-stabilizing role of voltage-gated proton channels in IgE-mediated activation of human basophils. *Proceedings of the National Academy of Sciences*, 105(31), 11020-11025. <https://doi.org/10.1073/pnas.0800886105>
- Musset, B., Smith, S. M. E., Rajan, S., Morgan, D., Cherny, V. V., & DeCoursey, T. E. (2011). Aspartate 112 is the selectivity filter of the human voltage-gated proton channel. *Nature*, 480(7376), Article 7376. <https://doi.org/10.1038/nature10557>
- Nair, A., Chauhan, P., Saha, B., & Kubatzky, K. F. (2019). Conceptual Evolution of Cell Signaling. *International Journal of Molecular Sciences*, 20(13), Article 13. <https://doi.org/10.3390/ijms20133292>
- Neher, E., & Sakmann, B. (1976). Single-channel currents recorded from membrane of denervated frog muscle fibres. *Nature*, 260(5554), Article 5554. <https://doi.org/10.1038/260799a0>
- Nelson, M. D., & Fitch, D. H. A. (2011). Overlap Extension PCR: An Efficient Method for Transgene Construction. En V. Orgogozo & M. V. Rockman (Eds.), *Molecular*

- Methods for Evolutionary Genetics* (pp. 459-470). Humana Press.
https://doi.org/10.1007/978-1-61779-228-1_27
- Nimigean, A. A. S., Chen Fan, Dorothy M. Kim, Jason G. McCoy, Crina M. (2023). Ion Selectivity and Conductance. En *Textbook of Ion Channels Volume I*. CRC Press.
- Pang, H., Wang, X., Zhao, S., Xi, W., Lv, J., Qin, J., Zhao, Q., Che, Y., Chen, L., & Li, S. J. (2020). Loss of the voltage-gated proton channel Hv1 decreases insulin secretion and leads to hyperglycemia and glucose intolerance in mice. *Journal of Biological Chemistry*, 295(11), 3601-3613. <https://doi.org/10.1074/jbc.RA119.010489>
- Pantazis, A., & Olcese, R. (2012). Relative transmembrane segment rearrangements during BK channel activation resolved by structurally assigned fluorophore–quencher pairing. *Journal of General Physiology*, 140(2), 207-218.
<https://doi.org/10.1085/jgp.201210807>
- Puljung, M. C. (2021). Chapter Three - ANAP: A versatile, fluorescent probe of ion channel gating and regulation. En D. L. Minor & H. M. Colecraft (Eds.), *Methods in Enzymology* (Vol. 654, pp. 49-84). Academic Press.
<https://doi.org/10.1016/bs.mie.2021.01.048>
- Puljung, M., Vedovato, N., Usher, S., & Ashcroft, F. (2019). Activation mechanism of ATP-sensitive K⁺ channels explored with real-time nucleotide binding. *eLife*, 8, e41103.
<https://doi.org/10.7554/eLife.41103>
- Qiu, F., Rebolledo, S., Gonzalez, C., & Larsson, H. P. (2013). Subunit Interactions during Cooperative Opening of Voltage-Gated Proton Channels. *Neuron*, 77(2), 288-298.
<https://doi.org/10.1016/j.neuron.2012.12.021>
- Ramsey, I. S., Mokrab, Y., Carvacho, I., Sands, Z. A., Sansom, M. S., & Clapham, D. E. (2010). An aqueous H⁺ permeation pathway in the voltage-gated proton channel Hv1. *Nature structural & molecular biology*, 17(7), 869-875.
- Ramsey, I. S., Moran, M. M., Chong, J. A., & Clapham, D. E. (2006). A voltage-gated proton-selective channel lacking the pore domain. *Nature*, 440(7088), 1213-1216.
<https://doi.org/10.1038/nature04700>
- Ramsey, I. S., Ruchti, E., Kaczmarek, J. S., & Clapham, D. E. (2009). Hv1 proton channels are required for high-level NADPH oxidase-dependent superoxide production during the phagocyte respiratory burst. *Proceedings of the National Academy of Sciences*, 106(18), 7642-7647. <https://doi.org/10.1073/pnas.0902761106>
- Randolph, A. L., Mokrab, Y., Bennett, A. L., Sansom, M. S., & Ramsey, I. S. (2016). Proton currents constrain structural models of voltage sensor activation. *eLife*, 5, e18017.
<https://doi.org/10.7554/eLife.18017>
- Rangel-Yescas, G., Cervantes, C., Cervantes-Rocha, M. A., Suárez-Delgado, E., Banaszak, A. T., Maldonado, E., Ramsey, I. S., Rosenbaum, T., & Islas, L. D. (2021). Discovery and characterization of Hv1-type proton channels in reef-building corals. *eLife*, 10, e69248. <https://doi.org/10.7554/eLife.69248>
- Sakata, S., Jinno, Y., Kawanabe, A., & Okamura, Y. (2016). Voltage-dependent motion of the catalytic region of voltage-sensing phosphatase monitored by a fluorescent

- amino acid. *Proceedings of the National Academy of Sciences*, 113(27), 7521-7526. <https://doi.org/10.1073/pnas.1604218113>
- Salvage, S. C., Huang, C. L.-H., & Jackson, A. P. (2020). Cell-Adhesion Properties of β -Subunits in the Regulation of Cardiomyocyte Sodium Channels. *Biomolecules*, 10(7), 989. <https://doi.org/10.3390/biom10070989>
- Sasaki, M., Takagi, M., & Okamura, Y. (2006). A voltage sensor-domain protein is a voltage-gated proton channel. *Science*, 312(5773), 589-592.
- Schladt, T. M., & Berger, T. K. (2020). Voltage and pH difference across the membrane control the S4 voltage-sensor motion of the Hv1 proton channel. *Scientific Reports*, 10(1), Article 1. <https://doi.org/10.1038/s41598-020-77986-z>
- Shu, X., Shaner, N. C., Yarbrough, C. A., Tsien, R. Y., & Remington, S. J. (2006). Novel Chromophores and Buried Charges Control Color in mFruits. *Biochemistry*, 45(32), 9639-9647. <https://doi.org/10.1021/bi060773l>
- Sigworth, F. J. (1995). Electronic Design of the Patch Clamp. En B. Sakmann & E. Neher (Eds.), *Single-Channel Recording* (pp. 95-127). Springer US. https://doi.org/10.1007/978-1-4419-1229-9_4
- Smith, S. M. E., & DeCoursey, T. E. (2013). Chapter Twelve—Consequences of Dimerization of the Voltage-Gated Proton Channel. En J. Giraldo & F. Ciruela (Eds.), *Progress in Molecular Biology and Translational Science* (Vol. 117, pp. 335-360). Academic Press. <https://doi.org/10.1016/B978-0-12-386931-9.00012-X>
- Smith, S. M. E., Morgan, D., Musset, B., Cherny, V. V., Place, A. R., Hastings, J. W., & DeCoursey, T. E. (2011). Voltage-gated proton channel in a dinoflagellate. *Proceedings of the National Academy of Sciences of the United States of America*, 108(44), 18162-18167. <https://doi.org/10.1073/pnas.1115405108>
- Sperelakis, N. (1995). 6—Origin of Resting Membrane Potentials**Adapted and reprinted by permission from the author's chapter 3 in *PHYSIOLOGY* (Sperelakis, N. and Banks, R. O., Editors). Copyright © 1993 by Nicholas Sperelakis and Robert O. Banks. Published by Little, Brown and Company. En N. Sperelakis (Ed.), *Cell Physiology Source Book* (pp. 67-90). Academic Press. <https://doi.org/10.1016/B978-0-12-656970-4.50012-9>
- Stefani, E., Ottolia, M., Noceti, F., Olcese, R., Wallner, M., Latorre, R., & Toro, L. (1997). Voltage-controlled gating in a large conductance Ca^{2+} -sensitive K^{+} channel (hsl α). *Proceedings of the National Academy of Sciences*, 94(10), 5427-5431. <https://doi.org/10.1073/pnas.94.10.5427>
- Suárez-Delgado, E., & Islas, L. D. (2020). Patch-Clamp Fluorometry and Its Applications to the Study of Ion Channels. En N. J. D. Wright (Ed.), *Basic Neurobiology Techniques* (pp. 155-183). Springer US. https://doi.org/10.1007/978-1-4939-9944-6_7
- Takeshita, K., Sakata, S., Yamashita, E., Fujiwara, Y., Kawanabe, A., Kurokawa, T., Okochi, Y., Matsuda, M., Narita, H., Okamura, Y., & Nakagawa, A. (2014). X-ray crystal structure of voltage-gated proton channel. *Nature Structural & Molecular Biology*, 21(4), 352-357. <https://doi.org/10.1038/nsmb.2783>

- Talwar, S., & Lynch, J. W. (2015). Investigating ion channel conformational changes using voltage clamp fluorometry. *Neuropharmacology*, *98*, 3-12. <https://doi.org/10.1016/j.neuropharm.2015.03.018>
- Tao, X., Lee, A., Limapichat, W., Dougherty, D. A., & MacKinnon, R. (2010). A Gating Charge Transfer Center in Voltage Sensors. *Science*, *328*(5974), 67-73. <https://doi.org/10.1126/science.1185954>
- Taraska, J. W., & Zagotta, W. N. (2010). Fluorescence applications in molecular neurobiology. *Neuron*, *66*(2), 170-189. <https://doi.org/10.1016/j.neuron.2010.02.002>
- Thomas, P., & Smart, T. G. (2005). HEK293 cell line: A vehicle for the expression of recombinant proteins. *Journal of Pharmacological and Toxicological Methods*, *51*(3), 187-200. <https://doi.org/10.1016/j.vascn.2004.08.014>
- Thomas, R. C., & Meech, R. W. (1982). Hydrogen ion currents and intracellular pH in depolarized voltage-clamped snail neurones. *Nature*, *299*(5886), Article 5886. <https://doi.org/10.1038/299826a0>
- Tombola, F., Ulbrich, M. H., & Isacoff, E. Y. (2008). The voltage-gated proton channel Hv1 has two pores, each controlled by one voltage sensor. *Neuron*, *58*(4), 546-556.
- Tombola, F., Ulbrich, M. H., Kohout, S. C., & Isacoff, E. Y. (2010). The opening of the two pores of the Hv1 voltage-gated proton channel is tuned by cooperativity. *Nature structural & molecular biology*, *17*(1), 44-50.
- Vereb, G., Szöllösi, J., Matkó, J., Nagy, P., Farkas, T., Vigh, L., Mátyus, L., Waldmann, T. A., & Damjanovich, S. (2003). Dynamic, yet structured: The cell membrane three decades after the Singer–Nicolson model. *Proceedings of the National Academy of Sciences*, *100*(14), 8053-8058. <https://doi.org/10.1073/pnas.1332550100>
- Villalba-Galea, C. A. (2014). Hv1 Proton Channel Opening Is Preceded by a Voltage-independent Transition. *Biophysical Journal*, *107*(7), 1564-1572. <https://doi.org/10.1016/j.bpj.2014.08.017>
- Villalba-Galea, C. A., Sandtner, W., Dimitrov, D., Mutoh, H., Knöpfel, T., & Bezanilla, F. (2009). Charge Movement of a Voltage-Sensitive Fluorescent Protein. *Biophysical Journal*, *96*(2), L19-L21. <https://doi.org/10.1016/j.bpj.2008.11.003>
- Walter, B. A., Alexander Johnson, Julian Lewis, Martin Raff, Keith Roberts, Peter. (2007). Membrane Structure. En *Molecular Biology of the Cell* (5.^a ed.). W.W. Norton & Company.
- Wisedchaisri, G., & Gamal El-Din, T. M. (2022). Druggability of Voltage-Gated Sodium Channels—Exploring Old and New Drug Receptor Sites. *Frontiers in Pharmacology*, *13*. <https://www.frontiersin.org/articles/10.3389/fphar.2022.858348>
- Wu, X., Zhang, L., & Hong, L. (2022). The role of Phe150 in human voltage-gated proton channel. *iScience*, *25*(11). <https://doi.org/10.1016/j.isci.2022.105420>
- Young, V. C., & Artigas, P. (2021). Displacement of the Na⁺/K⁺ pump's transmembrane domains demonstrates conserved conformational changes in P-type 2 ATPases. *Proceedings of the National Academy of Sciences*, *118*(8), e2019317118. <https://doi.org/10.1073/pnas.2019317118>

- Zagotta, W. N. (2023). Ligand-Dependent Gating Mechanism. En *Textbook of Ion Channels Volume I*. CRC Press.
- Zagotta, W. N., Gordon, M. T., Senning, E. N., Munari, M. A., & Gordon, S. E. (2016). Measuring distances between TRPV1 and the plasma membrane using a noncanonical amino acid and transition metal ion FRET. *Journal of General Physiology*, *147*(2), 201-216.
- Zagotta, W. N., Sim, B. S., Nhim, A. K., Raza, M. M., Evans, E. G., Venkatesh, Y., Jones, C. M., Mehl, R. A., Petersson, E. J., & Gordon, S. E. (2021). An improved fluorescent noncanonical amino acid for measuring conformational distributions using time-resolved transition metal ion FRET. *eLife*, *10*, e70236.
<https://doi.org/10.7554/eLife.70236>
- Zakany, F., Kovacs, T., Panyi, G., & Varga, Z. (2020). Direct and indirect cholesterol effects on membrane proteins with special focus on potassium channels. *Biochimica Et Biophysica Acta. Molecular and Cell Biology of Lipids*, *1865*(8), 158706.
<https://doi.org/10.1016/j.bbailip.2020.158706>
- Zhang, L., Bellve, K., Fogarty, K., & Kobertz, W. R. (2016). Fluorescent Visualization of Cellular Proton Fluxes. *Cell Chemical Biology*, *23*(12), 1449-1457.
<https://doi.org/10.1016/j.chembiol.2016.10.013>
- Zhang, X. C., Yang, H., Liu, Z., & Sun, F. (2018). Thermodynamics of voltage-gated ion channels. *Biophysics Reports*, *4*(6), 300-319. <https://doi.org/10.1007/s41048-018-0074-y>
- Zhao, R., Kennedy, K., De Blas, G. A., Orta, G., Pavarotti, M. A., Arias, R. J., de la Vega-Beltrán, J. L., Li, Q., Dai, H., Perozo, E., Mayorga, L. S., Darszon, A., & Goldstein, S. A. N. (2018). Role of human Hv1 channels in sperm capacitation and white blood cell respiratory burst established by a designed peptide inhibitor. *Proceedings of the National Academy of Sciences*, *115*(50), E11847-E11856.
<https://doi.org/10.1073/pnas.1816189115>

Anexos

- I. Activation-pathway transitions in human voltage-gated proton channels revealed by a non-canonical fluorescent amino acid.
- II. Discovery and characterization of H_v1-type proton channels in reef-building corals.
- III. Patch-Clamp Fluorometry and Its Applications to the Study of Ion Channels.
- IV. K_v1.2 channels inactivate through a mechanism similar to C-type inactivation.
- V. Currents through H_v1 channels deplete protons in their vicinity.

Activation-pathway transitions in human voltage-gated proton channels revealed by a non-canonical fluorescent amino acid

Esteban Suárez-Delgado[†], Maru Orozco-Contreras, Gisela E Rangel-Yescas, Leon D Islas*

Department of Physiology, School of Medicine, Universidad Nacional Autónoma de México, México City, Mexico

Abstract Voltage-dependent gating of the voltage-gated proton channels (H_v1) remains poorly understood, partly because of the difficulty of obtaining direct measurements of voltage sensor movement in the form of gating currents. To circumvent this problem, we have implemented patch-clamp fluorometry in combination with the incorporation of the fluorescent non-canonical amino acid Anap to monitor channel opening and movement of the S4 segment. Simultaneous recording of currents and fluorescence signals allows for direct correlation of these parameters and investigation of their dependence on voltage and the pH gradient (ΔpH). We present data that indicate that Anap incorporated in the S4 helix is quenched by an aromatic residue located in the S2 helix and that motion of the S4 relative to this quencher is responsible for fluorescence increases upon depolarization. The kinetics of the fluorescence signal reveal the existence of a very slow transition in the deactivation pathway, which seems to be singularly regulated by ΔpH . Our experiments also suggest that the voltage sensor can move after channel opening and that the absolute value of the pH can influence the channel opening step. These results shed light on the complexities of voltage-dependent opening of human H_v1 channels.

*For correspondence:
leon.islas@gmail.com

Present address: [†]Department of Biology, Xenon Pharmaceuticals Inc, Burnaby, Canada

Competing interest: See page 18

Funding: See page 18

Preprinted: 01 July 2022

Received: 28 December 2022

Accepted: 19 January 2023

Published: 25 January 2023

Reviewing Editor: Stephan A Pless, University of Copenhagen, Denmark

© Copyright Suárez-Delgado et al. This article is distributed under the terms of the [Creative Commons Attribution License](https://creativecommons.org/licenses/by/4.0/), which permits unrestricted use and redistribution provided that the original author and source are credited.

Editor's evaluation

This work by Suarez-Delgado et al. employs the fluorescent non-canonical amino acid Anap to explore the mechanisms by which the H_v1 proton channel is modulated by voltage and pH. Two kinetically distinct fluorescence components support the presence of at least three conformational states in the activation pathway of H_v1 and measurements using different pH gradients suggest that voltage sensor movement and channel opening are similarly affected by pH gradients. The work provides a rigorous and thorough characterization of how Anap can be used to explore mechanisms of gating and regulation and will be of interest to physiologists and biophysicists interested in mechanistic studies of membrane proteins using non-canonical fluorescent amino acids.

Introduction

Voltage-gated, proton-permeable ion currents in a large variety of cell types and organisms are produced by the H_v1 gene (HVCN1 in humans), which encodes a membrane protein that is a member of the superfamily of voltage-sensing domains (VSDs; *Sasaki et al., 2006; Ramsey et al., 2006*). These VSDs are also encountered in voltage-sensitive phosphatases (VSPs) and voltage-gated ion channels (VGICs), and their principal function is to detect the membrane potential difference and translate it into a conformational change that activates VSP and opens VGIC (*Catacuzzano and Franciolini, 2022*).

H_v1 is thought to form ion channels activated by voltage and employing a mechanism of activation similar to the VSDs of canonical voltage-gated potassium, sodium, and calcium channels (**Gonzalez et al., 2012**). The functions of H_v1 channels are diverse, including intracellular pH regulation (**Ma et al., 2022**), charge compensation during immune response (**Ramsey et al., 2009**), modulation of flagellar beating in spermatozoa (**Lishko and Kirichok, 2010**), bioluminescence (**Eckert and Sibaoka, 1968**), and possible roles in calcification processes in marine organisms (**Taylor et al., 2011; Rangel-Yescas et al., 2021**). Also, H_v1 is involved in different pathologies such as B cell malignancy (**Hondares et al., 2014**), breast cancer (**Wang et al., 2012**), and post-ischemic brain injury (**Wu, 2014; Yu et al., 2020**); consequently, in recent years, H_v1 has emerged as a possible pharmacological target (**Zhao et al., 2018; Zhang et al., 2022**).

Among all voltage-gated proton channels sequenced, the human ortholog, hH_v1, is the most widely studied (**Musset et al., 2008**). This channel is thought to be a functional dimer formed by two subunits comprising an intracellular N-terminus, a bundle of four transmembrane helices (TMHs, S1–S4) in the VSD fold, and a long intracellular alpha helix that mediates a coiled-coil interaction, mainly responsible for dimerization and cooperative activation (**Koch et al., 2008; Lee et al., 2008; Tombola et al., 2008**). The fourth alpha helix, S4, contains positive charges represented by three arginine residues (R205, R208, and R211) in the characteristic VSD repeats. S4 is thought to undergo an outward displacement and rotation in response to depolarization, mostly in accordance to the helical screw rotation and displacement model of voltage gating (**Li et al., 2015**). Unlike canonical VGIC, H_v1 lacks the two TMH that make up the pore region in canonical ion channels (S5 and S6); therefore, the VSD of H_v1 has a double function: it is responsible for detecting the electrical potential across the membrane and forming the pathway through which the protons will move once the channel is activated.

A characteristic of H_v1 activation is its dependence on the pH gradient or ΔpH ($\text{pH}_o - \text{pH}_i$). Native proton channels were first shown to open at more negative voltages when the proton gradient points in the outward direction (**Cherny et al., 1995**). It was shown that for every unit of ΔpH , the voltage of mid-activation shifts ~ 40 mV. Subsequently, all native and cloned proton channels have been found to approximately follow this rule (**Sasaki et al., 2006; Ramsey et al., 2006; Rangel-Yescas et al., 2021; Musset et al., 2008; Smith et al., 2011; Zhao and Tombola, 2021**). Recent experiments suggest that the proton gradient produces this effect by acting on the voltage sensor and not only affecting a close-to-open transition since gating currents and channel opening are similarly modulated (**Schladt and Berger, 2020; Carmona et al., 2021**). However, the molecular mechanisms through which protons modulate voltage-sensor function are not known. Due to technical difficulties, such as not having a pore structure separate from VSD or the impossibility of patch-clamping without protons in the experiments, gating current recordings of H_v1 channels have been obtained from mutants of the *Ciona* H_v1 (ciH_v1) ortholog (**Carmona et al., 2018; Carmona et al., 2021**) or mutants of human H_v1 (**De La Rosa and Ramsey, 2018**).

Patch-clamp fluorometry (PCF) has been used to overcome these difficulties as a powerful tool that allows investigation of electrically silent conformational changes in VSDs associated with channel gating (**Kusch and Zifarelli, 2014**), through following fluorescence intensity changes of a dye that generally is attached to the channel protein via chemical modification of cysteine residues or a fluorescent protein genetically encoded (**Kusch and Zifarelli, 2014**). In ciH_v1 and hH_v1 proton channels, this technique has been employed to obtain evidence of cooperative gating, S1 movement during activation, and the pH sensitivity of S4 movement (**Mony et al., 2015; Schladt and Berger, 2020; Qiu et al., 2013**).

As in other voltage-gated channels, these studies made use of the fluorophore tetramethylrhodamine (TMR), which was tethered to the S3–S4 linker, an extracellular-facing part of the channel (**Cowgill and Chanda, 2019**). While fluorophores like TMR have provided a means to observe conformational changes in many VGICs, including H_v1, due to their large size and cysteine reactive nature, they are difficult to incorporate in membrane-embedded portions of channels, without possible large perturbation of the protein fold or result in unspecific incorporation. For these reasons, incorporating a small fluorophore in the middle of TMHs would be advantageous. Here, we exploit the small size, comparable to aromatic amino acids, of a genetically encoded fluorescent non-canonical amino acid (NCAA), Anap (**Chatterjee et al., 2013**). By incorporating Anap at various positions in the S4 segment, we assess the conformational changes of the human voltage-gated proton channel (hH_v1) in response to voltage activation and pH modulation by performing PCF.

We find our measurements can resolve a transition during the deactivation process that is strongly modulated by pH. Furthermore, we find that the changes in Anap fluorescence could be partially due to interaction with aromatic amino acids within H_v1.

Results

Incorporation of Anap into hH_v1

To study voltage-dependent transitions in a voltage sensor using PCF, it is desirable that the introduced fluorescent probe does not produce a major structural perturbation of the target protein. The relatively recently developed probe Anap (3-[6-acetylnaphthalen-2-ylamino]-2-aminopropanoic acid) is a small non-canonical fluorescent amino acid (**Figure 1B**), which has been shown to be easily genetically encoded in proteins expressed in eukaryotic cells (**Chatterjee et al., 2013; Puljung, 2021**). Moreover, Anap has been successfully used as a reporter of voltage-dependent conformational changes (**Kalstrup and Blunck, 2013**) and as a Fluorescence Resonance Energy Transfer (FRET) pair (**Gordon et al., 2018**) to probe ion channel dynamics. In this study, Anap was inserted into specific positions of the S4 segment of the human H_v1 proton channel (hH_v1) sequence (**Figure 1A**), with the purpose of examining its voltage and pH-dependent dynamics.

We selected the S4 helix as insertion target since this region of the channel is proposed to undergo a voltage-dependent outward displacement that has been previously studied with different approaches, including voltage-clamp fluorometry (VCF) (**De-la-Rosa et al., 2016; Eckert and Sibaoka, 1968; Edelstein et al., 2014**).

We were able to successfully substitute amino acids by Anap at positions Q191 in the S3–S4 linker and A197, L198, G199, L200, L201, and I202 in the S4. Anap efficiently rescued the expression of channels containing an amber stop codon (TAG) in the selected position, as judged both by appearance of red fluorescence produced by the mCherry fluorescent protein appended in the C-terminus (**Figure 1C** and **Figure 1—figure supplement 1A**) or the appearance of proton currents recorded from HEK 293 cells in the whole-cell patch-clamp configuration (**Figure 1D, Figure 1—figure supplement 2** and **Supplementary file 1**).

The substituted channels gave rise to voltage-activated currents, with similar range of activation to WT as judged by their conductance vs. voltage (G-V) curves (except I202Anap channels). Furthermore, that Anap was able to specifically rescue TAG-containing channels was demonstrated by control experiments in cells cotransfected with mutant channels and the pANAP plasmid in the absence of Anap, which showed absence or very small proton currents as compared to cells cultured in the presence of Anap (**Figure 1—figure supplement 1B**). The observed fluorescence emission spectrum of the Anap signal present in the membrane (**Figure 1C**), which presumably originates mostly from Anap incorporated into channels, shows that there are no major or systematic variations on the peak emission wavelength (**Figure 1E**). The peak emission wavelength for all positions varies but is near 485 nm, except the most C-terminal and presumably deepest position, I202Anap, which is 477 nm (**Figure 1—figure supplement 3A**). This result suggests that the local environment of Anap in these positions, except 202Anap, is very similar and consistent with a mostly polar environment since the peak emission of Anap in aqueous solution is ~486 nm.

Figure 1E also shows that the emission spectra of positions other than Q191Anap exhibit a small extra peak near 610 nm that corresponds to the peak emission of mCherry. Since the excitation peak of mCherry is 587 nm (**Shaner et al., 2004**), we performed experiments with hH_v1-mCherry channels to measure direct mCherry excitation by our 405 nm laser. The results indicate that this peak is mostly produced by direct excitation of mCherry at 405 nm (**Figure 1—figure supplement 3B**).

Insensitivity of Anap to pH

In order to use Anap as a reporter of conformational changes in H_v1 proton channels, and given that these channels are able to change the pH of the surrounding solution (**De-la-Rosa et al., 2016; Zhang et al., 2016**), we first wanted to validate if this fluorophore is insensitive to pH changes. The amino acid form of Anap that we use is the methyl-ester, which contains amino and carboxy groups. The fluorescence of methyl-ester Anap could be affected by protonation because it could alter electron distribution; for this reason, we reasoned that the best assay to test the pH dependence of Anap fluorescence is to use already incorporated Anap. For this purpose, we used the mutant Q191Anap, which

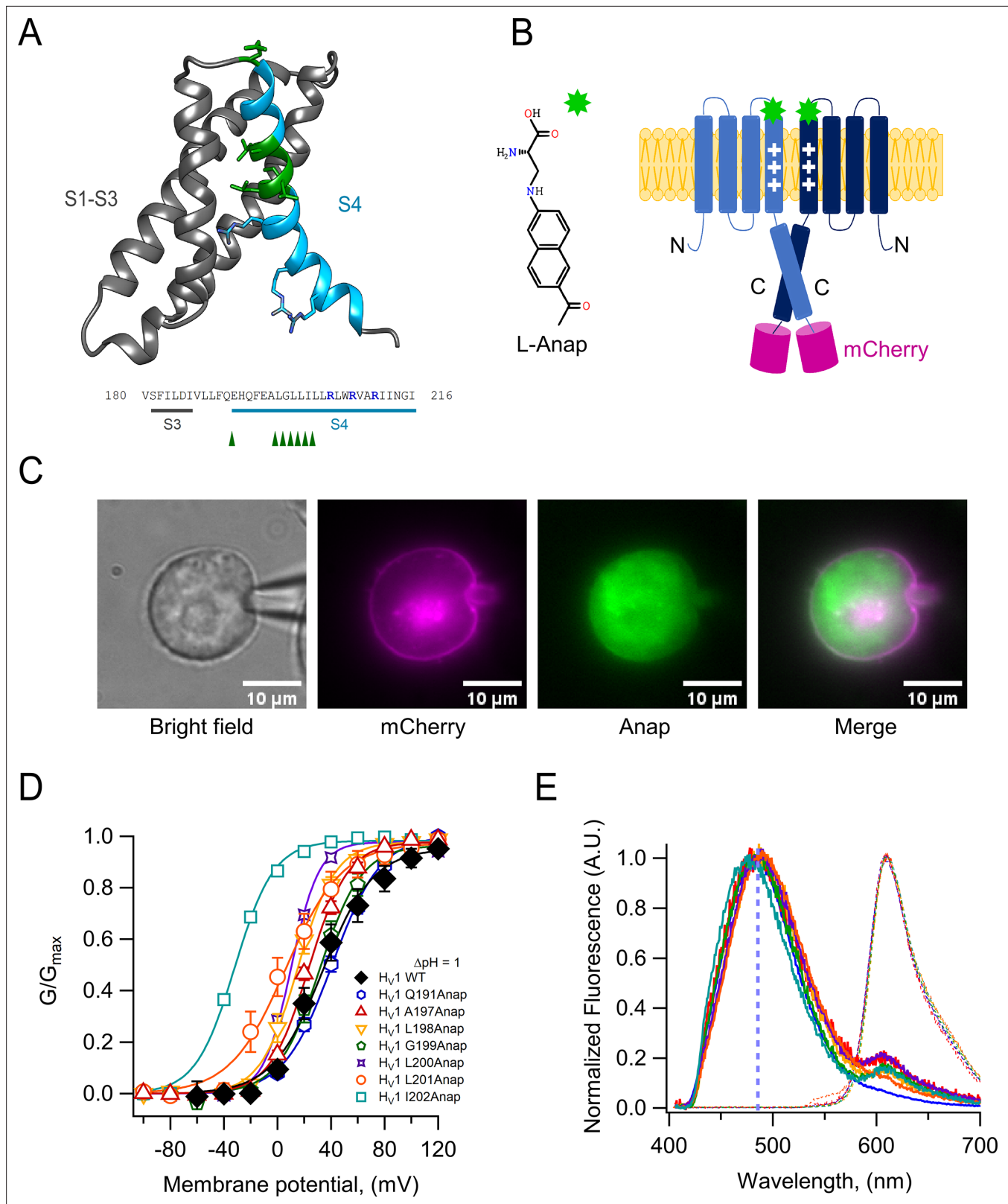


Figure 1. Anap as a fluorescent probe in hHv1. **(A)** Ribbon representation of transmembrane segments S1–S4 of closed hHv1 based on the model of **Randolph et al., 2016**. S1–S3 are in gray, whereas S4 is in light blue. S4 positively charged arginine residues are shown as cyan sticks, whereas the residues where Anap was incorporated individually in the S4 segment are depicted as green sticks and with green arrow heads in the S3–S4 sequence below; positively charged arginine residues are indicated in marine blue. **(B)** Structure of non-canonical amino acid Anap (left), and a schematic

Figure 1 continued on next page

Figure 1 continued

representation (right) that shows the incorporation of Anap (green star) into the hH_v1 dimer expressed in HEK293 cells. An mCherry fluorescent protein (magenta cylinder) was fused to the C-terminal end of hH_v1 as an Anap incorporation reporter. (C) Images of a representative patch-clamp fluorometry (PCF) experiment, showing the voltage-clamped cell and the co-localization of Anap and mCherry fluorescence in the cell membrane for Anap incorporated at position Q191 of hH_v1. (D) G-V curves obtained from currents produced by each hH_v1 mutant rescued by Anap incorporation. All G-V curves were obtained at $\Delta\text{pH} = 1$ and compared with hH_v1 WT (n=5); Q191(n=13); A197(n=6); L198(n=7); G199(n=5); L200(n=1); L201(n=4); I202(n=4). Continuous lines are the fit of the conductance data to **equation 1**; fit parameters are summarized in **Supplementary file 1**. The incorporation of Anap at the I202 site shifts the G-V ~ 65 mV to more negative potentials. Data shown are mean \pm SEM. (E) Normalized mean emission spectrum of Anap (continuous lines) and mCherry (dashed lines) at each incorporation site (color code from D) recorded at resting potential in non-patched cells. Q191(n=15); A197(n=8); L198(n=7); G199(n=6); L200(n=10); L201(n=8); I202(n=10). The vertical blue line indicates the peak emission of Anap in water (486 nm). A second emission peak can be distinguished in every position inside S4 where Anap was incorporated, except Q191Anap. This peak is located around 610 nm which coincides with the peak emission of mCherry.

The online version of this article includes the following source data and figure supplement(s) for figure 1:

Source data 1. Data for each experiment and summary of experiments for **Figure 1D and E**.

Figure supplement 1. L-Anap incorporation suppresses amber codons inserted in hH_v1.

Figure supplement 2. The fusion of mCherry in the C-terminus does not affect channel function and incorporating L-Anap in hH_v1 produces functional channels.

Figure supplement 3. Fluorescence of L-Anap attached at different hH_v1 S4 positions.

incorporates Anap in the S3–S4 loop, which faces the extracellular solution, even in the deactivated state of the channel (**Figure 1A**). Since the emission spectrum of Q191Anap channels was measured from non-voltage clamped transfected HEK cells, fluorescence was obtained only from membrane regions to ensure that the signal comes mostly from channels exposed to the extracellular solution changes and not channels in intracellular compartments, which will not be exposed to the pH changes.

To ensure that most of the fluorescence is collected from channels in the membrane, the membrane region was identified by the fluorescence of mCherry-containing channels that clearly delineates it (**Figure 2—figure supplement 1**). Spectra were then collected only from this small region of membrane.

These measurements showed that the fluorescence of channel-incorporated Anap is not significantly changed in intensity or shape of the emission spectrum over the pH range 3–9 (**Figure 2A and B**), indicating that this fluorophore is insensitive to pH and that Anap fluorescence should not be affected by local pH changes, which might be produced as a consequence of proton currents.

As a further test of our data showing the pH-insensitivity of channel-incorporated Anap and to validate the use of Anap in proton channels, we incorporated the amino acid in a position at the N-terminus of the channel, V62Anap. This amino acid is located in the intracellular part of the channel and should be subject to changes in local internal pH during channel activation (**De-la-Rosa et al., 2016**) but not show changes in fluorescence as a function of voltage-dependent conformational changes. As expected, we did not detect Anap fluorescence changes, although the amino acid was incorporated into functional channels, as judged from proton currents recorded simultaneously with fluorescence (**Figure 2C and D**). This result further supports the use of Anap in voltage-gated proton channels to measure conformational changes.

Voltage-dependent changes of Anap fluorescence

Previous experiments in which other dyes like TMR maleimide (TMRM) were used to label cysteine residues located in the amino-end of the S4 segment of VSDs, including the *Ciona* and human H_v1 channels (**Schladt and Berger, 2020; Mony et al., 2015; Qiu et al., 2013**), usually result in fluorescence signals that are reduced upon depolarization by a voltage-dependent quenching process (**Vaid et al., 2008; Cha and Bezannila, 1998**). In contrast, when we incorporate Anap at position A197, located toward the extracellular end of the S4, depolarization induced an increase of the fluorescence, along with proton currents. The fluorescence increase saturates at depolarized voltages, suggesting that it is produced by a saturable process such as voltage-sensor activation. The direction of this fluorescence change is the same when measured at a ΔpH of 0 or 2, suggesting the same conformational change in the S4 voltage sensor occurs at different pH gradients, albeit over a different range of voltages (**Figure 3A and B**).

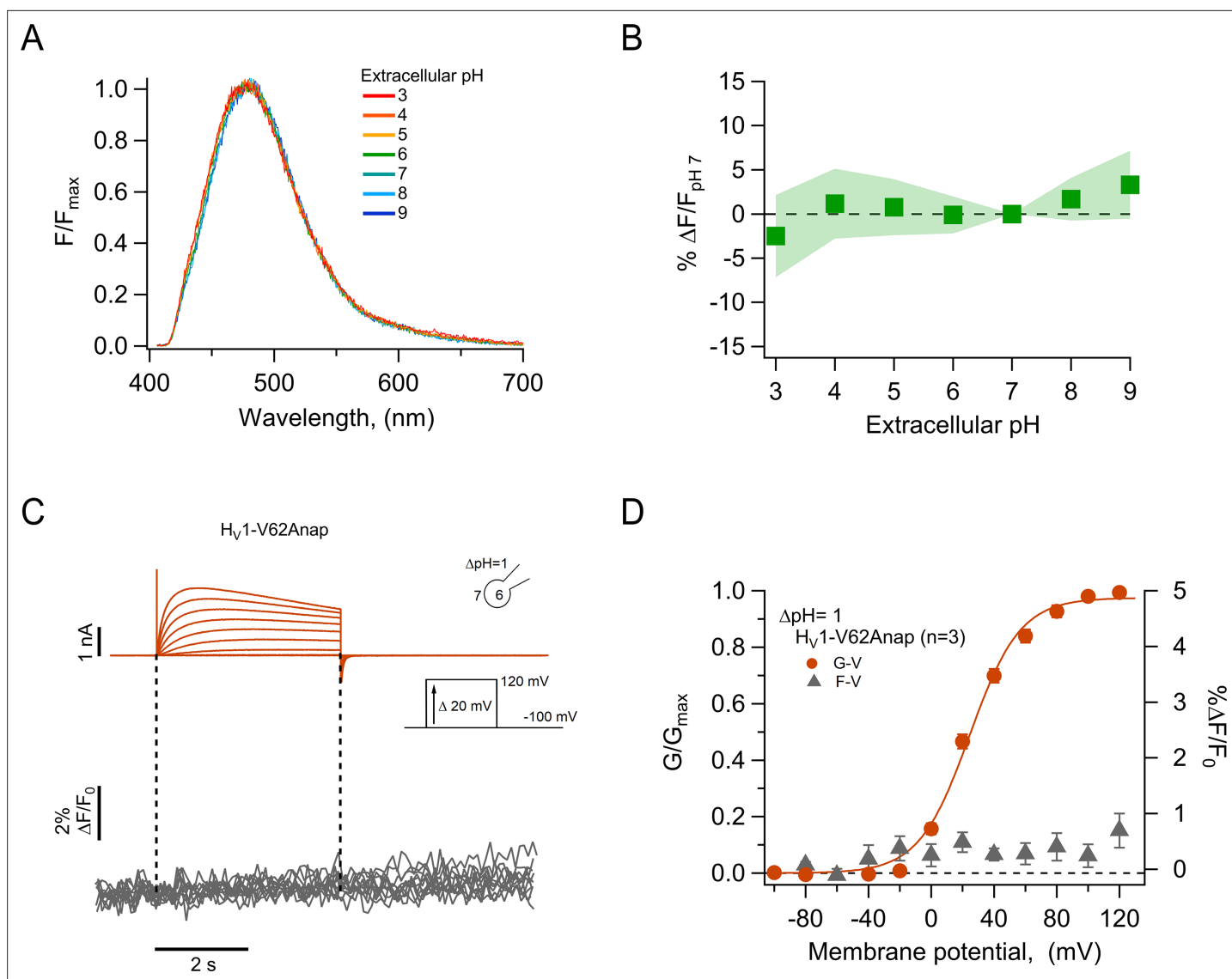


Figure 2. The fluorescence of incorporated Anap is stable to external acidity and local pH changes. **(A)** Mean spectra of Anap fluorescence in the $hH_V1-Q191Anap$ mutant at each external pH tested (pH_o) recorded at the resting potential in non-patched cells. The emission peak of spectra of Anap remained inside the wavelength range of 475–480 nm. **(B)** Percentage of fluorescence intensity change normalized to fluorescence at pH_o 7 in $hH_V1-Q191Anap$ mutant (n=13). The intensity was measured from the peak of emission spectra and found not to be significantly different with a two-way ANOVA test that evaluated the brightness at each value of pH_o (F-statistic=0.09, degrees of freedom = 6, and $p=0.99$). **(C)** Representative patch-clamp fluorometry (PCF) experiments with the $hH_V1-V62Anap$ mutant. Currents (upper panel, orange traces) and fluorescent signal (lower panel, gray traces) were elicited in response to voltage pulses from -100 mV to 120 mV in steps of 20 mV. **(D)** F-V and G-V relationships from the experiments shown in C. Relative fluorescence changes at the end of voltage test pulses are shown in gray triangles, and conductance is shown in orange circles (n=3). The orange continuous line is the fit to **equation 1** of G-V data (fit parameters: $V_{0.5}=24.4 \pm 1.6$ mV; $q=1.5 \pm 0.1$ e_0). Data in B and D are mean \pm SEM.

The online version of this article includes the following source data and figure supplement(s) for figure 2:

Source data 1. Data for each experiment and summary data for **Figure 2**.

Figure supplement 1. Procedure for Anap spectrum measurement in cells subjected to L-Anap incorporation conditions (pAnap + H_V1 TAG+L Anap).

We compared the kinetics of current and fluorescence by fitting an exponential function to the second half of the signal time course and plotted the time constant as a function of voltage (**Figure 3C**). Both current and fluorescence have the same voltage dependence, but the current is ~ 1.3 times faster than the fluorescence. Although not a very large difference, this can be explained by an overestimation of the current time course due to slight proton depletion observed with large currents.

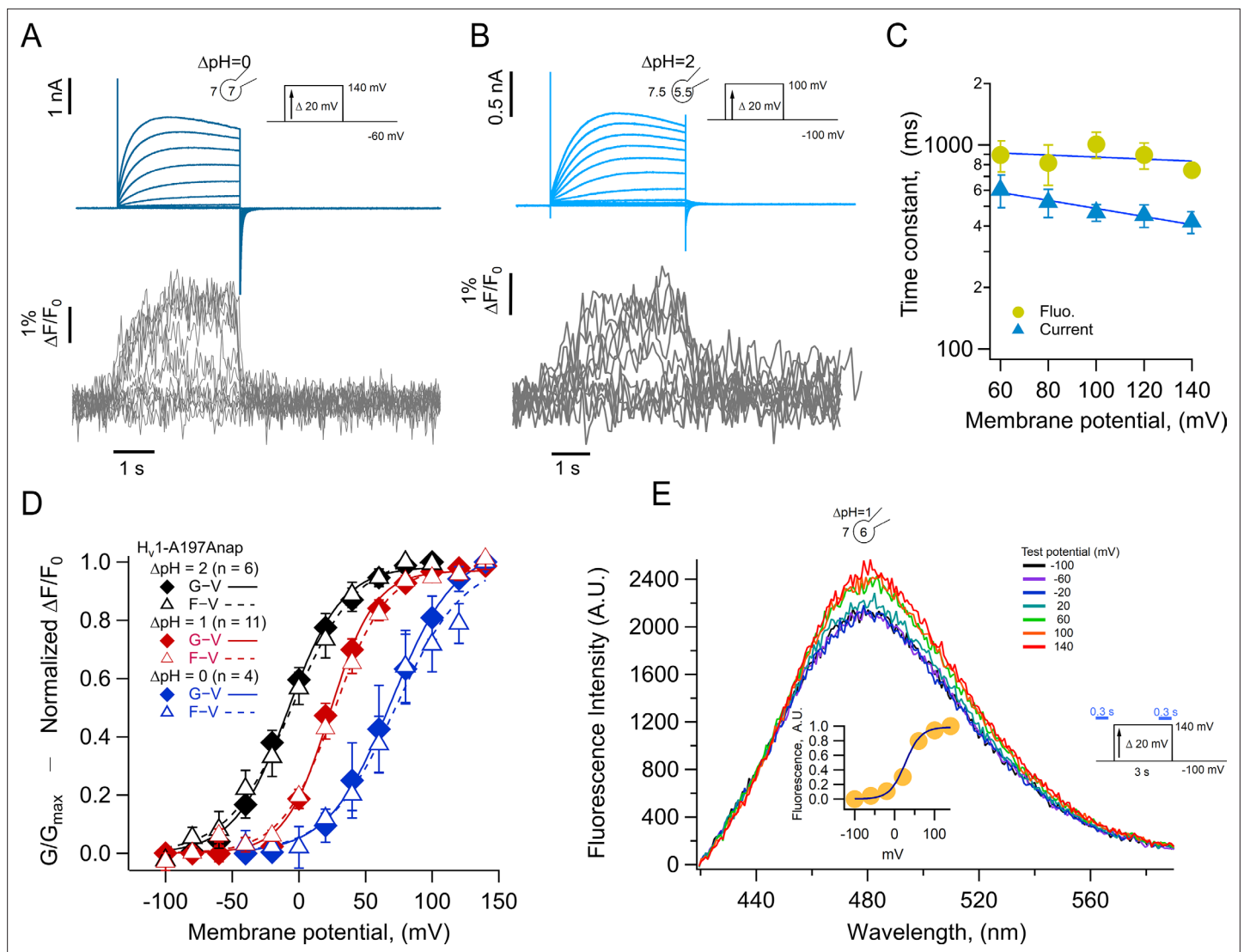


Figure 3. Anap incorporation in position A197 reveals that the movement of S4 is modulated by ΔpH . **(A–B)** Representative patch-clamp fluorometry (PCF) experiment with A197Anap at $\Delta\text{pH} = 0$ and $\Delta\text{pH} = 2$, respectively. Proton current families (upper panels) are shown in blue traces and fluorescent Anap signal (lower panel) in gray traces. **(C)** Activation time constant of current (blue) and fluorescent (lemon) signals at $\Delta\text{pH} = 0$ obtained by fitting **Equation 3** ($n=3$). The dark blue curve shows the exponential fit to **Equation 4**. The fit parameters were: $\tau(0)=976\text{ms}$ and $q=-0.03 e_0$ for fluorescence and 768ms and $-0.12 e_0$ for current. **(D)** F-V (empty triangles) and G-V (filled diamonds) curves and different ΔpH values ($\Delta\text{pH} = 0$ in blue, $n=4$; $\Delta\text{pH} = 1$ in red, $n=11$; $\Delta\text{pH} = 2$ in black, $n=6$). The data were fit to **Equation 1** (G-V, continuous curves; F-V, discontinuous curves) with the following parameters: $\Delta\text{pH} = 0$; F-V: $V_{0.5}=72.7 \pm 6\text{mV}$; $q=1.0 \pm 0.1 e_0$. G-V: $V_{0.5}=69.6 \pm 1.5\text{mV}$; $q=1.1 \pm 0.1 e_0$. $\Delta\text{pH} = 1$; F-V: $V_{0.5}=26.6 \pm 1.5\text{mV}$; $q=1.3 \pm 0.1 e_0$. G-V: $V_{0.5}=23.4 \pm 1.3\text{mV}$; $q=1.5 \pm 0.1 e_0$. $\Delta\text{pH} = 2$; F-V: $V_{0.5}=-4.5 \pm 1.7\text{mV}$; $q=1.0 \pm 0.1 e_0$. G-V: $V_{0.5}=-8.1 \pm 2.6\text{mV}$; $q=1.2 \pm 0.1 e_0$. **(E)** Emission spectra of Anap in the A197Anap mutant obtained in steady-state (300 ms at the end of holding potential and the end of the test pulse, green bars in the inset) in response to different voltages (color code indicates the test pulse in mV: purple, -60 ; dark blue, -40 ; light blue, 20 ; cyan, 0 ; light green, 20 ; dark green, 40 ; olive, 60 ; yellow, 80 ; orange, 100 ; dark red, 120 ; red, 140). The inset plots the amplitude of the emission peak as a function of test voltage. The smooth curve is the fit of the fluorescence data at $\Delta\text{pH} = 1$ shown in panel D. Summary data shown in C and D are mean \pm SEM.

The online version of this article includes the following source data and figure supplement(s) for figure 3:

Source data 1. Data for each experiment and summary data for **Figure 3C, D and E**.

Figure supplement 1. Properties of L-Anap fluorescence in solutions of solvents of different polarities.

When F-V and G-V curves are plotted together, it is evident that sensor movement paralleled the activation of the proton conductance. At three different values of the pH gradient ($\Delta\text{pH} 0, 1$, and 2), both the F-V and G-V curves are almost superimposable and shift along the voltage axis by the same amount of $\sim 40\text{mV/pH}$ unit (**Figure 3D**), which is expected of H_V1 channels (**Cherny et al., 1995**).

Only at $\Delta\text{pH} = 2$ the fluorescence signal is shifted to slightly more negative voltages than the conductance and only at voltages at which channel activation begins. The observed voltage shift of the G-V is ~ 31 mV from $\Delta\text{pH} 2-1$ and ~ 46 mV from $\Delta\text{pH} 1-0$ and is very similar for the F-V curves. This result indicates that the ΔpH -dependence of gating is preserved in channels with incorporated Anap and that the voltage sensor movement occurs in the same voltage range as the formation of the proton permeation pathway.

Anap is an environmentally sensitive dye which shifts its emission to red wavelengths in increasingly polar solvents (**Figure 3—figure supplement 1**). To understand the origin of the increased fluorescence observed during activation, we measured the emission spectra of A197Anap in voltage-clamped cells at different voltages. Fluorescence was measured from channels in the membrane region, which are identified by the mCherry signal, similar to **Figure 1C**. **Figure 3E** plots the spectra obtained at voltages ranging from -100 to 140 mV, and it shows that the fluorescence increases with depolarization and has the same voltage-dependence as the fluorescence measured in **Figure 3A, B and C** at the same ΔpH (**Figure 3E**, inset). On the other hand, the peak emission wavelength remains the same at negative or positive voltages, indicating that the increase in fluorescence is not due to depolarization-driven wavelength shifts of the emission spectra. We interpret this result as an indication that Anap incorporated at position A197 remains in a polar environment at all voltages or that small changes in polarity change the quantum yield of Anap but not the emission spectrum.

H_v1-197Anap is quenched by a phenylalanine in the S2

The increase of the Anap fluorescence at position 197 in the S4 seen with depolarization could be interpreted as a reflection of an outward movement of the S4 and exposure of Anap to a more polar environment (**Figure 3—figure supplement 1**), that in principle will produce a red shift of the emission spectrum and an increase of the fluorescence that is detected. However, as shown in **Figure 3E**, the shape of emission spectrum of Anap remains unchanged at all voltages and with a constant emission peak at ~ 480 nm, indicating that the fluorophore remains in a polar environment in the closed and open states and thus, a change in local polarity is likely not the principal cause of dequenching.

Many fluorophores can be quenched by aromatic amino acids through mechanisms such as π -stacking or photoinduced electron transfer, both mechanisms require close proximity (*Islas and Zagotta, 2006; Klymchenko, 2017; Pantazis and Olcese, 2012; Young and Artigas, 2021*). Evidence for the existence of a quenching group near Anap incorporated in the S4 can be obtained from examination of the ratio of fluorescence of Anap and mCherry in channels as a function of its position along the S4 (**Figure 4—figure supplement 1**). This analysis shows that for positions deeper into the S4 segment, the Anap/mCherry ratio diminishes, suggesting that in those sites Anap is closer to a quenching group.

For these reasons, it is conceivable that the Anap quencher in H_v1 could be an aromatic residue located near the introduced fluorophore in the closed state and upon S4 movement, increases its distance, generating the observed dequenching. We used a structural model of H_v1 derived from experimental data (*Randolph et al., 2016*) and replaced A197 with Anap. **Figure 4A** shows Anap in salmon-colored spheres and highlights aromatic residues within the transmembrane domains of a monomer as dotted spheres. A possible candidate for an Anap quencher is F150 (yellow spheres) because this residue is the closest aromatic to Anap that is not in the S4, and F150 will presumably remain in its position as 197Anap undergoes an outward displacement with depolarization. In contrast, other aromatic residues, which are closer to 197Anap and are part of the S4, will presumably move with all the S4 as a rigid body. Incidentally, an equivalent phenylalanine to F150 has been identified as the charge transfer center in canonical voltage-gated potassium channels and in H_v1 (*Tao et al., 2010; Hong et al., 2013*).

To test this hypothesis, we made the double mutant F150A-A197Anap and estimated the relative amount of basal Anap quenching by comparing the emission spectra of both Anap and mCherry in the same membrane region. **Figure 4B and C** show that the double mutant displays a significantly increased Anap fluorescence ($\sim 60\%$) relative to mCherry, when compared to A197Anap alone, suggesting that indeed, phenylalanine 150 is capable of quenching Anap in the closed state (at the resting potential of HEK cells of -20 to -40 mV [*Thomas and Smart, 2005*] and at the employed $\Delta\text{pH} \sim -0.2$ [$\text{pH}_o = 7$] most channels should be in the closed state).

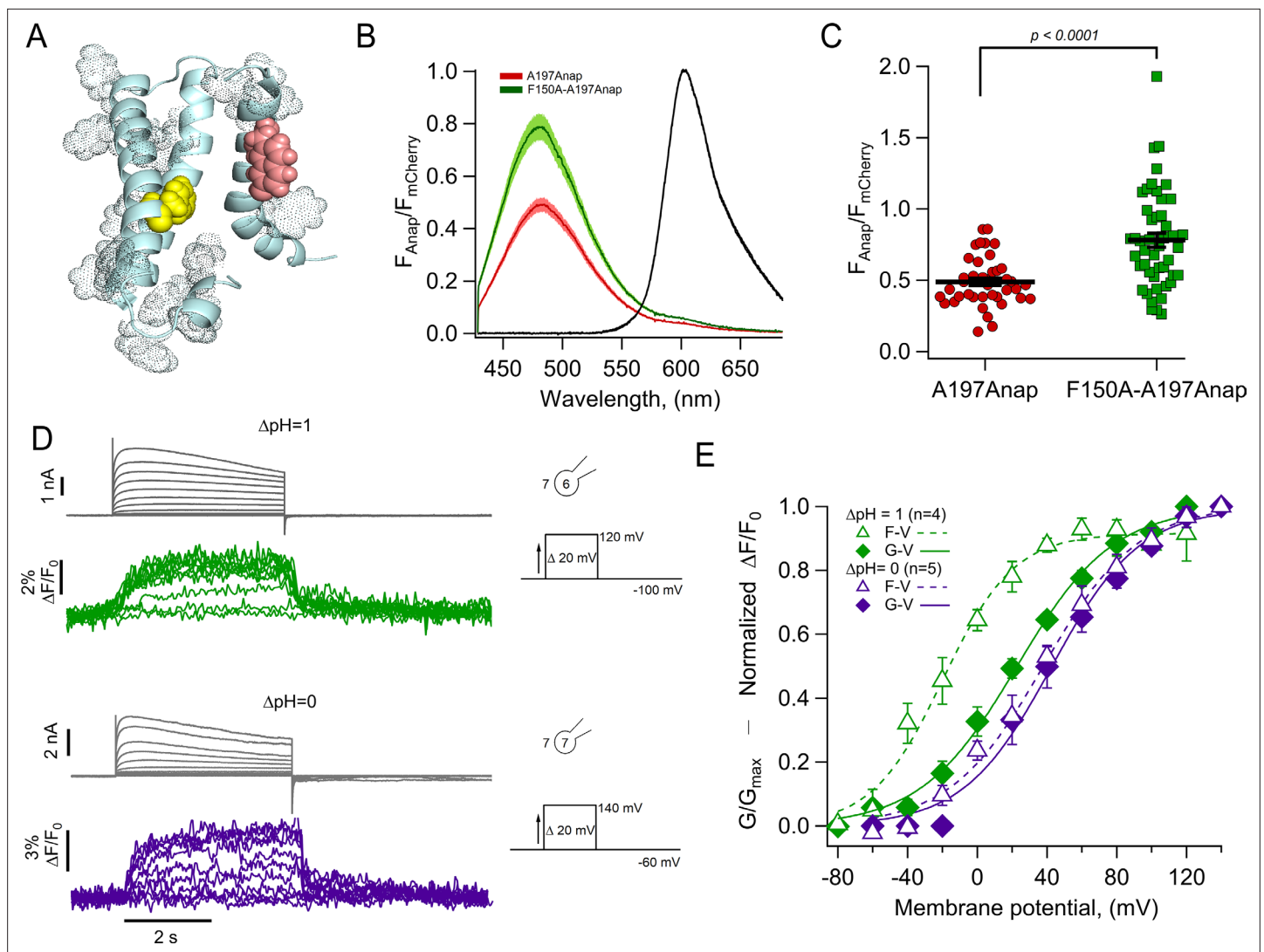


Figure 4. The charge transfer center (F150) is an Anap quencher. **(A)** Cartoon showing the presence of aromatic residues in hHv1 (rendered as space-filling dots, main chain in light blue, S3 was removed for illustration). F150 in yellow and Anap in pink. **(B)** Averages of spectra of Anap incorporated in both mutants (H_v1 -A197Anap, red; H_v1 -F150A-A197Anap, green) normalized to the fluorescence of mCherry (black). Spectra were obtained at the resting potential in non-patched cells. The double mutant's brightness is approximately 60% higher. Shadows represent SEM. **(C)** Comparison of the intensity of the emission spectrum peak of Anap normalized to the intensity of the fluorescent protein mCherry between the mutant H_v1 -A197Anap-Cherry (0.49 ± 0.03) and double mutant H_v1 -F150A-A197Anap-Cherry (0.79 ± 0.05), taken at 48 hr post-transfection. Each point indicates an individual spectrum measured from a single cell; $n=41$ and 49, respectively. Black horizontal lines are the mean \pm SEM. Unpaired Student's t-test with Welch's correction: T-statistic=5.2, degrees of freedom = 71.18, and $p=1.6 \times 10^{-6}$. **(D)** Representative current and fluorescence traces from patch-clamp fluorimetry (PCF) experiments of the double mutant H_v1 -F150A-A197Anap at $\Delta pH = 1$ (upper panel) and $\Delta pH = 0$ (lower panel). **(E)** Comparison of G-V (diamonds) and F-V (triangles) relationship between both ΔpH conditions ($\Delta pH = 1$ in green, $n=4$; $\Delta pH = 0$ in purple, $n=5$) of the double mutant H_v1 -F150A-A197Anap. F-V curve of H_v1 -F150A-A197Anap at $\Delta pH = 0$ is shifted negatively around 58 mV compared to $\Delta pH = 1$. Boltzmann fit parameters of H_v1 -F150A-A197Anap were: $\Delta pH = 1$ F-V: $V_{0.5} = -19.8 \pm 2.7$ mV; $q = 1.2 \pm 0.1 e_0$; G-V: $V_{0.5} = 22.7 \pm 2.3$ mV; $q = 0.9 \pm 0.1 e_0$. $\Delta pH = 0$ F-V: $V_{0.5} = 38.0 \pm 3.0$ mV; $q = 0.9 \pm 0.1 e_0$; G-V: $V_{0.5} = 42.6 \pm 3.8$ mV; $q = 1.0 \pm 0.1 e_0$. Data shown in B, C, and E are mean \pm SEM.

The online version of this article includes the following source data and figure supplement(s) for figure 4:

Source data 1. Data for each experiment and summary data for **Figure 4B, C and E**.

Figure supplement 1. The fluorescence of Anap is diminished as it is incorporated in residues closer to the center of the S4 segment.

Despite having removed the quenching group, F150A-A197Anap channels still show voltage-dependent fluorescence changes (**Figure 4D**), suggesting the presence of additional quenchers or that in the absence of F150, Anap at 197 becomes sensitive to polarity changes.

The voltage dependence of the fluorescence signals from F150A-A197Anap channels shows significant differences from those of A197Anap alone (**Figure 4E**). At values of ΔpH of 0 and 1, fluorescence precedes the increase in conductance, indicating that the conformational change of the S4 segment occurs at more negative voltages than the formation of the proton-permeable pathway. This effect is more pronounced at $\Delta\text{pH} = 1$. Interestingly, the difference of $V_{0.5}$ of the F-V curve between $\Delta\text{pH} = 0$ and 1 is ~ 58 mV, similar to A197Anap, which is ~ 46 mV.

A distinct gating transition detected by Anap fluorescence

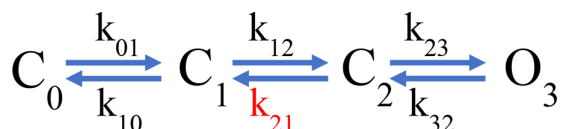
The fluorescence time course of the F150A-A197Anap channels shows an interesting characteristic; the OFF signals (F_{off}) that are produced at the return of the voltage to the holding potential and represent the return of the voltage sensor to the resting states show a two-component kinetic behavior. This is particularly evident at $\Delta\text{pH} = 0$ (**Figure 4D**), where F_{off} shows a very rapid quenching followed by a much slower component, suggesting that the voltage sensor can move back to its resting position at varying rates.

To explore the kinetics of fluorescence signals during repolarization, and since this double mutant removes a quenching group, we used the hH_v1-201Anap channels. We reasoned that this mutant channel, which has Anap in a deeper position in the S4 and presumably closer to F150 in the closed state, might be a better reporter of the kinetics of S4 movement.

Figure 5A, B and C show simultaneous current and fluorescence recordings from hH_v1-L201Anap channels at three different ΔpH values of 0, 1, and 2. As with the hH_v1-A197Anap construct, the voltage-dependence of the conductance and fluorescence is almost superimposable and shows a large shift of >40 mV/pH unit (**Figure 5D**).

The most remarkable feature of these fluorescence traces is that, at $\Delta\text{pH} = 0$, the OFF signal during repolarization (F_{off}) has two distinct kinetic components. The deactivation tail currents at -60 mV decay exponentially, with a time constant of 141 ± 55 ms, while the F_{off} can be fit to a sum of two exponentials with time constants of 129 ± 68 ms and 8.6 ± 0.74 s. (**Figure 5—figure supplement 1**). The presence of the two components in F_{off} suggests that the return of the voltage sensor to its resting state can occur at varying rates. In particular, the slow component is consistent with the immobilization of the off-gating charge observed in monomeric Ciona H_v1 channels (**Carmona et al., 2018**). The slow off-component is also present at $\Delta\text{pH} = 1$ and 2, although its amplitude is smaller. We did not undertake a systematic kinetic analysis of current and fluorescence traces during channel activation due to the alterations that proton depletion cause on the current time course, especially for the larger currents observed at $\Delta\text{pH} = 2$.

Instead, to qualitatively understand the kinetics of the fluorescence signals, we used a simplified kinetic model of channel activation (**Scheme 1**, simple gating scheme), similar to a model that was previously used to study the voltage-dependent kinetics of hH_v1 (**Villalba-Galea, 2014**).



Scheme 1. Simple gating scheme.

In this model, one of the backward transitions (k_{21}) between closed states is set to be much slower than the open to closed transition ($O_3 \rightarrow C_2$), resulting in a large difference between the closing kinetics of the ionic current, mostly determined by k_{32} , and the fluorescence signals. This kinetic difference can account for the biphasic behavior of the F_{off} signal and especially the slow component of its time course (**Figure 5E**). The model also indicates that when the internal pH is lower than the external pH ($\Delta\text{pH} = 2$), this slow rate constant is more affected than any other, indicating a conformational step that is especially sensitive to pH.

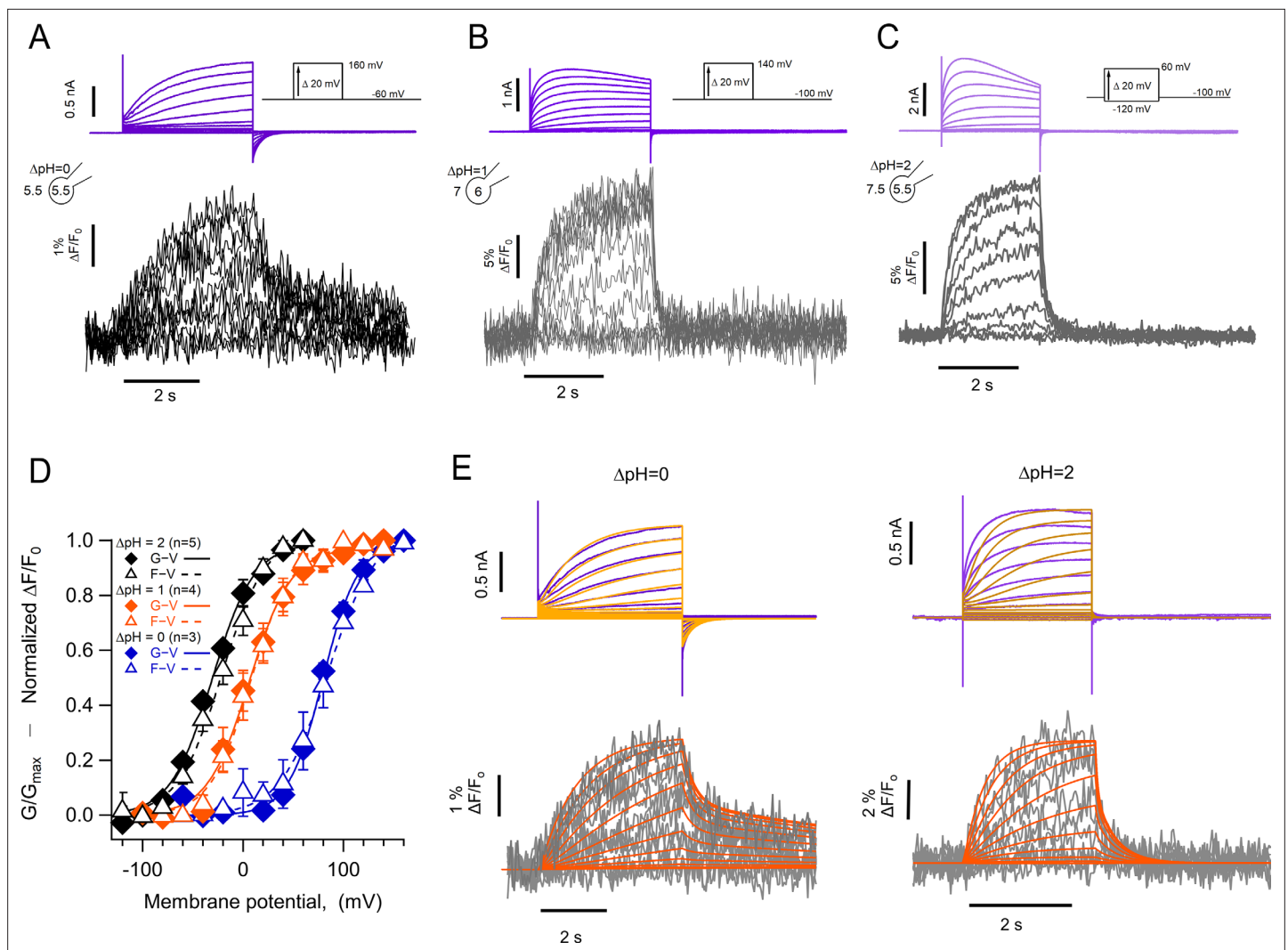


Figure 5. The kinetics of fluorescent signal during deactivation are strongly modulated by pH. Representative patch-clamp fluorometry (PCF) experiments with the hH_v1-L201Anap mutant at: (A) $\Delta\text{pH} = 0$. (B) $\Delta\text{pH} = 1$. (C) $\Delta\text{pH} = 2$. Current families are shown in the upper panel (purple traces) and fluorescent signals in the lower panel (black and gray traces). (D) G-V (filled diamonds) and F-V (empty triangles) relationships at $\Delta\text{pH} = 0$ (blue markers, $n=3$), $\Delta\text{pH} = 1$ (orange markers, $n=4$), and $\Delta\text{pH} = 2$ (black markers, $n=5$) of mutant hH_v1-L201Anap. Data are mean \pm SEM. Note that the difference between the activation at $\Delta\text{pH} = 1$ and $\Delta\text{pH} = 0$ is around 77 mV/ ΔpH unit. Boltzmann fit parameters: $\Delta\text{pH} = 0$, F-V; $V_{0.5}=84.6 \pm 2.1$ mV, $q=1.0 e_0 \pm 0.1$. G-V; $V_{0.5}=79.7 \pm 1.8$ mV, $q=1.4 \pm 0.1 e_0$. $\Delta\text{pH} = 1$, F-V; $V_{0.5}=7.7 \pm 1.6$ mV, $q=1.2 \pm 0.1 e_0$. G-V; $V_{0.5}=6.3 \pm 2.2$ mV; $q=1.2 \pm 0.1 e_0$. $\Delta\text{pH} = 2$, F-V; $V_{0.5}=-21.1 \pm 2.3$ mV; $q=1.1 \pm 0.1 e_0$. G-V; $V_{0.5}=-30.6 \pm 2.1$ mV; $q=1.2 \pm 0.1 e_0$. (E) Comparison of the current and fluorescence at two values of ΔpH with the predictions of the sequential activation model in **Scheme 1**. Experimental current and fluorescence traces are color coded as in (A). Simulated current traces are mustard colored, and fluorescence traces are orange. Simulation parameters can be found in **Supplementary file 2**. Source code files: DefinitionSchemeI_Fig5E.ipf and ProcedureToSimulateFig5E.ipf.

The online version of this article includes the following source data, source code, and figure supplement(s) for figure 5:

Source code 1. Definition of equations for scheme I.

Source code 2. Code to simulate current and fluorescence from scheme I.

Source data 1. Data for each experiments and summary data for **Figure 5D**.

Figure supplement 1. Kinetics of the OFF-fluorescence signals from H_v1-L201Anap channels.

Figure supplement 2. An allosteric model can explain the kinetics and voltage-dependence of fluorescence and conductance.

Figure supplement 2—source code 1. Definition of equations for scheme II.

Figure supplement 2—source code 2. Code to simulate current and fluorescence from scheme II.

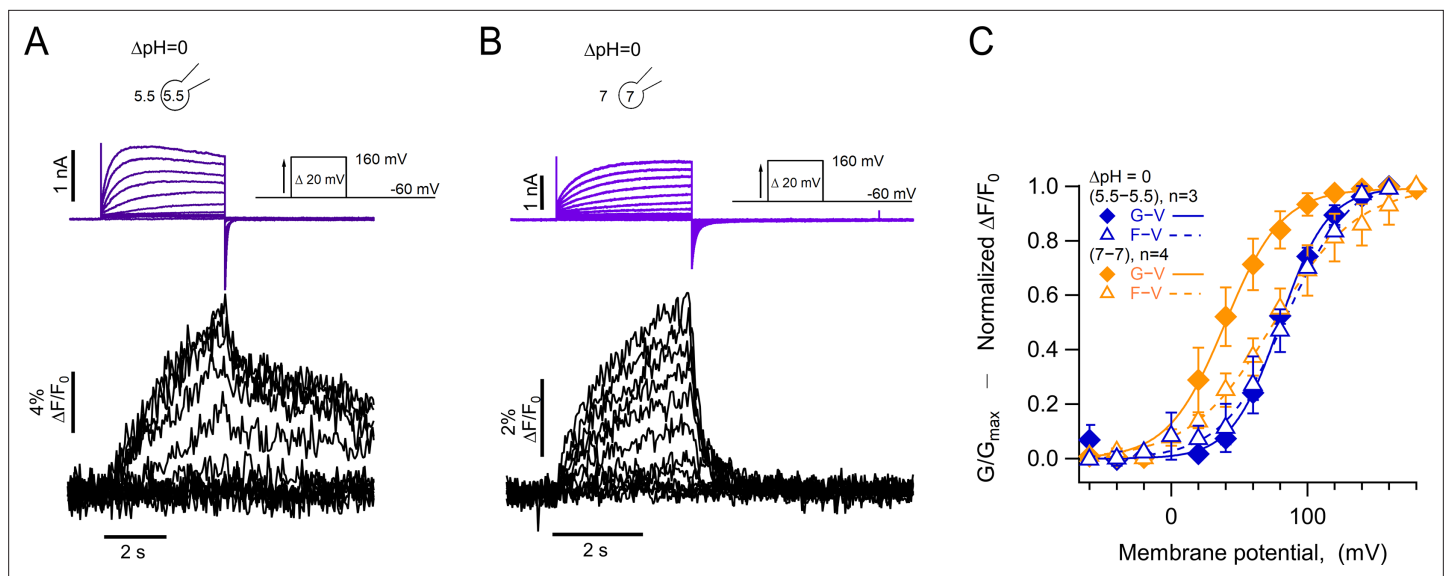


Figure 6. Absolute pH values are gating determinants in hHv1-L201Anap. **(A)** Representative patch-clamp fluorimetry (PCF) experiment at $\Delta\text{pH} = 0$ (5.5_o-5.5_i). Currents are purple and fluorescence black. **(B)** Similar experiment to **(A)** with $\Delta\text{pH} = 0$ (7_o-7_i). Current and fluorescence traces are color coded as in **(A)**. **(C)** G-V (filled diamonds) and F-V (empty triangles) curves at $\Delta\text{pH} = 0$ but with different absolute pH values ($\text{pH}_o/\text{pH}_i = 5.5, 5.5$ in blue $n=3$; $\text{pH}_o/\text{pH}_i = 7, 7$ in orange, $n=4$). Boltzmann fit parameters were $\text{pH}_o/\text{pH}_i = 7, 7$ F-V: $V_{0.5} = 75.3 \pm 2.2$ mV; $q = 0.8 \pm 0.04$ e_0 . G-V: $V_{0.5} = 39.6 \pm 1.3$ mV; $q = 1.2 \pm 0.1$ e_0 . $\text{pH}_o/\text{pH}_i = 5.5, 5.5$ F-V: $V_{0.5} = 84.6 \pm 2.1$ mV; $q = 1.0$ $e_0 \pm 0.1$. G-V: $V_{0.5} = 79.7 \pm 1.8$ mV; $q = 1.4 \pm 0.1$ e_0 . Data are mean \pm SEM.

The online version of this article includes the following source data for figure 6:

Source data 1. Data for each experiment and summary data for **Figure 6C**.

While the simple model in **Scheme 1** can account qualitatively for the observed kinetics of 201Anap channels, the experimental F-V relationship is superimposable on the G-V curve ($\Delta\text{pH} = 0$ and 1) or positively shifted by ~ 10 mV ($\Delta\text{pH} = 2$) with respect to the G-V curve, which is not a feature predicted by **Scheme 1** and is reminiscent of channels that can open to multiple open states, without the need of full-voltage sensor activation (*Stefani et al., 1997*). This observation suggests that hHv1 channels operate via a more complicated mechanism than the sequential gating illustrated by **Scheme 1**, which might include channel opening before complete voltage-sensor movement. We tested a simple version of such an allosteric model and show that it can account, at least qualitatively, for current and fluorescence kinetics and for the relationships between G-V and F-V curves at varying ΔpH (**Figure 5—figure supplement 2**). Interestingly, in this model, the slow deactivation rate constant is also the step with the most sensitivity to pH (**Supplementary file 3**).

Absolute pH values are determinants of voltage sensor movement

One of the most intriguing characteristics of Hv1 channel gating is its steep modulation by the pH gradient. While it has been shown that this modulation depends on the value of ΔpH , regardless of how it is set up (*Cherny et al., 1995*), there is evidence that the absolute value of pH can also exert an effect on gating (*Cherny et al., 2015*). In most of our experiments, the pH gradient was set up with a low value of intracellular pH, between 5.5 and 6.0. To test the effect of absolute pH, we carried out experiments with the same ΔpH of 0, with symmetric low (5.5/5.5) or high (7/7) intra/extracellular pH. The expectation was that, if pH gating of hHv1 depends only on the pH gradient, the voltage sensor should move with essentially the same characteristics. Surprisingly, the fluorescence signals display important differences, as do the proton currents. Our results in **Figure 6** show that when compared to $\Delta\text{pH} = 0$ (5.5/5.5), the fluorescence in symmetric pH_o and $\text{pH}_i = 7.0$ has a rapid return of the F_{off} signal (**Figure 6A and B**). Interestingly, the voltage dependence of the F-V relationship is very similar for (5.5/5.5) or (7/7) conditions, while in (7/7) the proton current appears at more negative voltages than the bulk of the fluorescence (**Figure 6C**).

These results suggest that the voltage range of movement of the voltage sensor, as reported by the fluorescence of 201Anap, is dependent on the ΔpH since the $V_{0.5}$ of the F-V is the same in pH_o/pH_i

= 5.5/5.5, while the opening of the proton conduction pathway in $pH_o/pH_i = 7/7$ can occur after only a fraction of the voltage sensor movement has occurred, and this coupling between voltage sensing and channel opening can be increased by low pH.

Discussion

In the experiments described here, we have implemented PCF in combination with the incorporation of a fluorescent NCAA to study voltage-dependent gating in hH_v1 proton channels. Although VCF using TMRM has been used previously to study H_v1 channels ([Qiu et al., 2013](#); [Mony et al., 2015](#); [Schladt and Berger, 2020](#)), employing the fluorescent Anap NCAA has the advantage of being a smaller size probe and improving the specificity of fluorescence signals since it is genetically encoded. The small size of Anap allowed us to incorporate the fluorophore into functional channels in several sites along the S4 and the S3–S4 loop. Since Anap was developed as an environmentally sensitive probe, the fact that the emission spectrum of Anap in these sites is very similar to that of Anap in water suggests that these residues are solvated in the native H_v1. The only position that shows a blue-shifted Anap spectrum is I202, which is the most C-terminal residue explored and might bury the Anap R-group in a more hydrophobic environment.

Since the activity of H_v1 proton channels can change the local concentration of protons near the conduction site, and fluorescence probes have been used to detect these proton fluxes ([De-la-Rosa et al., 2016](#); [Zhang et al., 2016](#)), we addressed whether Anap could change its fluorescence as a function of pH. We show that Anap is highly insensitive to pH in the range of 4–8, and it does not change fluorescence in conditions in which high outward fluxes can change the local intracellular pH. Our experiments confirm that Anap can be used without interference from local changes in proton concentration.

When incorporated at position 197, Anap produced fluorescence signals that indicate an increase in intensity with depolarization and saturate in magnitude at positive potentials. This behavior indicates dequenching of Anap as the S4 segments undergo an outward movement during the activation conformational change. Anap has been incorporated in other membrane proteins, including the *Shaker* potassium channel, in which Anap was incorporated in the S4–S5 linker and displayed fluorescence quenching upon depolarization ([Kalstrup and Blunck, 2018](#)). Anap has been incorporated in the S4 of the hyperpolarization-activated cyclic nucleotide-gated channel ([Dai et al., 2019](#)), where it is quenched or dequenched upon hyperpolarization in a position-dependent manner. It has also recently been incorporated at the bottom of the S4 in the voltage-dependent phosphatase, CiVSP ([Mizutani et al., 2022](#)), where it becomes quenched upon depolarization. The direction of the fluorescence changes due to S4 motion is difficult to predict since, as we have shown, Anap's fluorescence can be affected by both the local environment's polarity and interaction with specific quenching groups that are part of the channel sequence.

The fluorescence changes we observe in 197Anap channels indicate that the G-V and F-V relationships have almost the same voltage-dependence at the Δ pH values tested, suggesting that S4 movement closely follows channel opening and that S4 movement and activation of the proton conductance are equally affected by the proton gradient. A similar conclusion has been reached in studies measuring S4 movements of hH_v1 by fluorescence ([Schladt and Berger, 2020](#)) or in *Ciona* H_v1 by gating current recordings ([Carmona et al., 2021](#)). Interestingly, these changes in fluorescence as a function of voltage are not accompanied by changes in the emission spectrum of Anap, suggesting that the probe remains in a solvated environment regardless of the state of the channel. This is in accordance with the finding that the VSD that forms hH_v1 channels has a large extracellular cavity able to contain many water molecules ([Ramsey et al., 2010](#)).

Since Anap remains solvated in the closed and open state, what is the origin of the reported fluorescence changes? As is common with other fluorescent probes, we hypothesized that an aromatic residue could act as an Anap quencher and thus found that an aromatic outside the S4 close enough to have this function is F150. Mutation F150A in the 197Anap background produced an increased Anap/mCherry fluorescence intensity as compared to 197Anap alone, indicating reduced quenching. This result suggests that 197Anap moves away from F150 as the S4 segment moves outward during channel activation. It should be noted that F150A-197Anap channels still produce fluorescence changes upon depolarization. This suggests that other amino acid residues apart from F150 (aromatic

and charged) can also quench Anap, or changes in Anap's quantum yield are still being produced by voltage-dependent solvent accessibility.

F150 has been shown to be part of a 'hydrophobic gasket' through which S4 charges slide during channel activation. Mutations at this position and at W207 in the S4 produce altered gating (**Banh et al., 2019; Cherny et al., 2015; Wu et al., 2022**). In our case, F150A-197Anap shows a reduced shift of the G-V between ΔpH 0 and 1, from the expected ~ 40 mV to 22 mV, although the F-V curve shifts by 58 mV. These changes could be explained by altered movement of S4 through F150A, leading to changes in the coupling between voltage sensor movement and proton conductance activation. Also, this is the first time that F150 is reported as a possible actor in the pH-sensing mechanism of H_V1 .

Substitution of L201 for Anap allowed us to uncover a slow step in the deactivation pathway. The fluorescence signal observed upon channel closure by repolarization at $\Delta\text{pH} = 0$ shows two components, one of which is much slower than channel closing as reported by the tail current. The fact that tail current is faster than the slow component of the deactivation fluorescence signal indicates that the latter is produced by a slow-intermediate transition. This experimental observation is recapitulated by a simple kinetic model. Interestingly, recordings of gating currents in mutant *Ciona* H_V1 channels show that the charge return after depolarization can be very slow, producing gating charge immobilization (**Carmona et al., 2018**). This observation of a singular slow transition in hH_V1 activation illustrates the value of fluorescence recording with a small probe such as Anap.

Our data thus far indicates that a fraction of S4 movement, as reported by the F-V relation, occurs before the increase of the proton conductance and that S4 movement can continue after channel activation. Comparison of the $V_{0.5}$ values of Q-V and G-V curves in hH_V1 channels (**De La Rosa and Ramsey, 2018**) indicates that charge moves at slightly more negative values than conductance but not at all ΔpH values. Fluorescence changes depend on all the conformational states in which the fluorophore has distinct fluorescence values, while gating currents are produced during transitions between conformations with state-dependent charge distributions (**Cha and Bezanilla, 1997**). For these reasons, F-V and Q-V curves of multistate channels are not expected to be identical or contain the same information.

Our fluorescence data are consistent with recent experiments that have shown that the characteristic gating effect of the proton gradient on voltage-gated proton channels comes about by a conformational change that affects voltage sensor movement and not a channel opening transition happening after voltage-sensor activation. Furthermore, our modeling suggests that all transitions in the activation pathway, including a characteristic slow transition detected by fluorescence, are modulated by ΔpH .

The mechanism of ΔpH modulation is still unknown. It has been proposed that the energy stored in the pH gradient is directly coupled to S4 movement to produce ΔpH -dependent gating (**Carmona et al., 2021**). We have previously proposed an allosteric model in which both extracellular and intracellular protons can affect local electrostatic networks and bring about ΔpH -gating (**Rangel-Yescas et al., 2021**). This class of models predicts the existence of multiple open states, which is supported by the observation that S4 movement can happen after channel opening.

A mechanism in which the proton gradient energy is coupled to S4 movement predicts that the absolute value of pH should not influence gating. Interestingly, we have observed that the absolute pH values used to set up a $\Delta\text{pH} = 0$ do affect gating. When $\text{pH}_o = 5.5/\text{pH}_i = 5.5$, G-V and F-V are almost superimposed and the F_{off} signal has a fast and slow component; in contrast, when $\text{pH}_o = 7/\text{pH}_i = 7$, the F-V curve has almost the same voltage-dependence, but conductance can be observed at more negative voltages and the F_{off} signal only contains the fast component. These results suggest that the absolute pH in the extracellular side of the channel is a determinant of the steady-state gating, presumably modulating the slow rate constant in the activation pathway.

Materials and methods

Molecular biology and HEK cell expression

A plasmid containing the human voltage-gated proton channel (hH_V1) was a gift from Dr. Ian Scott Ramsey (Virginia Commonwealth University, Richmond, VA, USA). We used the fluorescent protein mCherry as a reporter to verify L-Anap incorporation. The construct hH_V1 -mCherry was made by the PCR overlap technique, adding the sequence of fluorescent protein mCherry after the C-terminus

of hH_v1 with the following linker sequence: (Gly-Gly-Ser)₃. This construct was subcloned into the pcDNA3.1(+) vector (ThermoFisher Scientific, USA). For all hH_v1-TAG mutants, an amber codon (TAG) was introduced using appropriate mutagenic oligonucleotides and a protocol for whole plasmid site-directed mutagenesis employing KOD polymerase (Merck Millipore, Germany) as detailed in manufacturer's instructions and previous work (Zheng *et al.*, 2004; Munteanu *et al.*, 2012). The bacterial methylated DNA templates were digested with the DpnI restriction enzyme, and the mutant plasmids were confirmed by automatic sequencing at the Instituto de Fisiología Celular, UNAM.

We used HEK293 cells (RRID: [CVCL_0045](#)) for channel expression and L-Anap incorporation experiments. The HEK cells used in this study were obtained from American Type Culture Collection (Cat. # CRL-1573) and were found free of mycoplasma infection (Sigma-Aldrich mycoplasma detection kit). These cells were cotransfected with 0.1–1 µg of mutant hH_v1-TAG plasmid and 0.7 µg of pAnap plasmid (a gift from Dr. Sharona Gordon, University of Washington, Seattle, WA, USA; RRID: [Addgene_48696](#)) using the transfection reagent JetPei (Polyplus-transfection).

The pANAP plasmid contains the orthogonal pair tRNA/aminoacyl tRNA synthetase specific to L-Anap. The Methyl ester form of L-Anap, L-Anap-Me (AsisChem Inc), was added to the medium of cells in 35 mm culture dishes from a storing stock solution of 10 mM to a final concentration of 10–20 µM. Through the text, we will refer to L-Anap as Anap for simplicity. Cells were incubated during 12–48 hr before experiments in Dulbecco's Modified Eagle Medium (DMEM, Invitrogen, USA) supplemented with 10% fetal bovine serum (Invitrogen, USA) and penicillin-streptomycin (100 units/ml — 100 µg/ml, Invitrogen, USA) at 37°C in a 5% CO₂ atmosphere. Around 4 hr before electrophysiological recordings, HEK293 cells were treated with 0.05% trypsin-EDTA (Trypsin-EDTA, Invitrogen, USA) to obtain rounded cells, which were then re-plated in 35 mm glass-bottom dishes (World Precision Instruments, USA) and used for experiments within 3–6 hr. All the experiments were performed at room temperature (~25°C).

Electrophysiology

Recordings of proton currents were performed in the whole-cell patch-clamp configuration using fire-polished borosilicate micropipettes (Sutter Instruments, USA). Currents were recorded by an Axoclamp 200B amplifier (RRID: [SCR_018866](#), Axon Instruments, USA) and acquired with an ITC-18 AD/DA converter (RRID: [SCR_023164](#), HEKA Elektronik, Germany), both controlled with Patchmaster software (RRID: [SCR_000034](#), HEKA Elektronik, Germany). Currents were low-passed filtered at 5 kHz and sampled at 20 kHz. The extracellular solution contained (in mM): 100 tetramethylammonium hydroxide and methanesulfonic acid (TMAOH-HMESO₃), 100 buffer (2-(N-morpholino) ethanesulfonic acid (MES) for pH 5.5 and 6.0; 4-(2-hydroxyethyl)-1-piperazineethanesulfonic acid (HEPES) for pH 7.0 and 7.5, 2 CaCl₂, 2 MgCl₂, 8 HCl, and pH-adjusted with TMAOH and HMESO. The intracellular solution contained (in mM): 80 (TMAOH-HMESO₃) 100 buffer (MES for pH 5.5 and 6.0; HEPES for pH 7.0 and 7.5), 10 ethylene glycol-bis(β-aminoethyl ether)-N,N,N',N'- tetraacetic acid (EGTA), 10 MgCl₂, and 4 HCl and pH-adjusted with TMAOH and HMESO. With these solutions, patch pipettes had a resistance of 2–5 MΩ. Since cells used in these experiments were round to improve space-clamp and currents were relatively small, no series-resistance compensation was employed. The voltage-clamp protocols varied depending on the value of ΔpH and are indicated in the figure legends. The interval between each test pulse was 45 s at the holding potential to facilitate return of slow fluorescence signals and minimize the effects of proton depletion. Some cells expressed very large currents (>5 nA) and displayed too much proton depletion. These cells were excluded from further analysis.

Fluorescence measurements

Fluorescence measurements in whole-cell PCF experiments were made using a TE-2000U (RRID: [SCR_023161](#), Nikon, Japan) inverted epifluorescence microscope with a 60× oil immersion objective (numerical aperture 1.4). A 405 nm solid-state laser (Compass 405–50 CW, COHERENT, USA) and a filter cube containing a 405/20 nm excitation filter, a 405 nm long pass dichroic mirror, and a 425 nm long-pass emission filter were used for Anap fluorescence excitation. For mCherry fluorescence, measurements were performed using an Ar-Ion laser (model 163, Spectra-Physics, Germany) and a filter cube with a 514/10 nm excitation filter, a 514 nm long pass dichroic mirror, and a 530 nm long-pass emission filter (Chroma, USA). Both lasers were through-air coupled, collimated using an optical cage system and appropriate optics (Thorlabs, USA) and then focused into the objective's

back focal plane through the microscope's rear port. Imaging was performed using Luca or Ixon Ultra EMCCD cameras (RRID:SCR_023165 and SCR_023166, Andor, Oxford instruments, Ireland) controlled by Micromanager software (RRID: SCR_016865; *Edelstein et al., 2014*). The fluorescence of a region without cells was measured with the same region of interest (ROI) employed with cells, and this background was subtracted from Anap fluorescence images. Image stacks from cells were recorded at 10–25 Hz (100–40 ms of exposure, respectively). To improve signal-to-noise ratio, 4×4 or 8×8 pixel binning was used. Initially, fluorescence time course was measured from a ROI that included only the membrane of the patched cell. Identical results were obtained by using an ROI encompassing all the cell.

Fluorescence and proton current recording synchronization was achieved through a home-programmed Arduino Uno microcontroller board (RRID: SCR_017284, Arduino, Italy) triggered by a PatchMaster-generated TTL pulse.

For spectral measurements, the light from the microscope was collected by a SpectraPro 2150i imaging spectrograph (RRID: SCR_023163, Princeton Instruments, USA) mounted between the microscope and EMCCD camera. The mCherry fluorescence was used as an indicator of membrane-associated channels. A small area from the membrane-associated mCherry fluorescence is selected using the spectrograph slit, and mCherry and Anap spectra were recorded by measuring a line scan 10 pixels wide from the cell membrane spectral image (**Figure 2—figure supplement 1**). Background fluorescence spectrum was recorded from a region of the image without cells and subtracted from Anap and mCherry fluorescence. Unless indicated, all the spectra were obtained at resting potential in non-patched cells (*Thomas and Smart, 2005*) and a $\Delta\text{pH} \sim -0.2$.

Data analysis

IgorPro (RRID: SCR_000325, Wavemetrics, USA) and ImageJ (RRID: SCR_003070, NIH) software were used to analyze the data. For the G-V relationships, conductance (G) was calculated from proton currents according to:

$$G(V) = \frac{I(V)}{V - V_{rev}}$$

Where V_{rev} is the proton current reversal potential, measured from the current-voltage relation. Then, G was normalized and fit to a Boltzmann function as follows:

$$\frac{G}{G_{max}} = \frac{1}{1 + \exp(q(V - V_{0.5})/K_B T)} \quad (1)$$

Where q is the apparent gating charge (in elementary charges, e_0), V is the membrane potential, $V_{0.5}$ is the potential at which half of the maximal activation is reached, K_B is the Boltzmann constant, and T is the temperature in Kelvin.

The time course of fluorescence in PCF experiments was obtained from all the background-subtracted images in a stack (F_i), and the changes through time were normalized to the first image (F_0) as follows:

$$\frac{F_i - F_0}{F_0} = \frac{\Delta F}{F_0}$$

Then, this normalization was multiplied by 100 to obtain the percent change of fluorescence. This procedure was carried out for each stack at each voltage. The voltage-dependence of the fluorescence was estimated from F-V relationships. The value of the fluorescence at the end of the voltage step was normalized and fit to a Boltzmann function:

$$\frac{F}{F_{max}} = \frac{1}{1 + \exp(q(V - V_{0.5})/K_B T)} \quad (2)$$

Where F is the percent of fluorescence change at V potential, and F_{max} is the maximum fluorescence percent change in each experiment at V potential. The meaning of q , V , $V_{0.5}$, and $K_B T$ is the same as in **Equation 1**. All data are presented as the mean \pm SEM.

The time constants activation of proton currents and fluorescence signals were obtained by fitting of the second half of each trace to the equation:

$$I \text{ or } F(t) = A_{ss} \left(1 - e^{\left(\frac{-(t-t_0)}{\tau} \right)} \right) \quad (3)$$

Where A_{ss} is the amplitude of the fluorescent signal (F) or current (I) at steady state, τ is the time constant, and t_0 is the time of start if the voltage pulse, both in ms. The voltage dependence of τ was calculated from a fit to equation:

$$\tau(V) = \tau(0) \cdot e^{\left(\frac{qV}{K_B T} \right)} \quad (4)$$

Where $\tau(0)$ is the activation time constant at 0 mV, q is the partial charge in e_0 units, and V , K_B , and T have the same meaning as in **Equation 1**.

Modeling

Modeling of current and fluorescence was carried out using custom-written programs in IgorPro. The occupancy of each discrete state in the models was calculated by numerically solving the differential equations describing the transitions between states. The occupancy of each discrete state i is P_i , and it was calculated by numerically solving the differential equations described by a master equation:

$$\frac{dP_i}{dt} = \sum_{j \neq i} (P_j k_{ji} - P_i k_{ij})$$

The rate constants k_{ij} or k_{ji} are given by:

$$k_{ij} = k_{ij}(0) \cdot \exp(-z_{ij} V / K_B T)$$

Where $k_{ij}(0)$ is the value of the rate constant at 0 mV, z_{ij} is the partial charge associated with the transition, and $K_B T$ have the same meaning as in **Equation 1**.

The current as a function of time t and voltage V was calculated as:

$$I(t, V) = \gamma_{ch} \cdot N \cdot (V - V_{rev}) \cdot P_o(t, V) + \gamma_{leak} \cdot (V - V_{rev}^{leak})$$

γ_{ch} is the single proton channel conductance, N is the number of channels, V_{rev} is the reversal potential, and P_o is the probability of the open state. γ_{leak} is the leak conductance, and V_{rev}^{leak} is the reversal potential of the leak currents.

The fluorescence was calculated as:

$$F(t, V) = \sum_{i=0}^n P_i(t, V) \cdot f_i$$

f_i is the fluorescence of the i -th state in arbitrary units.

The Igor code used for simulations in **Figure 5** and **Figure 5—figure supplement 2** is available as source code files.

Materials availability statement

All clones generated and employed in this study are available upon request.

Acknowledgements

We thank Eduardo Guevara for measurements of Anap spectra in different solvents and Manuel Hernández and Elsa Evaristo-Montes for excellent technical support. We thank Dr. Sebastian Brauchi for the loan of the 405 nm laser. This work was supported by DGAPA-PAPIIT-UNAM grant No. IN215621. E S-D is a doctoral student from Programa de Doctorado en Ciencias Bioquímicas-UNAM and was supported by a doctoral thesis scholarship from CONACyT No. 463819 (CVU 659182). M.O.-C. is a doctoral student from Programa de Doctorado en Ciencias Biomédicas-UNAM and is supported by a doctoral thesis scholarship from CONACyT No. 788807 (CVU 1101710).

Additional information

Competing interests

Leon D Islas: Reviewing editor, *eLife*. The other authors declare that no competing interests exist.

Funding

Funder	Grant reference number	Author
Programa de Doctorado en Ciencias Bioquímicas-UNAM	CONACyT No. 463819 (CVU 659182)	Esteban Suárez-Delgado
Programa de Doctorado en Ciencias Biomedicas-UNAM	CONACyT No. 788807 (CVU 1101710)	Maru Orozco-Contreras

The funders had no role in study design, data collection and interpretation, or the decision to submit the work for publication.

Author contributions

Esteban Suárez-Delgado, Data curation, Formal analysis, Investigation, Methodology, Writing – original draft, Project administration, Writing – review and editing; Maru Orozco-Contreras, Formal analysis, Investigation, Methodology, Writing – review and editing; Gisela E Rangel-Yescas, Resources, Methodology, Writing – review and editing; Leon D Islas, Conceptualization, Resources, Data curation, Software, Formal analysis, Supervision, Funding acquisition, Validation, Investigation, Methodology, Writing – original draft, Project administration, Writing – review and editing

Author ORCIDs

Esteban Suárez-Delgado  <http://orcid.org/0000-0003-0147-3451>

Maru Orozco-Contreras  <http://orcid.org/0000-0003-3315-4308>

Leon D Islas  <http://orcid.org/0000-0002-7461-5214>

Decision letter and Author response

Decision letter <https://doi.org/10.7554/eLife.85836.sa1>

Additional files

Supplementary files

- Supplementary file 1. Boltzmann equation fit parameters of each mutant at $\Delta\text{pH} = 1$ (**equation 1**).
- Supplementary file 2. Parameters used in the fits to the data in **Figure 5D** of the model in Scheme 1. Parameters with values labeled in bold indicate that these are ΔpH dependent.
- Supplementary file 3. Parameters used in the simulations with Scheme II shown in **Figure 5—figure supplement 2**. Parameter with values labeled in bold indicate that these are ΔpH dependent.
- MDAR checklist

Data availability

All data generated or analysed during this study are included in the manuscript and supporting file.

References

- Banh R, Cherny VV, Morgan D, Musset B, Thomas S, Kulleperuma K, Smith SME, Pomès R, DeCoursey TE. 2019. Hydrophobic gasket mutation produces gating pore currents in closed human voltage-gated proton channels. *PNAS* **116**:18951–18961. DOI: <https://doi.org/10.1073/pnas.1905462116>, PMID: 31462498
- Carmona EM, Larsson HP, Neely A, Alvarez O, Latorre R, Gonzalez C. 2018. Gating charge displacement in a monomeric voltage-gated proton (hv1) channel. *PNAS* **115**:9240–9245. DOI: <https://doi.org/10.1073/pnas.1809705115>, PMID: 30127012
- Carmona EM, Fernandez M, Alvear-Arias JJ, Neely A, Larsson HP, Alvarez O, Garate JA, Latorre R, Gonzalez C. 2021. The voltage sensor is responsible for δpH dependence in hv1 channels. *PNAS* **118**:e2025556118. DOI: <https://doi.org/10.1073/pnas.2025556118>, PMID: 33941706
- Catacuzzeno L, Franciolini F. 2022. The 70-year search for the voltage-sensing mechanism of ion channels. *The Journal of Physiology* **600**:3227–3247. DOI: <https://doi.org/10.1113/JP282780>, PMID: 35665931

- Cha A**, Bezanilla F. 1997. Characterizing voltage-dependent conformational changes in the Shaker K⁺ channel with fluorescence. *Neuron* **19**:1127–1140. DOI: [https://doi.org/10.1016/s0896-6273\(00\)80403-1](https://doi.org/10.1016/s0896-6273(00)80403-1), PMID: [9390525](https://pubmed.ncbi.nlm.nih.gov/9390525/)
- Cha A**, Bezanilla F. 1998. Structural implications of fluorescence quenching in the Shaker K⁺ channel. *The Journal of General Physiology* **112**:391–408. DOI: <https://doi.org/10.1085/jgp.112.4.391>, PMID: [9758859](https://pubmed.ncbi.nlm.nih.gov/9758859/)
- Chatterjee A**, Guo J, Lee HS, Schultz PG. 2013. A genetically encoded fluorescent probe in mammalian cells. *Journal of the American Chemical Society* **135**:12540–12543. DOI: <https://doi.org/10.1021/ja4059553>, PMID: [23924161](https://pubmed.ncbi.nlm.nih.gov/23924161/)
- Cherny VV**, Markin VS, DeCoursey TE. 1995. The voltage-activated hydrogen ion conductance in rat alveolar epithelial cells is determined by the pH gradient. *The Journal of General Physiology* **105**:861–896. DOI: <https://doi.org/10.1085/jgp.105.6.861>, PMID: [7561747](https://pubmed.ncbi.nlm.nih.gov/7561747/)
- Cherny VV**, Morgan D, Musset B, Chaves G, Smith SME, DeCoursey TE. 2015. Tryptophan 207 is crucial to the unique properties of the human voltage-gated proton channel, hHv1. *The Journal of General Physiology* **146**:343–356. DOI: <https://doi.org/10.1085/jgp.201511456>, PMID: [26458876](https://pubmed.ncbi.nlm.nih.gov/26458876/)
- Cowgill J**, Chanda B. 2019. The contribution of voltage clamp fluorometry to the understanding of channel and transporter mechanisms. *The Journal of General Physiology* **151**:1163–1172. DOI: <https://doi.org/10.1085/jgp.201912372>, PMID: [31431491](https://pubmed.ncbi.nlm.nih.gov/31431491/)
- Dai G**, Aman TK, DiMaio F, Zagotta WN. 2019. The HCN channel voltage sensor undergoes a large downward motion during hyperpolarization. *Nature Structural & Molecular Biology* **26**:686–694. DOI: <https://doi.org/10.1038/s41594-019-0259-1>, PMID: [31285608](https://pubmed.ncbi.nlm.nih.gov/31285608/)
- De La Rosa V**, Ramsey IS. 2018. Gating currents in the Hv1 proton channel. *Biophysical Journal* **114**:2844–2854. DOI: <https://doi.org/10.1016/j.bpj.2018.04.049>, PMID: [29925021](https://pubmed.ncbi.nlm.nih.gov/29925021/)
- De-la-Rosa V**, Suárez-Delgado E, Rangel-Yescas GE, Islas LD. 2016. Currents through Hv1 channels deplete protons in their vicinity. *The Journal of General Physiology* **147**:127–136. DOI: <https://doi.org/10.1085/jgp.201511496>, PMID: [26809792](https://pubmed.ncbi.nlm.nih.gov/26809792/)
- Eckert R**, Sibaoka T. 1968. The flash-triggering action potential of the luminescent dinoflagellate noctiluca. *The Journal of General Physiology* **52**:258–282. DOI: <https://doi.org/10.1085/jgp.52.2.258>, PMID: [5672004](https://pubmed.ncbi.nlm.nih.gov/5672004/)
- Edelstein AD**, Tsuchida MA, Amodaj N, Pinkard H, Vale RD, Stuurman N. 2014. Advanced methods of microscope control using µmanager software. *Journal of Biological Methods* **1**:e10. DOI: <https://doi.org/10.14440/jbm.2014.36>, PMID: [25606571](https://pubmed.ncbi.nlm.nih.gov/25606571/)
- Gonzalez C**, Contreras GF, Peyser A, Larsson P, Neely A, Latorre R. 2012. Voltage sensor of ion channels and enzymes. *Biophysical Reviews* **4**:1–15. DOI: <https://doi.org/10.1007/s12551-011-0061-8>, PMID: [28509999](https://pubmed.ncbi.nlm.nih.gov/28509999/)
- Gordon SE**, Munari M, Zagotta WN. 2018. Visualizing conformational dynamics of proteins in solution and at the cell membrane. *eLife* **7**:e37248. DOI: <https://doi.org/10.7554/eLife.37248>, PMID: [29923827](https://pubmed.ncbi.nlm.nih.gov/29923827/)
- Hondares E**, Brown MA, Musset B, Morgan D, Cherny VV, Taubert C, Bhamrah MK, Coe D, Marelli-Berg F, Gribben JG, Dyer MJS, DeCoursey TE, Capasso M. 2014. Enhanced activation of an amino-terminally truncated isoform of the voltage-gated proton channel hvcn1 enriched in malignant B cells. *PNAS* **111**:18078–18083. DOI: <https://doi.org/10.1073/pnas.1411390111>, PMID: [25425665](https://pubmed.ncbi.nlm.nih.gov/25425665/)
- Hong L**, Pathak MM, Kim IH, Ta D, Tombola F. 2013. Voltage-Sensing domain of voltage-gated proton channel Hv1 shares mechanism of block with pore domains. *Neuron* **77**:274–287. DOI: <https://doi.org/10.1016/j.neuron.2012.11.013>, PMID: [23352164](https://pubmed.ncbi.nlm.nih.gov/23352164/)
- Islas LD**, Zagotta WN. 2006. Short-Range molecular rearrangements in ion channels detected by tryptophan quenching of bimane fluorescence. *The Journal of General Physiology* **128**:337–346. DOI: <https://doi.org/10.1085/jgp.200609556>, PMID: [16940556](https://pubmed.ncbi.nlm.nih.gov/16940556/)
- Kalstrup T**, Blunck R. 2013. Dynamics of internal pore opening in K (V) channels probed by a fluorescent unnatural amino acid. *PNAS* **110**:8272–8277. DOI: <https://doi.org/10.1073/pnas.1220398110>, PMID: [23630265](https://pubmed.ncbi.nlm.nih.gov/23630265/)
- Kalstrup T**, Blunck R. 2018. S4-S5 linker movement during activation and inactivation in voltage-gated K⁺ channels. *PNAS* **115**:E6751–E6759. DOI: <https://doi.org/10.1073/pnas.1719105115>, PMID: [29959207](https://pubmed.ncbi.nlm.nih.gov/29959207/)
- Klymchenko AS**. 2017. Solvatochromic and fluorogenic dyes as environment-sensitive probes: design and biological applications. *Accounts of Chemical Research* **50**:366–375. DOI: <https://doi.org/10.1021/acs.accounts.6b00517>, PMID: [28067047](https://pubmed.ncbi.nlm.nih.gov/28067047/)
- Koch HP**, Kurokawa T, Okochi Y, Sasaki M, Okamura Y, Larsson HP. 2008. Multimeric nature of voltage-gated proton channels. *PNAS* **105**:9111–9116. DOI: <https://doi.org/10.1073/pnas.0801553105>, PMID: [18583477](https://pubmed.ncbi.nlm.nih.gov/18583477/)
- Kusch J**, Zifarelli G. 2014. Patch-Clamp fluorometry: electrophysiology meets fluorescence. *Biophysical Journal* **106**:1250–1257. DOI: <https://doi.org/10.1016/j.bpj.2014.02.006>, PMID: [24655500](https://pubmed.ncbi.nlm.nih.gov/24655500/)
- Lee SY**, Letts JA, Mackinnon R. 2008. Dimeric subunit stoichiometry of the human voltage-dependent proton channel hv1. *PNAS* **105**:7692–7695. DOI: <https://doi.org/10.1073/pnas.0803277105>, PMID: [18509058](https://pubmed.ncbi.nlm.nih.gov/18509058/)
- Li Q**, Shen R, Treger JS, Wanderling SS, Milewski W, Siwowska K, Bezanilla F, Perozo E. 2015. Resting state of the human proton channel dimer in a lipid bilayer. *PNAS* **112**:E5926–E5935. DOI: <https://doi.org/10.1073/pnas.1515043112>, PMID: [26443860](https://pubmed.ncbi.nlm.nih.gov/26443860/)
- Lishko PV**, Kirichok Y. 2010. The role of hv1 and catsper channels in sperm activation. *The Journal of Physiology* **588**:4667–4672. DOI: <https://doi.org/10.1113/jphysiol.2010.194142>
- Ma J**, Gao X, Li Y, DeCoursey TE, Shull GE, Wang H-S. 2022. The Hvcn1 voltage-gated proton channel contributes to pH regulation in canine ventricular myocytes. *The Journal of Physiology* **600**:2089–2103. DOI: <https://doi.org/10.1113/JP282126>, PMID: [35244217](https://pubmed.ncbi.nlm.nih.gov/35244217/)

- Mizutani N**, Kawanabe A, Jinno Y, Narita H, Yonezawa T, Nakagawa A, Okamura Y. 2022. Interaction between S4 and the phosphatase domain mediates electrochemical coupling in voltage-sensing phosphatase (VSP). *PNAS* **119**:e2200364119. DOI: <https://doi.org/10.1073/pnas.2200364119>, PMID: 35733115
- Mony L**, Berger TK, Isacoff EY. 2015. A specialized molecular motion opens the hv1 voltage-gated proton channel. *Nature Structural & Molecular Biology* **22**:283–290. DOI: <https://doi.org/10.1038/nsmb.2978>, PMID: 25730777
- Munteanu B**, Braun M, Boonrod K. 2012. Improvement of PCR reaction conditions for site-directed mutagenesis of big plasmids. *Journal of Zhejiang University. Science. B* **13**:244–247. DOI: <https://doi.org/10.1631/jzus.B1100180>, PMID: 22467364
- Musset B**, Cherny VV, Morgan D, Okamura Y, Ramsey IS, Clapham DE, DeCoursey TE. 2008. Detailed comparison of expressed and native voltage-gated proton channel currents: voltage-dependent proton channel gating. *The Journal of Physiology* **586**:2477–2486. DOI: <https://doi.org/10.1113/jphysiol.2007.149427>
- Pantazis A**, Olcese R. 2012. Relative transmembrane segment rearrangements during BK channel activation resolved by structurally assigned fluorophore-quencher pairing. *The Journal of General Physiology* **140**:207–218. DOI: <https://doi.org/10.1085/jgp.201210807>, PMID: 22802360
- Puljung MC**. 2021. ANAP: A versatile, fluorescent probe of ion channel gating and regulation. *Methods in Enzymology* **654**:49–84. DOI: <https://doi.org/10.1016/bs.mie.2021.01.048>, PMID: 34120725
- Qiu F**, Rebolledo S, Gonzalez C, Larsson HP. 2013. Subunit interactions during cooperative opening of voltage-gated proton channels. *Neuron* **77**:288–298. DOI: <https://doi.org/10.1016/j.neuron.2012.12.021>, PMID: 23352165
- Ramsey IS**, Moran MM, Chong JA, Clapham DE. 2006. A voltage-gated proton-selective channel lacking the pore domain. *Nature* **440**:1213–1216. DOI: <https://doi.org/10.1038/nature04700>, PMID: 16554753
- Ramsey IS**, Ruchti E, Kaczmarek JS, Clapham DE. 2009. Hv1 proton channels are required for high-level NADPH oxidase-dependent superoxide production during the phagocyte respiratory burst. *PNAS* **106**:7642–7647. DOI: <https://doi.org/10.1073/pnas.0902761106>, PMID: 19372380
- Ramsey IS**, Mokrab Y, Carvacho I, Sands ZA, Sansom MSP, Clapham DE. 2010. An aqueous H⁺ permeation pathway in the voltage-gated proton channel Hv1. *Nature Structural & Molecular Biology* **17**:869–875. DOI: <https://doi.org/10.1038/nsmb.1826>, PMID: 20543828
- Randolph AL**, Mokrab Y, Bennett AL, Sansom MS, Ramsey IS. 2016. Proton currents constrain structural models of voltage sensor activation. *eLife* **5**:e18017. DOI: <https://doi.org/10.7554/eLife.18017>, PMID: 27572256
- Rangel-Yescas G**, Cervantes C, Cervantes-Rocha MA, Suárez-Delgado E, Banaszak AT, Maldonado E, Ramsey IS, Rosenbaum T, Islas LD. 2021. Discovery and characterization of hv1-type proton channels in reef-building corals. *eLife* **10**:e69248. DOI: <https://doi.org/10.7554/eLife.69248>, PMID: 34355697
- Sasaki M**, Takagi M, Okamura Y. 2006. A voltage sensor-domain protein is a voltage-gated proton channel. *Science* **312**:589–592. DOI: <https://doi.org/10.1126/science.1122352>, PMID: 16556803
- Schladt TM**, Berger TK. 2020. Voltage and pH difference across the membrane control the S4 voltage-sensor motion of the hv1 proton channel. *Scientific Reports* **10**:21293. DOI: <https://doi.org/10.1038/s41598-020-77986-z>, PMID: 33277511
- Shaner NC**, Campbell RE, Steinbach PA, Giepmans BNG, Palmer AE, Tsien RY. 2004. Improved monomeric red, orange and yellow fluorescent proteins derived from *Discosoma* sp. red fluorescent protein. *Nature Biotechnology* **22**:1567–1572. DOI: <https://doi.org/10.1038/nbt1037>, PMID: 15558047
- Smith SME**, Morgan D, Musset B, Cherny VV, Place AR, Hastings JW, DeCoursey TE. 2011. Voltage-gated proton channel in a dinoflagellate. *PNAS* **108**:18162–18167. DOI: <https://doi.org/10.1073/pnas.1115405108>, PMID: 22006335
- Stefani E**, Ottolia M, Noceti F, Olcese R, Wallner M, Latorre R, Toro L. 1997. Voltage-controlled gating in a large conductance Ca²⁺-sensitive K⁺ channel (hsl). *PNAS* **94**:5427–5431. DOI: <https://doi.org/10.1073/pnas.94.10.5427>, PMID: 9144254
- Tao X**, Lee A, Limapichat W, Dougherty DA, MacKinnon R. 2010. A gating charge transfer center in voltage sensors. *Science* **328**:67–73. DOI: <https://doi.org/10.1126/science.1185954>, PMID: 20360102
- Taylor AR**, Chrachri A, Wheeler G, Goddard H, Brownlee C. 2011. A voltage-gated H⁺ channel underlying pH homeostasis in calcifying coccolithophores. *PLOS Biology* **9**:e1001085. DOI: <https://doi.org/10.1371/journal.pbio.1001085>, PMID: 21713028
- Thomas P**, Smart TG. 2005. HEK293 cell line: A vehicle for the expression of recombinant proteins. *Journal of Pharmacological and Toxicological Methods* **51**:187–200. DOI: <https://doi.org/10.1016/j.vascn.2004.08.014>, PMID: 15862464
- Tombola F**, Ulbrich MH, Isacoff EY. 2008. The voltage-gated proton channel Hv1 has two pores, each controlled by one voltage sensor. *Neuron* **58**:546–556. DOI: <https://doi.org/10.1016/j.neuron.2008.03.026>, PMID: 18498736
- Vaid M**, Claydon TW, Rezazadeh S, Fedida D. 2008. Voltage clamp fluorimetry reveals a novel outer pore instability in a mammalian voltage-gated potassium channel. *The Journal of General Physiology* **132**:209–222. DOI: <https://doi.org/10.1085/jgp.200809978>, PMID: 18625849
- Villalba-Galea CA**. 2014. Hv1 proton channel opening is preceded by a voltage-independent transition. *Biophysical Journal* **107**:1564–1572. DOI: <https://doi.org/10.1016/j.bpj.2014.08.017>, PMID: 25296308
- Wang Y**, Li SJ, Wu X, Che Y, Li Q. 2012. Clinicopathological and biological significance of human voltage-gated proton channel Hv1 protein overexpression in breast cancer. *The Journal of Biological Chemistry* **287**:13877–13888. DOI: <https://doi.org/10.1074/jbc.M112.345280>, PMID: 22367212

- Wu LJ.** 2014. Microglial voltage-gated proton channel Hv1 in ischemic stroke. *Translational Stroke Research* **5**:99–108. DOI: <https://doi.org/10.1007/s12975-013-0289-7>, PMID: 24323712
- Wu X, Zhang L, Hong L.** 2022. The role of phe150 in human voltage-gated proton channel. *IScience* **25**:105420. DOI: <https://doi.org/10.1016/j.isci.2022.105420>, PMID: 36388967
- Young VC, Artigas P.** 2021. Displacement of the Na^+/K^+ pump's transmembrane domains demonstrates conserved conformational changes in P-type 2 atpases. *PNAS* **118**:e2019317118. DOI: <https://doi.org/10.1073/pnas.2019317118>
- Yu Y, Luo X, Li C, Ding F, Wang M, Xie M, Yu Z, Ransom BR, Wang W.** 2020. Microglial Hv1 proton channels promote white matter injuries after chronic hypoperfusion in mice. *Journal of Neurochemistry* **152**:350–367. DOI: <https://doi.org/10.1111/jnc.14925>, PMID: 31769505
- Zhang L, Bellve K, Fogarty K, Kobertz WR.** 2016. Fluorescent visualization of cellular proton fluxes. *Cell Chemical Biology* **23**:1449–1457. DOI: <https://doi.org/10.1016/j.chembiol.2016.10.013>, PMID: 27916567
- Zhang Q, Ren Y, Mo Y, Guo P, Liao P, Luo Y, Mu J, Chen Z, Zhang Y, Li Y, Yang L, Liao D, Fu J, Shen J, Huang W, Xu X, Guo Y, Mei L, Zuo Y, Liu J, et al.** 2022. Inhibiting Hv1 channel in peripheral sensory neurons attenuates chronic inflammatory pain and opioid side effects. *Cell Research* **32**:461–476. DOI: <https://doi.org/10.1038/s41422-022-00616-y>, PMID: 35115667
- Zhao R, Kennedy K, De Blas GA, Orta G, Pavarotti MA, Arias RJ, de la Vega-Beltrán JL, Li Q, Dai H, Perozo E, Mayorga LS, Darszon A, Goldstein SAN.** 2018. Role of human hv1 channels in sperm capacitation and white blood cell respiratory burst established by a designed peptide inhibitor. *PNAS* **115**:E11847–E11856. DOI: <https://doi.org/10.1073/pnas.1816189115>, PMID: 30478045
- Zhao C, Tombola F.** 2021. Voltage-gated proton channels from fungi highlight role of peripheral regions in channel activation. *Communications Biology* **4**:261. DOI: <https://doi.org/10.1038/s42003-021-01792-0>, PMID: 33637875
- Zheng L, Baumann U, Reymond JL.** 2004. An efficient one-step site-directed and Site-saturation mutagenesis protocol. *Nucleic Acids Research* **32**:e115. DOI: <https://doi.org/10.1093/nar/gnh110>, PMID: 15304544

Discovery and characterization of H_v1-type proton channels in reef-building corals

Gisela Rangel-Yescas¹, Cecilia Cervantes¹, Miguel A Cervantes-Rocha¹, Esteban Suárez-Delgado¹, Anastazia T Banaszak², Ernesto Maldonado³, Ian Scott Ramsey⁴, Tamara Rosenbaum⁵, Leon D Islas^{1*}

¹Departamento de Fisiología, Facultad of Medicina, Universidad Nacional Autónoma de México, Mexico City, Mexico; ²Unidad Académica de Sistemas Arrecifales, Instituto de Ciencias del Mar y Limnología, Universidad Nacional Autónoma de México, Puerto Morelos, Mexico; ³EvoDevo Research Group, Unidad Académica de Sistemas Arrecifales, Instituto de Ciencias del Mar y Limnología, Universidad Nacional Autónoma de México, Puerto Morelos, Mexico; ⁴Department of Physiology and Biophysics, School of Medicine, Virginia Commonwealth University, Richmond, United States; ⁵Departamento de Neurociencia Cognitiva, Instituto de Fisiología Celular, Universidad Nacional Autónoma de México, Mexico City, Mexico

Abstract Voltage-dependent proton-permeable channels are membrane proteins mediating a number of important physiological functions. Here we report the presence of a gene encoding H_v1 voltage-dependent, proton-permeable channels in two species of reef-building corals. We performed a characterization of their biophysical properties and found that these channels are fast-activating and modulated by the pH gradient in a distinct manner. The biophysical properties of these novel channels make them interesting model systems. We have also developed an allosteric gating model that provides mechanistic insight into the modulation of voltage-dependence by protons. This work also represents the first functional characterization of any ion channel in scleractinian corals. We discuss the implications of the presence of these channels in the membranes of coral cells in the calcification and pH-regulation processes and possible consequences of ocean acidification related to the function of these channels.

*For correspondence:
leon.islas@gmail.com

Competing interest: See
page 17

Funding: See page 17

Preprinted: 09 April 2021

Received: 09 April 2021

Accepted: 30 June 2021

Published: 06 August 2021

Reviewing editor: László Csanády, Semmelweis University, Hungary

© Copyright Rangel-Yescas et al. This article is distributed under the terms of the [Creative Commons Attribution License](#), which permits unrestricted use and redistribution provided that the original author and source are credited.

Introduction

Scleractinian or stony corals are organisms in the phylum Cnidaria that deposit calcium carbonate (CaCO₃) in the form of aragonite to build an exoskeleton. Stony corals are the main calcifying organisms responsible for the construction of coral reefs, which are major ecosystems hosting numerous and diverse organisms. Coral reefs also act as natural barriers from strong ocean currents, waves, and tropical storms, providing coastal protection. This protection centers on the ability of scleractinian corals to produce enough CaCO₃. The increase in atmospheric CO₂ concentrations as a result of human activity poses threats to coral-reef-building organisms due to rising sea surface temperatures (*Hoegh-Guldberg, 1999*) and because CO₂ is taken up by the ocean, dangerously lowering the pH of the sea water (*Caldeira and Wickett, 2003*).

It is known that precipitation of the aragonitic form of calcium carbonate is facilitated at elevated pH values, at very low concentrations of protons. Calcification by scleractinian corals is a process that has been shown to be modulated by the pH of the solution in which calcium carbonate is precipitated (*Allemand et al., 2011*). To this end, corals produce a specialized compartment between the ectoderm and the external substrate or skeleton called calciblastic compartment, which

contains a fluid derived from the surrounding sea water. The composition of this calciblastic fluid or liquor is strictly regulated by the coral to maintain both an elevated pH, often close to one unit higher than the surrounding sea water, and an increased concentration of Ca^{2+} and carbonates. The molecular details of pH regulation in the calciblastic fluid are not understood completely. Involvement of proton pumps has been postulated and is likely to be part of proton transport in corals. Both P-type and V-type hydrogen pumps are present in coral transcriptomes and are known to play roles in the physiology of coral-algal symbiosis (Tresguerres *et al.*, 2017). V-type H^+ -ATPases have also been shown to be involved in calcification in foraminifera (Toyofuku *et al.*, 2017). If a proton pump is involved in lowering proton concentration in the calciblastic fluid to maintain high calcification rates, protons will be transported to the cytoplasm of the ectodermal cells that constitute the calciblastic epithelium, producing a profound acidification of the cytoplasmic pH (pH_i). Although measurements of the pH_i in corals indicate values of 7.13–7.4 (Venn *et al.*, 2009), it is unknown how coral cells regulate pH_i . Thus, an efficient pH-regulatory mechanism is to be expected to be present in corals. We hypothesized that proton channels might be fundamental to this physiological process and also required for calcification in hard corals.

Although a number of studies have delineated the physiological roles of H_v1 voltage-gated proton channels in vertebrate cells (DeCoursey, 2013), less is known about their role in invertebrates. These channels are potential mediators in processes that are critically dependent on proton homeostasis. As an example, they have been shown to be involved in regulating the synthesis of the calcium carbonate skeleton in coccolithophores, calcifying unicellular phytoplankton (Taylor *et al.*, 2011).

The range of voltages over which channel activation occurs is strongly modulated by the transmembrane proton gradient, characterized by $\Delta\text{pH} = \text{pH}_o - \text{pH}_i$, that is, the difference between the external and internal pH. In the majority of known H_v1 channels, the voltage at which half of the channels are activated, the $V_{0.5}$ or the apparent threshold for channel opening (V_{Thr}), shifts by roughly 40 mV per unit of ΔpH . Thus, the pH gradient strongly biases the voltage-independent free energy of channel activation (Cherny *et al.*, 1995). With few exceptions, channel activation occurs at voltages that are more positive than the reversal potential for protons, implying that protons are always flowing outward under steady-state conditions. The fact that most H_v1 s mediate outward currents is the reason these channels are mostly involved in reversing intracellular acidification or producing voltage-dependent cytoplasmic alkalization (Lishko and Kirichok, 2010; DeCoursey, 2013).

Here we report the presence of genes encoding H_v1 channels in two species of reef-building corals. We cloned and characterized the biophysical properties of these channels in an expression system using patch-clamp electrophysiology. The demonstration of the presence of voltage-gated proton channels in corals is an initial step to a deeper understanding of coral calcification and its dysregulation under ocean acidification conditions. We show that some of the coral H_v1 's biophysical properties are different from other known proton channels, and this behavior makes them interesting models to try to understand some basic biophysical mechanisms in these channels. To explain this behavior, we developed a novel activation model to describe voltage- and pH-dependent gating that has general applicability to H_v1 channels.

Results

Ion channels have not been characterized in corals. Here, we have initiated their study by searching the transcriptome of the Indo-Pacific coral *Acropora millepora* (Moya *et al.*, 2012) for sequences coding for putative voltage-sensing residues present in canonical H_v1 channels with the form RxxRxxRlx, which corresponds to the S4 segment of H_v1 channels and is also found in other voltage-sensitive membrane proteins. Blast searches detected four sequences that seem to correspond to a gene encoding the H_v1 voltage-activated proton-selective ion channel (Ramsey *et al.*, 2006; Sasaki *et al.*, 2006). *A. millepora* is one of the most widely studied species of scleractinian corals and is well represented in the commercial coral trade (Cleves *et al.*, 2018; Ying *et al.*, 2019). We proceeded to clone this gene from a small specimen of *A. millepora* obtained from a local aquarium (Reef Services, Mexico City). As indicated in the 'Materials and methods' section, total RNA was extracted from tissue and mRNA was retrotranscribed to obtain complementary DNA (cDNA). We managed to obtain a full-length clone and refer to this sequence as Am H_v1 or H_v1 -type proton channel of *A. millepora*.

We were interested in knowing if the same gene is present in a closely related species from the Caribbean Sea. Thus, we used the same primers to clone the H_v1 channel from *Acropora palmata*, a widespread coral in the same family, and which we call ApH_v1. The amino acid sequence is almost identical to AmH_v1 (**Figure 1—figure supplement 1A**); the greatest divergence is found between a few amino acid residues in the C-terminal region. This result suggests that despite the large biogeographic difference, these two genes have not diverged significantly. The ApH_v1 sequence also gives rise to fast-activating voltage-gated proton currents (**Figure 1—figure supplement 1B**).

The most diagnostic feature of the H_v1 protein is the sequence of the fourth transmembrane domain or S4, which contains three charged amino acids in a characteristic triplet repeat. The presence of these repeats in our sequence allowed us to initially identify our clone as an H_v1 channel. However, we decided to compare our sequence to those of several H_v1 orthologs. We selected a list of 130 H_v1 protein sequences that are well curated in the Gene Bank (<https://www.ncbi.nlm.nih.gov/>), representing several branches of the eukaryotes, from unicellular plants to mammals. As expected, the protein sequence of AmH_v1 has similarity to several other H_v1 genes from varied organisms (**Figure 1A**). The identity varies from 98%, when compared to other putative coral and anemone sequences, to less than 30%, when compared to plant and nematode sequences. In spite of this variability, the putative transmembrane domains of all these proteins show high conservation, and consensus sequence logos can detect the presence of highly conserved individual amino acid sequences that can be considered characteristic of H_v1 channels. **Figure 1B** compares these transmembrane domain consensus logos with our AmH_v1 sequence. It can be gleaned that AmH_v1 contains the highly conserved residues that form the voltage-sensing amino acid residues in S4 as well as their acidic pairs present in S2 and S3. The extracellular histidine residues involved in Zn²⁺ coordination are also present. These results suggest that our sequence is that of a bona fide H_v1 voltage-sensing domain (VSD).

Apart from canonical voltage-gated channels, several other proteins contain VSDs. Examples are the voltage-sensing phosphatases like VSPs (*Iwasaki et al., 2008*) and TPTE and TPTE2 (*Halaszovich et al., 2012*) proteins (transmembrane proteins with tensin homology) and genes like TMEM266. These proteins are relevant to us since some TPTEs have been shown to also mediate proton currents and TMEM266 can be modulated by Zn²⁺ (*Papp et al., 2019*). We compared the sequence of AmH_v1 with several orthologs of TPTEs and TMEM266. Although there is some similarity within transmembrane domains (**Figure 1—figure supplement 2**), the overall sequence comparison shows that AmH_v1 and these VSD-containing proteins are different.

As mentioned before, we performed a multiple sequence alignment with 130 H_v1 sequences. In **Figure 2**, we show the detailed sequence alignment of AmH_v1 with five of these sequences, which represent some of the best studied H_v1 genes. It can be seen that there is a high degree of identity, especially in the transmembrane domains. The least degree of conservation appears when comparing this sequence to the dinoflagellate *Karlodinium veneficum* H_v1 channel (**Figure 2A**). A search of available transcriptomes from several coral species allowed us to detect the presence of sequences that are found in H_v1 channels. This suggests that H_v1 proton channels might be found in many families of scleractinian corals (**Figure 2—figure supplement 1**), as has also been recently shown (*Capasso et al., 2021*).

Secondary-structure prediction suggests that AmH_v1 is a canonical H_v1 channel formed by a VSD with four transmembrane segments. The protein sequence was used for 3D modeling using the SWISS MODEL server (*Waterhouse et al., 2018*), which produced models based on the H_v1 chimera structure (*Takeshita et al., 2014*) and the Kv1.2 potassium channel VSD (*Long et al., 2005*). This structural model is shown in **Figure 2B**. The predicted model indicates a shortened N-terminal region, four transmembrane helices, and a long C-terminal helix.

Voltage-gated proton channels from *Ciona* (*Sasaki et al., 2006*) and humans (*Lee et al., 2008*) have been shown to express as dimers in the plasma membrane, and this dimeric form is understood to be the functional unit of these proton channels. The dimer is stabilized by a coiled-coil interaction mediated by an alpha helical C-terminal domain. As shown by the model in **Figure 2B**, AmH_v1 has a long C-terminal helix, which is predicted to engage in a coiled coil (Paircoil2; *McDonnell et al., 2006*). We calculated the probability per residue to form a coiled coil for all the C-terminal residues, both for human and AmH_v1 channels, using the program COILS (*Lupas et al., 1991*). **Figure 3A** shows that the coiled-coil probability for AmH_v1 C-terminus is at least as high or higher than that for hH_v1, an established dimer, strongly suggesting that coral H_v1 s might also form dimers.

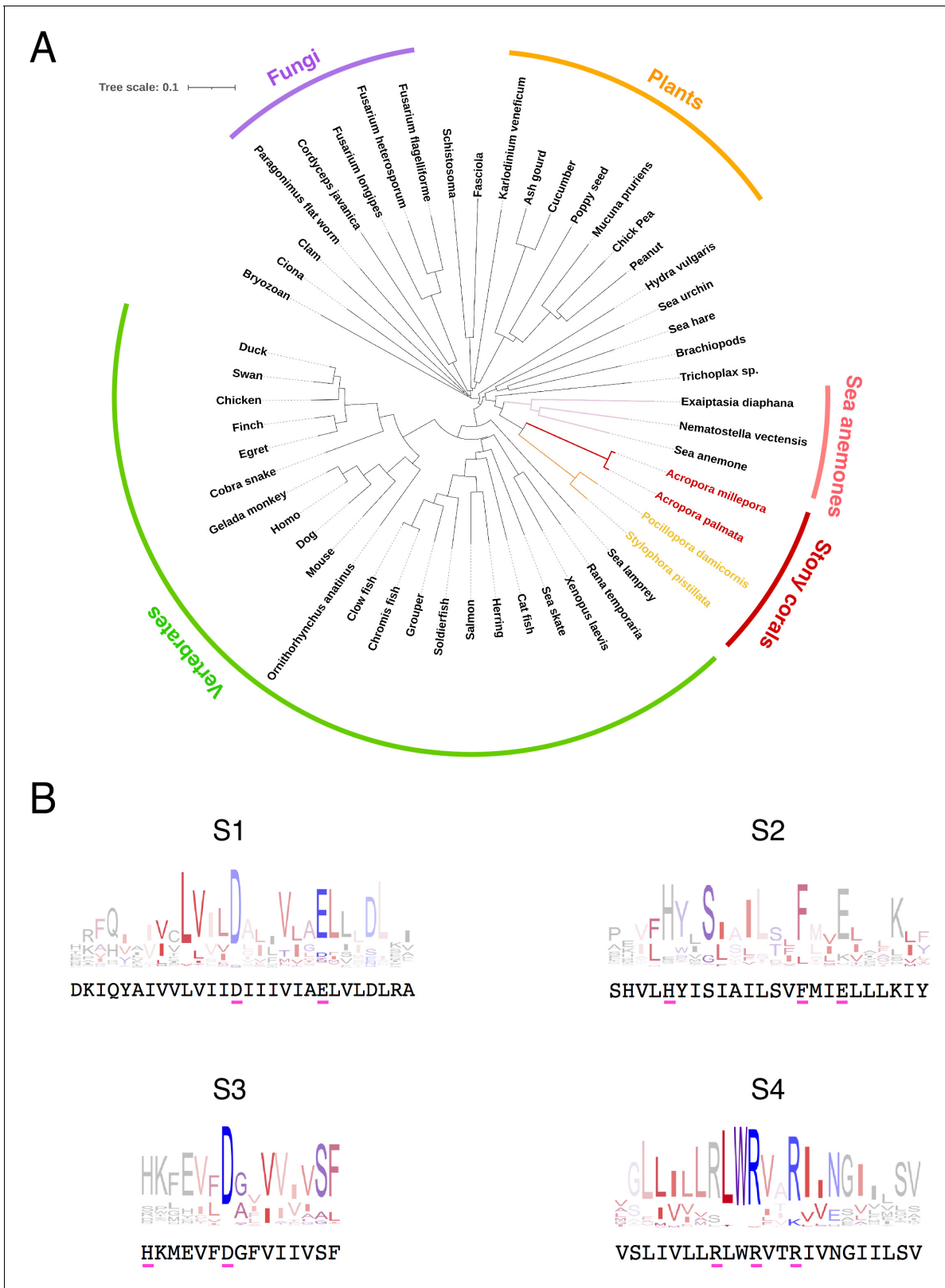


Figure 1. Conservation and phylogenetic relationships of H_v1 channels. (A) The tree obtained from a multiple sequence alignment from H_v1 channels in CLUSTAL-O. Highlighted in red and yellow are the branches containing coral H_v1 sequences. (B) Consensus logo sequences of transmembrane domains of H_v1 channels. The color code indicates the hydrophobicity of each residue, where blue indicates charged residues, red indicates non-polar residues, and other colors indicate either non-polar or charged residues with less conservation.

Figure 1 continued on next page

Figure 1 continued

The online version of this article includes the following source data and figure supplement(s) for figure 1:

Source code 1. Code for generating the tree in **Figure 1**.**Figure supplement 1.** Some characteristics of H_v1 from *Acropora palmata*.**Figure supplement 2.** Comparison of the sequence of AmH_v1 to other voltage-sensing proteins.

In order to study the oligomeric state of the coral H_v1, we performed FRET experiments with the AmH_v1 channel tagged with fluorescent proteins (FPs) as a FRET pair. **Figure 3B** shows that there is significant FRET efficiency between FP-tagged subunits, indicating a very close interaction between monomers. The measured apparent FRET efficiency vs the fluorescence intensity ratio can be fitted to a model where the subunits assemble as a dimer. From this fit, we can estimate a distance between fluorophores of ~60 Å, which is compatible with AmH_v1 being a dimer, at least in HEK293 cells.

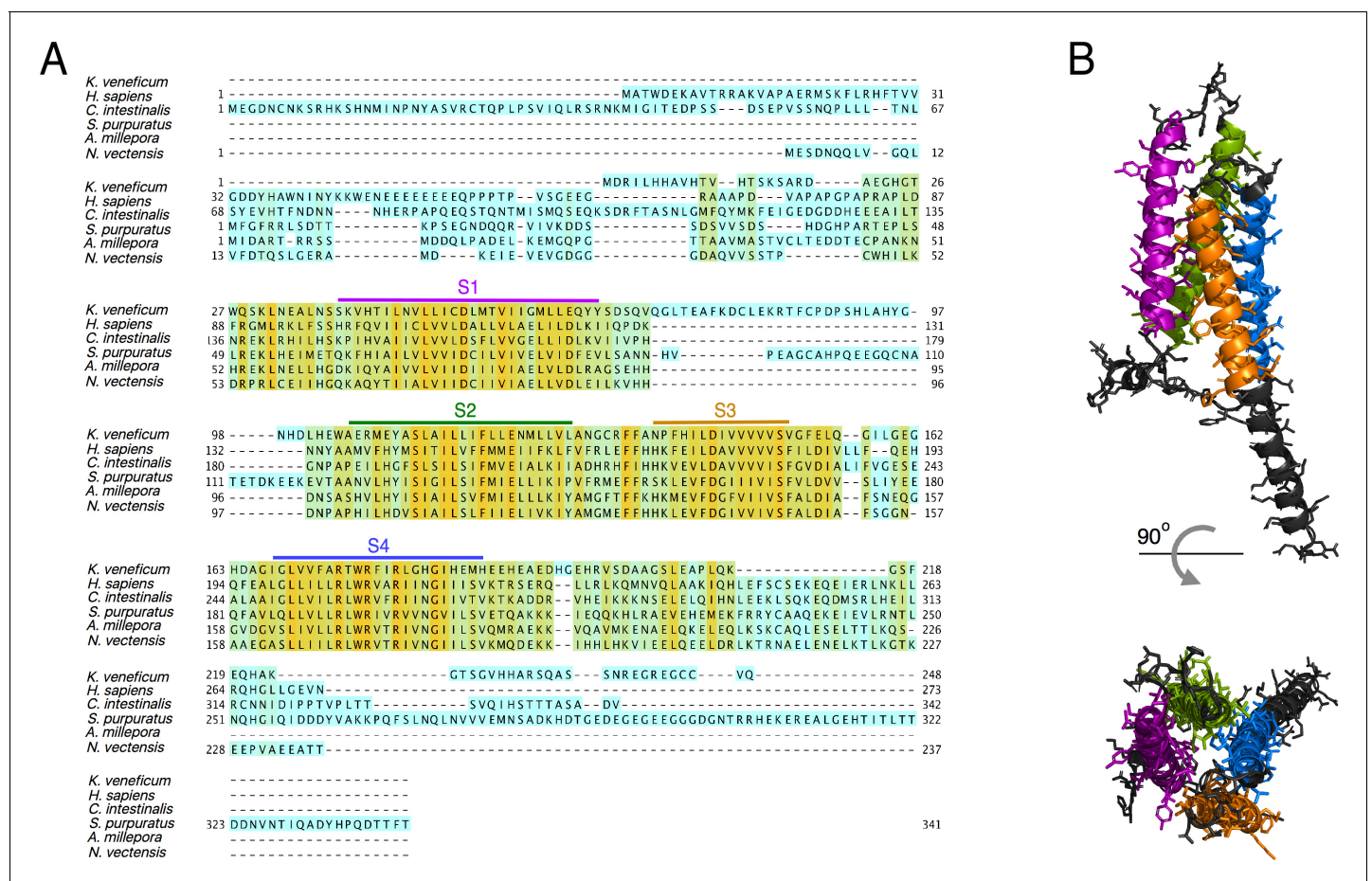


Figure 2. Protein sequence alignment of the AmH_v1 channel with selected H_v1s from other organisms. **(A)** Amino acid sequence alignment of *Acropora millepora* H_v1 (AmH_v1) with other known H_v1 orthologs provided by the CLUSTAL-O algorithm. The predicted transmembrane domains are shown by the colored horizontal lines and letters. The colors highlighting the sequence indicate sequence identity. Orange indicates identical amino acids, and cyan indicates no identity. **(B)** Predicted structural topology of AmH_v1. Transmembrane domains are colored to correspond with the sequences in **(A)**. The top panel is the view parallel to the membrane while the bottom panel is the view from the top (extracellular) side.

The online version of this article includes the following figure supplement(s) for figure 2:

Figure supplement 1. Comparison of the AmH_v1 protein sequence with similar sequences found in other coral species.

Functional expression of AmH_v1 voltage-dependence and kinetics

The cDNA of AmH_v1 was cloned in the pcDNA3 expression vector and transfected into HEK293 cells. Under whole-cell conditions, we recorded large voltage-dependent outward currents. **Figure 4A** shows a family of such currents. The data suggest that these currents were carried mostly by protons, since the reversal potential, measured from a tail current protocol, closely followed the equilibrium potential for protons, as given by the Nernst equation (**Figure 4B**).

The voltage-dependence of channel gating was estimated from a fit of the normalized conductance vs voltage (G-V) to **Equation 1**. The steepness of the curve corresponds to an apparent charge of $\sim 2 e_0$, comparable to other H_v1s under similar recording conditions (**Figure 4C**).

Interestingly, these channels seem to activate rapidly. This is apparent from the current traces, which approach a steady state within a few hundred ms (**Figure 4A**), as quantified in **Figure 4D**. **Equation 3** estimates two parameters, an activation time constant (τ) and a delay (δ). Both the time constant and the delay are similarly voltage-dependent at positive potentials. The existence of a delay in the time course implies that activation is a multiple-state process. The delay magnitude is

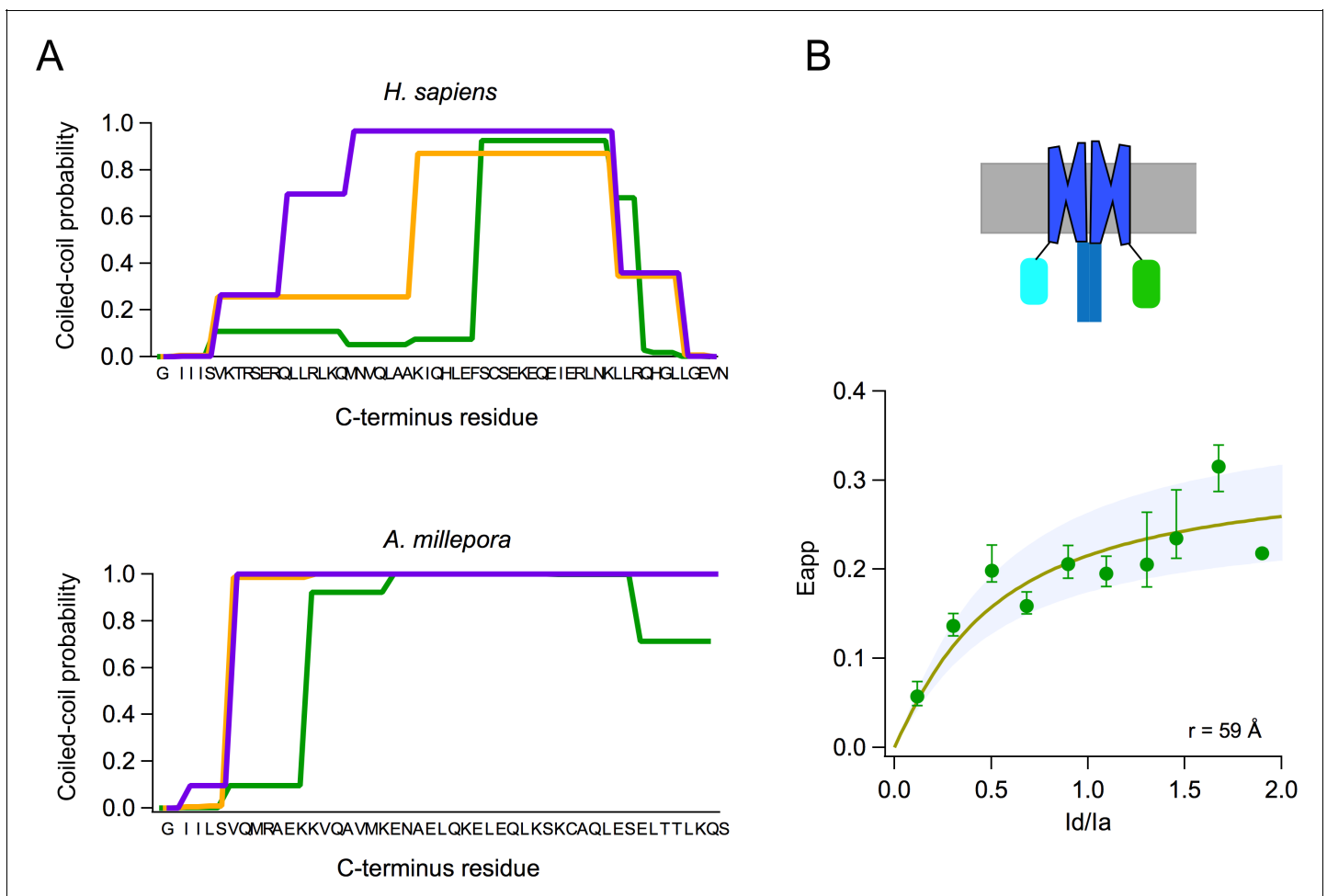


Figure 3. Subunits of the AmH_v1 channel associate to form dimers. (A) Probability of coiled-coil formation per amino acid residue of the C-terminus domain of hH_v1 (top) and *Acropora millepora* H_v1 (AmH_v1) (bottom). The different colors correspond to the three seven-residue windows used by the program to calculate the score. The sequence of the C-terminus is shown in the x-axis. (B) FRET measurement of dimer formation. The apparent FRET measured from 134 cells is plotted as a function of the ratio of donor to acceptor fluorescence (I_d/I_a). Shown is the average and sem for data in I_d/I_a windows of 0.1. The continuous curve is the fit of the data to the prediction of a model that considers random assembly of donor- and acceptor-tagged subunits into a dimer. The separation between the FRET pairs in a dimer is $\sim 60 \text{ \AA}$, according to the model. The upper panel depicts a cartoon of the presumed fluorescent protein (FP)-tagged dimer in the membrane.

The online version of this article includes the following source data for figure 3:

Source data 1. Source data for **Figure 3**.

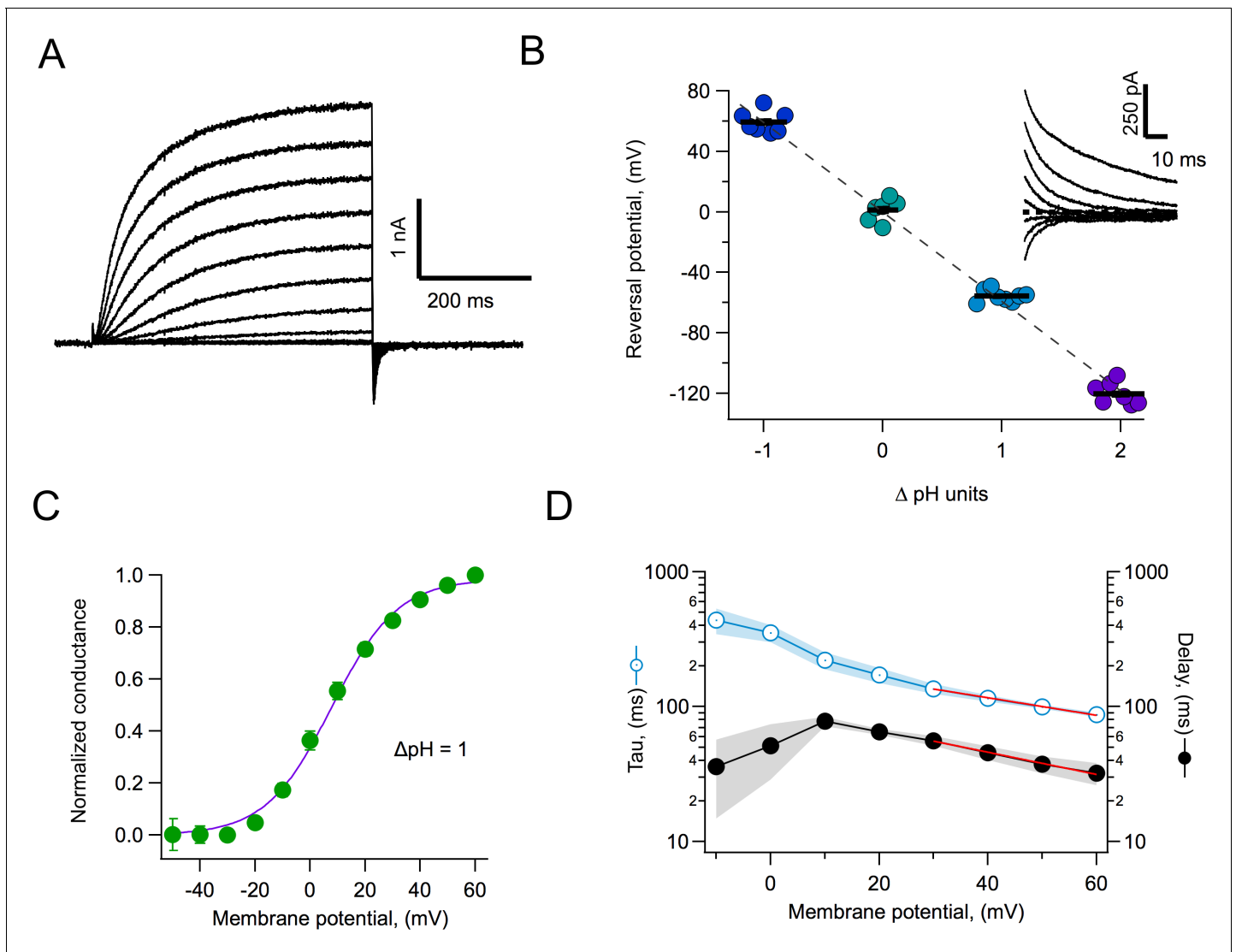


Figure 4. Proton currents mediated by AmH_v1 expressed in HEK293 cells. (A) A typical proton current family elicited by depolarizing pulses from -50 to 60 mV in 10 mV intervals. The duration of the pulses is 500 ms. Linear current components have been subtracted. (B) Reversal potential of currents as a function of the pH gradient. Symbols are individual data and the black horizontal lines are the mean. The dotted line is the expected reversal potential as predicted by the Nernst equation. The inset shows a tail current family from which instantaneous IV curves were extracted to measure the reversal potential. Recordings shown in (A) and (B) were obtained in the whole-cell configuration. (C) Normalized conductance-voltage curve at ΔpH = 1. The purple curve is the fit to **Equation 1** with parameters $V_{0.5} = 7.85$ mV and $q = 2.09 e_0$. Circles are the mean and error bars are the sem ($n = 7$). (D) Kinetic parameters of activation. Activation time constant and delay estimated from fits of current traces to **Equation 2**. Circles are the mean, and the sem is indicated by the shaded areas ($n = 6$). The voltage-dependence of the delay and tau of activation were estimated from a fit to **Equation 3**, which appears as the red curve. Parameters are $\delta(0) = 98.2$ ms and $q_\delta = 0.47 e_0$. The voltage-dependence parameters for tau are $\tau(0) = 212$ ms and $q_\tau = 0.37 e_0$.

The online version of this article includes the following source data for figure 4:

Source data 1. Source data for **Figure 4**.

smaller than the time constant at all voltages, which can be interpreted to mean that the rate-limiting step for opening comes late in the activation pathway (**Schoppa and Sigworth, 1998**).

Comparison to human H_v1 channel properties

Human H_v1 is probably the best characterized of the voltage-gated proton channels (**Musset et al., 2008**); so we compared some of the properties of AmH_v1 with hH_v1. AmH_v1 channels activate faster than their human counterpart. **Figure 5** compares the activation kinetics of these two channels under

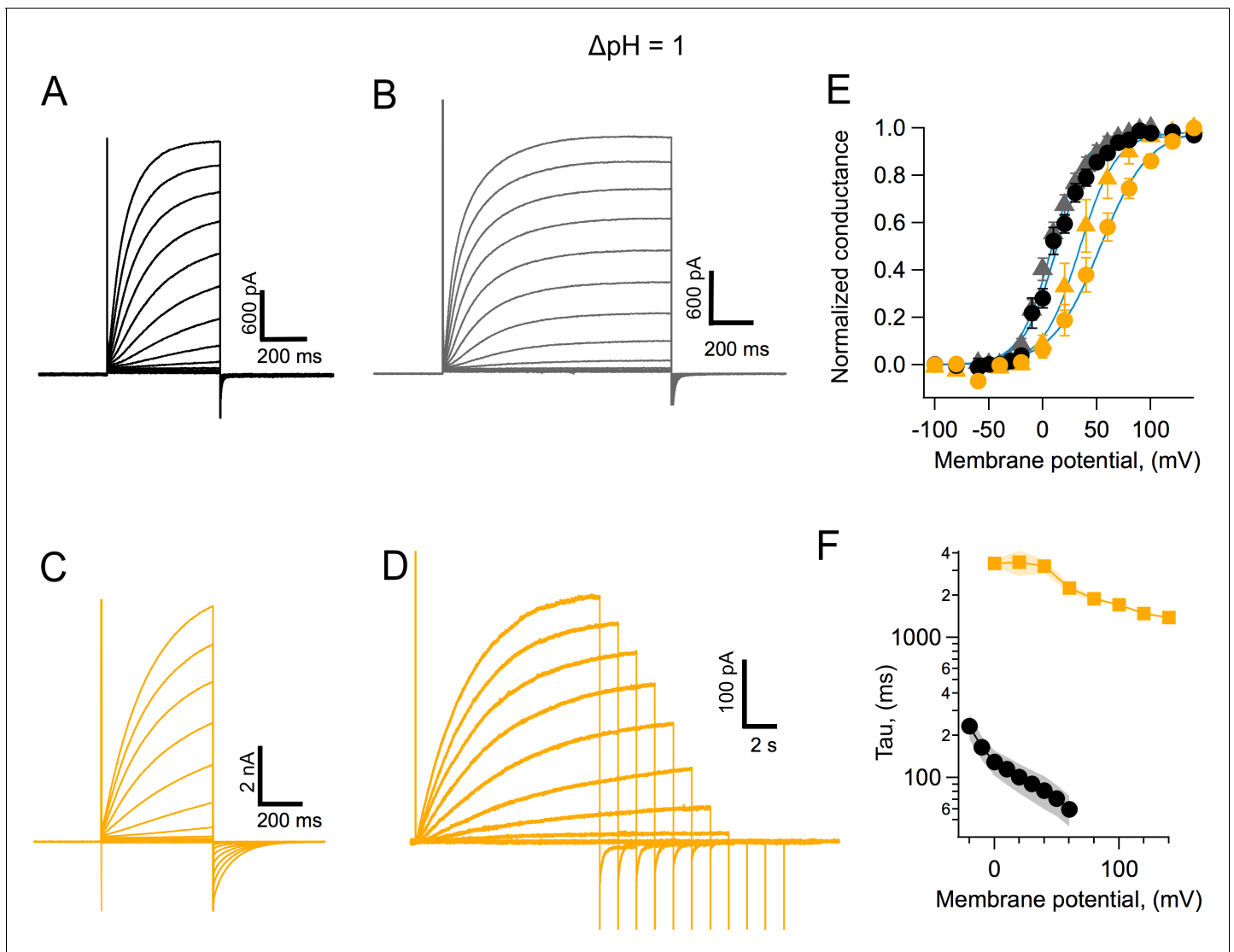


Figure 5. Coral H_v1 channels are faster and activate more readily than their human counterpart. (A) *Acropora millepora* H_v1 (Am H_v1) currents in response to voltage-clamp pulses from -100 to 120 mV and of 500 ms duration. (B) Am H_v1 currents in response to the same voltage-clamp pulses as in (A) but of a longer duration of 800 ms. (C) Currents through h H_v1 channels in response to voltage-clamp pulses from -100 to 120 mV of 500 ms duration, compared with (A). (D) h H_v1 currents recorded with long pulses designed to reach the steady state. Pulses were shortened in duration as depolarizations became larger, in an effort to reduce intracellular proton depletion. Pulses are from -100 to 140 mV. Recordings shown in (A), (B), (C), and (D) were obtained in the whole-cell configuration. (E) Comparison of the conductance-voltage relationship for both channels for short- (circles) and long (triangles)-duration pulses. Black symbols are the mean G/G_{max} for Am H_v1 and yellow symbols for h H_v1 . The error bars are the sem ($n = 3$, for short pulses, both channels, and $n = 4$, for long pulses, both channels). The continuous blue curves are fits to **Equation 1**. The fitted parameters are Am H_v1 , short pulses, $q = 1.62 e_o$, $V_{0.5} = 12.2$ mV; Am H_v1 , long pulses, $q = 1.7 e_o$, $V_{0.5} = 7.7$ mV; h H_v1 , short pulses, $q = 1.11 e_o$, $V_{0.5} = 53.1$ mV; h H_v1 , long pulses, $q = 1.47 e_o$, $V_{0.5} = 34.1$ mV. (F) The activation time constant estimated from fits of currents elicited by long pulses to **Equation 2**. Squares are the mean for h H_v1 and circles, for Am H_v1 . The shaded areas are the sem ($n = 4$, for both channels).

The online version of this article includes the following source data for figure 5:

Source data 1. Source data for **Figure 5**.

the same conditions. Steady state is apparently reached sooner after a voltage pulse in Am H_v1 (**Figure 5A**) when compared to h H_v1 (**Figure 5C**). The slower kinetics of the human ortholog is also evidenced in the more sluggish deactivation tail currents (**Figure 5C**). The range of voltages over which activation happens is also different between the two channels, with the coral H_v1 channel activating at more negative voltages than the human clone (**Figure 5E**; notice that the proton

gradient is such that $\Delta\text{pH} = 1$ and is the same for recordings of both channel types). Even though $\text{AmH}_{\text{v}1}$ activates at more negative voltages, the activation range is still more positive than the proton reversal potential; thus, coral proton currents activated by depolarization, in the steady state and at least as expressed in HEK293 cells, are always outward.

In order to better estimate both kinetics and activation, we performed experiments with longer pulse durations. This is especially important for the very slow activation of the human channel. The resulting currents are shown in **Figure 5B and D**. The normalized conductance for these currents that are closer to steady state are shown in **Figure 5E** by triangles. These G-V curves are shifted to more negative voltages than the G-V from shorter pulses, as expected. The faster kinetics of $\text{AmH}_{\text{v}1}$ is clearly evidenced when the time constant of activation, τ , estimated using fits of the activation time course to **Equation 2**, is compared for coral and human $\text{H}_{\text{v}1}$ channels. $\text{AmH}_{\text{v}1}$ is more than ten-fold faster at 0 mV and over a range of positive voltages (**Figure 5F**).

Effects of the pH gradient on gating

Both native and cloned voltage-gated proton channels are characteristically modulated by the pH gradient (**Cherny et al., 1995; Sasaki et al., 2006; Ramsey et al., 2006**). We carried out experiments to investigate the modulation of the coral $\text{H}_{\text{v}1}$ channels by different pH gradients. We first recorded whole-cell currents at various ΔpH values and estimated the voltage-dependence of the conductance. These G-V curves were fitted to **Equation 2** to obtain the voltage of half activation, $V_{0.5}$, and apparent gating charge, q , which determines the steepness of the fit. As is the case with other $\text{H}_{\text{v}1}$ channels, the $V_{0.5}$ shifts to negative voltages when ΔpH is greater than 0 and to positive voltages when ΔpH is less than 0 (**Figure 6A**). When we plot the $V_{0.5}$ as a function of ΔpH , the relationship seems to be mostly linear over the range of $\Delta\text{pH} -1$ to 2. This relationship is somewhat steeper than the generally observed -40 mV/ ΔpH (**Figure 6B**). We tried to obtain recordings over an extended range of ΔpH values. To this end, we performed inside-out recordings in which the composition of solutions can be better controlled, tends to be more stable, and the size of currents is smaller. However, recordings were unstable at extreme pH values, and we only managed to

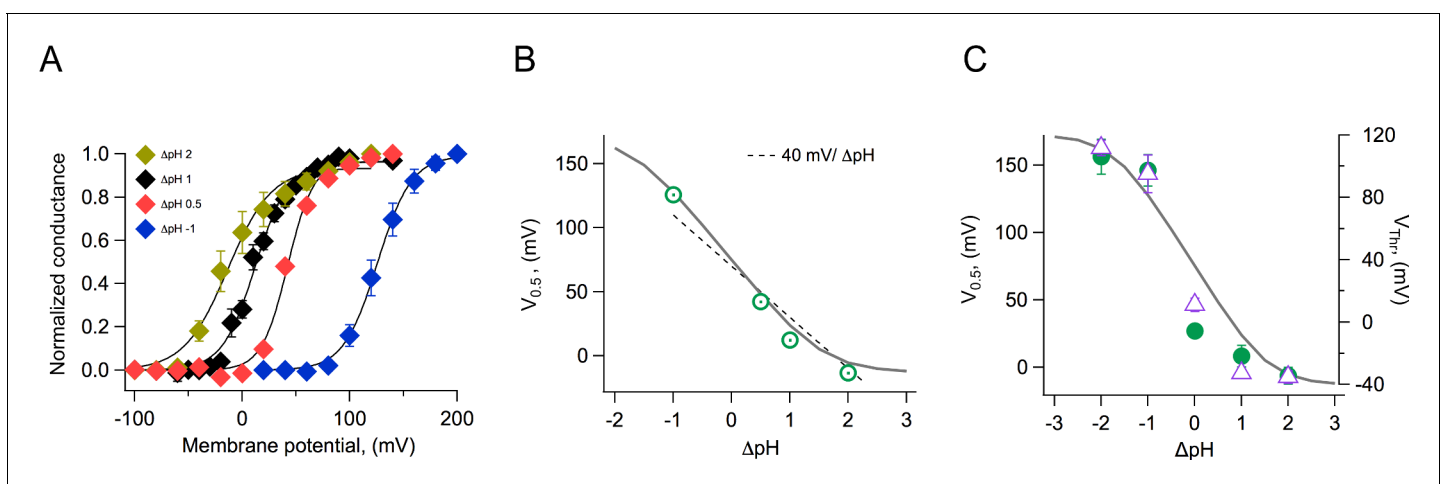


Figure 6. Modulation of channel activation by the pH gradient. (A) Conductance vs voltage relationships obtained at the indicated ΔpH values, from whole-cell recordings of *Acropora millepora* $\text{H}_{\text{v}1}$ ($\text{AmH}_{\text{v}1}$) proton currents. Continuous lines are fits to **Equation 1**. (B) The parameter $V_{0.5}$ was obtained from the fits in (A) and is displayed as a function of ΔpH . The dotted line is the 40 mV/ ΔpH linear relationship. The continuous gray curve is the prediction of the allosteric model (**Figure 7**). (C) Parameters $V_{0.5}$ (green circles) and V_{Thr} (purple triangles) obtained from a different set of inside-out current recordings. Data are mean \pm sem. The continuous gray curve is the same prediction of the allosteric model (**Figure 7**) that is shown in panel (B). The model parameters used to generate the theoretical curve are $E = 5 \times 10^5$, $D = 10^5$, $C = 0.0002$, $K_{\text{v}}(0) = 0.00005$, $q_{\text{g}} = 1.0 e_{\text{o}}$, $\text{p}K_{\text{o}} = 3.4$, and $\text{p}K_{\text{i}} = 7$. The online version of this article includes the following source data, source code and figure supplement(s) for figure 6:

Source data 1. Source data for **Figure 6**.

Figure supplement 1. Equations for the model in **Figure 7**.

Figure supplement 2. Simulations of the voltage- and pH-dependent behavior predicted by the allosteric model.

Figure supplement 2—source code 1. Source code for **Figure 6—figure supplement 2**.

reliably extend the data to a ΔpH value of -2 . **Figure 6C** shows the summary of the inside-out recordings. We have plotted both the $V_{0.5}$ and the threshold voltage, V_{Thr} . To obtain this last parameter, we fitted the exponential rise of the G-V curve to a function of the form

$$G(V) = G' \cdot \exp^{qV/K_B T}$$

V_{Thr} was calculated as the voltage at which the fit reaches 10% of the maximum conductance. The parameter V_{Thr} should be less sensitive than $V_{0.5}$ to the possible change in the proton gradient that can occur with large currents. It is clear from these data that at extreme values, the dependence of $V_{0.5}$ or V_{Thr} on ΔpH deviates from a simple linear relationship and instead appears to saturate at extreme values of ΔpH .

Allosteric model of voltage- and pH-dependent gating

Currently, there is only one quantitative model that has been used to explain ΔpH gating of H_v1 channels (**Cherny et al., 1995**). However, this model is heuristic and does not provide mechanistic insight into the process of proton modulation of the voltage dependence of proton-permeable channels. In order to explain the modulation of the range of activation by the proton gradient, parameterized by the $V_{0.5}$, we developed a structurally inspired allosteric model of voltage and proton activation. As many voltage-sensing domains, H_v1 has two water-occupied cavities exposed to the extracellular and intracellular media (**Ramsey et al., 2010; Islas and Sigworth, 2001; Ahern and Horn, 2005**). Recent evidence suggests that these cavities function as proton-binding sites through networks of electrostatic interactions (**De La Rosa et al., 2018**). In our model, we propose that these two proton-binding sites, one intracellular and one extracellular, allosterically modulate the movement of the voltage-sensing S4 segment and, thus, channel activation in opposite ways. The extracellular site is postulated as inhibitory, while the intracellular site is excitatory, facilitating voltage sensor movement. As a first approximation, we employed a simplified allosteric formalism based on a Monod-Wyman-Changeux (MWC) style model (**Horrigan and Aldrich, 2002; Changeux, 2012**). As a simplifying assumption, in this model we assume that the voltage sensor moves in a single voltage-dependent activation step. We assume the external and internal proton-binding sites have simple protonation given by a single pK_a value. These sites operate as two allosteric modules and are coupled to the voltage sensor according to coupling factors C and D, respectively. These binding sites in turn interact with each other through the coupling factor E. The modular representations of the model are illustrated in **Figure 7A**, while the full model depicting all open and closed states with all permissible transitions and the corresponding equilibrium constants for each transition is shown in **Figure 7B**. Full details of equations derived from these schemes are given in supplementary data.

This allosteric model represents the first attempt at producing a quantitative mechanistic understanding of the interaction of the voltage sensor and protons in H_v1 channels.

From the data shown in **Figure 6C**, it can be seen that the model is capable of reproducing the very steep dependence of $V_{0.5}$ on ΔpH and importantly, the saturation of this relationship at extreme values. Some H_v1 channels from other organisms show a linear dependence of gating over a large range of ΔpH values, while others show a reduced dependence and even saturation over some range of ΔpH (**Thomas et al., 2018**). Our model can explain these different behaviors as different channels having distinct values of pK_a s for the internal or external sites, differences in coupling factors, or differences in the voltage-dependent parameters (**Figure 6—figure supplements 1 and 2**).

Block by Zn^{2+}

The best-characterized blocker of proton channels is the divalent ion zinc (**Cherny et al., 2020; De La Rosa et al., 2018; Qiu et al., 2016**). We performed experiments to determine if AmH_v1 channels are also inhibited by zinc. We found that indeed, extracellular application of zinc in outside-out patches produced inhibition of the channels, reflected in reduced current amplitudes (**Figure 8A**). **Figure 8B** shows average current-voltage (I-V) relationships in the absence and presence of $10 \mu\text{M}$ external zinc. It can be seen that the fraction of current blocked is not the same at every voltage, indicating that this inhibition might be voltage-dependent. The fraction of blocked channels was calculated and is plotted at each voltage along with the I-V curves (**Figure 8B**). It can be clearly seen that inhibition by Zn^{2+} is voltage-dependent. A simple mechanism for voltage-dependent blockage was proposed by **Woodhull, 1973**. This model postulates that a charged blocker molecule interacts

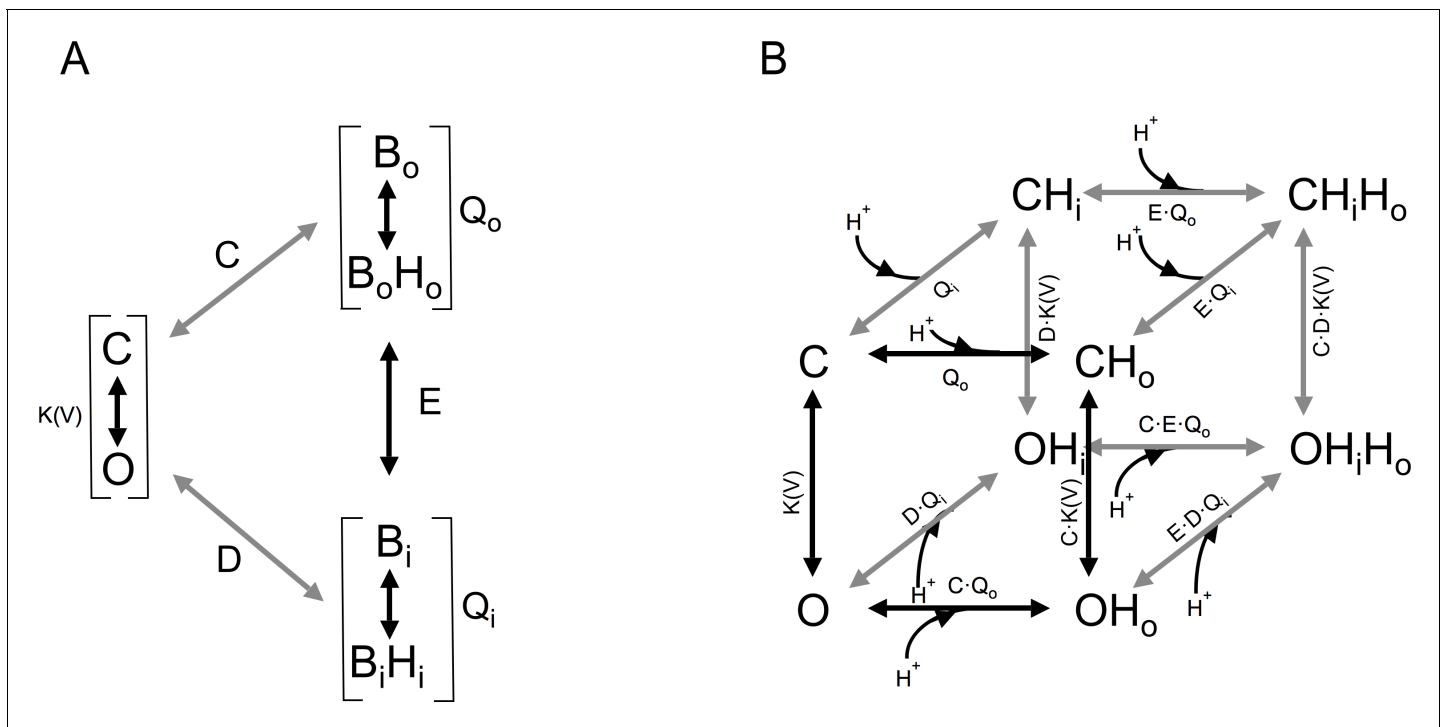


Figure 7. Gating scheme I. (A) Modular representation of a simple Monod-Wyman-Changeux (MWC) model; the channel opening transition is voltage-dependent, with equilibrium constant $K(V)$. B_o and B_i are the unbound states of the extracellular and intracellular proton-binding sites, respectively, and B_oH_o and B_iH_i are the proton-bound states of these binding sites. Q_o and Q_i are equilibrium constants that depend on the pK_a of each of these binding states. C, D, and E are the coupling constants between each of the indicated modules. (B) All the individual states implied in (A) are depicted, along with proton-binding states and the appropriate equilibrium constants. C, closed states, O, open states. OH_x , OH_xH_x and CH_x , CH_xH_x are single or double proton-occupied states, where x can be o for outside or i for inside-facing binding sites.

with a binding site in the target molecule that is located within the electric field. Fitting the data according to this model, and given that zinc is a divalent ion, its apparent binding site is located at a fraction $\delta = 0.2$ of the membrane electric field from the extracellular side (Figure 8B).

Zinc blockage proceeds very fast. At 1 mM, the channels are blocked almost instantaneously, and the inhibition washes off very fast as well (Figure 8C). Finally, we report the dose-response curve (Figure 8D). The inhibition dose-response curve can be fit by a Hill equation (Equation 4) with a slope factor of nearly 0.5 and an apparent dissociation constant, K_D , of 27 μM .

Discussion

A few ion transport mechanisms in reef-building corals have been described, but up to now, no ion channels have been characterized from any scleractinian species. Here we have shown that voltage-gated proton-permeable channels formed by the H_v1 protein are present in corals. In particular, we have cloned these channels from two species of the genus *Acropora*, *A. millepora* and *A. palmata*. It is interesting that the protein sequence of these proteins shows a very high degree of conservation, suggesting that, even when the two species are found in different oceans, they haven't had time to diverge substantially or alternatively; selective pressures on these channels are very similar in both species. The presence of H_v1 sequences in many other species of corals from disparate clades suggests that H_v1 plays an important role in coral physiology.

H_v1 channels are formed by a protein fold that is structurally equivalent to the VSDs of canonical voltage-gated channels (Sasaki et al., 2006; Ramsey et al., 2006). The VSD is formed by a bundle of four antiparallel alpha helices (Takeshita et al., 2014). In some species, it has been shown that H_v1 channels are dimeric (Lee et al., 2008; Mony et al., 2020; Lee et al., 2008). Accordingly, we have also shown here that the Am H_v1 is a dimer. Our FRET results are consistent with the high propensity to form a coiled coil shown by its C-terminal domain.

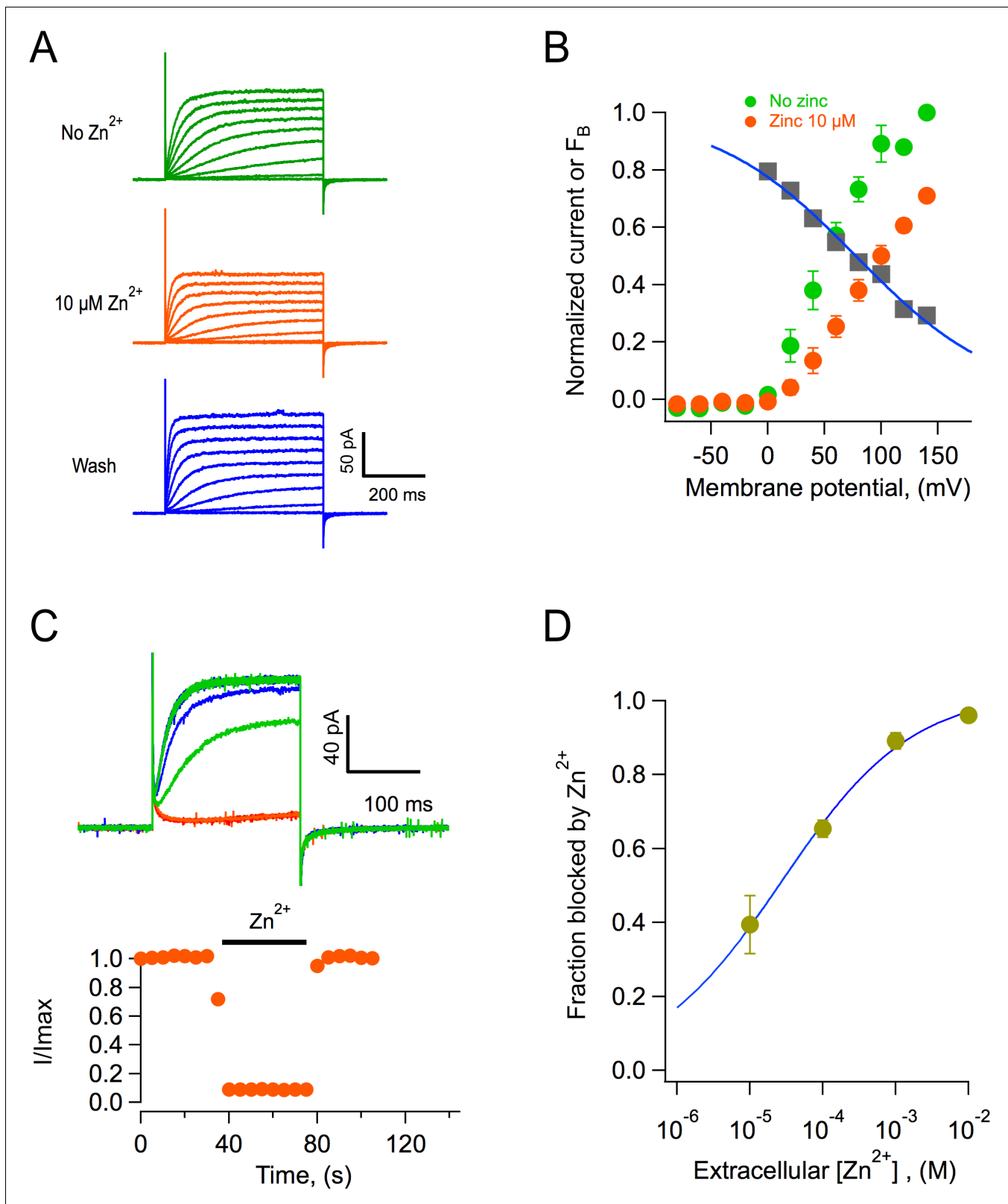


Figure 8. Block of AmH_v1 channels by extracellular zinc. (A) *Acropora millepora* H_v1 (AmH_v1)-mediated currents from an outside-out patch in the absence (top) and presence of 10 μM zinc (middle) and after washing of zinc (bottom). The scale bars apply to the three current families. Voltage pulses lasted 500 ms and were from -80 to 140 mV in 20 mV steps. The $\Delta pH = 1$ with $pH_i = 6$ and $pH_o = 7$. (B) Normalized current-voltage relationships before and in the presence of $10 \mu M$ zinc from four patches as in (A). The gray squares are the ratio $I_{zinc}(V)/I(V)$, which gives the voltage-dependence of Figure 8 continued on next page

Figure 8 continued

the blocking reaction. The blue curve is the fit to the Woodhull equation $F_B = \frac{1}{1 + e^{-\frac{\delta z (V - V_{0.5})}{K_B T}}}$, where F_B is the fraction of the current blocked, δ is the fraction of the electric field where the blocker binds, z is the valence of the blocker, $V_{0.5}$ is the potential where half of the current is blocked, K_B is Boltzmann's constant, and T is the temperature in Kelvin. The fitting parameters are $\delta = 0.19$, $V_{0.5} = 77.6$ mV. (C) The effect of zinc is fast. Application of 1 mM zinc to an outside-out patch produces almost instantaneous block of ~90% of the current. The effect also washes off quickly upon removal of zinc. Trace colors are as in (A). Voltage pulse was 100 mV applied every 5 s. (D) Dose-response curve of zinc block of AmH_v1 obtained at 100 mV. The continuous curve is a fit of the data to Equation 4 with apparent $K_D = 27.4$ μ M and $n = 0.48$. The online version of this article includes the following source data for figure 8:

Source data 1. Source data for Figure 8.

H_v1 channels are different from canonical voltage-gated channels in that both voltage sensing and permeation are mediated through a single protein domain. Voltage sensing is thought to occur through the interaction of charged amino acid side chains with the electric field, leading to the outward movement of the fourth domain or S4, in a similar fashion to other voltage-sensing domains (Carmona et al., 2018; De La Rosa and Ramsey, 2018). This outward movement of the S4 is coupled to protons moving through the VSD in a manner that is not completely understood (Randolph et al., 2016). Most proton-permeable channels seem to have evolved to extrude protons from the cell, and toward this end, their voltage dependence is tightly modulated by the proton gradient between extracellular and intracellular solutions (Cherny et al., 1995).

Our electrophysiology experiments show that these coral channels give rise to proton currents when expressed in HEK293 cells and that they retain the functional characteristics that have been shown to define the class in other species, such as very high selectivity for protons, activation by voltage, and modulation of this activation by the proton gradient. The new channels reported here activate faster than the human H_v1 channel. It has been known that different orthologs of H_v1 activate with varying kinetics. For example, sea urchin, dinoflagellate, and recently, fungal H_v1 channels activate rapidly, while most mammalian counterparts have slow activation rates (Musset et al., 2008; Smith et al., 2011; Zhao and Tombola, 2021). A comparative study suggests that two amino acids in the S3 transmembrane segment are important determinants of kinetic differences between sea urchin and mouse H_v1 (Sakata et al., 2016). The authors suggest that the time course of activation is slow in channels containing a histidine and a phenylalanine at positions 164 and 166, respectively (mouse sequence numbering). The AmH_v1 has a histidine at an equivalent position, 132, and a methionine at 134. It is possible that this last amino acid in AmH_v1 confers most of the fast kinetics phenotype. A separate work has shown that a lack of the amino-terminal segment in human sperm H_v1 also produced fast-activating channels (Berger et al., 2017). Interestingly, the *Acropora* channels have a shorter amino-terminal sequence, which could also contribute to their fast kinetics.

One of the most interesting characteristics found in these new proton channels is their modulation by the proton gradient. As opposed to other H_v1 channels, we can observe a trend toward saturation of the $V_{0.5}$ for activation as a function of Δ pH at extreme values of this variable. A tendency toward saturation of the $V_{0.5}$ - Δ pH relationship has been observed in mutants of the hH_v1 channel (Cherny et al., 2015) or at negative values of Δ pH for a snail H_v1 (Thomas et al., 2018), but it seems it can be fully appreciated in AmH_v1. Since our model explains the observation of saturation of voltage gating at extreme values of Δ pH as a consequence of the existence of two saturable sites for proton binding, we attribute this behavior to the large separation of pK_a values for the extracellular and intracellular proton-binding sites. Thus, channels that do not show saturation might have sites with well-separated and differing pK_a values. Evolutionary fine tuning of these pK_a values will produce channels with pH activation in ranges adapted to their physiological function.

It is important to point out that the external and internal proton-binding sites can be part of the voltage sensor itself. We envision these sites as being formed not by distinct protonatable amino acids but by a network of electrostatic interactions between amino acids in S4 and other transmembrane segments. In this context, the pK_a values of the sites in our model do not reflect pK_a s of individual amino acids but of the whole proton-binding site. Recent works by Carmona et al., 2021 and Schladt and Berger, 2020 suggest that voltage sensing is directly responsible for pH gating. These authors suggest that the energy of the pH gradient is part of the free energy needed for

voltage-sensor movement. This purely energetic statement is encompassed in our model as the coupling factors between voltage-sensor movement and proton binding, which are in fact energetic factors.

In our model, the strength of allosteric coupling of these sites and the voltage sensor determines if saturation is observed over a short or extended range of ΔpH values and the range of values of $V_{0.5}$ that a particular channel can visit. Coupling also determines the value of the slope of the ΔpH vs $V_{0.5}$ curve. Values larger or smaller than the typical ~ 40 mV/pH are obtained as a consequence of strong or weak coupling between binding and voltage-sensor movement, respectively (**Figure 6—figure supplement 2**). Our model should provide a framework to better understand the gating mechanisms in future work.

It is clear that more complicated models, with a larger number of voltage-dependent and -independent steps (**Villalba-Galea, 2014**) and coupling to protonation sites, should be the next step to improve data fitting and explore voltage- and proton-dependent kinetics. In particular, these types of models can help explain mutagenesis experiments exploring the nature of the protonation sites. For example, **Villalba-Galea, 2014** proposed the existence of a voltage-independent step in $H_{\text{v}}1$ gating, and this can be easily incorporated in the model proposed here, as is the fact that $hH_{\text{v}}1$ and $AmH_{\text{v}}1$ channels are dimers. The present form of the allosteric model has a single subunit. Since gating in dimeric channels seems to be cooperative, allosteric models have the advantage that cooperativity between subunits can be handled naturally by including coupling between two voltage sensors.

$H_{\text{v}}1$ proton channels seem fundamental in handling fluctuations in intracellular pH and take part in several well-characterized physiological processes that depend on proton concentration changes, such as intracellular pH regulation, sperm flagellum beating, reactive oxygen species production and bacterial killing in immune cells, initiation of bioluminescence in single-celled algae, and so on (**Castillo et al., 2015**).

What is the function of voltage-gated proton channels in corals? The deposition of a CaCO_3 exoskeleton is one of the main defining characteristics of scleractinians; however, the ionic transport mechanisms involved in this process are mostly unknown. In order for aragonite precipitation to occur favorably, the pH of the calicoblastic fluid, right next to the skeleton, is maintained at high levels, between 8.5 and 9 and above the pH of sea water (**Le Goff et al., 2017**). It has been posited that corals control this pH via vectorial transport of protons to the gastrodermal cavity (**Jokiel, 2013**). Since proton transport away from the site of calcification would incur a drastically lower intracellular pH in the cells of the aboral region, we propose that, given their ability to rapidly regulate the intracellular pH (**De-la-Rosa et al., 2016**), $H_{\text{v}}1$ proton channels contribute by transporting protons from the cells. Thus, these proton channels could be a major component of the mechanisms of intracellular pH regulation in corals. Given that the activation range of $H_{\text{v}}1$ is controlled by the pH gradient, a large intracellular acidification would facilitate opening of these channels at the resting potential of cells, which is presumably negative.

The finding that coral $H_{\text{v}}1$ channels retain their sensitivity to Zn^{2+} opens the possibility of using this ion as a pharmacological tool to study the role of proton channels in pH homeostasis. It is interesting that a recent report has shown detrimental effects of zinc supplementation on coral growth (**Tijssen et al., 2017**), a result that could be explained by zinc inhibition of $H_{\text{v}}1$.

The physiological role of $H_{\text{v}}1$ channels in corals might be essential in the response of these organisms to ocean acidification. Although further research is needed to understand the cellular and subcellular localization of these channels, we theorize that as the pH of sea water acidifies, gating of $H_{\text{v}}1$ should require stronger depolarization, thus hindering its capacity to transport protons from the cell. This will contribute to a diminished calcification rate and less aragonite saturation of the CaCO_3 skeleton. It would be interesting and important to study the effects of acidification on $H_{\text{v}}1$ physiology and pH regulation in corals *in vivo*. Essentially nothing is known about the electrophysiological properties of coral cells. This report represents the first time that an ion channel has been cloned and characterized in any coral and should open a new avenue of research, such as uncovering the cellular and possible subcellular localization of these channels and carefully measuring their physiological role *in vivo*.

Materials and methods

Identification of H_v1 sequences and cloning

Blast searches of the transcriptome of the Indo-Pacific coral *A. millepora* (Moya *et al.*, 2012) detected four sequences that we identified as belonging to a putative proton-permeable channel. The GenBank accession numbers for these are XM_015907823.1, XM_015907824.1, XM_029346499.1, and XM_029346498.1. We designed two pairs of oligonucleotides to amplify two of these sequences (Table 1). Total RNA was extracted from the tissue obtained from a fragment of *A. millepora* acquired from a local salt-water aquarium provider (Reefservices, Mexico City). RNA was extracted by dipping the whole fragment for 2 min in 5 ml of solution D (4 M guanidinium thiocyanate, 25 mM sodium citrate, 5% sarkosyl, and 0.1 M 2-mercaptoethanol). After incubation, the tissue was removed by gently pipetting the solution for 2 min. At this point, the calcareous skeleton was removed and RNA extraction continued according to Chomczynski and Sacchi, 1987. Total RNA (1 µg) from *A. millepora* was used for reverse transcription polymerase chain reaction (RT-PCR), employing oligo dT and SuperScripII reverse transcriptase (Invitrogen, USA). cDNA obtained from RT-PCR was used in three PCRs using oligos (1) AcHv1Nter5' and 3', (2) AcHv1Cter5' and 3', and (3) AcHv1Nter5' and AcHv1Cter3' (Table 1). The Platinum Pfx DNA polymerase (Invitrogen) was used for amplification according to the manufacturer's instructions. 1 µl of Taq DNA polymerase (Invitrogen, USA) was used for 10 min at 72°C to add a poly-A tail at 5' and 3' ends and facilitate cloning into the pGEM-T vector.

The PCR 3 gave rise to a full open reading frame (ORF) containing AmH_v1. New oligos, AcHv1Nter5' and AcHv1Cter3', containing restriction sites Kpn1 and Not1, respectively, were used to re-amplify the ORF in pGEM-T and subclone it into pcDNA3.1 for heterologous expression.

The H_v1 channel from *A. palmata* was cloned from a fragment of an adult specimen collected from the Limones Reef off of Puerto Morelos, Mexico. RNA extraction from small coral pieces was carried out by flash freezing in liquid nitrogen and grinding the frozen tissue. All other cloning procedures were as for *A. millepora*. All clones and DNA constructs were confirmed by automatic sequencing at the Molecular Biology Facility of the Instituto de Fisiología Celular at UNAM.

Heterologous expression of AmH_v1

All electrophysiological and FRET experiments were carried out in HEK293 cells heterologously expressing the specified clone or DNA construct. HEK293 cells were acquired from ATCC (Gaithersburg, MD, USA) and were found to be free of mycoplasma infection using a PCR-based detection kit (Sigma-Aldrich, USA). Cells were grown on 100 mm culture dishes with 10 ml of Dulbecco's Modified Eagle Medium (DMEM, Invitrogen) containing 10% fetal bovine serum (FBS) (Invitrogen, USA) and 100 units/ml-100 µg/ml of penicillin-streptomycin (Invitrogen, USA), incubated at 37°C in an incubator with 5.2% CO₂ atmosphere. When cells reached 90% confluence, the medium was removed, and the cells were treated with 1 ml of 0.05% trypsin-ethylenediaminetetraacetic acid (EDTA) (Invitrogen, USA) for 5 min. Subsequently, 1 ml of DMEM with 10% FBS was added. The cells were mechanically dislodged and reseeded in 35 mm culture dishes over 5x5 mm coverslips for electrophysiology or in 35 mm glass bottom dishes for FRET experiments. In both cases, 2 ml of complete medium was used. Cells at 70% confluence were transfected with pcDNA3.1-AmH_v1 prepared from a plasmid midiprep, using jetPEI transfection reagent (Polyplus Transfection, France). For patch-clamp experiments, pEGFP-N1 (BD Biosciences Clontech, USA) was cotransfected with the channel DNA to

Table 1. Oligonucleotides used to clone amino- and carboxy-terminal partial sequences of AmH_v1 from total reverse-transcribed mRNA from *A. millepora*.

Oligo name	Sequence
AcHvNt5'	ATGATTGATGCAAGAACCAGACGATCGAGCATGGATGAT
AcHvNt3'	TGATCCTGCTCTCAAGTCAAGAACCAACTCAGCAATGAC
AcHvCt5'	ATGGGATTACATTTTCAAGCACAAATGGAGGTGTTT
AcHvCt3'	TCAGCTTTGTTTTAATGTTGTCAATTCAGACTCCAACCTG

visualize successfully transfected cells via their green fluorescence. Electrophysiological recordings were done 1 or 2 days after transfection.

FRET measurement of stoichiometry

In order to measure the stoichiometry of subunit interaction employing FRET, we constructed fusion proteins between AmH_v1 and mCerulean and mCitrine FPs, to be used as the donor and acceptor, respectively. The FPs were fused to the N-terminus of the channel in order to disrupt as little as possible the C-terminus-mediated interaction. These constructs were transfected into HEK293 cells as described above. The apparent FRET efficiency between FP-containing constructs, E_{app} , was measured via sensitized emission of the acceptor, employing the spectral-FRET method (De-la-Rosa et al., 2013; Zheng et al., 2002). Fluorescence was measured in a home-modified TE-2000U inverted epifluorescence microscope (Nikon, Japan). The excitation light source was an Argon Ion laser (Spectra-Physics, Germany) mainly producing light at 458, 488, and 514 nm; the laser beam was focused and then collimated using a 3 mm ball lens and a 50-mm focal length planoconvex lens. Collimated light is steered with a mirror and then is focused into the objective back focal plane by a 300-mm focal length achromatic lens.

Cells were imaged with a Nikon 60x oil immersion objective (numerical aperture 1.4). The detection arm of the microscope is coupled to a spectrograph (Acton Instruments, USA) and an EM-CCD camera (Ixon Ultra, Andor, Ireland) controlled by Micromanager software (Edelstein et al., 2014). Excitation was achieved with appropriate excitation filters (Chroma, Vermont, USA) for mCerulean (458 nm) and mCitrine (488 nm). The emission filter was a long-pass filter in order to collect the full emission spectrum of the FRET pair. Apparent FRET efficiency is plotted as a function of the fluorescence intensity ratio ($I_{donor}/I_{acceptor}$). This relationship can be fitted with models of subunit association with a fixed stoichiometry, according to De-la-Rosa et al., 2013.

Electrophysiology

All chemicals for solutions were acquired from Sigma-Aldrich (Mexico). Proton current recordings were made from HEK293 cells expressing pCDNA3.1-AmH_v1 in the inside-out, whole-cell, and outside-out configurations of the patch-clamp recording technique. For whole-cell and inside-out recordings, the extracellular solution (bath and pipette, respectively) was (in mM) 80 tetramethylammonium and methanesulfonic acid (TMA-HMESO₃), 100 buffer ((2-(N-morpholino)ethanesulfonic acid (MES): pH 5.5, 6.0, and 6.5; 4-(2-hydroxyethyl)-1-piperazineethanesulfonic acid (HEPES): pH 7.0, 7.5), 2 CaCl₂, 2 MgCl₂, and pH-adjusted N-methyl-d-glucamine/tetramethylammonium hydroxide (NMDG/TMA-OH) and HCl. The intracellular solution (pipette and bath, respectively) was (in mM) 80 TMA-HMESO₃, 100 buffer (MES: pH 5.5, 6.0, and 6.5; HEPES: pH 7.0, 7.5), 1 ethylene glycol tetraacetic acid (EGTA), and pH-adjusted NMDG/TMA-OH and HCl.

Macroscopic currents were low-pass filtered at 2.5 kHz, sampled at 20 kHz with an Axopatch 200B amplifier (Axon Instruments, USA) using an Instrutech 1800 AD/DA board (HEKA Elektronik, Germany) or an EPC-10 amplifier (HEKA Elektronik, Germany). Acquisition control and initial analysis were done with PatchMaster software. Pipettes for recording were pulled from borosilicate glass capillaries (Sutter Instrument, USA) and fire-polished to a resistance of 4–7 M Ω when filled with recording solution for inside- and outside-out recordings and 1–3 M Ω for the whole-cell recording. The bath (intracellular) solutions in inside-out patches were changed using a custom-built rapid solution changer. For whole-cell recordings, all the bath solution was exchanged to manipulate pH. In some recordings, linear current components were subtracted using a p/4 subtraction protocol.

Conditions for recording zinc effects

The effect of zinc was evaluated in outside-out patches at a Δ pH of 1. The bath solution composition was (in mM) 100 TMA-HMESO₃, 100 HEPES, 8 HCl, 2 CaCl₂, 2 MgCl₂, and the indicated concentration of ZnCl₂. The pipette solution was (in mM) 100 TMA-MESO₃, 100 MES, 8 HCl, 10 EGTA, and 2 MgCl₂. Both solutions were adjusted to pH 7 and pH 6, respectively, with TMA-OH/HCl. Patches were placed in front of a perfusion tube that was gravity-fed with the appropriate solution. Tubes were changed with a home-built rapid perfusion system.

Data analysis

Conductance, G , was calculated from I-V relations assuming ohmic instantaneous currents, according to

$$I(V) = G \cdot (V - V_{rev})$$

The normalized G-V relations were fit to a Boltzmann function according to **Equation 1**,

$$\frac{G}{G_{max}} = \frac{1}{1 + \exp\left(\frac{q(V - V_{0.5})}{K_B T}\right)} \quad (1)$$

Here, $V_{0.5}$ is the voltage at which $G/G_{max} = 0.5$, q is the apparent gating charge (in elementary charges, e_0), K_B is the Boltzmann constant, and T is the temperature in Kelvin (22°C).

The time constant of activation was estimated via a fit of the second half of currents to the equation

$$I(t) = I_{ss} \cdot \left(1 - e^{\left(\frac{-(t-\delta)}{\tau}\right)}\right) \quad (2)$$

where I_{ss} is the amplitude of the current at steady state, δ is the delay of the exponential with respect to the start of the voltage pulse, and τ is the time constant, both with units of ms. The voltage-dependence of δ and τ was estimated from a fit to equation

$$k(V) = k(0)e^{(-Vq_i/K_B T)} \quad (3)$$

where i stands for δ or τ and $k(0)$ is the value of either parameter at 0 mV.

Currents in the presence of zinc were normalized to the current before application of the ion to obtain a normalized fraction of current blocked as $F_B = 1 - I/I_{max}$. The zinc dose-response curve was fitted to Hill's equation in the form

$$F_B = \frac{1}{1 + \left(\frac{K_D}{[Zn^{2+}]_o}\right)^{n_H}} \quad (4)$$

where K_D is the apparent dissociation constant, $[Zn^{2+}]_o$ is the extracellular zinc concentration, and n_H is the Hill coefficient.

Acknowledgements

We would like to thank Itzel A Llorente for the excellent technical assistance. We also thank Gerardo Coello from IFC-UNAM for help with analysis of coral transcriptomes. This work was funded in part by grant no. IN215621 from DGAPA-PAPIIT-UNAM to LDI, grant no. 247765 to ATB, and grant no. IN200720 to TR. EM was funded by Conacyt-Fronteras en la Ciencia Grant No. 2.

Additional information

Competing interests

Leon D Islas: Reviewing editor, *eLife*. The other authors declare that no competing interests exist.

Funding

Funder	Grant reference number	Author
Universidad Nacional Autónoma de México	IN215621	Leon D Islas
Universidad Nacional Autónoma de México	IN200720	Tamara Rosenbaum
Universidad Nacional Autónoma de México	IN247765	Anastazia T Banaszak

The funders had no role in study design, data collection and interpretation, or the decision to submit the work for publication.

Author contributions

Gisela Rangel-Yescas, Resources, Investigation, Project administration, Writing - review and editing; Cecilia Cervantes, Miguel A Cervantes-Rocha, Esteban Suárez-Delgado, Formal analysis, Investigation, Methodology, Writing - review and editing; Anastazia T Banaszak, Resources, Funding acquisition, Writing - review and editing; Ernesto Maldonado, Resources, Funding acquisition, Methodology, Writing - review and editing; Ian Scott Ramsey, Conceptualization, Writing - review and editing; Tamara Rosenbaum, Resources, Software, Formal analysis, Validation, Visualization, Writing - original draft, Writing - review and editing; Leon D Islas, Conceptualization, Resources, Data curation, Software, Formal analysis, Supervision, Funding acquisition, Validation, Investigation, Visualization, Methodology, Writing - original draft, Project administration, Writing - review and editing

Author ORCIDs

Miguel A Cervantes-Rocha  <http://orcid.org/0000-0001-7401-7567>

Esteban Suárez-Delgado  <http://orcid.org/0000-0003-0147-3451>

Anastazia T Banaszak  <http://orcid.org/0000-0002-6667-3983>

Ernesto Maldonado  <http://orcid.org/0000-0002-9627-967X>

Ian Scott Ramsey  <http://orcid.org/0000-0002-6432-4253>

Leon D Islas  <https://orcid.org/0000-0002-7461-5214>

Decision letter and Author response

Decision letter <https://doi.org/10.7554/eLife.69248.sa1>

Author response <https://doi.org/10.7554/eLife.69248.sa2>

Additional files

Supplementary files

- Transparent reporting form

Data availability

All data generated or analyzed during this study are included in the manuscript and supporting files. We have provided an Excel file with source data used for figures.

The following datasets were generated:

Author(s)	Year	Dataset title	Dataset URL	Database and Identifier
Rangel-Yescas G, Cervantes C, Cervantes-Rocha MA, Suárez-Delgado E, Banaszak AT, Maldonado E, Ramsey IS, Rosenbaum T, Islas LD	2021	Acropora millepora Hv1 proton-channel nucleotide sequence.	https://www.ncbi.nlm.nih.gov/nucleotide/MZ029046	NCBI GenBank, MZ029046
Rangel-Yescas G, Cervantes C, Cervantes-Rocha MA, Suárez-Delgado E, Banaszak AT, Maldonado E,	2021	Acropora palmata Hv1 proton-channel nucleotide sequence	https://www.ncbi.nlm.nih.gov/nucleotide/MZ029047	NCBI GenBank, MZ029047

Ramsey IS,
Rosenbaum T, Islas
LD

The following previously published datasets were used:

Author(s)	Year	Dataset title	Dataset URL	Database and Identifier
Australian National University	2019	Title voltage-gated hydrogen channel 1-like [Acropora millepora]	https://www.ncbi.nlm.nih.gov/protein/1666377134/	NCBI Protein, XP_029202331.1
King Abdullah University of Science and Technology	2017	voltage-gated hydrogen channel 1-like [Stylophora pistillata]	https://www.ncbi.nlm.nih.gov/protein/XP_022795192.1	NCBI Protein, XP_022795192.1
University of Miami	2018	voltage-gated hydrogen channel 1-like [Pocillopora damicornis]	https://www.ncbi.nlm.nih.gov/protein/XP_027057117.1	NCBI Protein, XP_027057117.1
QUT	2019	voltage-gated hydrogen channel 1-like [Actinia tenebrosa]	https://www.ncbi.nlm.nih.gov/protein/XP_031564162.1	NCBI Protein, XP_031564162.1
Joint Genome Institute (JGI)	2017	voltage-gated hydrogen channel 1 [Nematostella vectensis]	https://www.ncbi.nlm.nih.gov/protein/XP_001626501.1	NCBI Protein, XP_001626501.1
JCVI	2009	PREDICTED: voltage-gated hydrogen channel 1-like [Hydra vulgaris]	https://www.ncbi.nlm.nih.gov/protein/828190613/	NCBI Protein, XP_012554112.1
Anon	2012	voltage-gated proton channel [Strongylocentrotus purpuratus]	https://www.ncbi.nlm.nih.gov/protein/187282419/	NCBI Protein, NP_01119779.1
Anon	2006	voltage-gated hydrogen channel 1 [Ciona intestinalis]	https://www.ncbi.nlm.nih.gov/protein/NP_001071937.1	NCBI Protein, NP_001071937.1
Vertebrate Genomes Project	2020	voltage-gated hydrogen channel 1 [Petromyzon marinus]	https://www.ncbi.nlm.nih.gov/protein/XP_032803138.1	NCBI Protein, XP_032803138.1
Wellcome Sanger Institute	2021	voltage-gated hydrogen channel 1 [Rana temporaria]	https://www.ncbi.nlm.nih.gov/protein/XP_040202566.1	NCBI Protein, XP_040202566.1
Naturalis Biodiversity Center	2013	Voltage-gated hydrogen channel 1, partial [Ophiophagus hannah]	https://www.ncbi.nlm.nih.gov/protein/565320699/	NCBI Protein, ETE71598.1
Baylor College of Medicine	2005	voltage-gated hydrogen channel 1-like isoform X1 [Strongylocentrotus purpuratus]	https://www.ncbi.nlm.nih.gov/protein/XP_030847861.1	NCBI Protein, XP_030847861.1
China Agricultural University	2010	Voltage-gated hydrogen channel 1, partial [Anas platyrhynchos]	https://www.ncbi.nlm.nih.gov/protein/EOA95241.1	NCBI Protein, EOA95241.1
Anon	2002	voltage-gated hydrogen channel 1 [Xenopus laevis]	https://www.ncbi.nlm.nih.gov/protein/NP_001088875.1	NCBI Protein, NP_001088875.1
KAUST	2015	Voltage-gated hydrogen channel 1 [Exaiptasia diaphana]	https://www.ncbi.nlm.nih.gov/protein/KXJ27230.1	NCBI Protein, KXJ27230.1

The University of Queensland	2020	voltage-gated hydrogen channel 1 [Cygnus atratus]	https://www.ncbi.nlm.nih.gov/protein/XP_035421542.1	NCBI Protein, XP_035421542.1
Anon	2005	voltage-gated hydrogen channel 1 [Gallus gallus]	https://www.ncbi.nlm.nih.gov/protein/NP_001025834.1	NCBI Protein, NP_001025834.1
Vertebrate Genomes Project	2019	voltage-gated hydrogen channel 1 [Ornithorhynchus anatinus]	https://www.ncbi.nlm.nih.gov/protein/XP_028914661.1	NCBI Protein, XP_028914661.1
University of Washington	2018	voltage-gated hydrogen channel 1 [Theropithecus gelada]	https://www.ncbi.nlm.nih.gov/protein/XP_025257726.1	NCBI Protein, XP_025257726.1
Anon	2002	HVCN1 protein [Homo sapiens]	https://www.ncbi.nlm.nih.gov/protein/AAH07277.1	NCBI Protein, AAH07277.1
The Roslin Institute	2020	voltage-gated hydrogen channel 1 isoform X1 [Canis lupus familiaris]	https://www.ncbi.nlm.nih.gov/protein/XP_038292573.1	NCBI Protein, XP_038292573.1
Anon	2021	voltage-gated hydrogen channel 1 [Mus musculus]	https://www.ncbi.nlm.nih.gov/protein/NP_001035954.1	NCBI Protein, NP_001035954.1
Beijing Genomics Institute	2003	voltage-gated hydrogen channel 1 [Mus musculus]	https://www.ncbi.nlm.nih.gov/protein/XP_005424087.1	NCBI Protein, XP_005424087.1
College of Medicine and Forensics, Xi'an Jiaotong University	2014	voltage-gated hydrogen channel 1 [Egretta garzetta]	https://www.ncbi.nlm.nih.gov/protein/XP_009633183.1	NCBI Protein, XP_009633183.1
Vertebrate Genomes Project	2020	voltage-gated hydrogen channel 1 [Amblyraja radiata]	https://www.ncbi.nlm.nih.gov/protein/XP_032899181.1	NCBI Protein, XP_032899181.1
US Department of Agriculture, Agriculture Research Service	2018	voltage-gated hydrogen channel 1 [Fusarium longipes]	https://www.ncbi.nlm.nih.gov/protein/RGP61076.1	NCBI Protein, RGP61076.1
US Department of Agriculture, Agriculture Research Service	2018	voltage-gated hydrogen channel 1 [Fusarium flagelliforme]	https://www.ncbi.nlm.nih.gov/protein/RFN53390.1	NCBI Protein, RFN53390.1
US Department of Agriculture, Agriculture Research Service	2020	voltage-gated hydrogen channel 1 [Fusarium heterosporum]	https://www.ncbi.nlm.nih.gov/protein/KAF5660113.1	NCBI Protein, KAF5660113.1
The Institute of Vegetables and Flowers CAAS	2019	voltage-gated hydrogen channel 1 [Cordyceps javanica]	https://www.ncbi.nlm.nih.gov/protein/TQW00298.1	NCBI Protein, TQW00298.1
Broad Institute	2006	voltage-gated hydrogen channel 1 [Aplysia californica]	https://www.ncbi.nlm.nih.gov/protein/XP_005100666.1	NCBI Protein, XP_005100666.1
The Genomic Institute	2017	Voltage-gated hydrogen channel 1 [Fasciola hepatica]	https://www.ncbi.nlm.nih.gov/protein/THD25470.1	NCBI Protein, THD25470.1
Global Invertebrate Genomics Alliance (GIGA)	2020	HVCN1 [Bugula neritina]	https://www.ncbi.nlm.nih.gov/protein/KAF6036357.1	NCBI Protein, KAF6036357.1
NINGBO UNIVERSITY	2020	HVCN1 [Mytilus coruscus]	https://www.ncbi.nlm.nih.gov/protein/CAC5426376.1	NCBI Protein, CAC5426376.1
McDonnell Genome Institute	2020	Voltage-gated hydrogen channel 1 [Paragonimus heterotremus]	https://www.ncbi.nlm.nih.gov/protein/KAF5400532.1	NCBI Protein, KAF5400532.1

Fudan University	2019	Voltage-gated hydrogen channel 1 [Schistosoma japonicum]	https://www.ncbi.nlm.nih.gov/protein/TNN21174.1	NCBI Protein, TNN21174.1
BGI-Shenzhen	2012	voltage-gated hydrogen channel 1 [Cicer arietinum]	https://www.ncbi.nlm.nih.gov/protein/XP_012568882.1	NCBI Protein, XP_012568882.1
The Cucumber Genome Initiative	2009	voltage-gated hydrogen channel 1 [Cucumis sativus]	https://www.ncbi.nlm.nih.gov/protein/XP_011656484.2	NCBI Protein, XP_011656484.2
African Centre of excellence in Phytomedicine Resaerch	2018	Voltage-gated hydrogen channel 1, partial [Mucuna pruriens]	https://www.ncbi.nlm.nih.gov/protein/RDX63547.1	NCBI Protein, RDX63547.1
Xi'an Jiaotong University	2018	voltage-gated hydrogen channel 1 [Papaver somniferum]	https://www.ncbi.nlm.nih.gov/protein/XP_026460796.1	NCBI Protein, XP_026460796.1
International peanut genome project	2018	Voltage-gated hydrogen channel [Arachis hypogaea]	https://www.ncbi.nlm.nih.gov/protein/QHO09623.1	NCBI Protein, QHO09623.1
Chinese Academy of Agricultural Sciences	2019	voltage-gated hydrogen channel 1 [Benincasa hispida]	https://www.ncbi.nlm.nih.gov/protein/XP_038886538.1	NCBI Protein, XP_038886538.1
University of Veterinary Medicine Hannover	2018	Voltage-gated hydrogen channel 1 [Trichoplax sp. H2]	https://www.ncbi.nlm.nih.gov/protein/RDD43770.1	NCBI Protein, RDD43770.1
Fisheries and Oceans Canada	2020	voltage-gated hydrogen channel 1-like [Oncorhynchus keta]	https://www.ncbi.nlm.nih.gov/protein/XP_035634051.1	NCBI Protein, XP_035634051.1
Deakin University	2017	voltage-gated hydrogen channel 1 [Amphiprion ocellaris]	https://www.ncbi.nlm.nih.gov/protein/XP_023152539.1	NCBI Protein, XP_023152539.1
Wellcome Sanger Institute	2019	voltage-gated hydrogen channel 1 [Denticeps clupeoides]	https://www.ncbi.nlm.nih.gov/protein/XP_028830549.1	NCBI Protein, XP_028830549.1
Yellow Sea Fisheries Research Institute, Chinese Academy of Fishery Sciences	2019	voltage-gated hydrogen channel 1 [Epinephelus lanceolatus]	https://www.ncbi.nlm.nih.gov/protein/XP_033488479.1	NCBI Protein, XP_033488479.1
Wellcome Sanger Institute	2019	voltage-gated hydrogen channel 1 [Myripristis murdjan]	https://www.ncbi.nlm.nih.gov/protein/XP_029918050.1	NCBI Protein, XP_029918050.1
King Abdullah University of Science and technology	2017	voltage-gated hydrogen channel 1 [Acanthochromis polyacanthus]	https://www.ncbi.nlm.nih.gov/protein/XP_022070642.1	NCBI Protein, XP_022070642.1
BGI-SZ	2018	voltage-gated hydrogen channel 1-like [Tachysurus fulvidraco]	https://www.ncbi.nlm.nih.gov/protein/XP_027031192.1	NCBI Protein, XP_027031192.1
Mammalian Gene Collection Program Team	2002	HVCN1 protein [Homo sapiens]	https://www.ncbi.nlm.nih.gov/protein/AAH32672.1	NCBI Protein, AAH32672.1
Anon	2011	voltage-gated proton channel kHv1 [Karlodinium veneficum]	https://www.ncbi.nlm.nih.gov/protein/AEQ59286.1	NCBI Protein, AEQ59286.1
Okinawa Institute of Science and Technology Graduate University (OIST)	2015	voltage-gated hydrogen channel 1 [Lingula anatina]	https://www.ncbi.nlm.nih.gov/protein/XP_013413952.1	NCBI Protein, XP_013413952.1

References

- Ahern CA, Horn R. 2005. Focused electric field across the voltage sensor of potassium channels. *Neuron* **48**:25–29. DOI: <https://doi.org/10.1016/j.neuron.2005.08.020>, PMID: 16202706
- Allemand D, Tambutté É., Zoccola D, Tambutté S. 2011. Coral calcification, cells to reefs. In: Dubinsky Z, Stambler N (Eds). *Coral Reefs Ecosyst. Transit*. Springer. p. 119–150. DOI: https://doi.org/10.1007/978-94-007-0114-4_9
- Berger TK, Fußhöller DM, Goodwin N, Bönigk W, Müller A, Dokani Khesroshahi N, Brenker C, Wachten D, Krause E, Kaupp UB, Strünker T. 2017. Post-translational cleavage of Hv1 in human sperm tunes pH- and voltage-dependent gating. *The Journal of Physiology* **595**:1533–1546. DOI: <https://doi.org/10.1113/JP273189>, PMID: 27859356
- Caldeira K, Wickett ME. 2003. Anthropogenic carbon and ocean pH. *Nature* **425**:365. DOI: <https://doi.org/10.1038/425365a>
- Capasso L, Ganot P, Planas-Bielsa V, Tambutté S, Zoccola D. 2021. Intracellular pH regulation: characterization and functional investigation of H⁺ transporters in *Stylophora pistillata*. *BMC Molecular and Cell Biology* **22**:1–19. DOI: <https://doi.org/10.1186/s12860-021-00353-x>, PMID: 33685406
- Carmona EM, Larsson HP, Neely A, Alvarez O, Latorre R, Gonzalez C. 2018. Gating charge displacement in a monomeric voltage-gated proton (H_v1) channel. *PNAS* **115**:9240–9245. DOI: <https://doi.org/10.1073/pnas.1809705115>, PMID: 30127012
- Carmona EM, Fernandez M, Alvear-Arias JJ, Neely A, Larsson HP, Alvarez O, Garate JA, Latorre R, Gonzalez C. 2021. The voltage sensor is responsible for δ pH dependence in H_v1 channels. *PNAS* **118**:e2025556118. DOI: <https://doi.org/10.1073/pnas.2025556118>, PMID: 33941706
- Castillo K, Pupo A, Baez-Nieto D, Contreras GF, Morera FJ, Neely A, Latorre R, Gonzalez C. 2015. Voltage-gated proton (H_v1) channels, a singular voltage sensing domain. *FEBS Letters* **589**:3471–3478. DOI: <https://doi.org/10.1016/j.febslet.2015.08.003>, PMID: 26296320
- Changeux JP. 2012. Allostery and the Monod-Wyman-Changeux model after 50 years. *Annual Review of Biophysics* **41**:103–133. DOI: <https://doi.org/10.1146/annurev-biophys-050511-102222>, PMID: 22224598
- Cherny VV, Markin VS, DeCoursey TE. 1995. The voltage-activated hydrogen ion conductance in rat alveolar epithelial cells is determined by the pH gradient. *Journal of General Physiology* **105**:861–896. DOI: <https://doi.org/10.1085/jgp.105.6.861>, PMID: 7561747
- Cherny VV, Morgan D, Musset B, Chaves G, Smith SM, DeCoursey TE. 2015. Tryptophan 207 is crucial to the unique properties of the human voltage-gated proton channel, hHv1. *Journal of General Physiology* **146**:343–356. DOI: <https://doi.org/10.1085/jgp.201511456>, PMID: 26458876
- Cherny VV, Musset B, Morgan D, Thomas S, Smith SME, DeCoursey TE. 2020. Engineered high-affinity zinc binding site reveals gating configurations of a human proton channel. *Journal of General Physiology* **152**:202012664. DOI: <https://doi.org/10.1085/jgp.202012664>
- Chomczynski P, Sacchi N. 1987. Single-step method of RNA isolation by acid guanidinium thiocyanate-phenol-chloroform extraction. *Analytical Biochemistry* **162**:156–159. DOI: [https://doi.org/10.1016/0003-2697\(87\)90021-2](https://doi.org/10.1016/0003-2697(87)90021-2), PMID: 2440339
- Cleves PA, Strader ME, Bay LK, Pringle JR, Matz MV. 2018. CRISPR/Cas9-mediated genome editing in a reef-building coral. *PNAS* **115**:5235–5240. DOI: <https://doi.org/10.1073/pnas.1722151115>, PMID: 29695630
- De La Rosa V, Bennett AL, Ramsey IS. 2018. Coupling between an electrostatic network and the Zn²⁺ binding site modulates Hv1 activation. *Journal of General Physiology* **150**:863–881. DOI: <https://doi.org/10.1085/jgp.201711822>, PMID: 29743298
- De La Rosa V, Ramsey IS. 2018. Gating currents in the Hv1 proton channel. *Biophysical Journal* **114**:2844–2854. DOI: <https://doi.org/10.1016/j.bpj.2018.04.049>, PMID: 29925021
- De-la-Rosa V, Rangel-Yescas GE, Ladrón-de-Guevara E, Rosenbaum T, Islas LD. 2013. Coarse architecture of the transient receptor potential vanilloid 1 (TRPV1) ion channel determined by fluorescence resonance energy transfer. *Journal of Biological Chemistry* **288**:29506–29517. DOI: <https://doi.org/10.1074/jbc.M113.479618>, PMID: 23965996
- De-la-Rosa V, Suárez-Delgado E, Rangel-Yescas GE, Islas LD. 2016. Currents through Hv1 channels deplete protons in their vicinity. *The Journal of General Physiology* **147**:127–136. DOI: <https://doi.org/10.1085/jgp.201511496>, PMID: 26809792
- DeCoursey TE. 2013. Voltage-gated proton channels: molecular biology, physiology, and pathophysiology of the H(V) family. *Physiological Reviews* **93**:599–652. DOI: <https://doi.org/10.1152/physrev.00011.2012>, PMID: 23589829
- Edelstein AD, Tsuchida MA, Amodaj N, Pinkard H, Vale RD, Stuurman N. 2014. Advanced methods of microscope control using µmanager software. *Journal of Biological Methods* **1**:e10. DOI: <https://doi.org/10.14440/jbm.2014.36>, PMID: 25606571
- Halaszovich CR, Leitner MG, Mavrantoni A, Le A, Frezza L, Feuer A, Schreiber DN, Villalba-Galea CA, Oliver D. 2012. A human phospholipid phosphatase activated by a transmembrane control module. *Journal of Lipid Research* **53**:2266–2274. DOI: <https://doi.org/10.1194/jlr.M026021>, PMID: 22896666
- Hoegh-Guldberg O. 1999. Climate change, coral bleaching and the future of the world's coral reefs. *Marine & Freshwater Research* **50**:839–866. DOI: <https://doi.org/10.1071/MF99078>
- Horrigan FT, Aldrich RW. 2002. Coupling between voltage sensor activation, Ca²⁺ binding and channel opening in large conductance (BK) potassium channels. *Journal of General Physiology* **120**:267–305. DOI: <https://doi.org/10.1085/jgp.20028605>, PMID: 12198087

- Islas LD, Sigworth FJ. 2001. Electrostatics and the gating pore of shaker potassium channels. *Journal of General Physiology* **117**:69–90. DOI: <https://doi.org/10.1085/jgp.117.1.69>, PMID: 11134232
- Iwasaki H, Murata Y, Kim Y, Hossain MI, Worby CA, Dixon JE, McCormack T, Sasaki T, Okamura Y. 2008. A voltage-sensing phosphatase, Ci-VSP, which shares sequence identity with PTEN, dephosphorylates phosphatidylinositol 4,5-bisphosphate. *PNAS* **105**:7970–7975. DOI: <https://doi.org/10.1073/pnas.0803936105>, PMID: 18524949
- Jokiel PL. 2013. Coral reef calcification: carbonate, bicarbonate and proton flux under conditions of increasing ocean acidification. *Proceedings of the Royal Society B: Biological Sciences* **280**:20130031. DOI: <https://doi.org/10.1098/rspb.2013.0031>
- Le Goff C, Tambutté E, Venn AA, Techer N, Allemand D, Tambutté S. 2017. In vivo pH measurement at the site of calcification in an octocoral. *Scientific Reports* **7**:1–14. DOI: <https://doi.org/10.1038/s41598-017-10348-4>, PMID: 28894174
- Lee SY, Letts JA, Mackinnon R. 2008. Dimeric subunit stoichiometry of the human voltage-dependent proton channel Hv1. *PNAS* **105**:7692–7695. DOI: <https://doi.org/10.1073/pnas.0803277105>, PMID: 18509058
- Lishko PV, Kirichok Y. 2010. The role of Hv1 and CatSper channels in sperm activation. *The Journal of Physiology* **588**:4667–4672. DOI: <https://doi.org/10.1113/jphysiol.2010.194142>, PMID: 20679352
- Long SB, Campbell EB, Mackinnon R. 2005. Crystal structure of a mammalian voltage-dependent shaker family K⁺ channel. *Science* **309**:897–903. DOI: <https://doi.org/10.1126/science.1116269>, PMID: 16002581
- Lupas A, Van Dyke M, Stock J. 1991. Predicting coiled coils from protein sequences. *Science* **252**:1162–1164. DOI: <https://doi.org/10.1126/science.252.5009.1162>, PMID: 2031185
- McDonnell AV, Jiang T, Keating AE, Berger B. 2006. Paircoil2: improved prediction of coiled coils from sequence. *Bioinformatics* **22**:356–358. DOI: <https://doi.org/10.1093/bioinformatics/bti797>, PMID: 16317077
- Mony L, Stroebel D, Isacoff EY. 2020. Dimer interaction in the Hv1 proton channel. *PNAS* **117**:20898–20907. DOI: <https://doi.org/10.1073/pnas.2010032117>, PMID: 32788354
- Moya A, Huisman L, Ball EE, Hayward DC, Grasso LC, Chua CM, Woo HN, Gattuso JP, Forêt S, Miller DJ. 2012. Whole transcriptome analysis of the coral *Acropora millepora* reveals complex responses to CO₂-driven acidification during the initiation of calcification. *Molecular Ecology* **21**:2440–2454. DOI: <https://doi.org/10.1111/j.1365-294X.2012.05554.x>, PMID: 22490231
- Musset B, Cherny VV, Morgan D, Okamura Y, Ramsey IS, Clapham DE, DeCoursey TE. 2008. Detailed comparison of expressed and native voltage-gated proton channel currents. *The Journal of Physiology* **586**:2477–2486. DOI: <https://doi.org/10.1113/jphysiol.2007.149427>, PMID: 18356202
- Papp F, Lomash S, Szilagyi O, Babikow E, Smith J, Chang TH, Bahamonde MI, Toombes GES, Swartz KJ. 2019. TMEM266 is a functional voltage sensor regulated by extracellular Zn²⁺. *eLife* **8**:e42372. DOI: <https://doi.org/10.7554/eLife.42372>, PMID: 30810529
- Qiu F, Chamberlin A, Watkins BM, Ionescu A, Perez ME, Barro-Soria R, González C, Noskov SY, Larsson HP. 2016. Molecular mechanism of Zn²⁺ inhibition of a voltage-gated proton channel. *PNAS* **113**:E5962–E5971. DOI: <https://doi.org/10.1073/pnas.1604082113>, PMID: 27647906
- Ramsey IS, Moran MM, Chong JA, Clapham DE. 2006. A voltage-gated proton-selective channel lacking the pore domain. *Nature* **440**:1213–1216. DOI: <https://doi.org/10.1038/nature04700>, PMID: 16554753
- Ramsey IS, Mokrab Y, Carvacho I, Sands ZA, Sansom MSP, Clapham DE. 2010. An aqueous H⁺ permeation pathway in the voltage-gated proton channel Hv1. *Nature Structural & Molecular Biology* **17**:869–875. DOI: <https://doi.org/10.1038/nsmb.1826>, PMID: 20543828
- Randolph AL, Mokrab Y, Bennett AL, Sansom MS, Ramsey IS. 2016. Proton currents constrain structural models of voltage sensor activation. *eLife* **5**:e18017. DOI: <https://doi.org/10.7554/eLife.18017>, PMID: 27572256
- Sakata S, Miyawaki N, McCormack TJ, Arima H, Kawanabe A, Özkucur N, Kurokawa T, Jinno Y, Fujiwara Y, Okamura Y. 2016. Comparison between mouse and sea urchin orthologs of voltage-gated proton channel suggests role of S3 segment in activation gating. *Biochimica Et Biophysica Acta (BBA) - Biomembranes* **1858**:2972–2983. DOI: <https://doi.org/10.1016/j.bbame.2016.09.008>
- Sasaki M, Takagi M, Okamura Y. 2006. A voltage sensor-domain protein is a voltage-gated proton channel. *Science* **312**:589–592. DOI: <https://doi.org/10.1126/science.1122352>, PMID: 16556803
- Schladt TM, Berger TK. 2020. Voltage and pH difference across the membrane control the S4 voltage-sensor motion of the Hv1 proton channel. *Scientific Reports* **10**:1–13. DOI: <https://doi.org/10.1038/s41598-020-77986-z>, PMID: 33277511
- Schoppa NE, Sigworth FJ. 1998. Activation of shaker potassium channels. I. characterization of voltage-dependent transitions. *The Journal of General Physiology* **111**:271–294. DOI: <https://doi.org/10.1085/jgp.111.2.271>, PMID: 9450944
- Smith SM, Morgan D, Musset B, Cherny VV, Place AR, Hastings JW, DeCoursey TE. 2011. Voltage-gated proton channel in a dinoflagellate. *PNAS* **108**:18162–18167. DOI: <https://doi.org/10.1073/pnas.1115405108>, PMID: 22006335
- Takeshita K, Sakata S, Yamashita E, Fujiwara Y, Kawanabe A, Kurokawa T, Okochi Y, Matsuda M, Narita H, Okamura Y, Nakagawa A. 2014. X-ray crystal structure of voltage-gated proton channel. *Nature Structural & Molecular Biology* **21**:352–357. DOI: <https://doi.org/10.1038/nsmb.2783>, PMID: 24584463
- Taylor AR, Chrachri A, Wheeler G, Goddard H, Brownlee C. 2011. A voltage-gated H⁺ channel underlying pH homeostasis in calcifying coccolithophores. *PLOS Biology* **9**:e1001085. DOI: <https://doi.org/10.1371/journal.pbio.1001085>, PMID: 21713028

- Thomas S**, Cherny VV, Morgan D, Artinian LR, Rehder V, Smith SME, DeCoursey TE. 2018. Exotic properties of a voltage-gated proton channel from the snail *Helisoma trivolvis*. *Journal of General Physiology* **150**:835–850. DOI: <https://doi.org/10.1085/jgp.201711967>, PMID: 29743301
- Tijssen J**, Wijgerde T, Leal MC, Osinga R. 2017. Effects of zinc supplementation on growth and colouration of the scleractinian coral *Stylophora pistillata*. *PeerJ* **5**:e2858v1. DOI: <https://doi.org/10.7287/peerj.preprints.2858v1>
- Toyofuku T**, Matsuo MY, de Nooijer LJ, Nagai Y, Kawada S, Fujita K, Reichart GJ, Nomaki H, Tsuchiya M, Sakaguchi H, Kitazato H. 2017. Proton pumping accompanies calcification in foraminifera. *Nature Communications* **8**:1–6. DOI: <https://doi.org/10.1038/ncomms14145>, PMID: 28128216
- Tresguerres M**, Barott KL, Barron ME, Deheyn DD, Kline DI, Linsmayer LB. 2017. Cell biology of reef-building corals: ion transport, acid/base regulation, and energy metabolism. In: Weihrauch D (Ed). *Acid-Base Balance Nitrogen Excretion Invertebr.* Springer. p. 193–218. DOI: https://doi.org/10.1007/978-3-319-39617-0_7
- Venn AA**, Tambutté E, Lotto S, Zoccola D, Allemand D, Tambutté S. 2009. Imaging intracellular pH in a reef coral and symbiotic Anemone. *PNAS* **106**:16574–16579. DOI: <https://doi.org/10.1073/pnas.0902894106>, PMID: 19720994
- Villalba-Galea CA**. 2014. Hv1 proton channel opening is preceded by a voltage-independent transition. *Biophysical Journal* **107**:1564–1572. DOI: <https://doi.org/10.1016/j.bpj.2014.08.017>, PMID: 25296308
- Waterhouse A**, Bertoni M, Bienert S, Studer G, Tauriello G, Gumienny R, Heer FT, de Beer TAP, Rempfer C, Bordoli L, Lepore R, Schwede T. 2018. SWISS-MODEL: homology modelling of protein structures and complexes. *Nucleic Acids Research* **46**:W296–W303. DOI: <https://doi.org/10.1093/nar/gky427>, PMID: 29788355
- Woodhull AM**. 1973. Ionic blockage of sodium channels in nerve. *Journal of General Physiology* **61**:687–708. DOI: <https://doi.org/10.1085/jgp.61.6.687>, PMID: 4541078
- Ying H**, Hayward DC, Cooke I, Wang W, Moya A, Siemering KR, Sprungala S, Ball EE, Forêt S, Miller DJ. 2019. The Whole-Genome sequence of the coral *Acropora millepora*. *Genome Biology and Evolution* **11**:1374–1379. DOI: <https://doi.org/10.1093/gbe/evz077>, PMID: 31059562
- Zhao C**, Tombola F. 2021. Voltage-gated proton channels from fungi highlight role of peripheral regions in channel activation. *Communications Biology* **4**:1–13. DOI: <https://doi.org/10.1038/s42003-021-01792-0>
- Zheng J**, Trudeau MC, Zagotta WN. 2002. Rod cyclic nucleotide-gated channels have a stoichiometry of three CNGA1 subunits and one CNGB1 subunit. *Neuron* **36**:891–896. DOI: [https://doi.org/10.1016/S0896-6273\(02\)01099-1](https://doi.org/10.1016/S0896-6273(02)01099-1), PMID: 12467592



Patch-Clamp Fluorometry and Its Applications to the Study of Ion Channels

Esteban Suárez-Delgado and León D. Islas

Abstract

Patch-clamp remains the premier technique to study ion channel properties. Among the more useful extensions of patch-clamp, is the simultaneous use of fluorescence and spectroscopic techniques and electrophysiological recording known as patch-clamp fluorometry. This technique permits the simultaneous correlation of ionic current recordings with the activity of electrically silent protein conformational changes reported by the fluorescence measurement. Several recent and ongoing advances in fluorescent probes, genetically encoded fluorescent sensors based on fluorescent proteins or fluorescent noncanonical amino acids are making these methodologies more and more useful in the study of ion channel dynamics and regulation.

Key words Patch-clamp, Patch-clamp fluorometry, Electrophysiology, Membrane biophysics, Ion channels, Fluorescence, Spectroscopy, Live imaging, Fluorescent proteins

1 Introduction: Ion Channels

Transport and communication through cellular membranes have evolved a great variety of mechanisms that assure the availability of substrates and the coordination of different signals to maintain the fine balance in the organisms' metabolism.

Membrane-associated proteins that are responsible for transport can be categorized into two types: the carriers and the channels. The first ones are proteins that specifically bind the metabolite or solute that will be transported and then substrate is translocated across the bilayer through a conformational change that takes place during each transport cycle [1].

The second ones are ion channels, which are proteins that have a pore that traverses the cellular membrane and facilitates the transport of ions to both sides of the membrane. The source of energy for this transport is solely the electrochemical gradient for the specific ion.

Ion channels are widely distributed in nature, practically every organism contains them; they respond to a great variety of stimuli, either chemical (hormones, second messengers, neurotransmitters) or physical (mechanical stimulation, temperature, voltage), by opening their pores [2, 3]. The responses to these diverse stimuli are directly linked to the extensive number of functions that the cell performs: regulation of acidity and osmolarity, liberation of hormones and neurotransmitters, and without doubt the most remarkable, the generation and propagation of action potentials in excitable tissues. All these functions allow the organism to perceive and process environmental information and to respond accordingly [4].

Despite exhibiting structural differences among them, ion channels are composed of several specific domains, the actions of which are allosterically coordinated to achieve the final result of opening the conduction pore that allows for the movement of ions across the membrane.

In most channels one can distinguish at least two domains. The first one related to the activation mechanism (the sensing domain) and another related to channel opening and ion conduction (the pore and selectivity filter). The activation domain can respond to one or several activation stimuli, generally producing a structural rearrangement or conformational change, which is transmitted to the activation gate. This coupling is known as gating. When the gate moves, the pore allows the flux of ions, which can be detected as an ionic current. The pore of the channel is a very efficient structure that permits transport of ions at a rate of approximately ten million per second when the channel is activated. Despite such high rate, the pore has a region called selectivity filter, which preferentially interacts with one kind of ion, allowing for the high selectivity generally seen in ion channels [5, 6].

1.1 Methods of Study of Ion Channels

In the middle of last century, the work done by Hodgkin and Huxley in the giant squid axon permitted the description of the cellular membrane as an equivalent electrical circuit, providing the basis for the electrophysiology techniques that are used nowadays [7].

In biophysical terms, the cellular membrane can be represented by an RC circuit where the lipid bilayer functions as a capacitor with capacitance C , and passive ion transport is represented as a resistance, R . Channels for each one of the permeating ions are represented as variable resistances, which can depend on voltage or other gating stimuli. Each one of these conductances is associated with an appropriate electromotive driving force given by the equilibrium potential of the ion.

To be able to study the properties of channels, techniques that can record the characteristics of the equivalent circuit were developed. One of the more widely used such techniques is the

two-electrode voltage-clamp (TEVC) [8]. This technique introduces very thin glass pipettes into the cellular cytoplasm. The pipettes are electrically connected through a saline solution to electrodes, which go to the amplifier and allow both the injection and recording of current. Voltage control is achieved through feedback from the amplifier and currents can be recorded from medium to large size cells, being the *Xenopus laevis* oocyte one of the most commonly used. Another widely used technique is the cut-open oocyte voltage clamp (COVC), which allows for the recording of currents from a large area of the oocyte under better space-clamp conditions than TEVC [9, 10].

About 40 years ago electrical recording techniques had an important development. Neher and Sakmann created a method in which, instead of piercing the cellular membrane, a very strong seal is made between the cell membrane and the glass pipette [11]. This method, baptized as patch-clamp, has proven to be a spearhead in the study of the ion channels, so much so that, up to now, it is the main tool used for the fundamental evaluation of the biophysical properties of ion channels [12].

This technique offers several advantages, including the ability to record from only one channel, which permits direct estimates of the probability of the channel opening, as well as its unitary current behavior [13, 14]. Furthermore, it also allows recording of macroscopic currents arising from a large number of channels, as well as channel stimulation by both intracellular and extracellular modulators.

The patch-clamp method has multiple modalities that turn it into a useful and varied tool. Every seal begins with the approach and subsequent interaction of the glass pipette with the cellular membrane; this interaction is usually promoted by application of negative pressure in the pipette, which helps to introduce a portion of membrane into the pipette tip. The seal has been formed when an electrical resistance larger than 1 gigaohm ($G\Omega$) is obtained and along with it, the first modality which is the *cell-attached* or *on-cell* configuration. This modality allows performing electrophysiological recordings with an intact intracellular medium. Other configurations are possible, which permit access to the cytoplasmic part of the membrane (*inside-out*), the extracellular face (*outside-out*), or the entire membrane of the cell (*whole-cell*) [15, 16].

1.2 Patch-Clamp Fluorometry

In the decades following its invention, the patch-clamp method was refined and found to have multiple applications in the study of ion channel function. At the same time, knowledge about structure–function relationships in ion channels increased through the implementation of other techniques, such as chemical modification [17], mutagenesis [18, 19], and more recently, cryo-electron microscopy [20, 21], X-ray crystallography [6, 22], nuclear magnetic resonance (NMR) [23, 24] and “in-silico” modeling [25, 26].

Despite the wealth of information that these methods provide, direct correlation between structure and functional states is difficult to establish. Thus, in the middle of the 1990-decade, fluorescence techniques, so helpful in other areas of neuroscience, were merged with electrophysiological recordings to investigate conformational changes in ion channels while activation was on course [27, 28].

One of the first published works that measured ion channel rearrangements with fluorescence methods and electrical recordings, was carried out by Mannuzzu et al. in *Shaker* potassium channels [29]. This experiment made use of *Xenopus laevis* oocytes, under TEVC and was named voltage-clamp fluorometry (VCF). VCF generally makes use of fluorescent probes attached to cysteine residues introduced by mutagenesis in the channel's sequence. The great usefulness of VCF stems from the fact that the fluorescence signals can provide information about conformational changes that do not directly produce an electrical signal, which cannot be recorded by conventional voltage-clamp methods [28, 30].

A few years after this initial report, Zheng and Zagotta went further to develop an approach combining fluorescence and electrophysiological recordings in the *inside-out* configuration, dubbed patch-clamp fluorometry or PCF [31, 32]. This method offers new information beside that inherent to patch-clamping (high time resolution of current recordings and access to the intracellular side of channels). First of all, and possibly the most important attribute, is the ability to detect conformational changes associated with electrically silent states (closed, inactivated, and desensitized states). And second, an increased quality of the fluorescence signals is attained by excluding the intracellular contents of a cell [33].

Because of these advantages, PCF has been applied to a large number of different ion channels using a great variety of combined spectroscopic and electrophysiological tools. Some of these tools rely on the introduction of fluorescent probes at cysteine residues (either endogenous to the channel or introduced by mutagenesis) [32, 34, 35], which can provide clues of local environmental changes during gating. By measuring changes in the photo physical properties of such fluorophores, the dynamics of ion channels during gating can be measured. Examples of these are the measurement of fluorescence intensity changes, the use of tryptophan residues as quenchers of introduced bimane derivatives [36], genetically encoded fluorescent proteins as FRET reporters [37–39], or as reporters of the local environment [38], the use of ionic quenchers of fluorescence to probe accessibility [32], fluorescently labeled ligands [40, 41] or introduced noncanonical fluorescent amino acids as probes within the protein sequence [42].

Every patch-clamp configuration already mentioned is useful for PCF [43]. Such versatility makes this technique a powerful tool

for the study of not only channels, but also transporters [44] and receptors in general.

Given the enormous potential of patch-clamp fluorometry, we wish to provide a practical guide for the implementation of a PCF setup and an overview of the more recent possibilities of the technique.

This chapter describes the equipment and basic technical requirements to perform patch-clamp fluorometry, together with a series of tips that we hope can enhance the success rate of PCF experiments.

2 Materials

2.1 Microscopy Equipment

The preferred biological preparation for PCF is the oocyte of the frog *Xenopus laevis*. A microscope that permits easy access to these big cells is necessary. Generally, an inverted configuration with epifluorescence illumination allows for simultaneous measurements of fluorescent intensity while electrophysiological recording from membrane patches is performed. We use an inverted microscope (Nikon TE-2000 U). For illumination, the microscope is coupled via a custom optical system to one or more lasers (Fig. 1). Mercury or halogen lamps or even a power LED system can be used to excite the sample at different wavelengths of visible light. Optical components that allow control of the exposure time and the wavelength and light power that goes to the sample are placed after the light source. These are listed below:

- *Shutter*. A fast mechanical shutter (Uniblitz VMM-D1, Vincent Associates) that controls the laser exposure is used. This shutter is controlled by the imaging software.
- *Collecting lens*. A spherical lens (3 mm) that expands the laser beam diameter from 5 μm to 7 mm.
- *Collimation lens*. A lens that produces a collimated beam after expansion.
- *Neutral density filters*. Regulates the intensity of incoming light without disturbing the wavelength. These reduce the possible photo damage induced by the laser beam that can promote fluorophore photobleaching.
- *Focusing lens*. This lens focuses the collimated beam at the back focal plane of the objective, producing a homogeneous Köhler illumination at the sample plane.
- *Dichroic mirror*. A mirror with different transmission or reflection properties at two different wavelengths. In laser microscopy this is used for dividing the light that comes from the source of the light (laser) from the sample fluorescence.

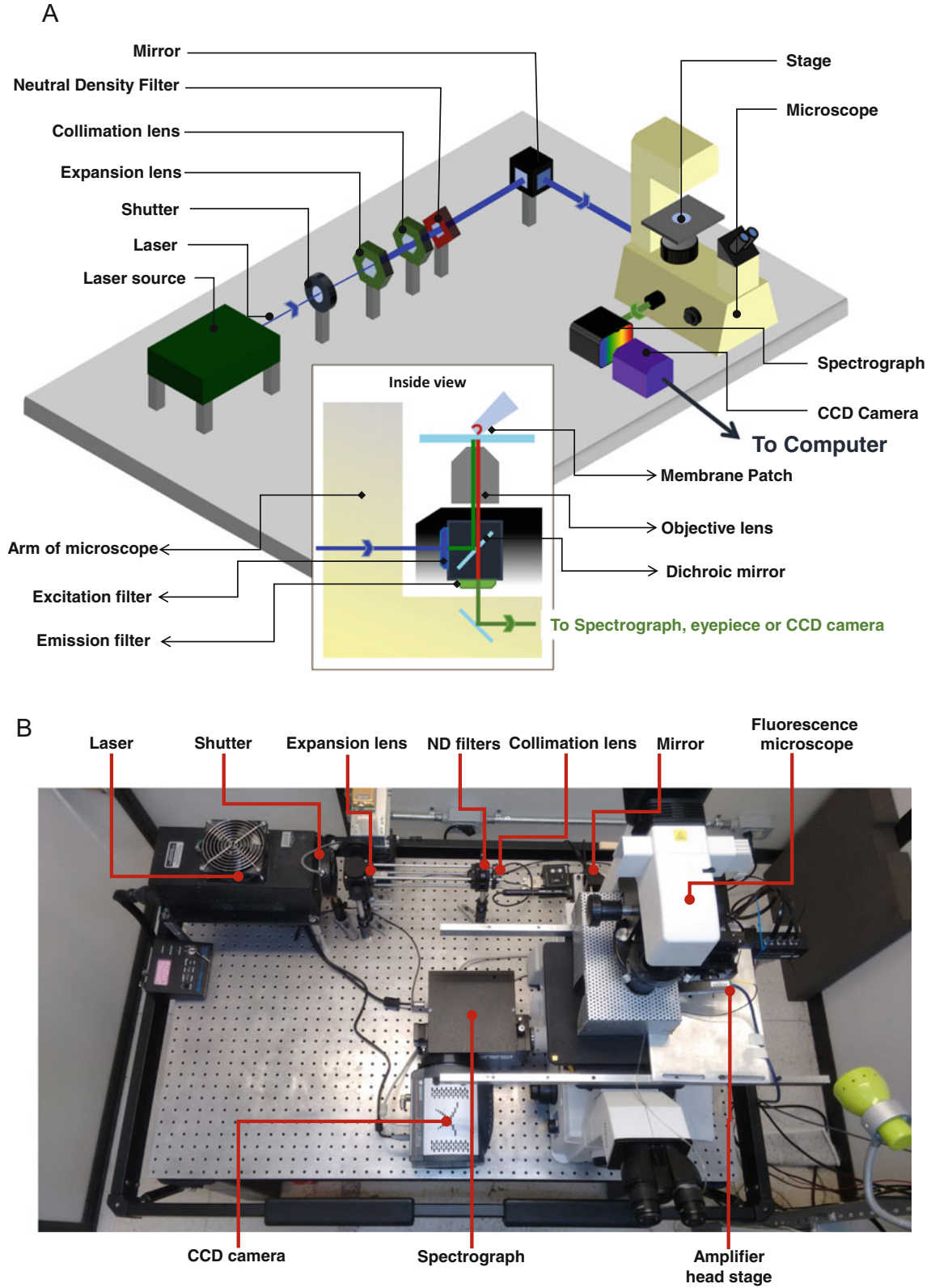


Fig. 1 Schematic of a patch-clamp fluorometry setup. (a) Schematic of the components for the illumination and detection paths. Laser is shown in blue and arrowheads mark its propagation direction. Note that the diameter of the laser beam becomes increases after going through a beam expander. The beam is attenuated

- *Excitation filter.* A filter that only passes certain wavelengths of light from the laser. Typically, it is a narrow band-pass filter and its bandwidth should fall completely inside the excitation range of fluorophore to stimulate.
- *Emission filter.* A filter that only passes certain wavelengths of light from the fluorophore attached to patch. Could be a long pass or bandpass, depending on the collection of light needed. To collect fluorophore spectra, a long pass filter is needed.

The three last elements are located in a preassembled filter cube that goes in the appropriate housing in the microscope and their properties are entirely dictated by the fluorophore to be used.

To collect emission light and serve as an illumination condenser, we use an oil immersion objective with a high numerical aperture (NA) of 1.4 (Nikon 60x) (*see Note 1*). For imaging purposes, the light collected by the objective is sent directly to a CCD camera (*see Note 2*). In experiments where the emission spectrum is needed, light is sent first to an imaging spectrograph (Spectra Pro 2150i, Acton Instruments).

Control of the camera, shutters and other devices can be carried out by the use of commercial software available from microscope manufacturers or other providers (MetaMorph, Molecular Devices). A versatile and more economical alternative is the use of open software such as Micromanager (version 1.4) (<https://micromanager.org>) [45].

2.2 Electro-physiology Equipment

As it was mentioned before, the inverted microscope allows easy access to the sample from above. As in all electrophysiological setups, it is important to mount the microscope and additional optical equipment on a vibration isolation table (VW-3646, Newport) [46]. The amplifier head stage is mounted on a micromanipulator which can be of a fine mechanical type (Newport) or a motorized micromanipulator (Sutter Instruments, MP model). In our PCF experiments we employ an Axopatch 200B (Axon) amplifier but any other patch-clamp amplifier is suitable. Analog to digital conversion of recorded currents is carried out with an ITC-18 board (HEKA Elektronik GMBH). The software we use for current recording and stimulus is Patchmaster (HEKA Elektronik GMBH).

Patch-clamp amplifiers are extremely sensitive; this facilitates pick up of spurious noise signals. For noise reduction, it is

←
Fig. 1 (continued) and steered by neutral density filters and a mirror situated at the back illumination port of the inverted microscope. The inset shows the light pathway in the filter cube set. Changes of wavelength are represented with different colors in the spectrograph. The light from the sample is collected by the objective and guided to the eyepieces, CCD or spectrograph devices. **(b)** Photograph of the actual setup, showing the location of components as in **a**

important to carefully ground all the equipment, including the microscope, micromanipulator and the illumination and light detection accessories (*see Note 3*). Frequently, a Faraday cage that isolates the whole workstation or only the sample space is used.

To obtain giant membrane patches we use borosilicate glass capillaries. The patch pipettes are obtained from these capillaries (external diameter 1.5 mm, internal diameter 0.86 mm, length 10 cm, Sutter Instrument) using a micropipette puller (P97, Sutter Instruments). These pipettes are initially pulled to a large diameter ($\sim 50 \mu\text{m}$) and then heavily fire-polished with a microforge (Narishige, MF-830) to a diameter of $\sim 10 \mu\text{m}$. The large size of the pipette tip is important for simultaneous recording of both fluorescence and patch currents. Note that the pipettes for the patch-clamp fluorometry method in oocytes are bigger than those used for mammalian cells (approximately 2–3 μm) (*see Note 4*).

2.3 Obtaining and Preparation of Oocytes

While the traditional patch-clamp method is used in different cell lineages of varied organisms, the mature oocyte of the frog *Xenopus laevis* is the most frequently employed in patch-clamp fluorometry (PCF) [47]. Obtaining and maintenance of these cells starts with the surgery of a mature female frog (bigger than 9 cm, Xenopus1, NASCO). In this procedure, a rigorous sterile technique is not necessary due to the antibiotic properties of the frog's skin; however, it is advisable to continually clean the surgical equipment to reduce even more the risks of infection. The frog is anesthetized in a solution of tricaine methanesulfonate (Sigma) at 0.22% (pH titrated to 7 with NaOH) for 5 min. The specimen is placed face up on wet gauze and a vertical incision is made in the abdominal region at 1 or 2 centimeters from the midline and approximately with 1 cm of length. When reaching the abdominal cavity, one can extract as many segments of ovary as needed by using dissection tweezers and scissors. The wound is closed by layers using a suture of absorbable material, usually chromic catgut, caliber 3-0 (Atramat) for the muscle and a nonabsorbable nylon suture of 3-0 caliber for the skin.

The ovary segments are placed in a petri dish with OR2 solution (in mM): 82.5 NaCl, 2 KCl, 1 MgCl₂, and 5 HEPES, titrated to a 7.5 pH with NaOH (*see also Table 1*) and they are manually disaggregated in small cumuli of oocytes, being careful not to damage them. Oocytes are covered by a layer of follicular cells that should be removed. To achieve this, we use a solution of collagenase (from *Clostridium histolyticum*, type IA, Sigma) in OR2 at a concentration of 1.5–2 mg/mL. The ovary segments are placed in this solution and are dispersed in an oscillating shaker at 60 rpm for about 30–40 min (*see Note 5*). After this enzymatic treatment, the solution is decanted and the oocytes are washed 3 or 4 times with OR2, to later be shaken again for 30–50 min in OR2 (*see Note 6*). After this treatment the defoliated oocytes are

Table 1
Components of solutions used in the extraction and maintenance of *Xenopus laevis* oocytes

OR 2 solution	ND 96 solution	ND 96 without calcium solution
<ul style="list-style-type: none"> • 82.5 mM NaCl • 2 mM KCl • 1 mM MgCl₂ • 5 mM HEPES 	<ul style="list-style-type: none"> • 96 mM NaCl • 2 mM KCl • 1.8 mM CaCl₂ • 1 mM MgCl₂ • 5 mM HEPES • pH = 7.5 with NaOH 	<ul style="list-style-type: none"> • 96 mM NaCl • 2 mM KCl • 1 mM MgCl₂ • 5 mM HEPES • pH = 7.5 with NaOH

transferred to an incubation solution. In our case, we use the ND96 solution that contains (in mM): 96 NaCl, 2 KCl, 1.8 CaCl₂, 1 MgCl₂, 2.5 of pyruvic acid, 5 HEPES, and 20 µg/mL of gentamicin, titrated to 7.5 pH with NaOH (*see* also Table 1) (*see* Note 7).

Oocyte selection for mRNA injection and subsequent use in PCF experiments is an important step. Usually oocytes in stages V or VI are preferred. These are characterized by having a diameter of 1000–1300 µm and clearly separated animal and vegetal poles.

The chosen oocytes must be incubated at 18 °C for at least 3 h before injecting, so that they recover from the collagenase treatment and to uncover those that have been damaged by the process. For mRNA injection, we use a micro-injector device (Nanostepper, Drummond Scientific) and borosilicate glass pipettes with a tip of 40–60 µm of internal diameter. The pipettes are completely filled with light mineral oil (Sigma) before mounting on the microinjector. When the pipette is already mounted, the solution of mRNA can be aspirated. About 30–50 nL of mRNA will be injected to each oocyte (*see* Note 8). After the injection, the oocytes in ND96 solution are returned to the incubator for a few days until the required level of channel expression is achieved [48].

2.4 mRNA for Injection

As it has been already stated, mRNA is used for the expression of the channel that will be studied. The mRNA that is injected in the oocyte is usually obtained through the in vitro transcription technique from a vector that contains the channel sequence, along with a tail of polyadenines in the 3' end and a cap in the 5' end to avoid mRNA degradation inside the cytoplasm. The mMessage mMachine in vitro transcription kit from Ambion is suitable for this purpose.

2.5 Solutions

The composition of each solution employed in the experiments will vary accordingly to the type of channel to be studied, the possible ligands that activate it and the permeant ion; nonetheless, some general considerations that may facilitate patch formation are appropriate [46].

The first aspect to consider is the osmolarity. In the *Inside-out* configuration, it is advisable that the bath solution (intracellular)

and the one inside the pipette (extracellular) have the same osmotic potential.

The second aspect is pH control. A buffer system with a pKa close to the desired pH should be used. For physiological pH solutions, the most common buffer is HEPES (4-(2-hydroxyethyl)-1-piperazineethanesulfonic acid, Sigma) that has a pKa of 7.5. Finally, for the intracellular solution the calcium concentration should be kept to a minimum by using chelating agents, such as EGTA (Sigma) at an appropriate concentration (10 mM). On the other hand, the extracellular solution should contain divalent cations (Ca^{2+} , Mg^{2+}) 1–2 mM, to facilitate patch formation.

3 Method

3.1 Obtaining the Patch

Experience with traditional patch-clamp techniques is useful for PCF experiments [49]. As stated in the introduction, the patch-clamp method consists in forming a patch of cellular membrane at the tip of a polished glass pipette and measuring the currents that flow through the channels present in this patch during activation.

Now, we will detail the steps to follow in order to achieve PCF in the *inside-out* modality. The steps described here apply to channels that are already fluorescently labeled, perhaps with genetically encoded fluorescent proteins or noncanonical fluorescent amino acids (Fig. 2). In a latter section we will describe methods to perform in-situ labeling of channels present in the patch.

3.1.1 Election of the Oocyte

Oocytes to be used for PCF should be as healthy as possible. This generally means that no discoloration of the animal pole or swelling of the cell has occurred during the incubation period. This period will dictate the day in which the experiments will be performed and it depends on how long the channel takes to be expressed in the membrane of the oocyte. Usually, this waiting time is between 2–5 days after injection of mRNA. The chosen oocyte is transferred to a Petri dish where the vitelline membrane is removed with the help of a pair of fine-tipped tweezers (*see Note 9*).

3.1.2 Setting up the Experiment

The recording chamber should have a small volume (less than 1 mL) and the bottom should be made of a thin glass coverslip. A perforation on the body of the chamber is useful to apply immersion oil to the objective without having to remove the chamber each time. Before transferring the oocyte to the recording chamber, all equipment and software should be running, thus reducing the time the oocyte is exposed before the experiment can commence.

The oocyte should be placed near the center of the recording chamber and its edge focused initially with a 10× objective. The gigaseal will be obtained under this magnification. The pipette is moved into the solution. Just before making contact with the

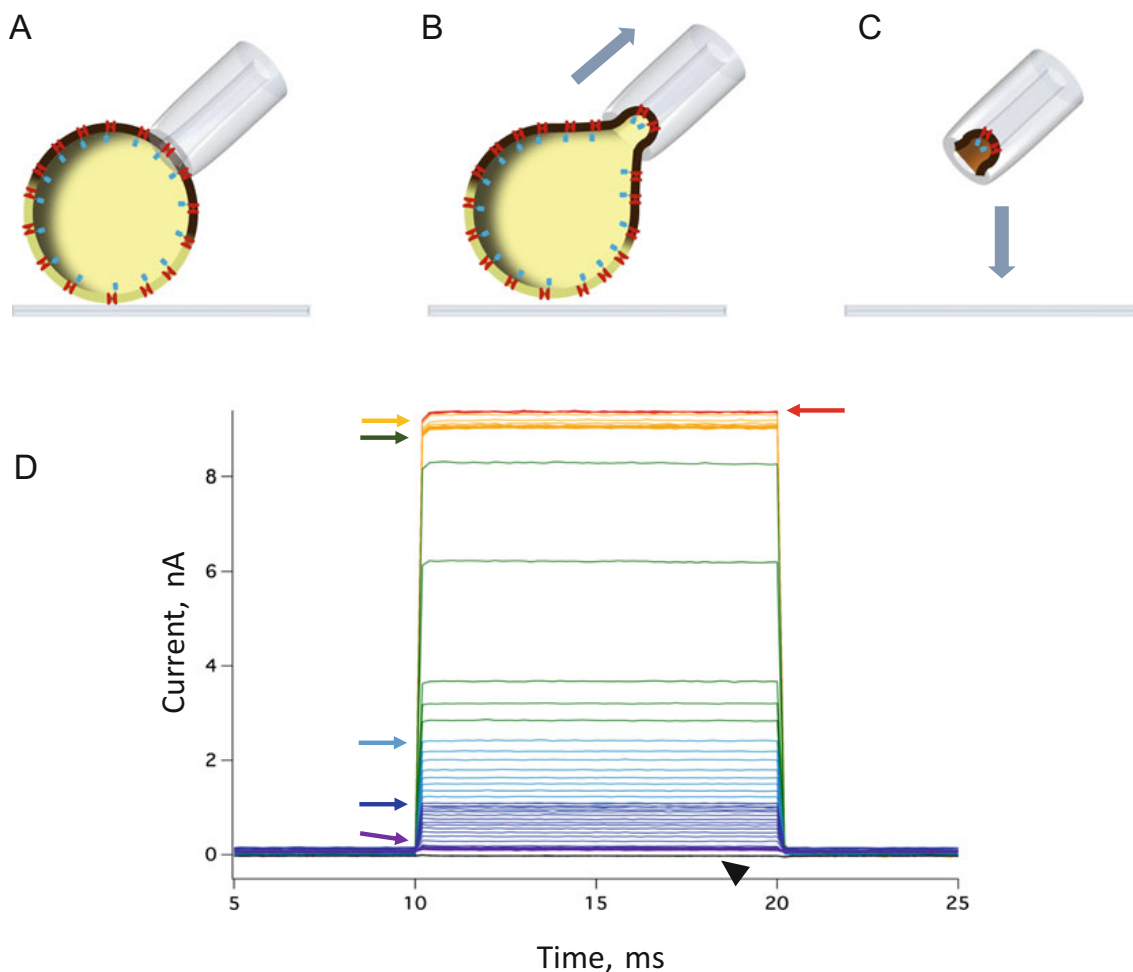


Fig. 2 Seal formation in *Xenopus laevis* oocytes. (a) Microinjected oocytes with the channel (red) fused to a fluorescent protein (blue) correctly expressed in the cell membrane. The patch pipette is sealed to the membrane, helped by a little suction. (b and c) The inside-out configuration is obtained by pulling the glass pipette away from the cell, the pipette tip moves toward the bottom of experimental chamber until sharply focused. (d) A family of pipette currents in response to pulses of 10 mV and 10 ms. Traces at 400 ms intervals are shown. In red is the pipette current before touching the membrane at the initial configuration (Red arrow). When the pipette makes contact with the oocyte membrane (yellow arrow), the current slightly decreases (yellow traces). Positive pressure in the pipette is released (green arrow), promoting entrance of the membrane into the pipette tip and the current quickly diminishes (green traces), indicating a sudden increase of resistance. Then soft suction is applied (light blue arrow) to improve the contact of the membrane with the glass, further increasing resistance (light blue traces). If the increase in resistance slows down or stops (dark blue arrow) the intensity of suction has to be gently increased to continue seal formation (dark blue traces). When the resistance is in the order of 700–900 M Ω (purple traces), suction can be increased (purple arrow) to finally achieve the gigaseal, which is also observed as small current of a few pA amplitude (black traces and black arrowhead)

surface of the bath solution, positive pressure is applied to the pipette to maintain the tip as clean as possible. This positive pressure will be kept up to the moment of contact with the oocyte membrane. As is customary, pipette resistance is monitored

via the application of a small voltage step (10 mV for 20 ms), (*see Note 10*). Before touching the membrane, the current of the pipette must be zeroed to provide a current level reference.

3.1.3 *Obtaining the Seal*

Upon contact with the membrane of the oocyte, the pipette should be pushed until the oocyte shows a slight deformation toward the internal region of the cell due to the horizontal push of the pipette. At this point, positive pressure will be released and immediately, soft suction should be applied. Resistance should increase to several tens of megaohms and suction will be maintained until resistance reaches a value larger than 1 G Ω (Fig. 2) (*see Note 11*). When the gigaohm seal is obtained, the tip of the pipette is removed in one even movement (*see Note 12*). Immediately after, the voltage is set to a value at which the channels are closed. This voltage is termed “holding potential.”

3.2 *Recording Fluorescence*

Before fluorescence imaging can begin, a good image of the patch at the tip of the pipette should be achieved. The pipette is moved as close as possible to the bottom of the chamber and the high NA objective is placed in the light path. Care should be taken that the pipette tip does not come in contact with the chamber bottom, to minimize movement artifacts during imaging. This can be achieved by direct observation or through observation of the imaging field in the CCD camera. The tip is centered in the imaging field, away from the rest of the oocyte. At this point the microscope lamp is switched off and the patch can be illuminated with the appropriate excitation light to record fluorescence. The focus can be adjusted to form a good fluorescence image of the patch (*see Note 13*) (Fig. 3).

3.3 *Simultaneous Measurement of Current and Fluorescence*

For ligand-activated channels, fluorescence images can be acquired in the steady-state, before perfusion of the bath with a solution containing the agonist and also in the presence of it. For voltage-gated channels the situation is a bit more complicated, since image capture should be precisely synchronized to the voltage stimulus. Some camera control software provides TTL pulses that can be used to trigger acquisition by the electrophysiology software. We use an approach provided by micromanager software, where a trigger pulse is delivered by the Patchmaster software to both open the shutter and take a picture, with precise timing. This permits acquisition of fluorescence when the channel is closed (negative potential) or open (positive potentials). Since photobleaching of the fluorophore can be an issue, especially when using high intensity illumination, it is advisable to take paired pictures at a fixed negative potential and at varying positive potentials, thus reducing the influence of photobleaching.

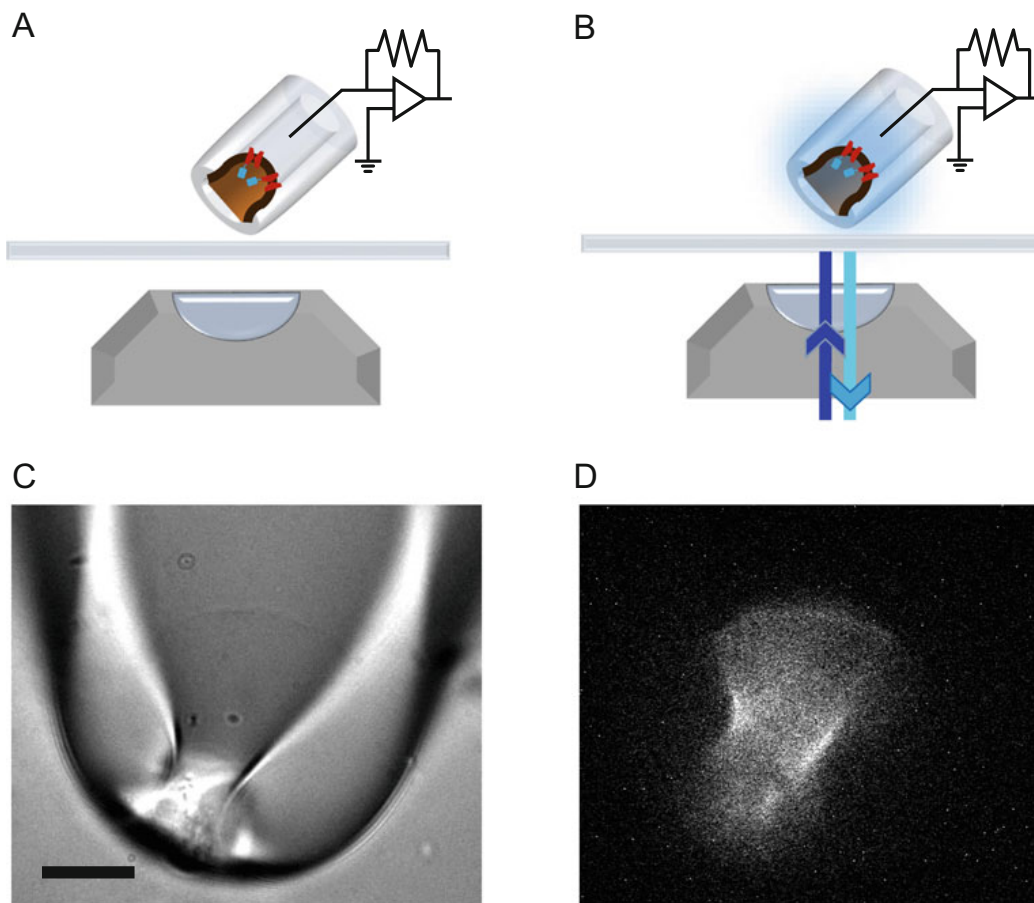


Fig. 3 Scheme of steps to achieve a patch-clamp fluorometry experiment. (a) The patch in the pipette is lowered toward the bottom of the chamber and focused. (b) The excitation source is turned on and fluorescence can be recorded. Images of a membrane patch from an oocyte which expresses the proton channel H_V1 fused to the Venus fluorescent protein. (c) Bright-field image, black bar represents 10 μm . (d) Fluorescence image of the patch in c. The scale bar is the same as in C. Fluorescence was excited at 488 nm and imaged with a band pass filter centered at 525 nm

3.4 Quantification of Fluorescence Intensity

After the acquisition of images, an initial step toward the analysis of fluorescence is to remove the background fluorescence. A region of interest (ROI) is selected in a part of the image where patch fluorescence is not expected. Then another ROI of the same size is placed around the patch. The value of counts of grey scale of the background is subtracted from the value of the patch ROI to acquire the absolute fluorescence and use it for more complex analysis (e.g., FRET) [28, 31]. Fluorescence can be quantified and plotted as relative fluorescence counts to allow comparison between patches with different channel expression levels.

3.5 In-Situ Labeling for Patch-Clamp Fluorometry

Another technique frequently used to monitor conformational changes in ion channels is the site-specific labeling with fluorescent dyes attached with thiol-reactive chemistry [27, 28, 50, 51]. This

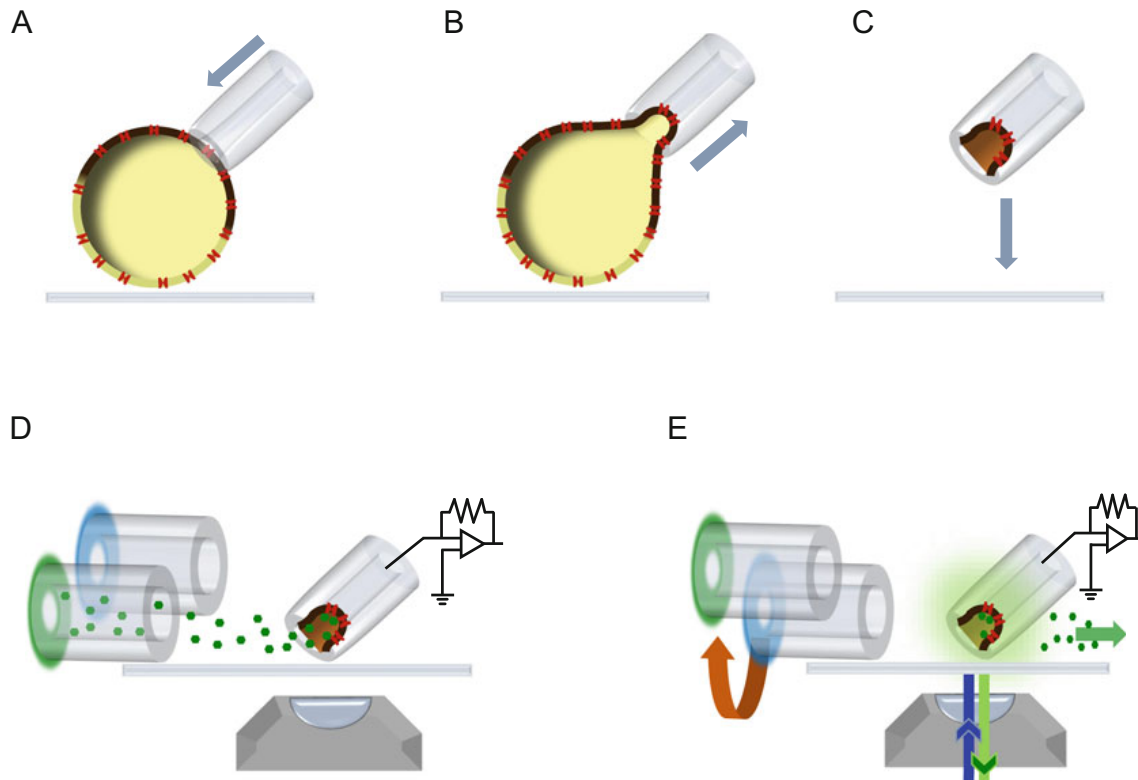


Fig. 4 Labeling of channels in the inside-out configuration. (a–c). Following the same steps as in Fig. 2, an inside-out patch is obtained. (d) The patch is perfused with the cysteine-reactive fluorescent dye that will be attached to a cysteine residue in the channel (green hexagons). (e) Later, dye excess is washed out to reduce the background signal and allow electrophysiology and fluorescence recording

method creates a covalent bond between a reactive group in the fluorescent probe and a sulfhydryl group of a cysteine in the amino acid sequence of the channel. The cysteine-reactive groups usually are methanethiosulfonate (MTS), iodoacetamide (IAA) or maleimide (Mal). Since very small volumes of dye are used to label the patch, a special perfusion system should be used. This is accomplished by using a small tip diameter (approximately 10 μm) glass pipette containing 10–20 μL of reactive dye. Light mineral oil is then used to fill up the rest of the pipette and this in turn is connected to plastic tubing and a 10–20 cc syringe with a two-way valve. The dye pipette is placed in front of the patch pipette and the dye is then fed by gravity. The labeling time will be dependent on the reactivity of the cysteine being labeled [31]. Before recording starts, the residual nonreacted dye is washed, reducing the intensity of background signal and improving signal to noise ratio (Fig. 4).

One important consideration is that the channel to be used should be a cysteine-less protein in which the specific cysteine to be labeled is introduced by mutagenesis. Most channels can be made cysteine-less, although generally at the cost of reduced expression

levels. The relative low frequency of cysteines in proteins helps improve specificity of labeling and introduction of cysteine residues at different sites in intracellular and extracellular domains is well tolerated. Cysteine introduction and subsequent labeling must be done being careful as not to significantly perturb the overall protein structure and activity. An advantage is that organic fluorophores with a relatively small size such as fluorescein (ThermoFisher Scientific), Alexa fluorophores (ThermoFisher Scientific), bimane (Sigma), and Badan (ThermoFisher Scientific) can be linked to cysteines without any gross modification in channel structure and function. This allows for the study of conformational changes with better resolution than that obtained with fluorescent proteins [52, 53].

Despite its advantages, dye labeling at cysteine residues cannot be totally devoid of background fluorescence largely due to labeling of other native transmembrane proteins that contain cysteine residues. To reduce this interfering factor, a residue with state-dependent accessibility is the best target. A nonfluorescent reactive molecule, like tetraglycine maleimide, can be used to react with exposed cysteines before treatment with the fluorescent probe [36]. Another method that can be applied is blocking of cysteines with maleimide at low temperature followed by incubation at higher temperature, allowing for new channels to be inserted in the membrane to more specifically label them [54]. Another way to protect the cysteines of the ion channel is to bind them temporarily with Cd^{2+} or Zn^{2+} while nonfluorescent modification happens [55].

The use of a wide variety of fluorophores provides diverse experimental configurations for the study of structure and conformational changes of ion channels. Organic fluorophores can be employed as a pair with FP (or other organic fluorophores) to measure FRET [32, 34, 40, 41, 56] or LRET changes [57] or as donors to a transition metal ion like Ni^{2+} , Cu^{2+} , and Co^{2+} in transition metal ion FRET [52]. Furthermore, these dyes can be linked to ligands (as cAMP, cGMP, or calmodulin) [40] or toxins (charybdotoxin, agitoxin) [57] that bind to the channel and so investigate the accessibility, movement and the structural changes induced by these.

3.6 Noncanonical Amino Acids

In order to minimize the limitations encountered by the use of big-sized dyes (such as Fluorescent Proteins), recently developed alternatives in protein labeling have begun to be used in conjunction with PCF. These involve the incorporation of noncanonical amino acids in the sequence of the protein, especially fluorescent amino acids. This is achieved by the use of an evolved orthogonal pair of aminoacyl-tRNA synthetase and a tRNA from bacterial or yeast [58, 59].

One example of this family of probes is the fluorescent non-canonical amino acid that is a chemically derived from prodan (*N,N*-dimethyl-6-propionyl-2-naphthylamine), which receives the name of ANAP (3-(6-acetylnaphthalen-2-ylamino)-2-aminopropanoic acid) [60]. This probe is very sensitive to polar environments, having an emission range around 420–490 nm depending on solvent polarity [61]. To introduce ANAP into the structure of ion channels, a mutation to an amber codon (TAG) is inserted in a chosen site. ANAP has been recently used as a donor in transition metal ion FRET in conjunction with patch-clamp fluorometry experiments [42].

4 Whole-Cell Patch-Clamp Fluorometry

Whole-cell patch clamp recording has been extremely useful in the study of the intrinsic electrophysiology of many cells types, from neurons [62] and myocytes [63] to immune system cells [64], to mention a few examples. Also, this technique is practical in the study of ion channels expressed in heterologous systems using mammalian cell lines [65]. With this configuration it is possible to directly measure the membrane potential of a cell type under current-clamp and evaluate the currents across complete cells under voltage-clamp and even record neurotransmitter secretion [66].

To achieve this modality, we begin with the “cell-attached” configuration, where a high resistance seal is made. Afterward, the researcher must break the membrane inside the pipette tip without disturbing the gigaseal. Once this is achieved, the pipette solution and the cytoplasm make contact [16, 67] and the intracellular solutions is washed out and substituted by the pipette solution, which could represent an advantage (control the components of cytoplasm) or a disadvantage (reduction of the concentration of metabolites and signaling molecules that could be important to the subject of study, either ion channels, neurotransmitter receptors and electrogenic ion carriers) [68].

This important electrophysiological tool has merged with fluorescence techniques as a way to diversify the study of the relations between structure and function of membrane proteins and has been used in the study of voltage-gated potassium ion channels [69], TRPV1 channels [70], voltage-gated Ca^{2+} channels [71], and P_2X_2 receptors [72]. In this section, we discuss the materials and the procedures necessary to achieve the whole-cell patch fluorometry technique in cultured mammalian cells.

4.1 Materials

In whole-cell patch fluorometry experiments, most of the equipment mentioned early for PCF in the inside-out modality is used, so in this section we will focus in the materials and procedures to prepare this kind of experiments. We will focus on HEK cells but these procedures should work equally with other cell lines.

4.1.1 Preparation of HEK 293 Cells

One of the most common biological models used is the cell line derived from human embryonic kidney, HEK 293 [73], these cells are cultured and maintained in an incubator (3110 Water-Jacketed CO₂ Incubator, Forma Scientific) with controlled environment that contains 95% of air, 5% of CO₂ and a constant temperature of 37 °C. The medium normally used for culturing HEK 293 cells is DMEM (Sigma-Aldrich). Around 24 or 48 hours before the experimental procedure, a plasmid containing the ion channel of interest is introduced by a method called transfection. There are several protocols to do transfection which use chemical and physical methods to introduce a sequence of nucleic acid inside the cell. In our laboratory, we use the polycationic transfection agent JetPei (Polyplus transfection) that forms complexes with DNA and is endocytosed by the cells. Usually 3–5 µL of transfection agent and 100–600 ng of genetic material are required, both of which are dissolved in 100 µL of a solution of 150 mM of NaCl. Then are softly mixed and incubated for 30 minutes. Later, the mixture is carefully placed in the culture dish that contains the HEK 293 cells with fresh medium. Cells are incubated until the day of the experiment.

HEK 293 cells could be cultured in many types of dishes (*see Note 14*). Usually, bottom glassed culture dishes are used (FluoroDish, World Precision Instruments). This kind of dish is useful because it makes it easier to work with high NA objectives (*see Note 1*).

Two types of HEK 293 with different growth modes are used in the laboratory: adherent and nonadherent (called “normal” for practical purposes). This feature is important because voltage control is more accurate in rounded cells. The adherent HEK 293 cells tend to be flatter and have more cellular processes and elongations than normal HEK cells. This makes sealing and correct voltage-clamp more difficult. To avoid these two setbacks, a treatment with 300 µL 0.05% trypsin–EDTA solution (Gibco) is applied to transfected HEK 293 cells after removal of DMEM for 4–5 min. Incorporating 300 µL of DMEM interrupts the action of trypsin. After this treatment, cells detach and become rounded and float in the culture dish. Cells are now transferred to another culture dish previously prepared with fresh DMEM. This treatment is applied 2–3 h prior to the experiments (in adherent HEK cells, in the case of normal HEK cells, this span may be 4 or 5 h) to allow HEK 293 cells to partially adhere and permitting recordings in rounded cells.

4.1.2 Whole Cell Recording Solutions

Prior to patching in transfected HEK 293 cells, DMEM is slowly replaced by bath solution with a Pasteur pipette to prevent cells from detaching from the glass. It is beneficial to remember that in this patch-clamp configuration the bath solution is extracellular and the pipette solution is intracellular. Both solutions must have the same osmolarity that the medium solution and if possible, the same

temperature to avoid cellular damage. The requirements of other components of solutions can be read in the previous section “Solutions” in this chapter.

4.1.3 *Electrophysiology*

The electrophysiological recording equipment needed in patch-clamp fluorometry is also used in whole-cell experiments. The most notable difference between the whole-cell experiments and oocyte patch-clamping is the size of pipette tip. For the whole-cell configuration, these pipettes must have a diameter of 2–4 μm . They are made out using capillaries, as mentioned, but programming the pipette puller to obtain pipettes with tips around 5 μm . Then, pipette tips are fire-polished with the microforge to the diameter needed. It is relevant to mention that a bigger tip diameter helps to reduce the pipette access resistance. If the pipette tip is too narrow, the access resistance will slow down voltage-clamping and generate large voltage errors, which will distort the properties of recorded currents. This problem is more serious for inward currents because it results in completely deformed currents. It is worth mentioning that the quantity of ions, especially chloride, in the pipette solution contributes to access resistance. Thus, a larger concentration of ions reduces the access resistance.

4.2 *Methods*

In this section, we explain the steps to follow in order to obtain whole-cell recordings in HEK 293 cells. As in the “methods” section of inside-out modality of PCF, the steps described apply to channels that were labeled with genetically encoded fluorescent proteins.

4.2.1 *Election of Experimental Cell*

HEK 293 cells that are useful to perform whole-cell patch-clamp are chosen by a couple of features which facilitates making a seal, voltage-clamping and the fluorescence recording. An ideal cell is one having a diameter approximately of 15–20 μm , is as round as possible and its membrane fluorescence can be distinguished from cytoplasmic fluorescence. This selection is made with the 60x objective to better appreciate the cell conditions. When a suitable cell is located, it is centered in the vision field and the objective is changed to one with less power, usually 40x. Next, the pipette is moved into the bath solution (*see Note 15*). Again, before contacting the bath surface, positive pressure is applied to the pipette. Once in the bath, the pipette is located by its shadow and lowered at the same time that focus is adjusted. The pipette is positioned as near the cell as possible; then, the 60x objective is newly elected to do the final approach. Also, the microscope optical path is turned from ocular to camera. If this final change is made after making the seal, it is likely that the seal will be lost because of the vibration caused by the internal mechanism of the microscope during optical path changing.

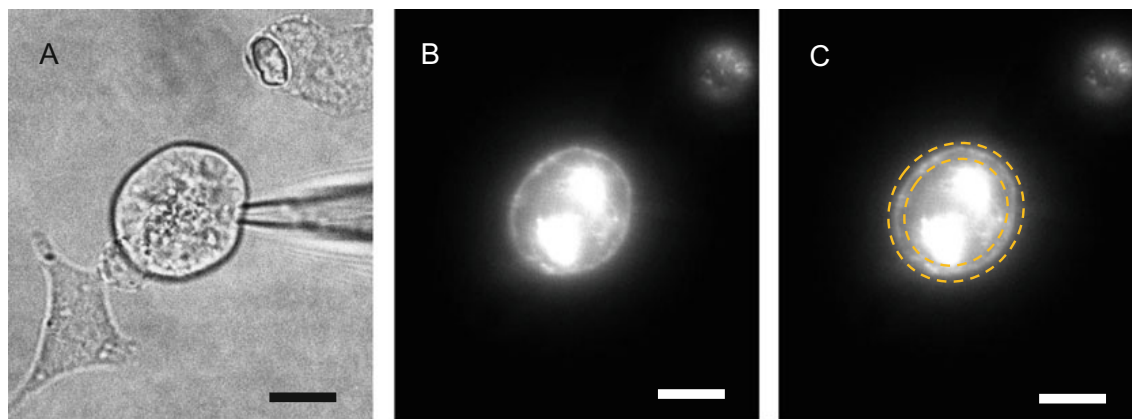


Fig. 5 Whole-cell patch-clamp fluorometry in a HEK 293 cell. Cells were expressing a fusion protein that contains a voltage-gated proton channel (Hv1) and a fluorescent protein (Venus). **(a)** Cell and pipette in light field. **(b)** Fluorescent image of the cell in A excited at 488 nm. The membrane fluorescence can be easily distinguished. **(c)** Region of interest (ROI) designed to quantify only the membrane fluorescence and discard the fluorescence of cell organelles. Scale bars, 10 μm

4.2.2 Making a Seal

Guided by the camera live image in the computer screen, contact of the pipette tip with the cell membrane could be made in two ways. In the first one, more traditional, contact is made from above the cell, placing the blurry silhouette of the pipette tip over the focused image of the cell. Later, the tip is slowly descended until the pipette resistance in the oscilloscope begins to change, indicating cell contact. The movement of the tip is stopped and positive pressure is released while a gently suction is immediately applied. The pipette resistance is monitored until the resistance reaches a value larger a 1 G Ω . It is important to remember that the current of the pipette must be zeroed before cell contact to provide a zero-current level reference.

The other form of contacting the cell membrane with the pipette tip is laterally (Fig. 5a). In this case, the tip is carefully focused in the same plane of the cell but a few microns away from the cell. Then, the tip is moved toward the membrane until the latter begins to deform. At this point, the positive pressure is released and a soft suction is immediately applied. This method is useful when the cells are still spherical or mostly rounded. When the gigaseal is reached, it is advisable to wait for a couple of minutes for it to stabilize, until the resistance value achieves several gigaohms.

4.2.3 Reaching the Whole-Cell Configuration

After seal stabilization, the patch membrane inside the pipette must be broken without losing the seal, to achieve the whole-cell configuration. This can be attained by applying one or several suction pulses with the mouth, strong enough to rupture the membrane. Another way is by using a syringe, applying negative pressure very slowly and waiting to damage the membrane inside the tip. The formation of whole-cell modality will be revealed as a sudden

increment of the capacitive current, which is caused by the increase of the membrane area being clamped. This increment depends on the cell size and the access of the pipette to the intracellular medium. Suction should be maintained until the capacitive transient becomes as fast as possible (*see Note 16*). If both bath and pipette solutions are similar to physiological extracellular and intracellular solutions, respectively, current recording can be started almost immediate. However, if the pipette solution has a different composition for experimental purposes, it is reasonable to wait between 5–7 min for the pipette solution to dialyze the cell. Also, waiting a couple of minutes before starting the experiment helps to stabilize the seal and whole-cell configuration.

4.2.4 Recording Fluorescence

When the whole-cell configuration is completed, all sources of light in the room are turned off and the cell is excited at the appropriate wavelength (Fig. 5b). The cell's fluorescence is imaged with the camera. This should be done as fast as possible to avoid photobleaching of the fluorophore. In order to record fluorescence and current simultaneously, the same components and protocols for coordinating between electrophysiology software (Patchmaster) and the image software (Micromanager) previously described (*see Subheading 3.3*) are used. These protocols can be changed as required by the experimental procedure.

4.3 Quantification of Cell Membrane Fluorescence Intensity

The images of cell membrane fluorescence obtained with the protocols are initially processed creating a specific ROI that encompasses only the membrane region (Fig. 5c). This “donut-shaped” ROI allows for exclusion of the fluorescence of vesicles and organelles, which do not contribute to membrane fluorescence. This improves the signal to noise ratio of the fluorescence recordings. As was mentioned earlier, the background fluorescence should be subtracted from the brightness value recorded in the ROI to obtain absolute fluorescence, which is the base for more complex analysis.

4.4 An Actual Experiment

As an example of a whole-cell patch clamp fluorometry experiment, we present recordings in HEK 293 cells of the fluorescence and currents of the genetically encoded voltage sensor (GEV) Arlight [74]. HEK 293 cells were transfected with 600 ng of Arlight containing plasmid (obtained from Addgene, www.addgene.org) 2 days before experiments and prepared according to the protocols presented here. After obtaining the whole-cell patch clamp configuration, the cell was held at a holding potential of -70 mV and then stepped to depolarizing voltages lasting for 500 ms. The whole cell currents (Fig. 6d) contain capacitive, leak and the sensing current of the voltage-sensing domain of Arlight. Since no linear component subtraction was applied in these recordings, it is difficult to observe

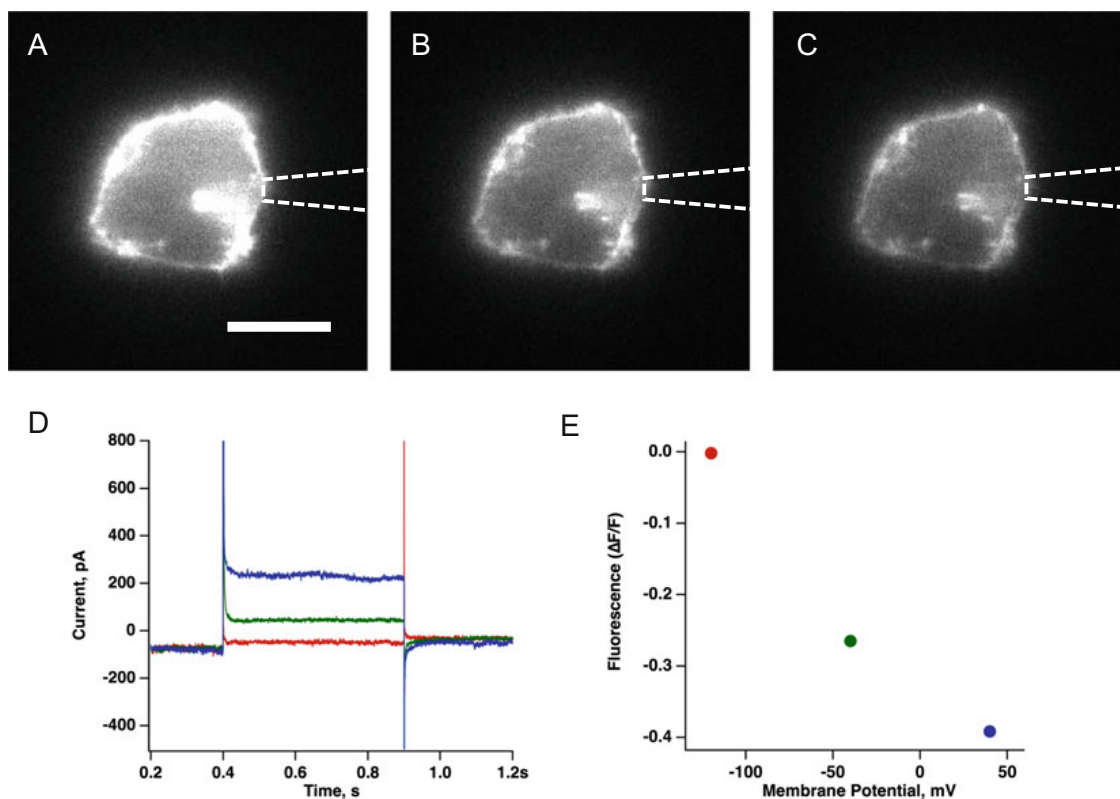


Fig. 6 Whole-cell fluorometry in a HEK 293 cell expressing the fluorescent voltage sensor protein ArcLight. The fluorescence of the same cell clamped to different voltages is imaged: (a) -120 mV, (b) -40 mV and (c) 40 mV. The excitation was achieved with the 488 nm line of an Argon ion laser and excitation was collected with a band pass filter centered at 525 nm. The outline of the patch pipette is shown by the dotted line. (d) Unsubtracted whole-cell currents are shown color coded to indicate the clamp voltage as follow. Red, -120 mV, green -40 mV and blue 40 mV. Depolarization pulses cause the voltage-sensing domain of ArcLight to change its conformation and decrease the fluorescence of the pFluorin fluorescent protein attached to it. Membrane fluorescence is quantified in (e) and shown as $\Delta F/F = ((F-F_0)/F_0)$ where F is the fluorescence in the test pulse and F_0 is the fluorescence before the test pulse). Scale bar, $10 \mu\text{m}$

the sensing currents, but they are discernible as changes in the kinetics of the capacitive transient. Fluorescence was imaged in the same conditions at all voltages, using a 300 ms exposure time. Before each positive voltage a negative pulse of 500 ms to -120 mV was applied and images were acquired during both voltage pulses. A donut-shaped ROI was drawn around the membrane area in the images in A, B and C and the total fluorescence counts were measured in ImageJ. ArcLight's fluorescence is quenched upon depolarization, which is readily visible from the cell fluorescence images. To quantify fluorescence, it is plotted as the difference between the fluorescence at each voltage (F) with respect to the fluorescence at the more negative voltage (F_0), normalized to the value F_0 . This form of presenting fluorescence data ($(F-F_0)/F_0 = \Delta F/F$) allows comparisons between different cells

or different experimental conditions. In the case of ArcLight, a negative value of $\Delta F/F$ indicates quenching of the fluorescence as a function of positive voltages, as expected [75].

5 Concluding Remarks

Patch-clamp fluorometry, in both inside-out and whole-cell configurations, is a powerful technique that allows the experimenter to probe the dynamics of ion channel function. As many techniques, it has benefitted from advances in other areas of research, such as the development and improving of fluorescent proteins, synthetic chemistry, and more recently, the expansion of the genetic code by the use of noncanonical amino acids. PCF is an approach that is seeing more and more use and that in the future will become a standard tool in the neuroscience arsenal.

6 Notes and Advice

1. Numerical aperture (NA). A high NA is preferred since it improves light collection. These objectives are usually 60 or 100 \times magnification, which also allows for better spatial patch resolution. High NA objectives have reduced working distances of a few micrometers, which means the patch should be close to the cover glass in the bottom of the recording chamber
2. Another alternative for light recording are photomultiplier tubes or photodiodes, instead of CCD cameras. These devices sacrifice imaging capabilities for the ability to record fast signals with good signal to noise ratios. Detectors like these can also be connected to beam splitting units with dichroic mirrors to allow simultaneous detections of at least two wavelengths for ratiometric fluorescence measurements.
3. Most research buildings should have a high quality grounding circuit. If a good ground does not exist, a connection to an independent physical ground or to drainage pipes of the building is suitable. It is important to emphasize the use of very low resistance material, like thick, short, copper wires. Also, it is advisable to provide a single ground point for all equipment and the use of a Faraday cage. These can be big enough to cover the whole table and everything on it or alternatively, only cover the stage of the microscope. This configuration allows easy access to all the optical components which are normally positioned on the vibration isolation table.
4. Pipettes for patch-clamp fluorometry in *Xenopus laevis* oocytes need a smooth shape and a wide aperture. To achieve this

shape, the pipette puller program should loop around eight or ten times to result in pipettes with 40–80 μm diameter, which should be heavily polished in the microforge to achieve a diameter around 10 μm .

5. Removal of the follicular cell layer. A common procedure for enzymatic removal of the follicular cell layer is to use up to 2 mg/mL of collagenase. This high concentration might be detrimental to some batches of oocytes. It is recommended to standardize the concentration beginning with 1.2 mg/mL and incubating during 30 minutes (longer times tend to reduce oocyte viability, regardless of the concentration). If after this time, approximately 50% of ovary segments are not disaggregated, the concentration should be increased. After collagenase treatment, the second wash should mostly remove the remaining follicular cells by mechanical force during agitation.
6. Variant of OR2 solution. OR2 solution has an osmolarity of 172 mOsm and lacks a carbon source. This could be detrimental to some oocytes. Sometimes OR2 can be replaced for an ND96 solution without CaCl_2 with an osmolarity of 199 mOsm, reducing the likelihood of oocyte deterioration when they are returned to ND96 after enzyme treatment. This absence of Ca^{2++} is essential to reduce the activation of proteases that can compromise the viability of oocytes.
7. Oocyte maintenance. It is known that during summertime the oocyte quality is reduced. We increase their lifetime a couple of days by adding 5% of fetal bovine serum to the ND 96 solution as well as adding antibiotic solution (Penicillin-Streptomycin) at 1%. This solution should be changed daily.
8. mRNA injection. The mRNA should remain at -20°C until the very moment of injection. Previously, defolliculated oocytes will be placed inside a 30 mm plastic petri dish with a scraped bottom in order to reduce oocyte mobility during injection. The microinjector with the injection pipette is aligned within the field of vision of the stereomicroscope. The tube of mRNA is then heated by hand and, when liquid, about 1–2 μL is placed on a clean surface, usually a small piece of Parafilm (Sigma). The drop of mRNA is immediately aspirated into the injection pipette and is ready to inject. Gently, the oocyte membrane is perforated with the pipette and 30–50 nL is injected inside the oocyte. After injection, oocytes should be kept in individual wells of a multiwell plate.
9. Removal of the vitelline membrane. The first step before placing the oocyte into the recording chamber is removal of the vitelline membrane. This membrane is transparent in almost all oocytes. Many times it can only be discovered by its absence in

small regions of the oocyte surface where the membrane makes a little protrusion. Using fine tweezers, the edge of the vitelline membrane is taken just within protrusion limits. Sometimes no edge of this membrane can be observed so a fast and delicate movement with the tweezers can be used to push into the oocyte until snagging a piece of the vitelline membrane. If this membrane is adhered to the cell membrane, this is an indicator that the oocyte is nearly dead.

10. Pipette Resistance. The resistance of the pipette in the bath solution is used as a proxy of the tip diameter. However, we must consider that the resistivity of the solution plays a major role in determining pipette resistance. Solutions with overall low electrolyte concentration or with low chloride concentration translate into a larger pipette resistance for a given size opening. Therefore, the size of the pipette tips to be used for giant patch recordings in PCF should be established using a calibrated ocular. The size of the pipettes we use is between 7 and 15 μm .
11. Obtaining a seal. This is the part that needs more practice and patience, especially with oocytes. After removing the vitelline membrane, it is important to try to obtain the patch as fast as possible. After releasing the positive pressure, suction needs to be gently but continuously applied, without losing sight of the resistance of the seal, which must rise continuously and faster as it reaches higher values. For example, at the beginning of seal establishment, resistance will rise to about 0.2–1 MOhm per second, then, after the seal reaches approximately 15 or 20 MOhm, it will increase to 2–5 MOhm per second and when the seal reaches around 50 MOhms, resistance will climb 8–10 MOhm per second, and so on until the gigaseal (larger than 1 GOhm) is obtained. Sometimes the maximum resistance is about 600 to 900 MOhm, and a gigaseal can be encouraged by changing the membrane potential, between -40 and -60 mV. If the resistance stops at lower values, then there is practically no chance of obtaining a gigaseal. The most important thing is to not lose patience and practice, practice, practice.
12. Dealing with intracellular content. It is frequent that cytosolic content near the membrane remains in the patch, even in the *inside-out* configuration. This material may represent an interference factor for fluorescence measurements, because the vesicle membrane is not subject to voltage clamp. It also results in an increase in the background signal. Therefore, the patch must be as clean as possible. When the gigaseal is achieved in the *cell-attached* configuration, the invasion of the patch by

intracellular vesicles can be observed. If this happens, an *inside-out* patch may be achieved by withdrawing the pipette very slowly. In this fashion, at the moment that the membrane is broken around the tip, intracellular content will be pulled out of the patch. This sometimes results in losing the patch because cytoplasmic contents are too attached; nonetheless, it is worth getting a clean patch. An alternative is to very gently blow into the patch trying to expel these vesicles, but the probability of breaking the seal is very high.

13. Photobleaching. Because the membrane patch will be exposed repeatedly to laser or other types of illumination, it is important to evaluate the level of photobleaching produced by it. With that intention, the extent of photobleaching for a given illumination intensity should be determined in some control patches. In addition, photobleaching of the particular fluorophore in use can be estimated by exposing oocyte membrane sheets adhered to coverslips previously treated with poly-D-lysine. If considerable photobleaching is present, a neutral density filter (ND) and low illumination intensity are chosen in order to obtain as much emission light with minimal photo destruction.
14. HEK 293 cells are to be cultured in normal plastic culture dishes while growth and transfection takes place and then sown into glass bottom culture dishes after the trypsin treatment is applied. An alternative to seeding HEK293 cells after trypsin treatment is to use round coverslips which are treated with poly-D-lysine solution to improve attachment of cells to the glass [76]. These coverslips are mounted in a special recording chamber. Round coverslips are more economic and permit higher experimental throughput.
15. In the beginning, centering the pipette tip upon the cell elected to do whole cell is difficult. To solve this, one can turn on the laser beam for a few seconds and move the pipette until it illuminates completely with the laser. When the pipette descends, only a few adjustments will be necessary to center the pipette.
16. Sometimes the membrane can be resealed under the pipette. This increases the access resistance to the cell and is undesirable. Resealing is observed as a slowdown and a reduction of capacitive current amplitude. To solve this problem, it is imperative to apply soft suction again until the capacitive current get faster and larger.

Acknowledgments

Work in the lab of LDI is supported by a grant from CONACYT No.252644; CONACYT-Fronteras de la Ciencia No.77 and DGAPA-PAPIIT IN209515.

References

- Hille B (2001) Ion channels of excitable membranes, 3rd edn. Sinauer, Sunderland, MA; [Great Britain]
- Catterall WA, Wisedchaisri G, Zheng N (2017) The chemical basis for electrical signaling. *Nat Chem Biol* 13(5):455–463. <https://doi.org/10.1038/nchembio.2353>
- Rasmussen T (2016) How do mechanosensitive channels sense membrane tension? *Biochem Soc Trans* 44(4):1019–1025. <https://doi.org/10.1042/BST20160018>
- Zheng J, Trudeau MC (2015) Handbook of Ion channels, 1st edn. CRC Press, Boca Raton, FL. <https://doi.org/10.1201/b18027>
- Ahern CA, Payandeh J, Bosmans F, Chanda B (2016) The hitchhiker's guide to the voltage-gated sodium channel galaxy. *J Gen Physiol* 147(1):1–24. <https://doi.org/10.1085/jgp.201511492>
- Doyle DA, Morais Cabral J, Pfuetzner RA, Kuo A, Gulbis JM, Cohen SL, Chait BT, MacKinnon R (1998) The structure of the potassium channel: molecular basis of K⁺ conduction and selectivity. *Science* 280(5360):69–77
- Hodgkin AL, Huxley AF (1952) A quantitative description of membrane current and its application to conduction and excitation in nerve. *J Physiol* 117(4):500–544
- Guan B, Chen X, Zhang H (2013) Two-electrode voltage clamp. In: Gamper N (ed) *Ion channels: methods and protocols*. Humana Press, Totowa, NJ, pp 79–89. https://doi.org/10.1007/978-1-62703-351-0_6
- Stefani E, Bezanilla F (1998) Cut-open oocyte voltage-clamp technique. *Methods Enzymol* 293:300–318
- Rudokas MW, Varga Z, Schubert AR, Asaro AB, Silva JR (2014) The *Xenopus* oocyte cut-open vaseline gap voltage-clamp technique with fluorometry. *J Vis Exp* (85). <https://doi.org/10.3791/51040>
- Neher E, Sakmann B, Steinbach JH (1978) The extracellular patch clamp: a method for resolving currents through individual open channels in biological membranes. *Pflugers Arch* 375(2):219–228
- Sakmann B, Neher E (1984) Patch clamp techniques for studying ionic channels in excitable membranes. *Annu Rev Physiol* 46:455–472. <https://doi.org/10.1146/annurev.ph.46.030184.002323>
- Auerbach A, Sachs F (1984) Patch clamp studies of single ionic channels. *Annu Rev Biophys Bioeng* 13:269–302. <https://doi.org/10.1146/annurev.bb.13.060184.001413>
- Islas L (2015) Patch clamping and single-channel analysis. In: *Handbook of ion channels*. CRC Press, Boca Raton, FL, pp 71–81. <https://doi.org/10.1201/b18027-9>
- Hamill OP, Marty A, Neher E, Sakmann B, Sigworth FJ (1981) Improved patch-clamp techniques for high-resolution current recording from cells and cell-free membrane patches. *Pflugers Arch* 391(2):85–100
- Neher E, Sakmann B (1992) The patch clamp technique. *Sci Am* 266(3):44–51
- Gorostiza P, Isacoff EY (2008) Nanoengineering ion channels for optical control. *Physiology (Bethesda)* 23:238–247. <https://doi.org/10.1152/physiol.00018.2008>
- Pless SA, Kim RY, Ahern CA, Kurata HT (2015) Atom-by-atom engineering of voltage-gated ion channels: magnified insights into function and pharmacology. *J Physiol* 593(12):2627–2634. <https://doi.org/10.1113/jphysiol.2014.287714>
- Lueck JD, Mackey AL, Infield DT, Galpin JD, Li J, Roux B, Ahern CA (2016) Atomic mutagenesis in ion channels with engineered stoichiometry. *Elife* 5. <https://doi.org/10.7554/eLife.18976>
- Yuchi Z, Van Petegem F (2016) Ryanodine receptors under the magnifying lens: insights and limitations of cryo-electron microscopy and X-ray crystallography studies. *Cell Calcium* 59(5):209–227. <https://doi.org/10.1016/j.ceca.2016.04.003>
- Fujiyoshi Y (2011) Electron crystallography for structural and functional studies of membrane proteins. *J Electron Microsc (Tokyo)* 60(Suppl




- 1):S149–S159. <https://doi.org/10.1093/jmicro/dfi033>
22. Payandeh J, Scheuer T, Zheng N, Catterall WA (2011) The crystal structure of a voltage-gated sodium channel. *Nature* 475(7356):353–358. <https://doi.org/10.1038/nature10238>
 23. Kaplan M, Pinto C, Houben K, Baldus M (2016) Nuclear magnetic resonance (NMR) applied to membrane-protein complexes. *Q Rev Biophys* 49:e15. <https://doi.org/10.1017/S003358351600010X>
 24. Blasic JR, Worcester DL, Gawrisch K, Gurnev P, Mihailescu M (2015) Pore hydration states of KcsA potassium channels in membranes. *J Biol Chem* 290(44):26765–26775. <https://doi.org/10.1074/jbc.M115.661819>
 25. Kulleperuma K, Smith SM, Morgan D, Musset B, Holyoake J, Chakrabarti N, Cherny VV, DeCoursey TE, Pomes R (2013) Construction and validation of a homology model of the human voltage-gated proton channel hHv1. *J Gen Physiol* 141(4):445–465. <https://doi.org/10.1085/jgp.201210856>
 26. Randolph AL, Mokrab Y, Bennett AL, Sansom MS, Ramsey IS (2016) Proton currents constrain structural models of voltage sensor activation. *Elife* 5. <https://doi.org/10.7554/eLife.18017>
 27. Blunck R (2015) Investigation of ion channel structure using fluorescence spectroscopy. In: *Handbook of ion channels*. CRC Press, Boca Raton, FL, pp 113–133. <https://doi.org/10.1201/b18027-12>
 28. Taraska JW, Zagotta WN (2010) Fluorescence applications in molecular neurobiology. *Neuron* 66(2):170–189. <https://doi.org/10.1016/j.neuron.2010.02.002>
 29. Mannuzzu LM, Moronne MM, Isacoff EY (1996) Direct physical measure of conformational rearrangement underlying potassium channel gating. *Science* 271(5246):213–216
 30. Gandhi CS, Olcese R (2008) The voltage-clamp fluorometry technique. *Methods Mol Biol* 491:213–231. https://doi.org/10.1007/978-1-59745-526-8_17
 31. Zheng J, Zagotta WN (2003) Patch-clamp fluorometry recording of conformational rearrangements of ion channels. *Sci STKE* 2003(176):PL7. <https://doi.org/10.1126/stke.2003.176.pl7>
 32. Zheng J, Zagotta WN (2000) Gating rearrangements in cyclic nucleotide-gated channels revealed by patch-clamp fluorometry. *Neuron* 28(2):369–374
 33. Kusch J, Zifarelli G (2014) Patch-clamp fluorometry: electrophysiology meets fluorescence. *Biophys J* 106(6):1250–1257. <https://doi.org/10.1016/j.bpj.2014.02.006>
 34. Taraska JW, Zagotta WN (2007) Cyclic nucleotide-regulated ion channels: spotlight on symmetry. *Structure* 15(9):1023–1024. <https://doi.org/10.1016/j.str.2007.08.004>
 35. Wang S, Lee SJ, Heyman S, Enkvetchakul D, Nichols CG (2012) Structural rearrangements underlying ligand-gating in Kir channels. *Nat Commun* 3:617. <https://doi.org/10.1038/ncomms1625>
 36. Islas LD, Zagotta WN (2006) Short-range molecular rearrangements in ion channels detected by tryptophan quenching of bimane fluorescence. *J Gen Physiol* 128(3):337–346. <https://doi.org/10.1085/jgp.200609556>
 37. Liu C, Xie C, Grant K, Su Z, Gao W, Liu Q, Zhou L (2016) Patch-clamp fluorometry-based channel counting to determine HCN channel conductance. *J Gen Physiol* 148(1):65–76. <https://doi.org/10.1085/jgp.201511559>
 38. De-la-Rosa V, Suárez-Delgado E, Rangel-Yescas GE, Islas LD (2016) Currents through Hv1 channels deplete protons in their vicinity. *J Gen Physiol* 147(2):127–136
 39. Miranda P, Giraldez T, Holmgren M (2016) Interactions of divalent cations with calcium binding sites of BK channels reveal independent motions within the gating ring. *Proc Natl Acad Sci U S A* 113(49):14055–14060. <https://doi.org/10.1073/pnas.1611415113>
 40. Trudeau MC, Zagotta WN (2003) Calcium/calmodulin modulation of olfactory and rod cyclic nucleotide-gated ion channels. *J Biol Chem* 278(21):18705–18708. <https://doi.org/10.1074/jbc.R300001200>
 41. Biskup C, Kusch J, Schulz E, Nache V, Schwede F, Lehmann F, Hagen V, Benndorf K (2007) Relating ligand binding to activation gating in CNGA2 channels. *Nature* 446(7134):440–443. <https://doi.org/10.1038/nature05596>
 42. Aman TK, Gordon SE, Zagotta WN (2016) Regulation of CNGA1 channel gating by interactions with the membrane. *J Biol Chem* 291(19):9939–9947. <https://doi.org/10.1074/jbc.M116.723932>
 43. Zheng J (2006) Patch fluorometry: shedding new light on ion channels. *Physiology (Bethesda)* 21:6–12. <https://doi.org/10.1152/physiol.00041.2005>
 44. Geibel S, Kaplan JH, Bamberg E, Friedrich T (2003) Conformational dynamics of the Na⁺/K⁺-ATPase probed by voltage clamp fluorometry. *Proc Natl Acad Sci U S A* 100

- (3):964–969. <https://doi.org/10.1073/pnas.0337336100>
45. Stuurman N, Amdodaj N, Vale R (2007) Micro-manager: open source software for light microscope imaging. *Microscopy Today* 15(3):42–43
 46. Molleman A (2003) Requirements. In: Patch clamping. John Wiley & Sons, Ltd., Chichester, pp 43–93. <https://doi.org/10.1002/0470856521.ch3>
 47. Goldin AL (1992) Maintenance of *Xenopus laevis* and oocyte injection. *Methods Enzymol* 207:266–279
 48. Soreq H, Seidman S (1992) *Xenopus* oocyte microinjection: from gene to protein. *Methods Enzymol* 207:225–265
 49. Brown AL, Johnson BE, Goodman MB (2008) Patch clamp recording of ion channels expressed in *Xenopus* oocytes. *J Vis Exp* (20):936. <https://doi.org/10.3791/936>
 50. Holmgren M, Liu Y, Xu Y, Yellen G (1996) On the use of thiol-modifying agents to determine channel topology. *Neuropharmacology* 35(7):797–804
 51. Lundblad RL (2004) Techniques in protein modification, 2nd edn. CRC Press, Boca Raton, FL
 52. Taraska JW, Puljung MC, Olivier NB, Flynn GE, Zagotta WN (2009) Mapping the structure and conformational movements of proteins with transition metal ion FRET. *Nat Methods* 6(7):532–537
 53. Taraska JW, Zagotta WN (2007) Structural dynamics in the gating ring of cyclic nucleotide-gated ion channels. *Nat Struct Mol Biol* 14(9):854–860. <https://doi.org/10.1038/nsmb1281>
 54. Loots E, Isacoff EY (2000) Molecular coupling of S4 to a K(+) channel's slow inactivation gate. *J Gen Physiol* 116(5):623–636
 55. Puljung MC, Zagotta WN (2011) Labeling of specific cysteines in proteins using reversible metal protection. *Biophys J* 100(10):2513–2521. <https://doi.org/10.1016/j.bpj.2011.03.063>
 56. Kusch J, Biskup C, Thon S, Schulz E, Nache V, Zimmer T, Schwede F, Benndorf K (2010) Interdependence of receptor activation and ligand binding in HCN2 pacemaker channels. *Neuron* 67(1):75–85. <https://doi.org/10.1016/j.neuron.2010.05.022>
 57. Posson DJ, Ge P, Miller C, Bezanilla F, Selvin PR (2005) Small vertical movement of a K+ channel voltage sensor measured with luminescence energy transfer. *Nature* 436(7052):848–851. <https://doi.org/10.1038/nature03819>
 58. Liu CC, Schultz PG (2010) Adding new chemistries to the genetic code. *Annu Rev Biochem* 79:413–444. <https://doi.org/10.1146/annurev.biochem.052308.105824>
 59. Serfling R, Coin I (2016) Incorporation of unnatural amino acids into proteins expressed in mammalian cells. *Methods Enzymol* 580:89–107. <https://doi.org/10.1016/bs.mic.2016.05.003>
 60. Lee HS, Guo J, Lemke EA, Dimla RD, Schultz PG (2009) Genetic incorporation of a small, environmentally sensitive, fluorescent probe into proteins in *Saccharomyces cerevisiae*. *J Am Chem Soc* 131(36):12921–12923. <https://doi.org/10.1021/ja904896s>
 61. Chatterjee A, Guo J, Lee HS, Schultz PG (2013) A genetically encoded fluorescent probe in mammalian cells. *J Am Chem Soc* 135(34):12540–12543. <https://doi.org/10.1021/ja4059553>
 62. Segev A, Garcia-Oscos F, Kourrich S (2016) Whole-cell patch-clamp recordings in brain slices. *J Vis Exp* (112). <https://doi.org/10.3791/54024>
 63. Li S, Deng Z, Wei L, Liang L, Ai W, Shou X, Chen X (2011) Reduction of large-conductance Ca²⁺-activated K(+) channel with compensatory increase of nitric oxide in insulin resistant rats. *Diabetes Metab Res Rev* 27(5):461–469. <https://doi.org/10.1002/dmrr.1196>
 64. Cherny VV, Murphy R, Sokolov V, Levis RA, DeCoursey TE (2003) Properties of single voltage-gated proton channels in human eosinophils estimated by noise analysis and by direct measurement. *J Gen Physiol* 121(6):615–628. <https://doi.org/10.1085/jgp.200308813>
 65. Gandini MA, Sandoval A, Felix R (2014) Whole-cell patch-clamp recording of recombinant voltage-sensitive Ca²⁺ channels heterologously expressed in HEK-293 cells. *Cold Spring Harb Protoc* 2014(4):396–401. <https://doi.org/10.1101/pdb.prot073213>
 66. Sontheimer H, Olsen ML (2007) Whole-cell patch-clamp recordings. In: Walz W (ed) Patch-clamp analysis: advanced techniques. Humana Press, Totowa, NJ, pp 35–68. https://doi.org/10.1007/978-1-59745-492-6_2
 67. Cahalan M, Neher E (1992) Patch clamp techniques: an overview. *Methods Enzymol* 207:3–14
 68. Molleman A (2003) Basic theoretical principles. In: Patch clamping. John Wiley & Sons, Ltd., Chichester, pp 5–42. <https://doi.org/10.1002/0470856521.ch2>

69. Kobrinsky E, Stevens L, Kazmi Y, Wray D, Soldatov NM (2006) Molecular rearrangements of the Kv2.1 potassium channel termini associated with voltage gating. *J Biol Chem* 281(28):19233–19240. <https://doi.org/10.1074/jbc.M601231200>
70. Yang F, Cui Y, Wang K, Zheng J (2010) Thermosensitive TRP channel pore turret is part of the temperature activation pathway. *Proc Natl Acad Sci U S A* 107(15):7083–7088. <https://doi.org/10.1073/pnas.1000357107>
71. Kobrinsky E, Tiwari S, Maltsev VA, Harry JB, Lakatta E, Abernethy DR, Soldatov NM (2005) Differential role of the alpha1C subunit tails in regulation of the Cav1.2 channel by membrane potential, beta subunits, and Ca²⁺ ions. *J Biol Chem* 280(13):12474–12485. <https://doi.org/10.1074/jbc.M412140200>
72. Fisher JA, Girdler G, Khakh BS (2004) Time-resolved measurement of state-specific P2X₂ ion channel cytosolic gating motions. *J Neurosci* 24(46):10475–10487. <https://doi.org/10.1523/JNEUROSCI.3250-04.2004>
73. Graham FL, Smiley J, Russell WC, Nairn R (1977) Characteristics of a human cell line transformed by DNA from human adenovirus type 5. *J Gen Virol* 36(1):59–74. <https://doi.org/10.1099/0022-1317-36-1-59>
74. Jin L, Han Z, Platasa J, Woollorton JRA, Cohen LB, Pieribone VA (2012) Single action potentials and subthreshold electrical events imaged in neurons with a fluorescent protein voltage probe. *Neuron* 75(5):779–785
75. Han Z, Jin L, Chen F, Loturco JJ, Cohen LB, Bondar A, Lazar J, Pieribone VA (2014) Mechanistic studies of the genetically encoded fluorescent protein voltage probe ArcLight. *PLoS One* 9(11):e113873
76. Heuser J (2000) The production of ‘cell cortices’ for light and electron microscopy. *Traffic* 1(7):545–552. <https://doi.org/10.1034/j.1600-0854.2000.010704.x>

ARTICLE

K_V1.2 channels inactivate through a mechanism similar to C-type inactivation

 Esteban Suárez-Delgado¹, Teriws G. Rangel-Sandín¹, Itzel G. Ishida², Gisela E. Rangel-Yescas¹, Tamara Rosenbaum³, and León D. Islas¹

Slow inactivation has been described in multiple voltage-gated K⁺ channels and in great detail in the *Drosophila Shaker* channel. Structural studies have begun to facilitate a better understanding of the atomic details of this and other gating mechanisms. To date, the only voltage-gated potassium channels whose structure has been solved are KvAP (x-ray diffraction), the K_V1.2-K_V2.1 “paddle” chimera (x-ray diffraction and cryo-EM), K_V1.2 (x-ray diffraction), and ether-à-go-go (cryo-EM); however, the structural details and mechanisms of slow inactivation in these channels are unknown or poorly characterized. Here, we present a detailed study of slow inactivation in the rat K_V1.2 channel and show that it has some properties consistent with the C-type inactivation described in *Shaker*. We also study the effects of some mutations that are known to modulate C-type inactivation in *Shaker* and show that qualitative and quantitative differences exist in their functional effects, possibly underscoring subtle but important structural differences between the C-inactivated states in *Shaker* and K_V1.2.

Introduction

Voltage-dependent potassium channels undergo several types of gating processes that limit the conductance on a time-dependent manner. Among the many gating transitions of this type is a slow inactivation process termed C-type inactivation. Although it was described 29 yr ago (Hoshi et al., 1991), this slow process is still not fully understood (Hoshi and Armstrong, 2013).

Inactivation processes in potassium channels have different functional manifestations and molecular origins (Hoshi et al., 1991; Kurata and Fedida, 2006). While rapid, ball-and-chain type inactivation is mediated by the N-terminus or β-subunits in *Shaker*-type channels (Hoshi et al., 1990; Rettig et al., 1994; Vergara-Jaque et al., 2019), slow inactivation is a more subtle process which likely involves conformational changes in the pore domain and the selectivity filter (De Biasi et al., 1993). Slow inactivation has been divided into C-, P-, and U-types, which might be unique or coexist in the same channel. Their different corresponding molecular mechanisms, if they exist, are not clear (Loots and Isacoff, 1998; Cordero-Morales et al., 2007; Cheng et al., 2011; Bähring et al., 2012). In this paper, we will use the term slow inactivation, which in this case might be identified with the C-type inactivation amply described in *Drosophila Shaker* channels with genetically removed fast inactivation (Hoshi et al., 1990; Klemic et al., 2001).

K_V1.2 are mammalian *Shaker*-like potassium channels that possess up to 82% homology with the *Drosophila Shaker* gene

product and have become an indispensable model for biophysical studies of potassium channels, principally because of the availability of structures determined by x-ray diffraction as well as cryo-EM (Long et al., 2005; Pau et al., 2017; Matthies et al., 2018). These structures serve as templates to interpret biophysical data arising from other voltage-gated potassium channels. As mentioned, another important model in channel biophysics is the *Shaker* channel, especially mutants in which fast N-type inactivation has been removed. However, no high-resolution structures of *Shaker* exist, and all experimental observations in *Shaker* are interpreted using the K_V1.2 structures or computational models based on K_V1.2. Recently, a structure determined by cryo-EM was obtained for the K_V1.2 channel in nanodiscs (Matthies et al., 2018) and it was suggested that the structure might possibly correspond to a C-type slow-inactivated state. However, no comprehensive description of slow inactivation of K_V1.2 is available, although previous work has indicated the presence of a slow inactivation process as well as feasible similarities between *Shaker* C-type inactivation and slow inactivation in K_V1.2 (Cordero-Morales et al., 2011). Our goal in this work was to characterize the inactivation process in rat K_V1.2 channels and investigate the effect of some equivalent mutants that in *Shaker* channels affect C-type inactivation. We found that K_V1.2 channels are slower to inactivate than *Shaker*

¹Departamento de Fisiología, Facultad de Medicina, Universidad Nacional Autónoma de México, Mexico City, Mexico; ²Rockefeller University, New York, NY; ³Instituto de Fisiología Celular, Universidad Nacional Autónoma de México, Mexico City, Mexico.

Correspondence to León D. Islas: leon.islas@gmail.com

This work is part of the special collection entitled “Electrical Signaling in the Heart and Nervous System: A Joint Meeting of the Society of General Physiologists and Latin American Society of Biophysicists.”

© 2020 Suárez-Delgado et al. This article is distributed under the terms of an Attribution–Noncommercial–Share Alike–No Mirror Sites license for the first six months after the publication date (see <http://www.rupress.org/terms/>). After six months it is available under a Creative Commons License (Attribution–Noncommercial–Share Alike 4.0 International license, as described at <https://creativecommons.org/licenses/by-nc-sa/4.0/>).

and that, although this might be identified with C-type inactivation, the effects of mutations and ions are sufficiently distinctive to suggest that the detailed slow inactivated conformation of $K_v1.2$ is different from that of *Shaker*.

Materials and methods

Channels, mutagenesis, and oocyte injection

The rat $K_v1.2$ channel in the pMAX plasmid was a gift from B. Roux (University of Chicago, Chicago, IL). Mutagenesis was performed by a single PCR reaction using the KOD Hot Start DNA polymerase (Novagen) and appropriate mutagenic oligonucleotides (Sigma-Aldrich). Mutants were confirmed first by restriction essays and finally by sequencing at the Molecular Biology Facility at the Instituto de Fisiología Celular, Universidad Nacional Autónoma de México. WT $K_v1.2$ and the generated mutants' cDNA were linearized with *PacI* endonuclease. mRNA was synthesized from linearized cDNA with the T7 polymerase mMessage mMachine kit (Ambion) and resuspended in pure H_2O at a concentration of 0.5–1 $\mu\text{g}/\mu\text{l}$.

Xenopus laevis handling was done according to National Institutes of Health standards (National Research Council, 2010). Stage VI oocytes were obtained by surgery after frogs were anesthetized with tricaine (2.2 mg/ml). Oocyte defolliculation was achieved first by mechanical separation with fine tweezers and then by enzymatic treatment with collagenase type IA (Sigma-Aldrich) at a concentration of 1.2 mg/ml in calcium-free OR2 medium for 30 min. After thorough washing in calcium-free ND96 solution for 30 min, oocytes were kept in regular ND96 solution. Healthy oocytes were microinjected with ~ 40 nl of $K_v1.2$ WT or mutant mRNA 1 d after surgery, and experiments were performed 2–6 d after injection. For patch-clamp recording, the vitelline membrane was mechanically removed with fine tweezers before the experiments.

Electrophysiology

Two-electrode voltage-clamp (TEVC)

Ionic and gating current recordings were performed using a TEVC (Warner Instruments, OC-725C). Glass microelectrodes were fabricated in a P-97 micropipette puller (Sutter Instruments) from borosilicate glass capillaries (Sutter Instruments, BF150-86-10) and had a resistance of 1–2 $M\Omega$ when filled with 3 M KCl and dipped in ND96 solution. Current was filtered at 3 kHz with an analogue filter (Frequency Devices) and sampled at 10 kHz. Ionic currents were recorded in response to voltage-clamp pulses and using a $-p/4$ subtraction protocol to remove linear components of the current. Currents obtained from long pulses were not subtracted.

Gating currents were recorded in TEVC with ND96 as external solution. Linear current components were subtracted using a $-p/4$ subtraction protocol. Gating currents were sampled at 28 kHz. 10 sweeps were averaged at each voltage. These recordings were obtained from the double mutants: W366F/V381T, W366F/V381A, and W366F/V381I. The mutants W366F/V381W and W366F/V381L did not show functional expression.

Voltage control and current recording were accomplished with the freely available program WinWCP running on a

Windows XP PC (J. Dempster, University of Strathclyde, Glasgow, Scotland, UK; Dempster, 2001) and a National Instruments card (NI USB-6251). All recordings were performed in ND96 as the bath solution unless otherwise indicated in the text. For 100 mM K^+ external solutions, NaCl in ND96 was reduced to 10 mM. When external TEA was proved, TEA-Cl equimolarly replaced NaCl.

Patch-clamp

Currents in the inside-out configuration of the patch-clamp were recorded with an Axopatch 200-B amplifier (Molecular Devices) and an Instrutech ITC-18 interface (HEKA Elektronik) controlled by PatchMaster software (HEKA Elektronik). Pipettes had resistance of 0.5–1 $M\Omega$ and were filled with a solution containing (in mM): 60 KCl, 60 NaCl, 3 HEPES, and 1.8 $CaCl_2$, pH 7.4 (KOH). The bath solution contained (in mM): 130 KCl, 3 HEPES, and 1 EDTA, pH 7.4 (KOH). For nonstationary noise analysis, 50–300 current sweeps were recorded, filtering at 10 kHz and sampling at 50 kHz in response to a pulse from -90 to 100 mV with duration of 100 ms. No subtraction of linear current components was applied. The variance was calculated from the current sweeps using pairwise subtraction to reduce the influence of channel run-down or run-up (Heinemann and Conti, 1992). The variance versus mean relationship was plotted and fitted to the equation (Sigworth, 1980)

$$\sigma^2 = i\langle I \rangle - \frac{\langle I \rangle^2}{N}. \quad (1)$$

In this equation, σ^2 is the variance of the current, i is the unitary channel current, N is the number of channels in the patch, and $\langle I \rangle$ is the current average. The channel open probability, P_o , was obtained from these parameters as $P_o = \langle I \rangle / iN$.

Data analysis

Analysis was performed with procedures written in-house in Igor Pro 6.0 (Wavemetrics). The conductance, $G(V)$, at each voltage, V , was measured from steady-state ionic currents, I , as: $G = I / (V - V_{rev})$, where V_{rev} is the reversal potential. For inactivating currents, the peak current was measured to calculate the peak conductance. The normalized conductance was defined as G/G_{max} , where G_{max} is the conductance at 50 mV. G/G_{max} as a function of voltage, V , was fitted to a Boltzmann-like function,

$$\frac{G}{G_{max}} = \left(\frac{1}{1 + K_o \exp^{z_{app} V / K_B T}} \right)^4. \quad (2)$$

This equation assumes the sequential movement of four identical subunits with apparent charge movement per subunit given by z_{app} . The parameter K_o describes the position of the curve along the V -axis. K_B is the Boltzmann constant, and T is the temperature in Kelvin. We find that this equation provides a better fit to the G - V curves than a simple Boltzmann function.

The slow ionic current decay elicited by long, 20-s pulses was fitted to the equation

$$I(t) = B(A_1 e^{-t/\tau_1} + A_2 e^{-t/\tau_2}). \quad (3)$$

The constant, B , is a scaling factor, A_i is the amplitude of the slow and fast components, and τ_i is the time constant.

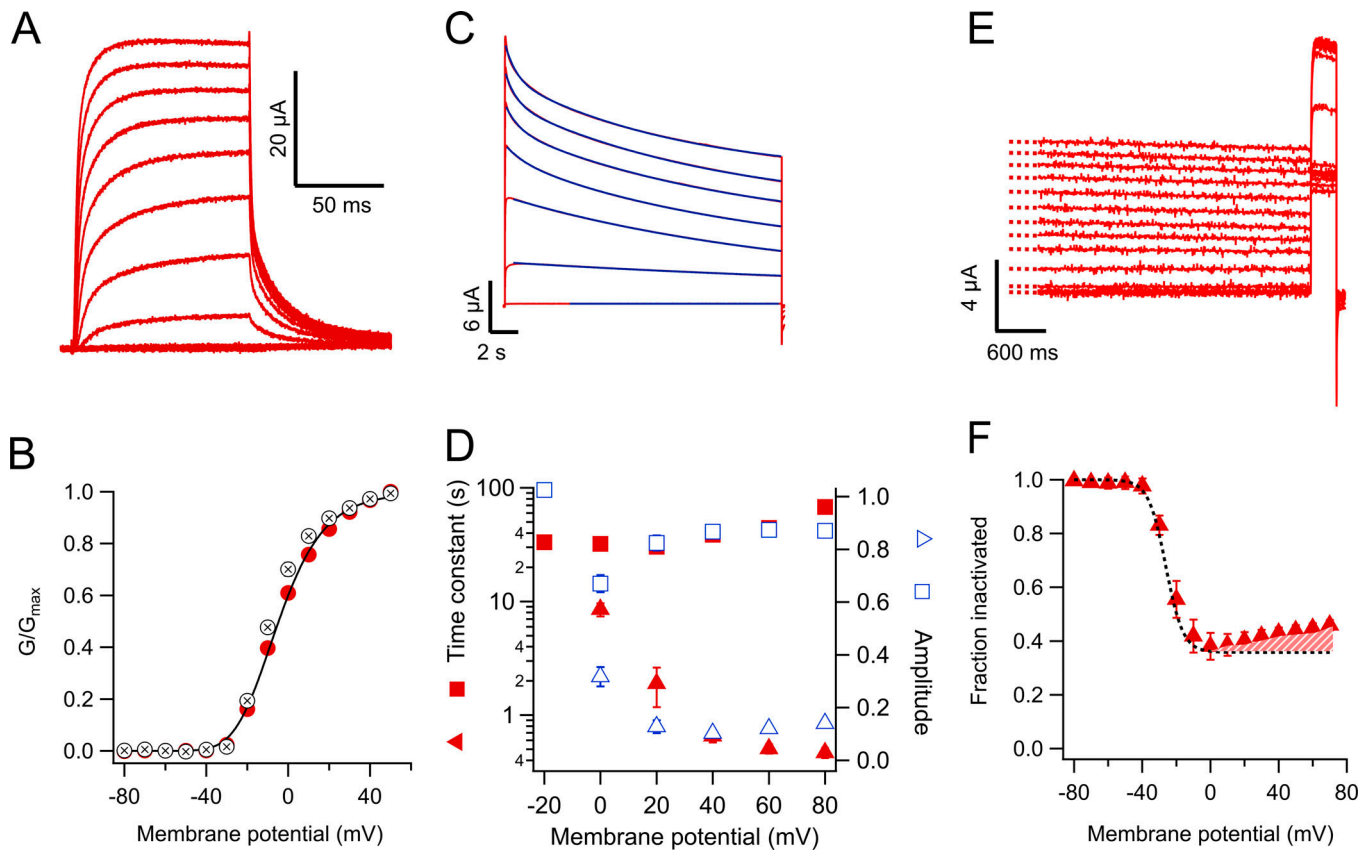


Figure 1. $K_v1.2$ WT channels slow-inactivate incompletely. (A) Currents in response to short voltage-clamp pulses to 50 mV applied from a holding potential of -80 mV and lasting 100 ms. Tail currents are observed upon return to a potential of -30 mV. (B) Voltage dependence of the normalized conductance at the test potential (red circles) or the normalized size of the tail current at the beginning of the -30 mV pulse. The data are the mean and error bars are the SEM from $n = 7$ oocytes (conductance) or $n = 15$ (tails). The black curve is the fit of the conductance data to Eq. 2 with parameters $K_o = 0.13$, $z_{app} = 1.77 e_o$. (C) Currents in response to long (20-s) pulses from -40 to 80 mV in 20-mV steps. The current slowly decays in amplitude as a result of a slow inactivation process. The decay kinetics can be fitted by a sum of two exponential functions. The fit to Eq. 3 is shown by the continuous blue lines, except the -20 mV trace, which was fitted to a single exponential. (D) Inactivation time constants are plotted as a function of voltage. The filled square symbols are the slow time constant, and the filled triangles are the fast time constant. Amplitudes are shown by empty symbols. (E) Protocol to determine the voltage dependence of steady-state inactivation at the end of a 20-s pulse. The current elicited by a 50-mV pulse and 300-ms duration after the long 20-s pulses is reduced as a consequence of accumulated inactivation. (F) Quantitation of the steady-state inactivation in an h_∞ -like curve. Note that inactivation is relieved at voltages more positive than 20 mV. The dashed black curve is the fit of a Boltzmann-like function to the data from -80 to 0 mV, with an apparent valence of $5 e_o$. The difference at positive voltages between the fit and the data emphasizes the U-type inactivation character of the process.

Steady-state inactivation was assessed with a conventional prepulse protocol. For WT $K_v1.2$, the prepulse had duration of 20 s and was changed from -80 to 70 mV in 10-mV increments. Then the voltage was brought to 50 mV during 300 ms. For the W366F mutant, the prepulse lasted 300 ms and was carried from -120 to 10 mV in 10-mV increments. After the prepulse, the voltage was stepped to 50 mV for 100 ms.

The current at the 50-mV pulse was normalized and plotted as a function of prepulse voltage. These data were fitted to the following equation:

$$\frac{I}{I_{max}} = I_{max} + (I_{max} - I_{min}) \left(\frac{1}{1 + K_o \exp\left(\frac{z_{app} V}{K_B T}\right)} \right). \quad (4)$$

The ON-gating currents were integrated numerically to obtain the charge movement, Q_{on} . Q_{on} was plotted as a function of voltage and fitted to the equation

$$Q_{on}(V) = \left[\frac{a}{1 + \exp^{q(V-V_{1/2})/K_B T}} \right] + \left[\frac{b}{1 + \exp^{q'(V-V'_{1/2})/K_B T}} \right]. \quad (5)$$

This equation assumes two main components of charge movement, q and q' , with amplitudes a and b and midpoints of charge movement given by the values of $V_{1/2}$ and $V'_{1/2}$.

The voltage dependence of any given time constant was fitted to the equation

$$\tau(V) = \tau_o \cdot \exp\left(\frac{qV}{K_B T}\right). \quad (6)$$

Here, τ_o is the value of the time constant at 0 mV, q is the partial charge, and V , K_B , and T have the same meaning as in the previous equations.

Molecular modeling

Mutations were introduced in the $K_v1.2$ - $K_v2.1$ paddle chimera channel (PDB accession no. 2R9R; Long et al., 2007) using the

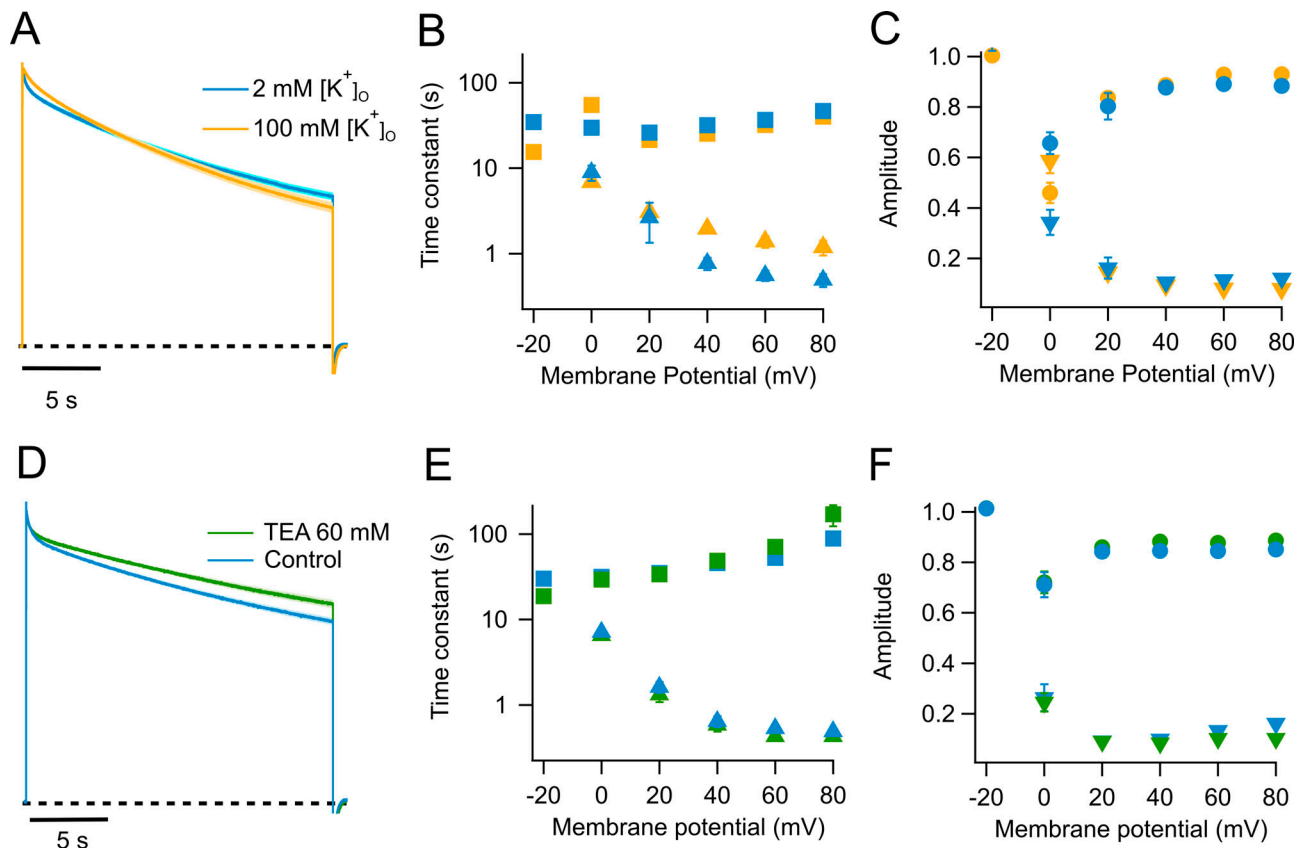


Figure 2. **Effect of extracellular potassium and TEA on slow inactivation in WT Kv1.2.** (A) Outward currents in response to a 60-mV, 20-s pulse. The blue trace is the normalized average current from eight experiments recorded in 2 mM external K⁺. The yellow trace is the normalized average current from eight traces recorded in the presence of 100 mM external K⁺. (B) Quantitation of the effect of potassium on the time constants of inactivation. The color code is the same as in A; squares, slow time constant; triangles, fast time constant. (C) Amplitudes of the fast (inverted triangles) and slow (circles) components are plotted. (D) Effect of external TEA on the kinetics of slow inactivation. The blue trace is the normalized average current at 60 mV from seven traces in the absence of TEA and at 2 mM external potassium. The green trace is the normalized average current from seven sweeps in the presence of 60 mM external TEA also with 2 mM external potassium. (E) Effect of TEA in the slow (squares) and fast (triangles) time constants. (F) Effect of TEA on the amplitudes of the fast (inverted triangles) and slow (circles) time constants. In A and D, the light-colored shade along the current trace is the SEM. Error bars in B, C, E, and F are ± SEM.

mutagenesis module in PyMol. The rotamers with fewer molecular clashes were chosen to represent the final model. Structural figures were rendered in PyMol.

Results

As previously shown (Roberds and Tamkun, 1991; Tao and MacKinnon, 2008; Ishida et al., 2015), Kv1.2 produces steeply voltage-dependent, outward-rectifying potassium currents (Fig. 1, A and B). In the absence of coexpression with a β-subunit, these currents do not inactivate in a time scale of milliseconds; however, when long positive voltage pulses (20 s) are applied, the currents decay with a double-exponential time course with time constants of ~1 and 40 s at voltages more positive than 20 mV, with the slow component contributing the majority of the amplitude (Fig. 1, C and D). At 40 mV and after 20 s, 49.2 ± 0.21% of the current remains (Fig. 1 F). For comparison, the slow inactivation in *Shaker* channels with the N-terminal inactivation particle removed is also biexponential with comparable time constants ~4 and 24 s, but the reduction of current at the end of

the pulse is more complete (Olcese et al., 1997). At steady state, the voltage dependence of inactivation, evaluated by a prepulse experiment, is very steep, with an apparent voltage dependence equivalent to ~5 e₀ (Fig. 1, E and F). Steady-state slow inactivation is incomplete and nonmonotonic, becoming less prominent at potentials more positive than 0 mV. This is evidenced by the deviation of the sigmoidal fit at positive potentials (Fig. 1 F, dashed area). This behavior is reminiscent of the U-type or closed-state dependent inactivation, which has been described in other voltage-dependent potassium channels (Klemic et al., 1998).

An important hallmark of C-type inactivation in other channels is its modulation by extracellular cations, in particular potassium ions. Higher potassium extracellular concentrations ([K⁺]_o) slow down the inactivation rate in *Shaker* (López-Barneo et al., 1993). We find that inactivation of Kv1.2 channels is also slowed down by increased [K⁺]_o (Fig. 2 A), although the effect is not as large as in *Shaker*. The main effect of elevated potassium is to slow down the fast component of inactivation, from ~0.5 to 1.4 s at 60 mV, while the slow time constant is left almost intact

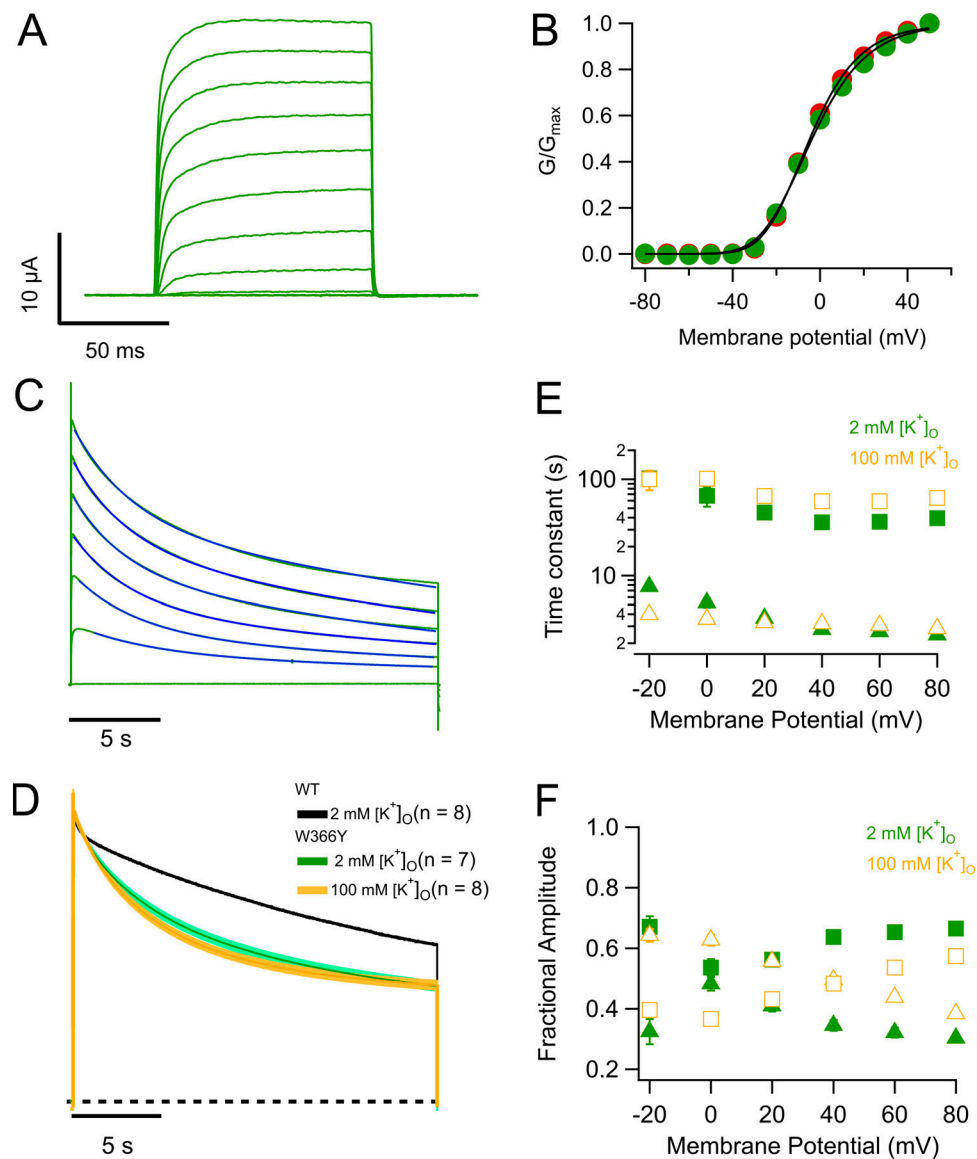


Figure 3. Mutation W366Y accelerates slow inactivation. (A) Ionic currents in response to 100-ms depolarizing pulses from -80 to 50 mV in 10 -mV steps, from a holding potential of -80 mV. Currents are very similar to WT channels. (B) Comparison of the voltage dependence of W366Y and WT $K_{V1.2}$. The normalized conductance of both channel types is plotted as a function of voltage. Red circles correspond to WT and green circles to W366Y. The continuous curve corresponds to the fit to Eq. 2 with parameters $z_{app} = 1.77 e_o$, $K_o = 0.135$ (WT); $z_{app} = 1.59 e_o$, $K_o = 0.149$ (W366Y). (C) Mutant channels also inactivate slowly and more completely than WT channels. Blue lines are the fit to Eq. 3. (D) High potassium speeds up inactivation. Green trace is the normalized average current at 60 mV from seven oocytes in the presence of 2 mM external K^+ . The yellow trace is the normalized current average from eight oocytes in 100 mM external K^+ . In both cases, the shaded areas represent \pm SEM. The black dashed curve is the average WT current time course, also at 60 mV. (E) Voltage dependence of the time course of slow inactivation. Filled symbols are the slow and fast time constants in ND96 extracellular medium ($[K^+]_o = 2$ mM). Empty symbols are the slow and fast time constants in the presence of 100 mM extracellular potassium. Squares are the slow time constant and triangles the fast time constant. (F) Amplitudes of the two components in E. Squares are the slow time constant amplitude and triangles the fast time constant amplitude. Error bars in B, E, and F are \pm SEM.

(Fig. 2 B). The rate of slow inactivation can also be modulated by extracellular TEA. We have used a higher concentration of extracellular TEA, since the apparent K_d for TEA block in $K_{V1.2}$ is ~ 500 mM (Grissmer et al., 1994), unlike what is reported in *Shaker*, with a K_d of 18 mM (González-Pérez et al., 2008). Addition of 60 mM TEA to the bath decelerates inactivation, mostly affecting the slow time constant. At 60 mV, it increases from ~ 50 to 72 s (Fig. 2 E). This effect is quantitative and qualitatively different from the effect of 100 mM external potassium (Fig. 2,

D–F). The response of $K_{V1.2}$ with respect to addition of external K^+ and TEA is a hallmark of C-type inactivation as seen in *Shaker* (Choi et al., 1991; López-Barneo et al., 1993; Molina et al., 1997; Andalib et al., 2004). To assess if this slow inactivation is similar to P/C-type slow inactivation, we investigated in $K_{V1.2}$ the effects of some *Shaker* mutants that have helped define this type of inactivation.

In *Shaker* channels, a tryptophan residue at position 434 (W434) is very important in modulating C-type inactivation

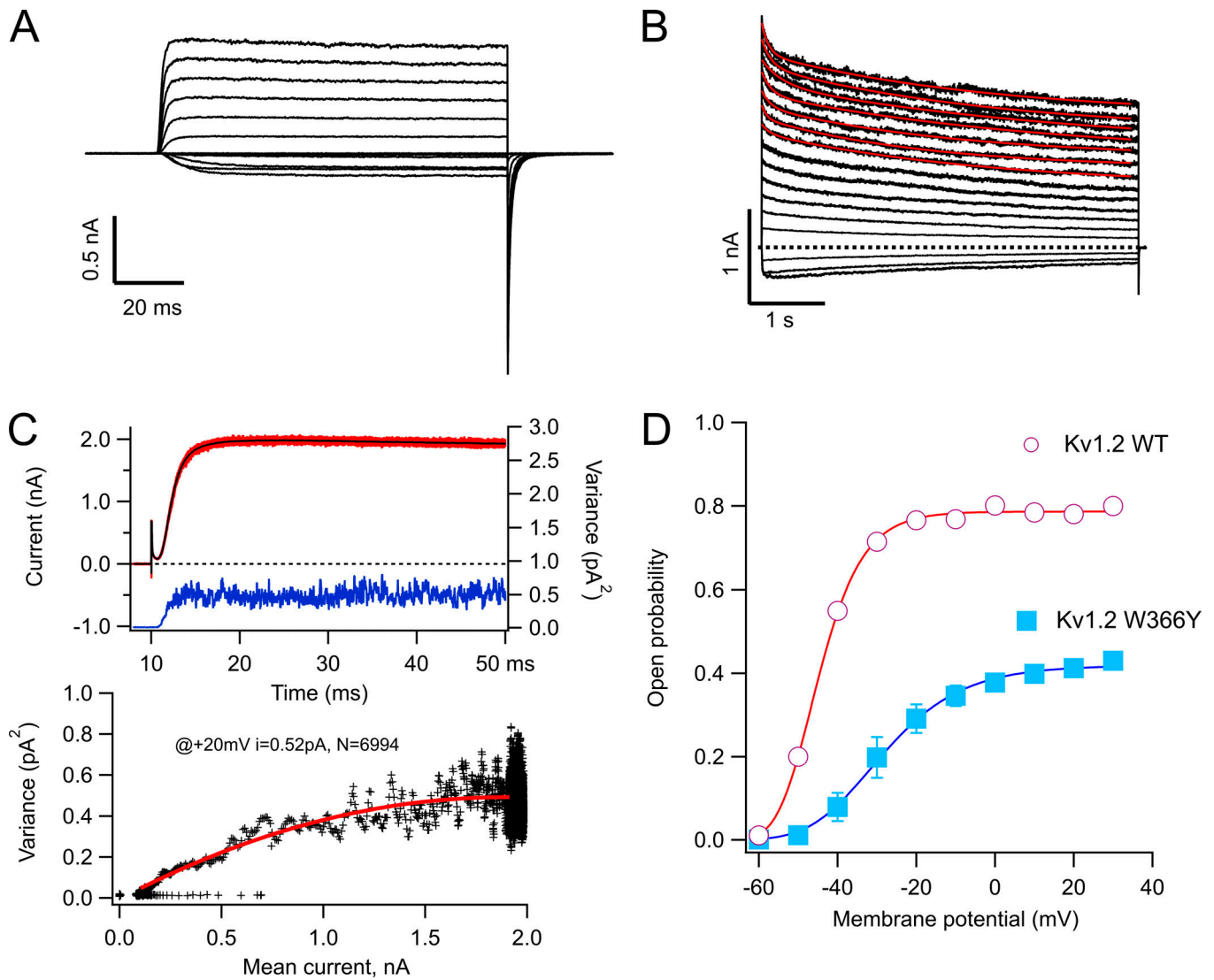


Figure 4. The W366Y mutant induces a rapidly equilibrating state occurring after the open state. (A) Inside-out patch recording of potassium currents through W366Y channels. Currents were elicited by voltage pulses of 100-ms duration, from -60 to 30 mV from a holding potential of -90 mV. (B) Slow inactivation is also present in cell-free recordings and is incomplete at the end of 5-s pulses. The inside-out data show that inactivation proceeds via two exponentials, comparably to the behavior of currents obtained in TEVC (red curves are fit to a double-exponential function). (C) Nonstationary noise analysis of currents at 20 mV. In the upper panel, 100 current sweeps are shown in red with the mean current plotted in black. The blue trace is the point-by-point variance calculated from the 100 traces. The bottom panel shows the mean–variance relationship (black crosses) with the fit to Eq. 1 shown in red. The parameters of the fit are $I = 0.52$ pA, $n = 6,994$. (D) The voltage dependence of activation of WT (red circles) and W366Y (blue squares) channels. The amplitude of the tail current at the end of 100-ms pulses is plotted as a function of the voltage of the pulse and is normalized to the maximum open probability obtained from noise measurements as in C. Data are mean \pm SEM. WT, $n = 10$; W366Y, $n = 7$.

(Perozo et al., 1993; Yang et al., 1997; Pless et al., 2013), and the mutation W434Y has been shown to produce channels with accelerated inactivation (Cordero-Morales et al., 2011). Surprisingly, the equivalent mutant in $K_v1.2$, W366Y, produced channels that upon first inspection seem very similar to WT. The channels activate in a voltage-dependent fashion and over a range of voltages almost identical to that of WT (Fig. 3, A and B). Long depolarizing pulses also induce inactivation of the currents, with a double-exponential time course that is faster than in WT (Fig. 3, C and D). The inactivation process in W366Y is also sensitive to extracellular potassium, but for this mutant it becomes slightly more prominent than the effect of $[K^+]_o =$

100 mM on WT (Fig. 3 D). Interestingly, in this mutant potassium does not change the fast constant much and increases the slow time constants, also increasing the amplitude of the fast time constant and reducing the amplitude of the slow one, resulting in an overall speeding up of the decay of the current (Fig. 3, E and F).

To better understand the gating behavior of this mutant, we performed patch-clamp experiments. As seen in TEVC, the ionic currents recorded from inside-out patches of W366Y in response to short depolarizations are similar to WT (Fig. 4 A). The slow inactivation elicited by longer pulses (5 s) is also present and occurs along a double-exponential time course (Fig. 4 B). With the purpose of estimating gating parameters, we performed

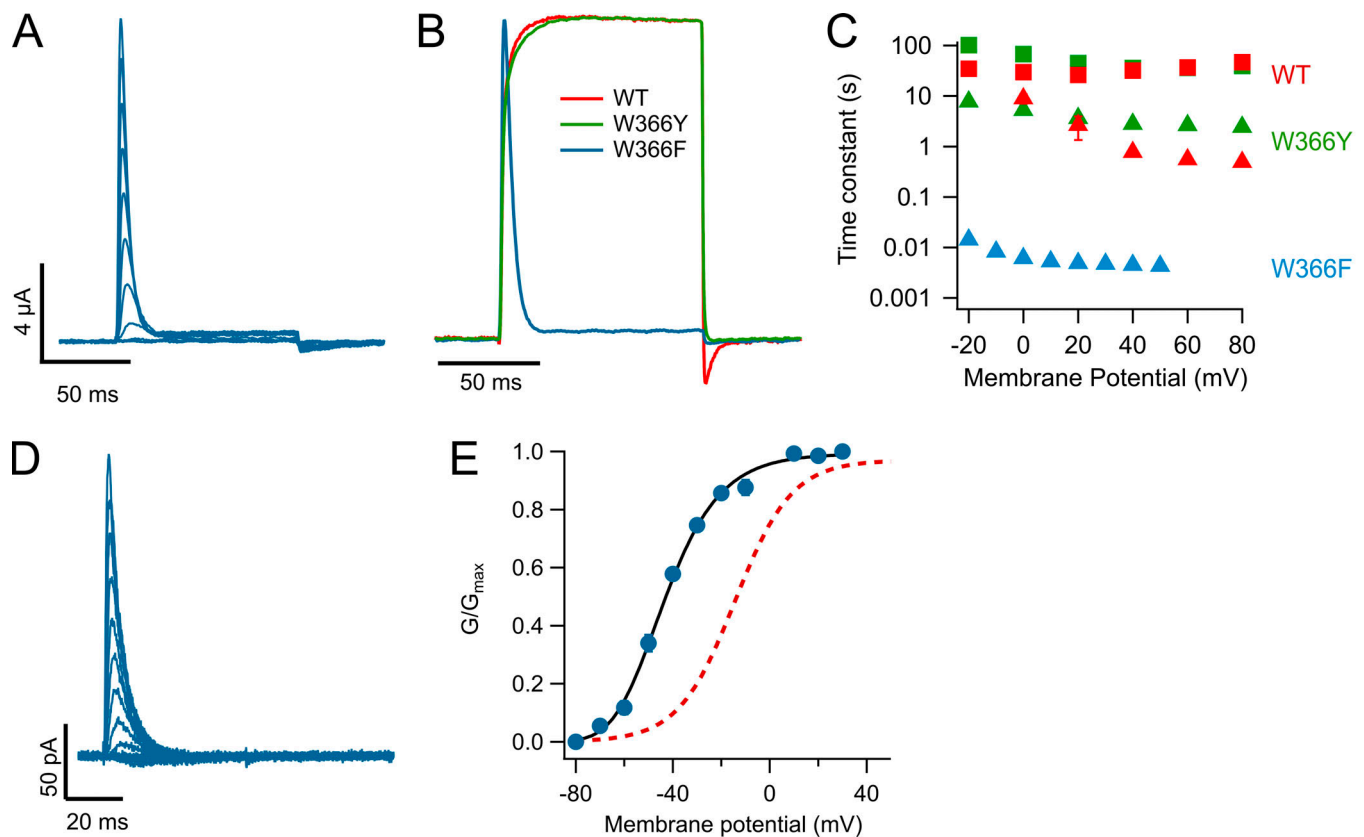


Figure 5. The W366F mutation produces channels with fast inactivation. (A) Family of currents showing fast inactivation even with short (100-ms) pulses. Depolarizing pulses stepped from -80 to 50 mV in 10 -mV increments, from a holding potential of -80 mV. (B) Comparison of the time course of currents activated by a 100 -ms pulse to 50 mV for WT, W366F, and W366Y channels. Currents were normalized to their maximum value. (C) Inactivation time constants for the two mutants and WT channels. The fast and slow time constants for WT (red) and W366Y (green) were obtained from currents elicited by 20 -s pulses as in Figs. 1 D and 3 C. The inactivation time constant for W366F (light blue) was obtained from a fit to a single-exponential function of the decay of currents elicited by 100 -ms pulses. Data are the mean of nine experiments and error bars are \pm SEM. (D) Fast-inactivating currents obtained from an inside-out patch expressing W366F channels. (E) The voltage dependence of these currents is shifted to negative voltages when 60 mM extracellular potassium is used. The continuous black curve is the fit to Eq. 2 with parameters $z_{app} = 1.75 e_0$, $K_0 = 0.0091$ ($n = 6$). For comparison, the voltage dependence of currents in 2 mM external potassium is shown (red dotted curve).

nonstationary noise analysis experiments. We decided on the use of noise analysis over single-channel recording since the single-channel conductance of $K_v1.2$ is small. Mean-variance analysis of these currents (Fig. 4 C) shows that the single-channel current of the mutant is reduced to 0.53 ± 0.014 pA, compared with 0.7 pA at 20 mV for WT $K_v1.2$ (Ishida et al., 2015), and that the main effect of the mutation is to significantly reduce the open probability of the channels to near half the value of the WT (Fig. 4 D).

Another mutation in *Shaker* that is known to modulate the time course of C-type inactivation is the W434F substitution, which accelerates inactivation to such an extent that channels with extremely reduced open probability and very brief openings are produced. As a consequence, when enough channel expression is achieved, only charge movement in the form of gating currents is observed, as if channels were permanently C-type inactivated (Perozo et al., 1993; Yang et al., 1997).

Surprisingly, mutation W366F, which is equivalent to *Shaker* W434F, produces only rapidly inactivating channels (Fig. 5 A). This result had been previously reported (Cordero-Morales et al., 2011). Side-by-side comparison of normalized currents

of the two mutants at position 366 and WT is shown in Fig. 5 B. It is readily seen that W366F channels inactivate within milliseconds, with a time course that can be fitted with a single exponential. This time constant is 2.5 orders of magnitude faster than the fastest component of inactivation in WT or W366Y (Fig. 5 C). This fast inactivation was also observed in inside-out patch recordings (Fig. 5 D). These inside-out recordings were performed in the presence of 60 mM $[K^+]_o$. Under these conditions, the conductance activates at more negative voltages compared with the conductance in the presence of 2 mM $[K^+]_o$, also in inside-out recordings (Fig. 5 E).

An important question is if the inactivated state that seems to be stabilized in $K_v1.2$ -W366F is the same slow-inactivated state seen in WT and W366Y. As with these channels, application of 100 mM extracellular K^+ to $K_v1.2$ -W366F results in a significant slowing of the inactivation rate (Fig. 6, A and B), as reported for C-type inactivation in other potassium channels. The extent of this slowing is larger than in WT, reaching ~ 3.4 -fold versus 1.3 -fold at positive voltages.

As shown in inside-out patch-clamp recordings (Fig. 5 E), in TEVC increased $[K^+]_o$ also modulates the range of activation by voltage. 100 mM $[K^+]_o$ shifts the midpoint of activation

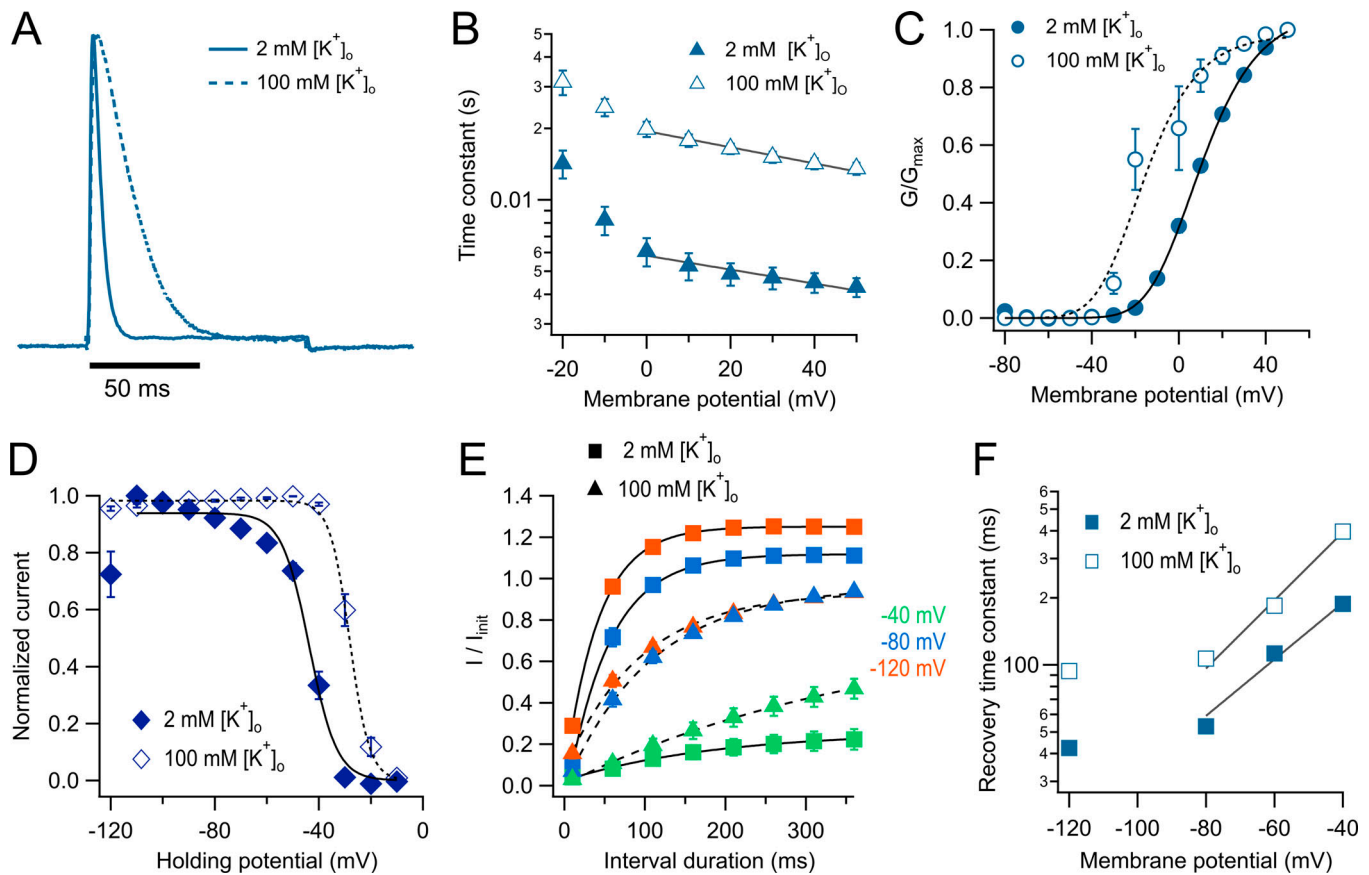


Figure 6. Inactivation characteristics of the W366F mutant. (A) Current elicited by a 50-mV pulse of 100-ms duration obtained in the presence of 2 mM extracellular K^+ (continuous line). The dotted line is a representative current at the same voltage in the presence of 100 mM extracellular K^+ . (B) The inactivation time constant obtained from a single exponential fit to currents in the presence of 2 mM $[K^+]_o$ (filled symbols) or 100 mM $[K^+]_o$ (hollow symbols). The black lines show an exponential fit to Eq. 6. The apparent charges in high and low external potassium are similar (-0.17 and $-0.19 e_o$, respectively), and the value of τ_o is increased from 0.005 to 0.019 s by the high potassium. (C) Effect of external potassium on the voltage dependence of the conductance calculated from the peak current. Filled symbols are the normalized peak conductance in 2 mM $[K^+]_o$ from $n = 9$ experiments, and the continuous line is the fit to Eq. 2 with parameters $z_{app} = 1.52 e_o$, $K_o = 0.35$. Hollow symbols are the normalized peak conductance in 100 mM $[K^+]_o$. The parameters of the fit (dashed curve) are $z_{app} = 1.64 e_o$, $K_o = 0.068$ ($n = 9$). (D) Steady-state inactivation. A prepulse of varying voltage from -120 to -10 mV of 300-ms duration was applied before a fixed 100-ms pulse to 50 mV. The current elicited by the 50-mV pulse was normalized and plotted as a function of prepulse voltage. The data are fitted by Eq. 4. Filled symbols are in 2 mM $[K^+]_o$ and hollow symbols in 100 mM $[K^+]_o$. The parameters of the fit are 2 mM $[K^+]_o$ and 100 mM $[K^+]_o$. (E) Recovery from inactivation was measured with a two-pulse protocol with pulses of 100-ms duration at 50 mV. The pulses were separated by increasing time intervals from 10 to 360 ms in 50-ms increments. The voltage of the interval between two pulses was held at -120 , -80 , and -40 mV. The recovery time course was fitted to a single exponential function, and the voltage dependence of the recovery was plotted in F. The experiment was done at 2 mM $[K^+]_o$ (squares, $n = 9$) and 100 mM $[K^+]_o$ (triangles, $n = 9$). (F) Recovery rates are shown as a function of prepulse voltage, and their voltage dependence was assessed by a fit to Eq. 6, indicating that the apparent charge of recovery is increased by 100 mM external K^+ from 0.73 to 0.88 e_o . Mean and SEM are plotted in panels B, C, D, and F.

by -30 mV (Fig. 6 C). The antagonistic action of elevated $[K^+]_o$ on inactivation is also evidenced by the effects on the voltage dependence of steady-state inactivation. High $[K^+]_o$ shifts the voltage dependence of inactivation by $+20$ mV. Importantly, a significant proportion of channels (26%) is inactivated at -120 mV in 2 mM $[K^+]_o$. This inactivated fraction of channels at negative voltages disappears when $[K^+]_o$ is brought to 100 mM (Fig. 6 D).

Recovery from inactivation is highly voltage dependent, becoming faster as the holding potential is made more negative (Fig. 6 E), and the rate of recovery is also modulated by $[K^+]_o$. However, the modulation of inactivation by external potassium is counterintuitive, since 100 mM $[K^+]_o$ makes recovery slower and not faster (Fig. 6 F). In a simple model, recovery from inactivation is the backward transition from entry into

inactivation. In such a situation, allostery requires potassium to either have no effect or have the opposite effects on entry and recovery from inactivation. This result suggests that recovery from slow inactivation might occur via several pathways and might be expected if closed- and open-state inactivation coexist.

Extracellular TEA has also been used as a probe of C-type inactivation (Kurata et al., 2005; Carrillo et al., 2013). As with WT $K_v1.2$ (Fig. 2), we applied 20 mM TEA to the bath and observed a modest but detectable slowing of the inactivation rate of $K_v1.2$ -W366F (Fig. 7, A and B), a result consistent with similar experiments in *Shaker* channels. Remarkably, application of intracellular TEA (20 mM) to inside-out patches also slowed down inactivation, although the effect was visible at more negative voltages than with extracellular TEA (Fig. 7 C).

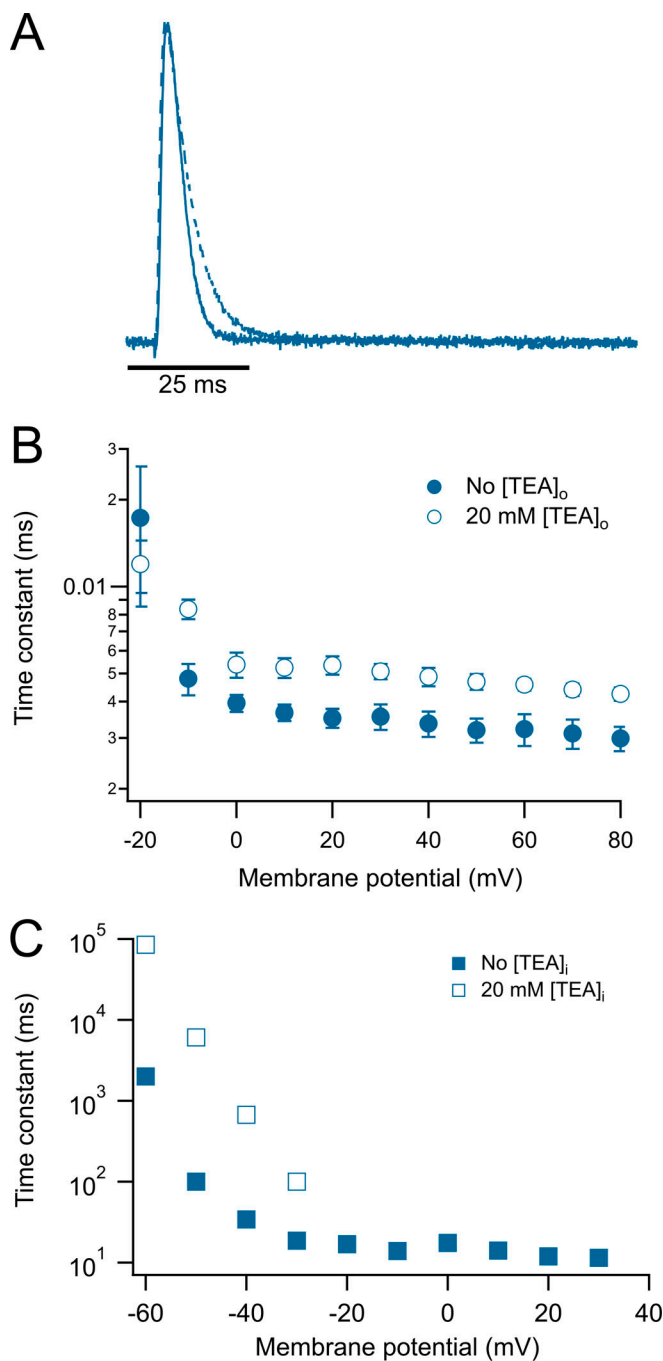


Figure 7. **Extracellular and intracellular TEA slows down the inactivation kinetics of the W366F mutant.** (A) Representative current traces at 60 mV in the absence (continuous trace) and presence (dashed trace) of 20 mM extracellular TEA. (B) Voltage dependence of the time constant of inactivation. External TEA data are shown by hollow symbols, while control data are shown by filled symbols. (C) Effect of intracellular TEA. 20 mM intracellular TEA was applied to inside-out patches. In the presence of TEA, current inactivation is slowed down appreciably at negative voltages. Data shown in B and C are mean \pm SEM.

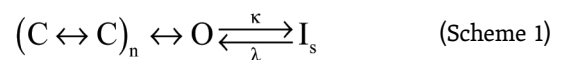
Taken together, this set of experiments with $[K^+]_o$ and $[TEA]_o$ suggest that the inactivation induced by the $K_V1.2$ -W366F mutant has characteristics compatible with it being an accelerated form of the slow inactivation present in WT channels.

Why is it that the W366F mutation in $K_V1.2$ does not produce permanently inactivated channels as in *Shaker*? Several amino acid residues have been shown to be involved in modulating the rate of slow inactivation in *Shaker* channels. In particular, when a threonine is located at position 449 (*Shaker* WT), the channels inactivate in the course of seconds. Inactivation is greatly enhanced by a charged (positive or negative) amino acid or an alanine, while valine almost completely abolishes inactivation (López-Barneo et al., 1993). In $K_V1.2$ channels, the equivalent position is V381, and when mutated to threonine, combined into the double mutant W366F/V381T (Goodchild et al., 2012) channels that only display gating currents are produced.

We also made the W366F/V381T double mutant, along with W366F/V381A, W366F/V381I, W366F/V381W, and W366F/V381L. Of these double mutants, only W366F/V381A, W366F/V381I, and W366F/V381T expressed functionally. These three double mutants gave rise to channels that only displayed charge movement. Gating currents were readily recorded in whole oocytes (Fig. 8 A) and showed characteristics similar to WT gating currents recorded in oocytes via patch-clamp (Ishida et al., 2015). The Q-V relationship shows that charge moves in two main components (Fig. 8 B) that occur at voltages more negative than the peak conductance of the background mutant, W366F. The kinetics of the ON-gating currents is similar between mutants, especially at positive potentials. At negative voltages, the mutant W366F/V381T shows slightly slower kinetics (Fig. 8 C). The OFF-gating currents are variously contaminated by the tail currents of endogenous oocyte channels, so a comparison of on-charge versus off-charge was not performed.

Discussion

Slow inactivation in potassium channels is a gating transition of functional importance. In spite of this, its fundamental mechanism remains poorly understood. This is in part because more than one form of inactivation coexists in several channels. Even the better-understood *Shaker* channel shows evidence of more than one way to enter an inactivated state (Ayer and Sigworth, 1997; Klemic et al., 2001). C-type inactivation (sometimes also called C/P-type; Kurata and Fedida, 2006; Bähring et al., 2012) seems to be associated with conformational changes in the selectivity filter that occur after the channel has reached the open state (Scheme 1). U-type inactivation seems to be related to conformational changes in the pore that can occur while the channel is in its closed conformation. A key consequence of closed-state inactivation is that the shape of the voltage dependence of steady-state inactivation is not a simple sigmoid, but a U-shaped function, since channels enter the inactivated state more favorably from intermediate, closed states than from the open state (Bähring and Covarrubias, 2011). These two forms of inactivation coexist in *Shaker* channels and constitute an often-overlooked confounding factor in inactivation studies.



Here, we have shown that WT $K_V1.2$ channels slow-inactivate, and this inactivation process also has mixed characteristics of

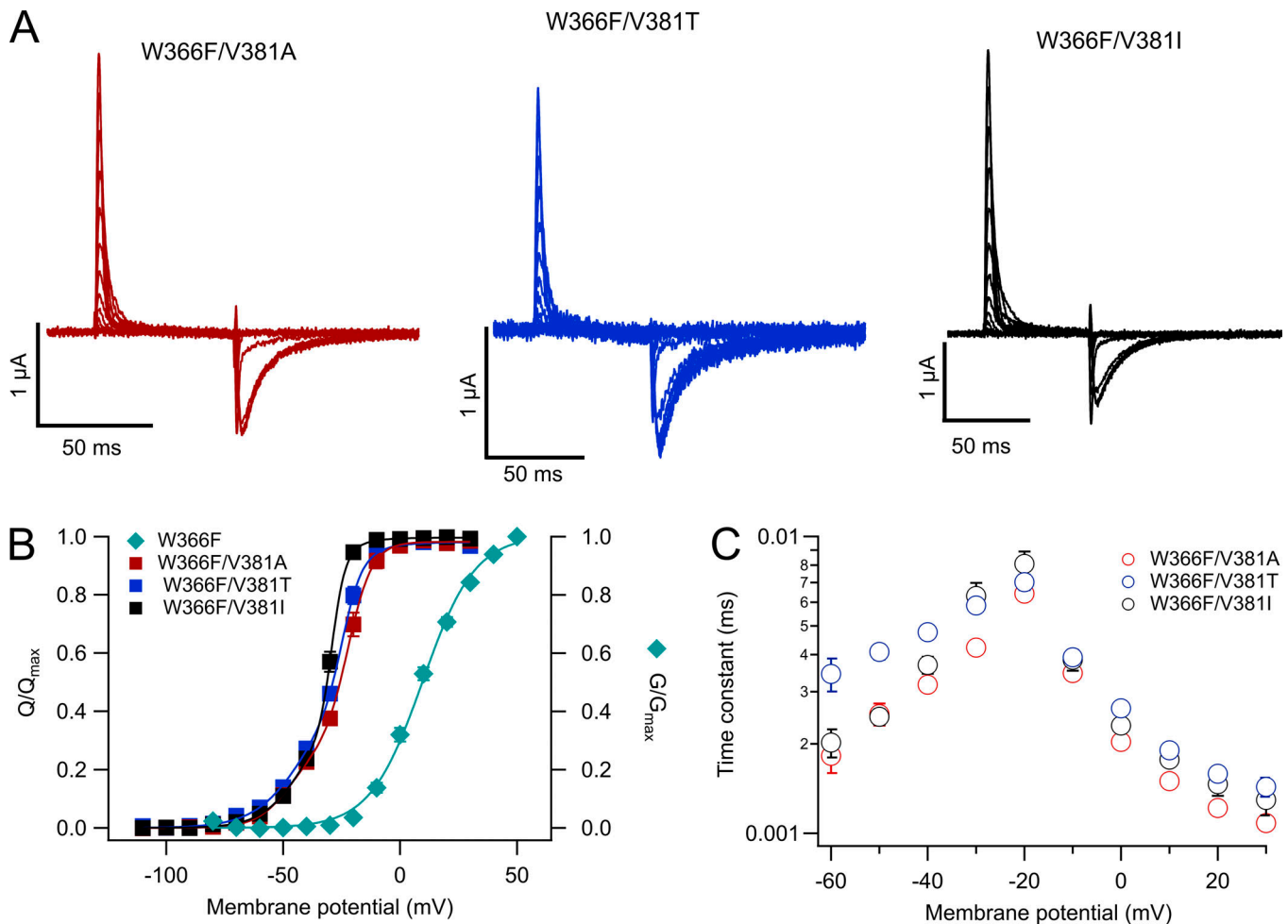


Figure 8. **Mutations at V381 in the W366F background produce permanently inactivated channels.** (A) Representative traces of gating currents recorded from the expressed channels indicated in each panel. Currents were elicited by voltage-clamp pulses of 60-ms duration ranging from -110 to 30 mV in 10 -mV steps from a holding potential of -100 mV. (B) Normalized voltage dependence of charge movement (Q - V) of the three mutants plotted (following its color code from A) and compared with the voltage dependence of the background mutation W366F (cyan rhombuses). Q - V data were fitted to Eq. 5. The number of experiments were W366F/V381A, $n = 13$; W366F/V381T, $n = 5$; and W366F/V381I, $n = 9$. (C) The time course of current decay of the three double mutants is plotted as a function of pulse voltage. ON-gating current decay was fitted to a single exponential to determine the time constant. Number of experiments is as in B. Data in B and C are mean \pm SEM.

C/P-type and U-type inactivation. Compared with slow inactivation in *Shaker* (Hoshi et al., 1991), $K_v1.2$'s is less pronounced. This is perhaps due to the presence of a valine at position 381, which in *Shaker* is a threonine. Valine at the equivalent position in *Shaker* also produces channels with less complete and slower inactivation (López-Barneo et al., 1993). We compare some inactivation parameters between *Shaker* and $K_v1.2$ in Table S1.

A simplified kinetic model can partially explain the behavior of WT and the mutations studied in this work (Scheme 1).

A model such as Scheme 1 assumes sequential charge movement and a single open state. Slow inactivation (I_s) can occur only from the open state. For the W366Y channels, the rate constant κ is increased with respect to WT, leading to faster and more complete inactivation at the end of a long activating pulse. Additionally, the rate constants previous to the open state are also reduced by the mutation W366Y, since the peak open probability is reduced in this mutant.

The behavior of the W366F mutant can be explained if κ is much greater than λ , leading to a much faster and complete

inactivation. This model is not unique and is likely only part of a full explanation of the mutants' effects. Since WT $K_v1.2$ shows evidence of U-type inactivation, this would require the existence of inactivated states accessed from closed states (Cheng et al., 2011; Bähring et al., 2012; Jamieson and Jones, 2013).

Evidence that slow inactivation in WT and the mutants is similar to C-type inactivation in *Shaker* is provided by the effects of external K^+ and TEA (Levy and Deutsch, 1996). Both compounds slow down the time course of inactivation in WT and the W366Y and W366F mutants, which is indicative of a common mechanism.

The behavior of W366F is very interesting. These channels have a fast and complete inactivation whose time course is not very voltage dependent ($0.17 e_0$) and becomes slower with high extracellular potassium, but not significantly different in voltage dependence ($0.19 e_0$). However, recovery from inactivation is more voltage dependent ($0.73 e_0$) and becomes even more so in high external potassium ($0.88 e_0$). External potassium has a

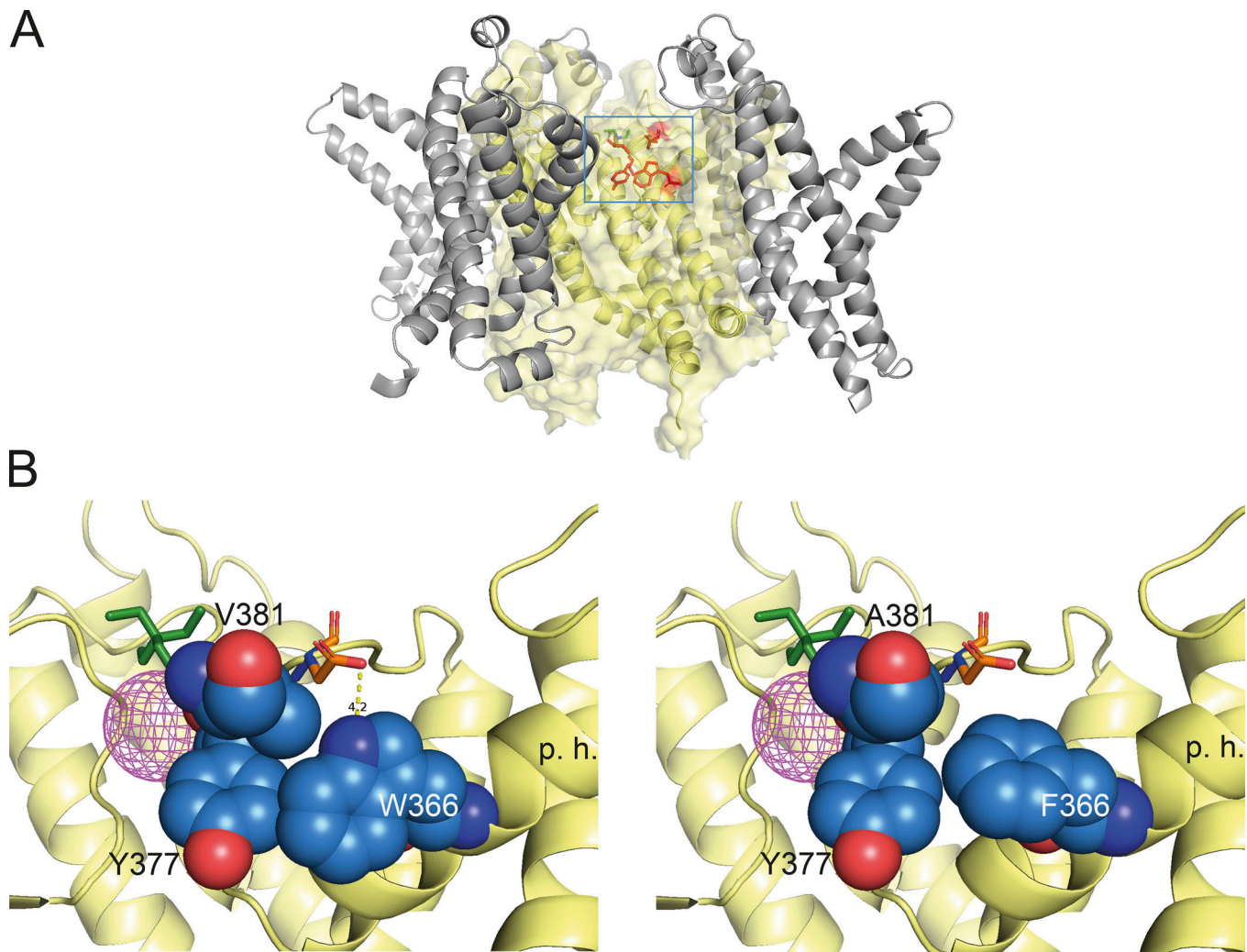


Figure 9. **Structural basis of modulation of inactivation by mutants at positions W366 and V381.** (A) Representation of the area near the selectivity filter of the $K_v1.2$ - $K_v1.1$ chimera, showing the residues involved in slow inactivation. The voltage-sensing domain is shown in gray ribbons and the filter domain is rendered in transparent yellow volume and ribbons. Residues W366, Y377, and V381 are shown in red. A TEA molecule is shown in green to indicate the position of the extracellular pore entrance. The blue square indicates the magnified area in B. (B) Left: Residues involved in slow inactivation near the extracellular region of the selectivity filter of the WT $K_v1.2$ - $K_v1.1$ chimera. The spheres' representation in colors corresponds to residues W366, V381, and Y377. Residue D379 is shown in sticks. The dotted yellow line shows the hydrogen bond between W366 and D379. Right: The double mutant W366F/V381A. The main changes in this mutant are an increased space and reduced interaction between W366F and Y377 and elimination of the hydrogen bond between W366 and D379. V381A might enhance the effects of W366F, because it should help the expansion of the space between W366F and Y377. The magenta mesh sphere is the density of a potassium ion occupying the S1 site in the selectivity filter. The green stick model is a TEA molecule occupying the S0 site. High occupancy of these two sites seems to partially antagonize slow inactivation through steric hindrance. p.h., position of the pore helix.

paradoxical effect on inactivation. While it slows down entry into the inactivated state and removes the steady-state inactivation present at negative voltages, it also slows down recovery from inactivation. The existence of closed-state inactivation could explain the slowing down of the recovery from inactivation in the presence of high external potassium in W366F.

The effects of extracellular TEA have been used as a probe of the conformational changes occurring in the external region of the pore during slow inactivation (Andalib et al., 2004). We found that, as in *Shaker*, application of external TEA slows down the transition to the inactivated state. This is indicative of similar steric and electrostatic interactions in both channels during inactivation.

It has been shown that in *Shaker*, intracellular TEA interferes with C-type inactivation more prominently than external TEA (González-Pérez et al., 2008), suggesting that internal TEA might hinder the U-type inactivation component while external TEA slows down C-type inactivation. Surprisingly, we found a similar behavior in W366F, where application of intracellular TEA to this mutant also slowed down the inactivation rate. Our experimental evidence suggests that the conformational changes leading to a slow-inactivated state in $K_v1.2$ and *Shaker* are similar. However, the detailed effects of the mutants are not the same in these two channels.

The phenotype of W366F is remarkable in that it does not produce permanently C-type inactivated channels. It was

previously demonstrated that this mutation combined with V381T, which mimics the background of the mutant W434F in *Shaker*, abolishes ionic current and produces channels with only gating currents (Goodchild et al., 2012).

When other amino acid residues are substituted at position V381 in the W366F background, channels with only gating currents are also produced. Of all the mutants we tried, only W366F/V381A, W366F/V381I, and W366F/V381T produced functional channels. A bulkier amino acid such as tryptophan was not tolerated, as was leucine instead of isoleucine. It seems that slow inactivation in $K_v1.2$ and *Shaker* channels is only quantitatively different. $K_v1.2$ seems less prone to slow-inactivate due to specific amino acid differences, included those studied herein. Our data suggest that slow inactivation is produced by two distinct mechanisms, grouped under the distinction of U- and P/C-type, happening around the selectivity filter. We believe that the effects of the mutants can be interpreted in terms of a mechanism that might be responsible for the initiation and establishment of the slow-inactivated state.

A sequence of events leading to slow inactivation

The effects of the mutants presented in this work lead us to propose a sequence of events that in conjunction constitute slow inactivation in $K_v1.2$ channels (Fig. 9). Prolonged flux of potassium through the selectivity filter leads to a conformational change (perhaps initiated by strong electrostatic interactions) that starts at tyrosine Y377, located in the selectivity filter, and in which carbonyl oxygen forms part of the S2 potassium binding site. Rotation of this tyrosine into W366, which is initially 3–4 Å apart, will destabilize the interaction of a K^+ ion with the S2 binding site in the selectivity filter. This is supported by the crystal structure of a dilated and presumably slow-inactivated selectivity filter of the KcSA channel, which features a destabilized S2 potassium-binding site (Cuello et al., 2010). Another part of the slow inactivation mechanism can be gleaned from *Shaker* channels. It has been shown that a hydrogen bond between W434 and D447 in the linker between selectivity filter and S5 segment (Pless et al., 2013) helps stabilize the noninactivated conformation. Neutralization of D447 leads to slow C-inactivated channels.

When a tyrosine or a phenylalanine is present at position 366 in $K_v1.2$, not only is there more space for Y377, but also the hydrogen bond cannot be formed with D379 (equivalent to *Shaker* D447), so the inactivated state is favored with faster kinetics. In the double mutant W366F/V381T, this inactivated conformation will be further enhanced due to repulsive interactions between T381 and D379. The mutants W366F/V381A and W366F/V381I must produce similar end effects but through different mechanisms; the presence of A381 leaves so much empty space and no interactions with D379 that the entire molecular packing of the pore must be altered (Fig. 9 B). Similarly, I381 possibly leaves little space and pushes D379 away. The deeply inactivated behavior of the double mutant channels suggest that they could be used in structural studies as a template for the slow-inactivated state of $K_v1.2$, possibly shedding light on the structural changes involved in the slow-inactivated states of other channels.

Overall, there are multiple inter- and intramolecular interactions leading to the slow inactivated state. The mutants that we have analyzed in $K_v1.2$ might be involved only in the conformational changes in the external parts of the pore. If U-type inactivation is part of the slow-inactivated state, these separate conformational changes might occur in the inner pore vestibule, as has been previously suggested for *Shaker* channels (González-Pérez et al., 2008).

Online supplemental material

Table S1 provides the $K_v1.2$ and *Shaker* inactivation time constants.

Acknowledgments

Merritt C. Maduke served as editor.

We thank Itzel Llorente from Instituto de Fisiología Celular, Universidad Nacional Autónoma de México, for technical support.

This work was financed by grants from Consejo Nacional de Ciencia y Tecnología (252644) and Dirección General de Asuntos del Personal Académico, Universidad Nacional Autónoma de México, Programa de Apoyo a Proyectos de Investigación e Innovación Tecnológica (IN209515) to L.D. Islas.

The authors declare no competing financial interests.

Author contributions: E. Suárez-Delgado carried out electrophysiology experiments and data analysis and read the manuscript. T.G. Rangel-Sandín carried out electrophysiology experiments and read the manuscript. I.G. Ishida carried out patch-clamp experiments and data analysis and contributed to making mutants. G.E. Rangel-Yescas contributed reagents, carried out molecular biology experiments, and read the paper. T. Rosenbaum conceived research and wrote and read the paper. L.D. Islas conceived research, carried out data analysis, contributed analysis programs, and wrote the paper.

Submitted: 26 September 2019

Accepted: 2 February 2020

References

- Andalib, P., J.F. Consiglio, J.G. Trapani, and S.J. Korn. 2004. The external TEA binding site and C-type inactivation in voltage-gated potassium channels. *Biophys. J.* 87:3148–3161. <https://doi.org/10.1529/biophysj.104.046664>
- Ayer, R.K. Jr., and F.J. Sigworth. 1997. Enhanced closed-state inactivation in a mutant *Shaker* K^+ channel. *J. Membr. Biol.* 157:215–230. <https://doi.org/10.1007/s002329900230>
- Bähring, R., and M. Covarrubias. 2011. Mechanisms of closed-state inactivation in voltage-gated ion channels. *J. Physiol.* 589:461–479. <https://doi.org/10.1113/jphysiol.2010.191965>
- Bähring, R., J. Barghaan, R. Westermeier, and J. Wollberg. 2012. Voltage sensor inactivation in potassium channels. *Front. Pharmacol.* 3:100. <https://doi.org/10.3389/fphar.2012.00100>
- Carrillo, E., I.I. Arias-Olguín, L.D. Islas, and F. Gómez-Lagunas. 2013. Shab K (+) channel slow inactivation: a test for U-type inactivation and a hypothesis regarding K (+) -facilitated inactivation mechanisms. *Channels (Austin)*. 7:97–108. <https://doi.org/10.4161/chan.23569>
- Cheng, Y.M., J. Azer, C.M. Niven, P. Mafi, C.R. Allard, J. Qi, S. Thouta, and T.W. Claydon. 2011. Molecular determinants of U-type inactivation in $K_v2.1$ channels. *Biophys. J.* 101:651–661. <https://doi.org/10.1016/j.bpj.2011.06.025>

- Choi, K.L., R.W. Aldrich, and G. Yellen. 1991. Tetraethylammonium blockade distinguishes two inactivation mechanisms in voltage-activated K⁺ channels. *Proc. Natl. Acad. Sci. USA* 88:5092–5095. <https://doi.org/10.1073/pnas.88.12.5092>
- Cordero-Morales, J.F., V. Jogini, A. Lewis, V. Vásquez, D.M. Cortes, B. Roux, and E. Perozo. 2007. Molecular driving forces determining potassium channel slow inactivation. *Nat. Struct. Mol. Biol.* 14:1062–1069. <https://doi.org/10.1038/nsmb1309>
- Cordero-Morales, J.F., V. Jogini, S. Chakrapani, and E. Perozo. 2011. A multipoint hydrogen-bond network underlying KcsA C-type inactivation. *Biophys. J.* 100:2387–2393. <https://doi.org/10.1016/j.bpj.2011.01.073>
- Cuello, L.G., V. Jogini, D.M. Cortes, and E. Perozo. 2010. Structural mechanism of C-type inactivation in K⁽⁺⁾ channels. *Nature*. 466:203–208. <https://doi.org/10.1038/nature09153>
- De Biasi, M., H.A. Hartmann, J.A. Drewes, M. Tagliatala, A.M. Brown, and G.E. Kirsch. 1993. Inactivation determined by a single site in K⁺ pores. *Pflügers Arch.* 422:354–363. <https://doi.org/10.1007/BF00374291>
- Dempster, J. 2001. *The Laboratory Computer. A Practical Guide for Physiologists and Neuroscientists*. First edition. Academic Press, London. p. 340.
- González-Pérez, V., A. Neely, C. Tapia, G. González-Gutiérrez, G. Contreras, P. Orio, V. Lagos, G. Rojas, T. Estévez, K. Stack, and D. Naranjo. 2008. Slow inactivation in Shaker K channels is delayed by intracellular tetraethylammonium. *J. Gen. Physiol.* 132:633–650. <https://doi.org/10.1085/jgp.200810057>
- Goodchild, S.J., H. Xu, Z. Es-Salah-Lamoureux, C.A. Ahern, and D. Fedida. 2012. Basis for allosteric open-state stabilization of voltage-gated potassium channels by intracellular cations. *J. Gen. Physiol.* 140:495–511. <https://doi.org/10.1085/jgp.201210823>
- Grissmer, S., A.N. Nguyen, J. Aiyyar, D.C. Hanson, R.J. Mather, G.A. Gutman, M.J. Karmilowicz, D.D. Auperin, and K.G. Chandy. 1994. Pharmacological characterization of five cloned voltage-gated K⁺ channels, types Kv1.1, 1.2, 1.3, 1.5, and 3.1, stably expressed in mammalian cell lines. *Mol. Pharmacol.* 45:1227–1234.
- Heinemann, S.H., and F. Conti. 1992. Nonstationary noise analysis and application to patch clamp recordings. *Methods Enzymol.* 207:131–148.
- Hoshi, T., and C.M. Armstrong. 2013. C-type inactivation of voltage-gated K⁺ channels: pore constriction or dilation? *J. Gen. Physiol.* 141:151–160. <https://doi.org/10.1085/jgp.201210888>
- Hoshi, T., W.N. Zagotta, and R.W. Aldrich. 1990. Biophysical and molecular mechanisms of Shaker potassium channel inactivation. *Science*. 250:533–538. <https://doi.org/10.1126/science.2122519>
- Hoshi, T., W.N. Zagotta, and R.W. Aldrich. 1991. Two types of inactivation in Shaker K⁺ channels: effects of alterations in the carboxy-terminal region. *Neuron*. 7:547–556. [https://doi.org/10.1016/0896-6273\(91\)90367-9](https://doi.org/10.1016/0896-6273(91)90367-9)
- Ishida, I.G., G.E. Rangel-Yescas, J. Carrasco-Zanini, and L.D. Islas. 2015. Voltage-dependent gating and gating charge measurements in the Kv1.2 potassium channel. *J. Gen. Physiol.* 145:345–358. <https://doi.org/10.1085/jgp.201411300>
- Jamieson, Q., and S.W. Jones. 2013. Role of outer-pore residue Y380 in U-type inactivation of KV2.1 channels. *J. Membr. Biol.* 246:633–645. <https://doi.org/10.1007/s00232-013-9577-0>
- Klemic, K.G., G.E. Kirsch, and S.W. Jones. 2001. U-type inactivation of Kv3.1 and Shaker potassium channels. *Biophys. J.* 81:814–826. [https://doi.org/10.1016/S0006-3495\(01\)75743-8](https://doi.org/10.1016/S0006-3495(01)75743-8)
- Klemic, K.G., C.-C. Shieh, G.E. Kirsch, and S.W. Jones. 1998. Inactivation of Kv2.1 potassium channels. *Biophys. J.* 74:1779–1789. [https://doi.org/10.1016/S0006-3495\(98\)77888-9](https://doi.org/10.1016/S0006-3495(98)77888-9)
- Kurata, H.T., and D. Fedida. 2006. A structural interpretation of voltage-gated potassium channel inactivation. *Prog. Biophys. Mol. Biol.* 92:185–208. <https://doi.org/10.1016/j.pbiomolbio.2005.10.001>
- Kurata, H.T., K.W. Doerksen, J.R. Eldstrom, S. Rezaadadeh, and D. Fedida. 2005. Separation of P/C- and U-type inactivation pathways in Kv1.5 potassium channels. *J. Physiol.* 568:31–46. <https://doi.org/10.1113/jphysiol.2005.087148>
- Levy, D.I., and C. Deusch. 1996. Recovery from C-type inactivation is modulated by extracellular potassium. *Biophys. J.* 70:798–805. [https://doi.org/10.1016/S0006-3495\(96\)79619-4](https://doi.org/10.1016/S0006-3495(96)79619-4)
- Long, S.B., E.B. Campbell, and R. MacKinnon. 2005. Crystal structure of a mammalian voltage-dependent Shaker family K⁺ channel. *Science*. 309:897–903. <https://doi.org/10.1126/science.1116269>
- Long, S.B., X. Tao, E.B. Campbell, and R. MacKinnon. 2007. Atomic structure of a voltage-dependent K⁺ channel in a lipid membrane-like environment. *Nature*. 450:376–382. <https://doi.org/10.1038/nature06265>
- Loots, E., and E.Y. Isacoff. 1998. Protein rearrangements underlying slow inactivation of the Shaker K⁺ channel. *J. Gen. Physiol.* 112:377–389. <https://doi.org/10.1085/jgp.112.4.377>
- López-Barneo, J., T. Hoshi, S.H. Heinemann, and R.W. Aldrich. 1993. Effects of external cations and mutations in the pore region on C-type inactivation of Shaker potassium channels. *Receptors Channels*. 1:61–71.
- Mathies, D., C. Bae, G.E.S. Toombes, T. Fox, A. Bartesaghi, S. Subramaniam, and K.J. Swartz. 2018. Single-particle cryo-EM structure of a voltage-activated potassium channel in lipid nanodiscs. *eLife*. 7:e37558. <https://doi.org/10.7554/eLife.37558>
- Molina, A., A.G. Castellano, and J. López-Barneo. 1997. Pore mutations in Shaker K⁺ channels distinguish between the sites of tetraethylammonium blockade and C-type inactivation. *J. Physiol.* 499:361–367. <https://doi.org/10.1113/jphysiol.1997.sp021933>
- National Research Council. 2010. *Guide for the care and use of laboratory animals*. National Academies Press, Washington, DC.
- Olcese, R., R. Latorre, L. Toro, F. Bezanilla, and E. Stefani. 1997. Correlation between charge movement and ionic current during slow inactivation in Shaker K⁺ channels. *J. Gen. Physiol.* 110:579–589. <https://doi.org/10.1085/jgp.110.5.579>
- Oliva, C., V. González, and D. Naranjo. 2005. Slow inactivation in voltage gated potassium channels is insensitive to the binding of pore occluding peptide toxins. *Biophys. J.* 89:1009–1019. <https://doi.org/10.1529/biophysj.105.060152>
- Pau, V., Y. Zhou, Y. Ramu, Y. Xu, and Z. Lu. 2017. Crystal structure of an inactivated mutant mammalian voltage-gated K⁺ channel. *Nat. Struct. Mol. Biol.* 24:857–865. <https://doi.org/10.1038/nsmb.3457>
- Perozo, E., R. MacKinnon, F. Bezanilla, and E. Stefani. 1993. Gating currents from a nonconducting mutant reveal open-closed conformations in Shaker K⁺ channels. *Neuron*. 11:353–358. [https://doi.org/10.1016/0896-6273\(93\)90190-3](https://doi.org/10.1016/0896-6273(93)90190-3)
- Pless, S.A., J.D. Galpin, A.P. Niciforovic, H.T. Kurata, and C.A. Ahern. 2013. Hydrogen bonds as molecular timers for slow inactivation in voltage-gated potassium channels. *eLife*. 2:e01289. <https://doi.org/10.7554/eLife.01289>
- Rettig, J., S.H. Heinemann, F. Wunder, C. Lorra, D.N. Parcej, J.O. Dolly, and O. Pongs. 1994. Inactivation properties of voltage-gated K⁺ channels altered by presence of β-subunit. *Nature*. 369:289–294. <https://doi.org/10.1038/369289a0>
- Roberds, S.L., and M.M. Tamkun. 1991. Cloning and tissue-specific expression of five voltage-gated potassium channel cDNAs expressed in rat heart. *Proc. Natl. Acad. Sci. USA*. 88:1798–1802. <https://doi.org/10.1073/pnas.88.5.1798>
- Sigworth, F.J. 1980. The variance of sodium current fluctuations at the node of Ranvier. *J. Physiol.* 307:97–129. <https://doi.org/10.1113/jphysiol.1980.sp013426>
- Tao, X., and R. MacKinnon. 2008. Functional analysis of Kv1.2 and paddle chimera Kv channels in planar lipid bilayers. *J. Mol. Biol.* 382:24–33. <https://doi.org/10.1016/j.jmb.2008.06.085>
- Vergara-Jaque, A., F. Palma-Cerda, A.S. Lowet, A. de la Cruz Landrau, H. Poblete, A. Sukharev, J. Comer, and M. Holmgren. 2019. A Structural Model of the Inactivation Gate of Voltage-Activated Potassium Channels. *Biophys. J.* 117:377–387. <https://doi.org/10.1016/j.bpj.2019.06.008>
- Yang, Y., Y. Yan, and F.J. Sigworth. 1997. How does the W434F mutation block current in Shaker potassium channels? *J. Gen. Physiol.* 109:779–789. <https://doi.org/10.1085/jgp.109.6.779>

Currents through Hv1 channels deplete protons in their vicinity

Víctor De-la-Rosa, Esteban Suárez-Delgado, Gisela E. Rangel-Yescas, and León D. Islas

Departamento de Fisiología, Facultad de Medicina, Universidad Nacional Autónoma de México, México DF 04510, México

Proton channels have evolved to provide a pH regulatory mechanism, affording the extrusion of protons from the cytoplasm at all membrane potentials. Previous evidence has suggested that channel-mediated acid extrusion could significantly change the local concentration of protons in the vicinity of the channel. In this work, we directly measure the proton depletion caused by activation of Hv1 proton channels using patch-clamp fluorometry recordings from channels labeled with the Venus fluorescent protein at intracellular domains. The fluorescence of the Venus protein is very sensitive to pH, thus behaving as a genetically encoded sensor of local pH. Eliciting outward proton currents increases the fluorescence intensity of Venus. This dequenching is related to the magnitude of the current and not to channel gating and is dependent on the pH gradient. Our results provide direct evidence of local proton depletion caused by flux through the proton-selective channel.

INTRODUCTION

Cells from different lineages possess proton currents with distinct physiological roles, varying from cytoplasmic pH regulation to specialized roles in the innate immune response (DeCoursey, 2013; Okamura et al., 2015). The physical identity of the channels mediating these currents was first revealed by the molecular cloning of the Hv1 and VSOP proton channels, which, unexpectedly, are formed by voltage-sensing domains possessing a proton-selective pathway (Ramsey et al., 2006; Sasaki et al., 2006).

Although the details of the proton transport mechanism are still not clear, it has been proposed that protons are carried by a diffusion-limited mechanism and that proton channels have a discrete conductance, similarly to other bona fide ion channels. A noise analysis study has reported estimates of the single-channel conductance of proton currents in eosinophils (Cherny et al., 2003). This conductance is very small, in the order of 140 fS at an intracellular pH (pH_i) of 5.5, partly because the proton concentration is very small. The single-channel conductance of the cloned Hv1 is unknown but assumed to be similarly small to that of native channels. In addition to being proton-permeable, hHv1 channels display a pH-dependent gating mechanism, in which the voltage dependence of channel opening is shifted to negative voltages when the proton gradient increases and favors outward proton flux. The mechanism of this pH dependence is unknown, but it ensures that protons are always transported outside of the cell upon hHv1 activation (Cherny et al., 1995).

Large changes in the local concentration of ions are expected in the vicinity of ion channels, especially when the equilibrium ionic concentrations are very asymmetric. This is the case of calcium (Ca^{2+}) ions and calcium channels, where the existence of microdomains with very high Ca^{2+} concentrations near the intracellular mouth of the ion channel have been well documented and even shown to have a functional role (Wagner and Keizer, 1994; Berridge, 2006). A similar but somewhat inverse situation is to be expected of protons. The cytoplasmic proton concentration under physiological conditions is in the order of 60 nM (approximate pH 7.2), so even small outward fluxes could significantly alter the local intracellular concentration of protons.

The physiological concentration of protons is very low; thus, previous work has attempted to determine whether the single-channel conductance of proton channels is limited by diffusion of the buffer to the entrance of the channel or by the rate of a protonation–deprotonation reaction at the intracellular entrance of the channel. Those experiments concluded that the rate-limiting step in conduction occurs in the permeation pathway (DeCoursey and Cherny, 1996). However, several other experiments have shown evidence of insufficient control of pH and proton depletion, indicating that buffer diffusion might play an important role in determining proton conduction (Kapus et al., 1993; Cherny et al., 2003). In this work, we provide direct evidence derived from fluorescence measurements in the immediate vicinity of the channel of a decreased availability of protons as a consequence of proton transport through Hv1 channels.

Correspondence to León D. Islas: lislas@canales.facmed.unam.mx

V. De-la-Rosa's present address is Dept. of Physiology and Biophysics, Virginia Commonwealth University, Richmond, VA 23298.

Abbreviations used in this paper: FP, fluorescent protein; GFP, green FP; pH_i , intracellular pH.

© 2016 De-la-Rosa et al. This article is distributed under the terms of an Attribution–Noncommercial–Share Alike–No Mirror Sites license for the first six months after the publication date (see <http://www.rupress.org/terms>). After six months it is available under a Creative Commons License (Attribution–Noncommercial–Share Alike 3.0 Unported license, as described at <http://creativecommons.org/licenses/by-nc-sa/3.0/>).

Molecular biology and channel expression

The human proton channel hHv1 construct was a gift from I.S. Ramsey (Virginia Commonwealth University, Richmond, VA). This construct contains the Venus variant of green fluorescent protein (FP [GFP]) at the N terminus of the channel and is cloned into pcDNA6.2-DEST, and in this work it is referred to as Venus-Hv1. Using this construct, mutation H148G was inserted into Venus (VenusH148G-hHv1). An additional construct where Venus was placed at the end of the C terminus of hHv1 was made and termed Hv1-Venus. Other constructs were made based on Hv1-Venus. All C-terminal constructs have a GGGG linker between the end of the channel and the Venus FP. The mutant C-terminal -4 has a deletion of the sequence KTRS at the beginning of the C-terminal coiled-coil helices, whereas the C-terminal +4 mutant has the insertion of the sequence ERQL immediately after KTRS. Overlap PCR was used to make these mutant channels. Plasmids were linearized with the AgeI restriction enzyme, and mRNA was synthesized in vitro with the mMACHINE mMESSAGE T7 transcription kit (Ambion).

Xenopus laevis oocytes were surgically extracted and defolliculated as previously described (Ishida et al., 2015). Oocytes were incubated at 18°C in ND96 solution containing (mM) 96 NaCl, 2 KCl, 1.8 CaCl₂, 1 MgCl₂, 5 HEPES, 2.5 pyruvic acid, and 20 µg/ml gentamycin (pH 7.5, NaOH). Oocytes were injected with 40–50 nl of mRNA (~1 µg/ml) at least 6 h after harvesting using a Manual Oocyte Microinjector (Drummond Scientific) and glass capillaries drawn to ~20-µm-diameter opening. Experiments were performed 3–4 d after injection.

Patch-clamp fluorometry

hHv1-mediated proton currents were recorded in the inside-out patch-clamp configuration with an Axopatch 200B patch-clamp amplifier (Axon Instruments, Inc.). Data were recorded through an ITC-18 interface (InstruTech, Inc.) using the Pulse software package (HEKA). Analysis was performed with Pulse and Igor Pro software (WaveMetrics). Macroscopic currents were filtered at 2 kHz and sampled at 10 kHz. Patch pipettes had a resistance of ~3 MΩ. Bath and pipette solutions contained (mM) 1 EGTA, 2 MgCl₂, 10 MES/HEPES, and 90 sucrose, and the pH was adjusted with NMDG.

Fluorescence images were recorded in a TE-2000U (Nikon) inverted epifluorescence microscope with a Luca EMCCD camera (Andor) while the proton current was simultaneously recorded. Fluorescence was acquired by imaging the patch pipette with a 60× oil immersion objective (numerical aperture 1.4; Nikon). The excitation light source was an Ar-Ion laser (Spectra-Physics). The laser was coupled to a single-mode optical fiber, collimated, and then focused into the objective back focal plane using optics mounted in an optical cage system (Thorlabs). An excitation filter selected the 488-nm laser line and fluorescence emission was filtered with a 530/10-nm band pass emission filter. Images were acquired and analyzed with Micro-Manager software and ImageJ (National Institutes of Health; Edelstein et al., 2010).

Membrane patches were held at -80 mV, the voltage was stepped to -100 mV for 1.2 s, and during this voltage step, fluorescence emission was acquired with a 300-ms exposure that ended ~50 ms before the test pulse. Then the voltage was stepped from -100 to 100 mV in 20-mV steps for 1.2 s (test pulse) during which a second fluorescence image was captured with the same exposure (the last 300 ms of the test pulse); finally, the voltage was returned to -30 mV in some experiments or to -80 mV, as indicated in each figure. Currents were not corrected for linear leak and capacitive components. Proton currents, I_H , were converted to conductance, G_H , according to

$$I_H = G_H(V - V_H). \tag{1}$$

Here, V_H is the proton current reversal potential, given by the Nernst equation.

The voltage dependence of G_H was fitted to

$$G_H(V) = \frac{1}{1 + \exp[q_a(V - V_{0.5})/kT]}. \tag{2}$$

The parameter q_a is the apparent valence associated with gating, in elementary charge (e_o) units, and $V_{0.5}$ is the voltage of mid activation.

For image analysis, fluorescence intensity was measured from the whole patch or from a horseshoe-like region of interest (ROI) drawn around the patch dome with similar results. Change in fluorescence was calculated by dividing the intensity obtained at the test pulse by the intensity at -100 mV for the same sweep. Some pipettes exhibited areas of significant fluorescence outside of the patch area; because these membrane segments are not voltage-clamped, fluorescence from them was excluded from the measurements; nevertheless, this fluorescence serves as a negative control for the changes in fluorescence in the patch membrane. All images were background-subtracted using a region outside the pipette image as background.

Fluorescence imaging of membrane sheets

The vitelline membrane from *Xenopus* oocytes expressing Venus or VenusH148G-labeled channels was mechanically removed. These oocytes were then placed in a poly-D-lysine-coated glass coverslip, which also constituted the bottom of the chamber for fluorescence imaging. After 15–30 min, the oocyte was carefully removed from the chamber, leaving a small sheet of membrane attached to the glass (De-la-Rosa et al., 2013). Membrane sheets were washed with a solution of 500 mM NaCl to remove yolk vesicles, and the bathing solution was then changed to varying pH solutions ranging from 3 to 10, with the same composition as used for patch-clamp recording. Fluorescence appears spotty because of channel cluster formation. Mean emission intensity of a single spot or a large area of the membrane sheet was measured with identical results. Fluorescence intensity was normalized to the value at the highest pH. Results were fitted to a titration curve of the form

$$F = F_o + \frac{(1 - F_o)}{1 + 10^{(pK_a - pH)}}, \tag{3}$$

where F_o is the residual fluorescence at low pH and pK_a is the pH at which $F = (1 + F_o)/2$.

Online supplemental material

Supplemental material is included in the form of one figure (Fig. S1) that contains the mean conductance versus voltage curves of Hv1-Venus channels obtained at two different pH gradients used in these experiments. Online supplemental material is available at <http://www.jgp.org/cgi/content/full/jgp.201511496/DC1>.

RESULTS

Given the very small concentration of protons in the cytoplasm, it has been suggested that as protons permeate through proton channels, the local proton concentration would be altered. Indirect evidence for this can be seen in the current “droop” or apparent inactivation that is produced when large proton currents are achieved

(DeCoursey and Cherny, 1996). Given that this depletion could potentially produce significant changes in local pH, we reasoned that a pH-sensitive FP attached to the channel could behave as a local pH reporter.

The GFP is highly sensitive to pH, losing fluorescence intensity when its fluorophore becomes protonated. This is the reason why GFP and other variants of it have been used as indicators of cellular and organellar bulk pH (Bizzarri et al., 2009).

Fig. 1 A shows patch-clamp fluorometry recordings of the fluorescence of Hv1 channels that have been tagged with the Venus FP in the N terminus. Venus is a variant of the yellow FP (YFP) that has increased brightness and retains pH sensitivity (Nagai et al., 2002). These recordings were performed at a nominal pH_i of 5.5 in the presence of 100 mM MES buffer. The fluorescence of channels in the patch could be readily detected and proton currents recorded simultaneously. As the

depolarizing pulse was made more positive, outward currents were elicited, and in fact, at very positive potentials there was a time-dependent decrease of the current magnitude, which has been taken as an indication of permeant ion depletion (Fig. 1 B).

Measurement of the patch fluorescence near the end of the depolarizing pulse showed that its magnitude increased, relative to the fluorescence at a negative potential (Fig. 1 D). The magnitude of the fluorescence increase can be superimposed on the current to voltage relationship (I-V curve), indicating that fluorescence is a function of current magnitude, even at voltages where channel activation, measured by the conductance calculated according to Eq. 1, reaches saturation (Fig. 1, C and D). It should be noted that because of proton depletion, the G-V curve is underestimated, but it should still provide an estimate of Hv1 channel gating. One possible explanation for the increase in fluorescence is

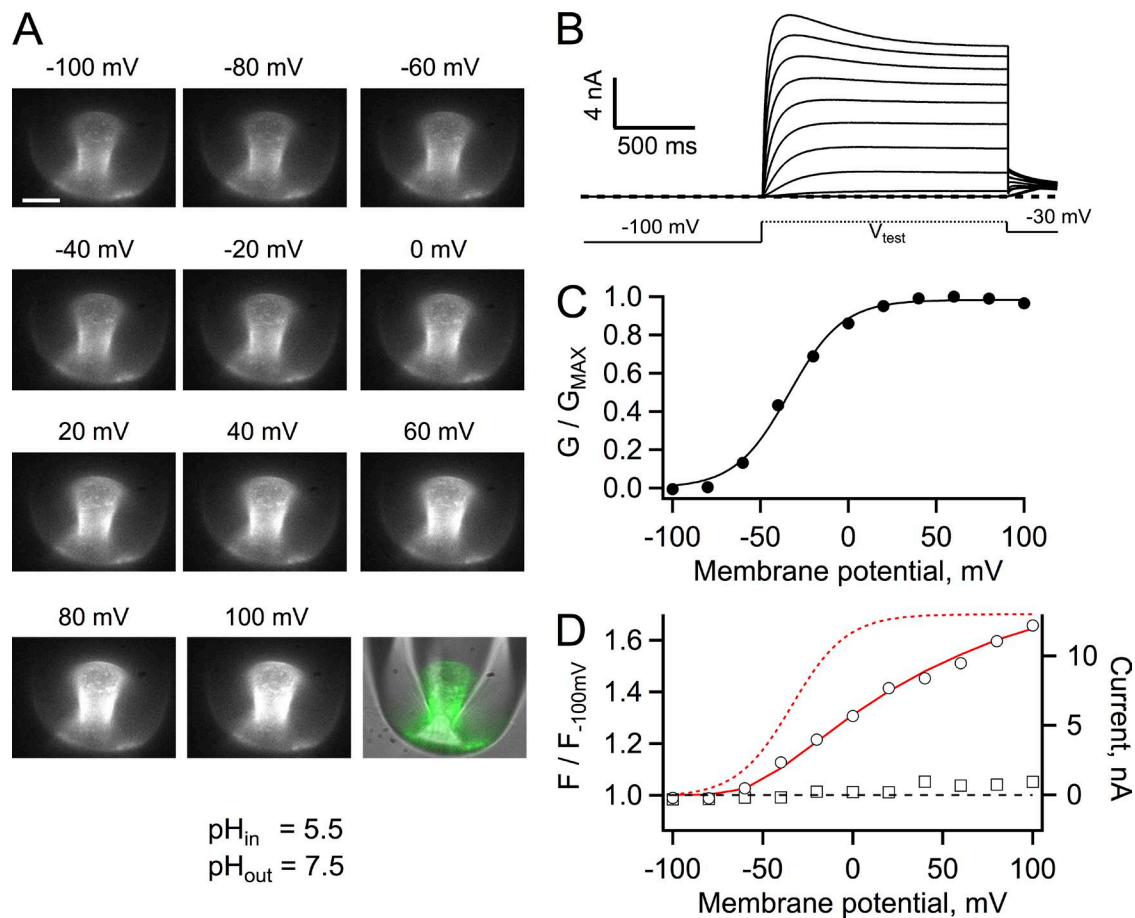


Figure 1. Patch-clamp fluorometry of Venus-Hv1. (A) Fluorescence images of an inside-out patch held at the indicated membrane potential. The image in the bottom right corner is a superposition of the fluorescence image at 100 mV (green) and the transmitted light image of the pipette to show the location of the membrane patch within the pipette. Bar, 10 μm . (B) Proton currents from the patch in A elicited by depolarizing voltage-clamp pulses. (C) Conductance versus voltage curve derived from the currents in B. The continuous line is a fit to Eq. 2 with parameters $q_a = 1.63 e_0$ and $V_{0.5} = -33.8$ mV. (D) Fluorescence measured from the whole patch area at each voltage was normalized to the fluorescence at -100 mV (circles). A ratio greater than one indicates an increase (dequenching) of the fluorescence. The fluorescence of a region of membrane attached to the pipette but outside of the patch is also plotted (squares). The red continuous line is the I-V curve from the currents in A, whereas the red dashed curve is the fit to the G-V curve in C. The bath solution contained 100 mM MES buffer, and the pH of solutions is indicated.

that the FP could be tracking activation of Hvl, as in other engineered fluorescent voltage sensors (Baker et al., 2012; Mutoh et al., 2012). This explanation is unlikely because the fluorescence signal is related to the magnitude of the current and not to channel gating (Fig. 1, C and D). Moreover, the magnitude of the fluorescence change is very large and represents an increase of fluorescence, which is opposite to the small amplitude quenching that is observed in most fluorescent voltage sensors based on a single FP.

The patch in Fig. 1 had exceptionally large currents. More typical currents were $<1,000$ pA at 80 mV, and under these conditions fluorescence dequenching in 100 mM buffer, although present, was difficult to quantify. We decided to carry out the rest of the experiments in the presence of 10 mM buffer, still a condition with very high buffering power. Experiments with the more typical current magnitudes gave the same qualitative result (Fig. 2).

Fig. 2 shows that the same fluorescence dequenching behavior could be observed if the FP was placed in the C or N terminus of hHv1. As for the data in Fig. 1, the fluorescence follows the I-V curve and not the G-V curve, again indicating that it is related to proton permeation

and not channel gating. In these particular patches, the magnitude of fluorescence dequenching was smaller than in Fig. 1, in accordance with the smaller current magnitude as can be seen from the value of the currents in the superimposed I-V curves. These data show that the fluorescence in a single patch follows the increase in current regardless of the position of the FP. The crystal structure of the C terminus of VSOP extends beyond the cytoplasmic side of the membrane by ~ 80 Å (Fujiwara et al., 2012; Fujiwara and Okamura, 2014), and the fusion of the FP should add ~ 30 Å. Increasing or decreasing this distance by 4 aa, ~ 10 Å, did not produce noticeably different fluorescence increases as a function of current (see Fig. 4), indicating that the proton depletion zone extends beyond 10 nm into the cytoplasm (Fujiwara et al., 2012).

The pK_a of the fluorescence of Venus is 5.73 (see Fig. 5 and Nagai et al. [2002]), so if the fluorescence increase was indeed related to proton depletion and not to a voltage-dependent process, it would be expected that at a higher pH_i the fluorophore in Venus would be deprotonated and its fluorescence would be independent of current. Fig. 3 shows that at pH_i 7 proton currents

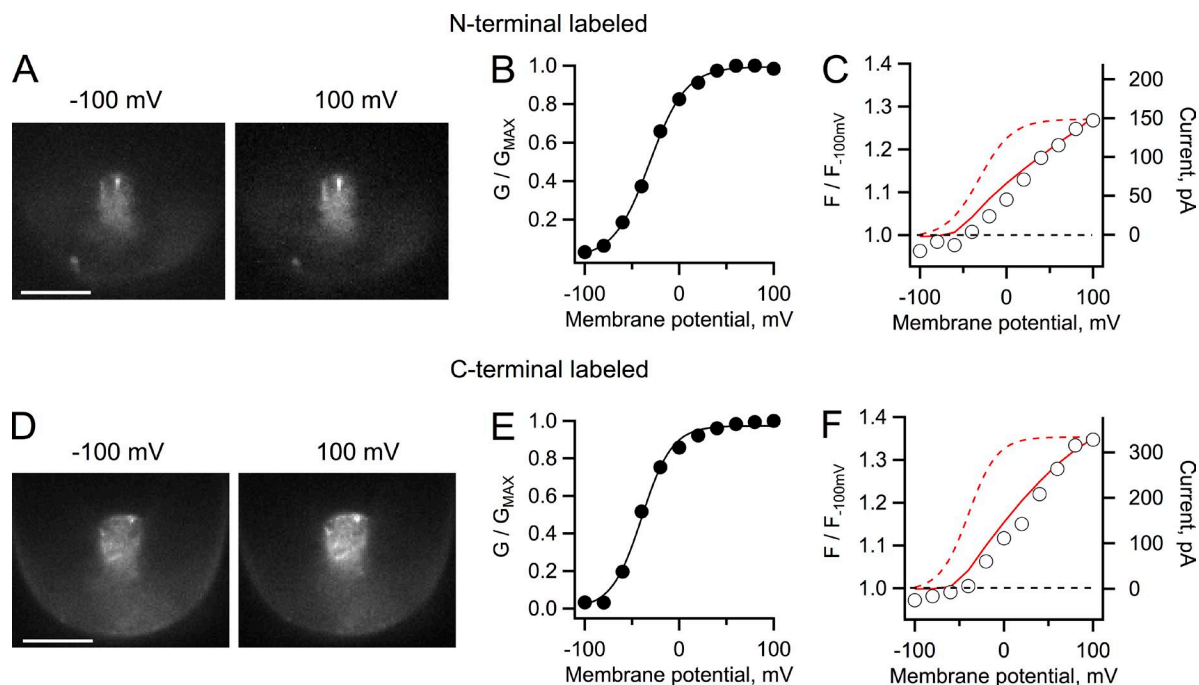


Figure 2. Patch-clamp fluorometry of Venus-Hv1 and Hv1-Venus constructs. (A) Fluorescence images of an inside-out patch from an oocyte expressing Hv1 channels labeled with Venus in the N terminus. The patch was held at the indicated membrane potential. (B) G-V curve from proton currents from the patch in A elicited by depolarizing voltage-clamp pulses. The continuous line is a fit to Eq. 2 with parameters $q_a = 1.31 e_0$ and $V_{0.5} = -31.2$ mV. (C) Fluorescence measured from the whole area of the patch in A at each voltage, plotted as normalized intensity with respect to the fluorescence intensity at -100 mV. (D) Fluorescence images from an inside-out patch from oocytes expressing the Hv1 construct labeled at the C terminus. (A and D) Bars, 10 μ m. (E) G-V curve from proton currents from the same patch in D elicited by depolarizing voltage-clamp pulses. The continuous line is a fit to Eq. 2 with parameters $q_a = 1.56 e_0$ and $V_{0.5} = -39.6$ mV. (F) Fluorescence measured from the whole patch area and analyzed as in C. For the analysis in C and F, a ratio greater than one indicates an increase (dequenching) of the fluorescence as the patch is held at increased positive potentials. The red continuous line is the I-V curve from the currents in the corresponding patch, whereas the dashed curve is the fit to the G-V curve. The buffer concentration for these experiments was 10 mM MES, and the pH gradient is as in Fig. 1.

activated at higher potentials and with slower kinetics, as expected from the pH dependence of Hvl gating (Fig. 3, B and C; and Fig. S1). In this recording condition, even though proton currents should be producing proton depletion, the fluorescence no longer increased as a function of current (Fig. 3 D), presumably because at pH 7 Venus is completely deprotonated and its fluorescence is no longer sensitive to pH. This result provided further evidence that the fluorescence change is related to the proton current magnitude.

The data presented in Figs. 1, 2, and 3 can be explained if the outward proton flux produced a local pH_i increase in the periphery of the Venus FP, leading to dequenching of the fluorescence.

In Fig. 4, the magnitude of the fluorescence increase was plotted as a function of the size of the proton current at the same voltage of 80 mV for a series of different patches and constructs. The data show that there is a nonlinear correlation between the two quantities. Because even at pH_i 5.5 the proton concentration is only 3.16 μM, the proton current I_H is sustained by the flux of protonated buffer. A previous study (Cherny et al., 2003) developed a quantitative treatment of the expected proton depletion effects caused by proton fluxes. The theoretical results in that work predict that the local proton concentration should be a function of channel current amplitude, just as our experimental observation. We have combined their equation A12, which relates the proton concentration to the proton current, with the

titration curve expected for a FP to give an equation relating fluorescence to proton current amplitude:

$$F = \frac{1}{1 + 10^{\beta pK_a - \text{pH}}}$$

and

$$\text{pH} = -\log \left\{ K_a \left(\frac{1 - \alpha_o - \beta_i I_H}{\alpha_o + \beta_i I_H} \right) \right\}. \quad (4)$$

In these equations, βpK_a is the pK_a of the FP, K_a is the buffer dissociation constant, α_o is the degree of buffer dissociation, I_H is the magnitude of the proton current, and β_i is a factor that takes into account the dimensions of the patch pipette under the supposition that the patch can be represented as a truncated cone:

$$\beta_i = \frac{1}{\pi b F D_{BH} B_{\text{total}}} \left(\frac{1}{r_o} - \frac{1}{r_p} \right)$$

with

$$b = \frac{r_p - r_o}{l_p}.$$

Here, F is Faraday's constant, D_{BH} is the buffer diffusion coefficient, B_{total} is the total concentration of buffer, and

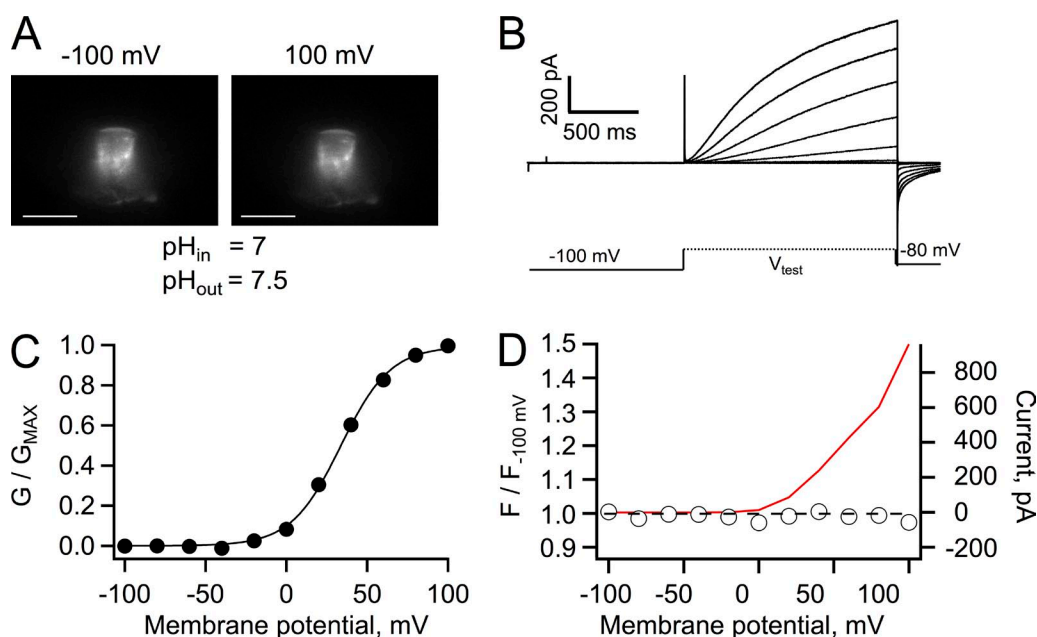


Figure 3. Patch-clamp fluorometry of Venus-Hv1 at pH_i 7. (A) Fluorescence images of an inside-out patch held at the indicated membrane potential. Bars, 10 μm. (B) Proton currents from the patch in A elicited by depolarizing voltage-clamp pulses, as indicated by the schematic protocol. (C) Conductance versus voltage curve derived from the currents in B. The continuous line is a fit to Eq. 2 with parameters $q_a = 1.62 e_o$ and $V_{0.5} = 33.6$ mV. (D) Fluorescence measured from the whole patch area at each voltage was normalized to the fluorescence at -100 mV. A ratio equal to one at all voltages indicates the absence of dequenching of the fluorescence of Venus. The red continuous line is the I-V curve from the currents in B. The bath solution contained 10 mM HEPES buffer.

r_o , r_p , and l_p are the radius of pipette opening, radius of the patch, and the length of the patch, respectively. These factors can readily be estimated from our fluorescence patch images (Fig. 4 A). The continuous line in Fig. 4 B is the predicted magnitude of the fluorescence dequenching as a function of proton current amplitude (Eq. 4), calculated for the recording conditions of pH_i 5.5, K_a for MES, and α_o for MES at pH 5.5. The used pK_a is that of Venus. The agreement between the experimental data and the theoretical expectation strongly suggests that the increased fluorescence signal is reporting on increased local pH at the FP.

An immediate prediction of the data in Figs. 3 and 4 is that if the FP had a higher pK_a , we should recover the increase in fluorescence even at pH_i 7. To test this hypothesis, we sought to change the pK_a of Venus by introducing a mutation at position H148. This amino acid has been shown to influence the pK_a of GFP-related proteins profoundly (Wachter et al., 1998; Hanson

et al., 2002). The mutation H148G shifted the pK_a of Venus from 5.73 to 7.62, as estimated by titrating the fluorescence of membrane sheets prepared from oocytes expressing the corresponding Venus fused to the N terminus of Hv1 (Fig. 5). When currents and fluorescence from the construct VenusH148G-Hv1 were recorded at pH_i 7, we recovered the fluorescence increase. Importantly, fluorescence dequenching now occurred at more positive potentials and overlapped

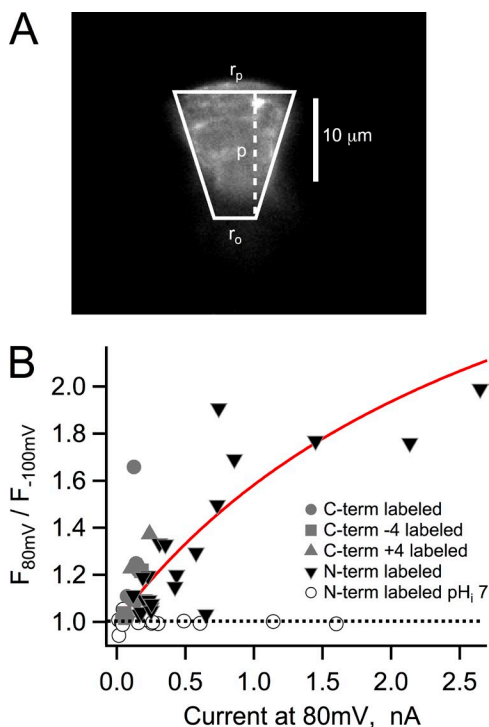


Figure 4. Fluorescence dequenching and proton depletion. (A) Fluorescence image of a typical patch expressing Hv1-Venus and approximation of its geometry by a truncated cone with the indicated dimensions used in the model in Eq. 4. (B) The value of the observed dequenching at 80 mV is plotted as a function of the current for that particular patch also at 80 mV. All of the experiments in this figure were obtained with an intracellular solution of pH 5.5, with the exception of those patches represented by the open circles. The continuous red curve is the dequenching as a function of current magnitude predicted by Eq. 4. The parameters that went into Eq. 4 were $r_p = 10 \mu\text{m}$, $r_o = 5 \mu\text{m}$, $l_p = 15 \mu\text{m}$, $K_a = 7.08 \times 10^{-7}$, $\alpha_o = 0.1812$, $f\text{pK}_a = 5.6$, $D_{BH} = 5 \times 10^{-10} \text{m}^2/\text{s}$, and $B_{\text{total}} = 10 \text{mM}$. The dotted line indicates lack of dequenching and describes the recordings from N-labeled channels at pH_i 7.

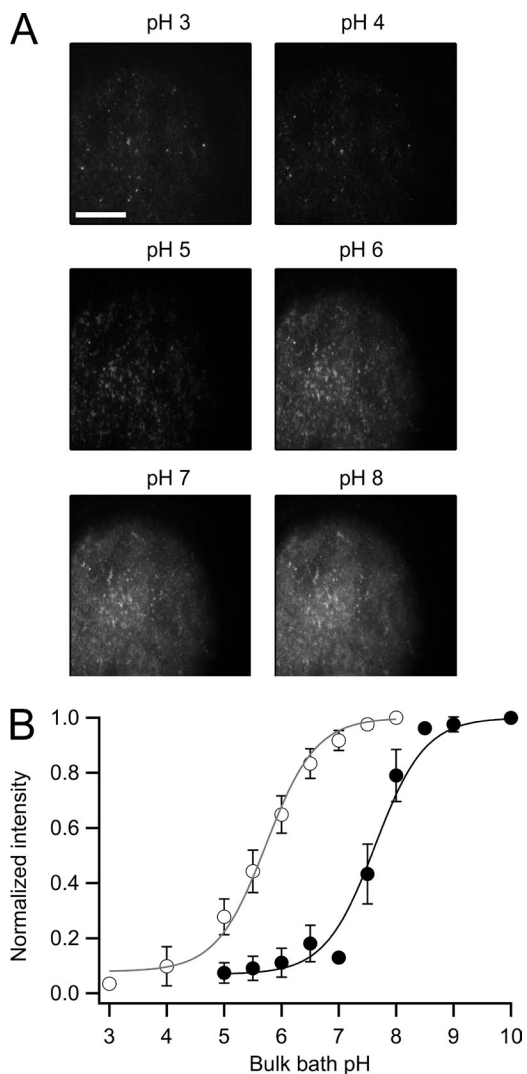


Figure 5. Measurement of the pK_a of fluorescent constructs. (A) Representative membrane sheet from oocytes injected with the Venus-Hv1 construct. The membrane was imaged under different pH conditions, indicated at the top of each frame. Fluorescence was measured as the mean of an ROI encompassing a large area of the membrane sheet or from individual clusters of channels with the same results. Bar, $20 \mu\text{m}$ (same for all images). (B) The fluorescence was normalized to the value at the highest pH for each construct to build the full titration curve. The data were fitted to the titration function (Eq. 3). The pK_a for Venus-Hv1 (open circles) is 5.63 and 7.62 for VenusH148G-Hv1 (closed circles). The data are the mean of five experiments for both constructs, and error bars are the standard error of the mean.

the development of outward proton current, as expected from the positively shifted voltage dependence at symmetrical pH (Fig. 6 D). Data from several patches again showed the correlation between dequenching and current magnitude, confirming that the local pH_i is being increased by the proton flux. It should be noted that the fluorescence increase was smaller in magnitude than that observed at pH_i 5.5 (Fig. 4), in part because of the reduced concentration of protons at pH_i 7 and the smaller expression level of the construct VenusH148G-Hv1. Still, the data can be explained by the dequenching model embodied in Eq. 4 (Fig. 6 E).

DISCUSSION

Local proton depletion produced by activation of Hv1 channels is to be expected as part of their function. Simultaneous recordings of pH_i and proton current activation have been performed in the past in intact cells and have shown that whole-cell proton flux in small cells is enough to alkalinize the bulk cytoplasm by about +1 pH unit (Thomas and Meech, 1982; Kapus et al.,

1993). Here we show that, remarkably, even in an inside-out patch where the buffer is available in essentially infinite supply (with respect to the proton flux), a proton current can locally deplete hydronium ions by a large amount.

In analogy with Ca^{2+} ion concentration microdomains (Berridge, 2006), the existence of pH microdomains around proton channels might play a functionally important role, especially if pH-sensitive proteins associate with proton channels or are localized in their immediate vicinity.

Even though our fluorescence measurements are not absolutely calibrated as a function of pH, we can estimate the change in pH from the titration curves of the fluorescent chimeric channels (Fig. 5). From these data, it can be expected that the fluorescence of the Venus-Hv1 construct at pH 5.5 would be quenched by 56%. Thus, the observed increase of 60% in the fluorescence at 80 mV, as in Fig. 1 D, represents a change of 1 pH unit. Even when current magnitude is <20 times that in Fig. 1, dequenching at maximum conductance (80 mV) can be >40%, which translates into an alkalinization of just under a pH unit.

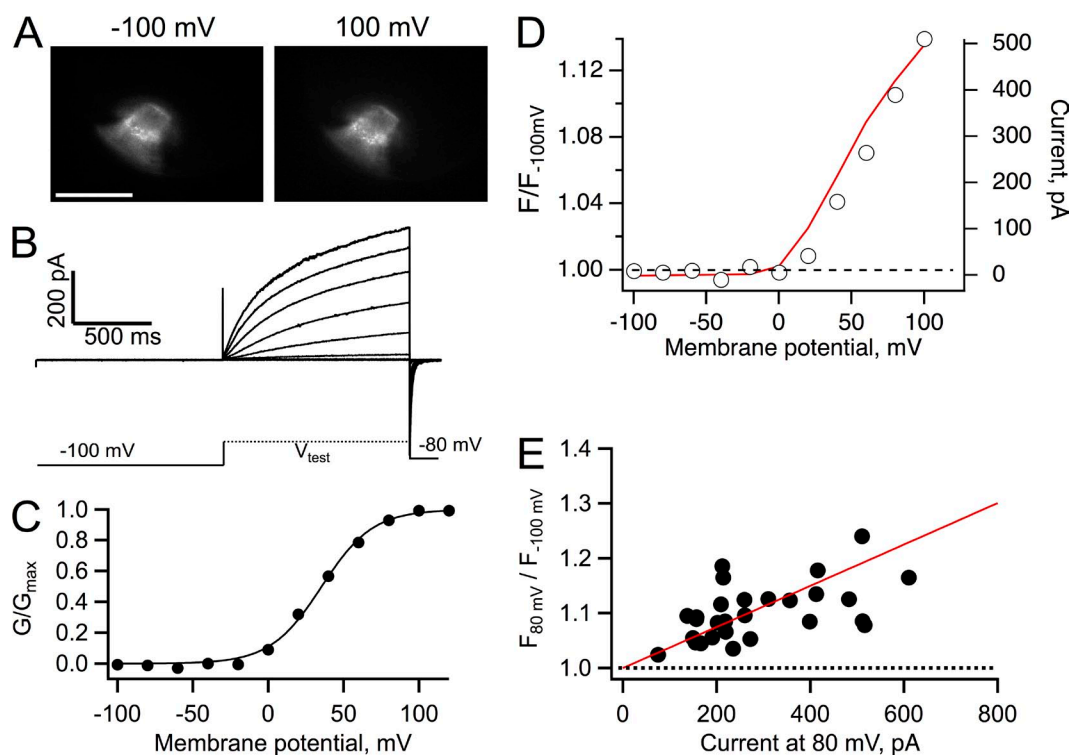


Figure 6. Recovery of fluorescence dequenching in VenusH148G-Hv1 at pH_i 7. (A) Fluorescence images of an inside-out patch from an oocyte expressing the construct VenusH148G-Hv1 held at the indicated membrane potential. Bar, 10 μm . (B) Proton currents from the patch in A elicited by depolarizing voltage-clamp pulses. (C) Conductance versus voltage curve derived from the currents in B. The continuous line is a fit to Eq. 2 with parameters $q_a = 1.47 e_0$ and $V_{0.5} = 35.4$ mV. (D) Fluorescence dequenching measured from the whole area of the patch in A. The red curve is the I-V curve for the same patch. (E) The fluorescence from 28 patches similar to A was measured at 80 mV, normalized to the fluorescence at -100 mV, and plotted as a function of the current magnitude at 80 mV, as in Fig. 4. A ratio greater than one at all voltages indicates dequenching of the fluorescence of VenusH148G. The bath solution contained 10 mM HEPES buffer. The continuous red line is the predicted dequenching by Eq. 4 with parameters $r_p = 10$ μm , $r_o = 5$ μm , $l_p = 15$ μm , $K_a = 2.81 \times 10^{-8}$, $\alpha_o = 0.26$, $f_p K_a = 7.6$, $D_{BH} = 5 \times 10^{-10}$ m^2/s , and $B_{total} = 10$ mM.

Cherny et al. (2003), assuming that the main limitation to proton conductance is buffer diffusion and deprotonation, provided a quantitative description of proton depletion at the channel entrance. We have used this as the basis for a description of the effect of local proton depletion on the fluorescence reported by Venus. This model can reasonably account for the data, but some assumptions need commenting. Eq. 4 supposes a conical geometry for the patch, and our images can be well approximated by this geometry, thus allowing for a direct estimation of the model parameters related to patch shape. However, the prediction in Fig. 4 B assumes a mean patch, so the scatter of the data might result from the different sizes and relative parameters of the membrane patches involved in the analysis in Fig. 4.

Why is the proton depletion effect so marked in Hv1 channels? An initial simple model for depletion is to consider a proton channel as a point sink for protons (Fig. 7 A). If the outward proton current, I_H , is given by q , the proton concentration c , considering only radial

diffusion in the r direction, is given by the solution to the diffusion equation with appropriate boundary and initial conditions (Crank, 1979):

$$c(r,t) = c_\infty - \frac{q}{2\pi D_H r} \left(\operatorname{erfc} \left(\frac{r}{2\sqrt{D_H t}} \right) \right),$$

where D_H is the diffusion coefficient of protons in water and c_∞ is the bulk proton concentration.

In the steady state, this equation simplifies to

$$c(r) = c_\infty - \frac{q}{2\pi D_H r}. \quad (5)$$

This function is plotted in Fig. 7 B for different values of the bulk concentration and the same value of q and D_H . If the value of c_∞ is large, in the millimolar to high micromolar range, the flux q is not enough to reduce the proton concentration significantly from its bulk value, until r is smaller than an angstrom; however, for values of c_∞ in

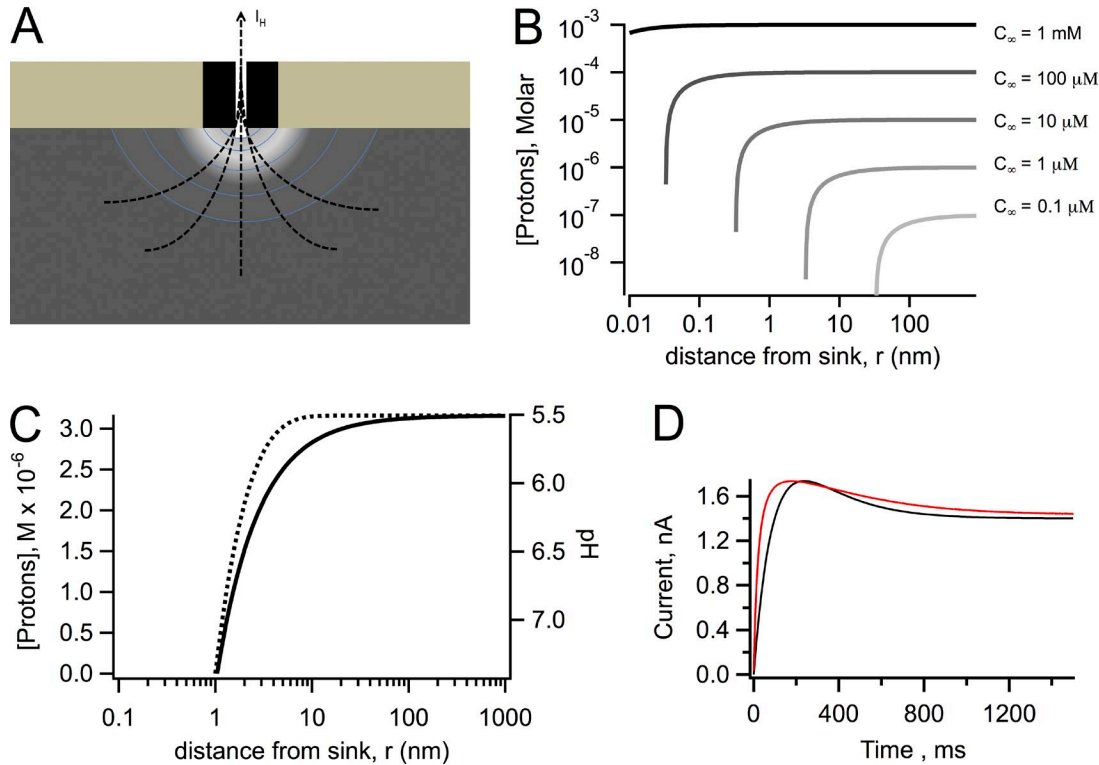


Figure 7. Diffusion model calculations. (A) Schematic representation of the proton depletion zone generated by an outward proton current through an Hv1 channel. (B) Calculations using Eq. 5 of the extent of the depletion of protons as a function of the radial coordinate, r , for different values of the bulk proton concentration, c_∞ , as indicated; the value of $q = 14$ fA is the same for all curves as well as $D_H = 7,000 \mu\text{m}^2/\text{s}$. (C) Calculation of the effect of the presence of buffer. The black curve was calculated with Eq. 5. The effect of the presence of buffer is illustrated by the dotted line, which was calculated with Eq. 6. The values of the constants are $c_\infty = 3.16 \mu\text{M}$, $[B] = 100$ mM, $a = 1$ nm, $k_b = 10^{10} \text{M}^{-1}\text{s}^{-1}$, and $D_H = 7,000 \mu\text{m}^2/\text{s}$. Data are presented as molar proton concentration (left axis) and corresponding pH (right axis). (D) Experimental (red) and simulated (black) currents in response to a 100-mV depolarization. Simulated current trace was generated taking into account a pH change during current development of 1 pH unit, which changes the single-channel current from 5 fA to 1.4 fA. The current is given by Eq. 7 in the form $I(H,t) = N \cdot (1 - e^{-t/\tau}) \left[5 - (5 - 1.4)(1 - e^{-t/\tau}) \right]$, with $\tau = 200$ ms and N as an arbitrary whole number chosen to match the size of the experimental current.

the low micromolar range, the flux can significantly reduce the concentration even at distances greater than several tens of angstroms from the sink, creating a depletion microdomain around the proton channel pore.

The presence of buffers does not make the depletion effect disappear. A simple model of proton diffusion in the presence of a rapidly equilibrating buffer has been proposed in Decker and Levitt (1988) and Nunogaki and Kasai (1988). The solution for the proton concentration $c(r)$ profile in the presence of a rapid buffer is given by

$$c(r) = c_{\infty} \left(1 - (a/r) e^{-\lambda(r-a)} \right),$$

with

$$\lambda^2 = k_b [B] / D_H, \quad (6)$$

where $[B]$ is the concentration of buffer, k_b is the association rate constant, and a is the capture radius of the channel pore. This function also predicts a large depletion of protons in the vicinity of a proton channel, although it happens over a narrower range of values of r (Fig. 7 C).

In our experiments with patches with very large currents and in published whole-cell recordings also with large proton fluxes (Kapus et al., 1993; DeCoursey and Cherny, 1996; Iovannisci et al., 2010), it is observed that the time course of proton current shows an apparent inactivation phenomenon, which is not present in smaller currents or currents recorded in the absence of a pH gradient. Similar apparent inactivation phenomena have been observed in CNG channels and are caused by permeant ion depletion and accumulation (Zimmerman et al., 1988). To what extent can our estimates of local proton changes explain the kinetics of the apparent inactivation? Noise analysis experiments in native proton currents (Cherny et al., 2003) have estimated the dependence of the single-channel proton current, i_s , on intracellular proton concentration. They report that for a 1 pH unit decrease, i_s increases approximately four times; so for the 1 pH change from 5.5 to ~ 6.5 estimated for the data in Fig. 1, i_s goes from ~ 5 fA to ~ 1.4 fA. A simple model of the macroscopic proton current is given by

$$I_H(t, H) = N \cdot P_o(t) \cdot i_s(t, H). \quad (7)$$

Assuming first-order kinetics for P_o and a time course for the change in i_s with the same kinetics as P_o , the calculated time course of current at 100 mV ($P_o \sim 1$) using Eq. 7 is very similar to the experimental time course with the pseudo-inactivation (Fig. 7 D), strongly suggesting that the estimated pH change around the channel can qualitatively explain the altered kinetics.

Our findings confirm that even in the presence of a large buffering power, proton currents significantly deplete protons in the vicinity of the channel and alter

pH, even in inside-out patch recording conditions, so that the concentration of protons near the channel is not well controlled, when the total membrane proton current is too large. Proton channels have very small single-channel conductance but still are capable of playing a role in pH_i regulation. This is possible in part because the intracellular proton concentration is very small, thus even small fluxes can easily change pH, and in part because the cell must be able to insert a high number of channel molecules in the membrane to ensure sufficient proton flux. Finally, our data show that currently, Hvl channels cannot be used as the basis for fluorescent membrane potential sensors, unless truly pH-insensitive FPs are used. In contrast, constructs such as the one used here could be used in conjunction with bulk cytoplasmic pH sensors to study pH dynamics in different regions of the cell.

The authors would like to thank Dr. T. Rosenbaum for helpful discussions.

This work was supported by grant no. IN209515 from DGAPA-PAPIIT-UNAM.

The authors declare no competing financial interests.

Sharona E. Gordon served as editor.

Submitted: 11 August 2015

Accepted: 21 December 2015

REFERENCES

- Baker, B.J., L. Jin, Z. Han, L.B. Cohen, M. Popovic, J. Platisa, and V. Pieribone. 2012. Genetically encoded fluorescent voltage sensors using the voltage-sensing domain of *Nematostella* and *Danio* phosphatases exhibit fast kinetics. *J. Neurosci. Methods*. 208:190–196. <http://dx.doi.org/10.1016/j.jneumeth.2012.05.016>
- Berridge, M.J. 2006. Calcium microdomains: organization and function. *Cell Calcium*. 40:405–412. <http://dx.doi.org/10.1016/j.ceca.2006.09.002>
- Bizzarri, R., M. Serresi, S. Luin, and F. Beltram. 2009. Green fluorescent protein based pH indicators for in vivo use: a review. *Anal. Bioanal. Chem.* 393:1107–1122. <http://dx.doi.org/10.1007/s00216-008-2515-9>
- Cherny, V.V., V.S. Markin, and T.E. DeCoursey. 1995. The voltage-activated hydrogen ion conductance in rat alveolar epithelial cells is determined by the pH gradient. *J. Gen. Physiol.* 105:861–896. <http://dx.doi.org/10.1085/jgp.105.6.861>
- Cherny, V.V., R. Murphy, V. Sokolov, R.A. Levis, and T.E. DeCoursey. 2003. Properties of single voltage-gated proton channels in human eosinophils estimated by noise analysis and by direct measurement. *J. Gen. Physiol.* 121:615–628. <http://dx.doi.org/10.1085/jgp.200308813>
- Crank, J. 1979. *The Mathematics of Diffusion*. Second edition. Oxford University Press, New York. 414 pp.
- De-la-Rosa, V., G.E. Rangel-Yescas, E. Ladrón-de-Guevara, T. Rosenbaum, and L.D. Islas. 2013. Coarse architecture of the transient receptor potential vanilloid 1 (TRPV1) ion channel determined by fluorescence resonance energy transfer. *J. Biol. Chem.* 288:29506–29517. <http://dx.doi.org/10.1074/jbc.M113.479618>
- Decker, E.R., and D.G. Levitt. 1988. Use of weak acids to determine the bulk diffusion limitation of H⁺ ion conductance through the gramicidin channel. *Biophys. J.* 53:25–32. [http://dx.doi.org/10.1016/S0006-3495\(88\)83062-5](http://dx.doi.org/10.1016/S0006-3495(88)83062-5)

- DeCoursey, T.E. 2013. Voltage-gated proton channels: molecular biology, physiology, and pathophysiology of the H_v family. *Physiol. Rev.* 93:599–652. <http://dx.doi.org/10.1152/physrev.00011.2012>
- DeCoursey, T.E., and V.V. Cherny. 1996. Effects of buffer concentration on voltage-gated H⁺ currents: does diffusion limit the conductance? *Biophys. J.* 71:182–193. [http://dx.doi.org/10.1016/S0006-3495\(96\)79215-9](http://dx.doi.org/10.1016/S0006-3495(96)79215-9)
- Edelstein, A., N. Amodaj, K. Hoover, R. Vale, and N. Stuurman. 2010. Computer control of microscopes using μManager. *Curr. Protoc. Mol. Biol.* Chapter 14:20.
- Fujiwara, Y., and Y. Okamura. 2014. Temperature-sensitive gating of voltage-gated proton channels. *Curr. Top. Membr.* 74:259–292. <http://dx.doi.org/10.1016/B978-0-12-800181-3.00010-5>
- Fujiwara, Y., T. Kurokawa, K. Takeshita, M. Kobayashi, Y. Okochi, A. Nakagawa, and Y. Okamura. 2012. The cytoplasmic coiled-coil mediates cooperative gating temperature sensitivity in the voltage-gated H⁺ channel Hv1. *Nat. Commun.* 3:816. <http://dx.doi.org/10.1038/ncomms1823>
- Hanson, G.T., T.B. McAnaney, E.S. Park, M.E. Rendell, D.K. Yarbrough, S. Chu, L. Xi, S.G. Boxer, M.H. Montrose, and S.J. Remington. 2002. Green fluorescent protein variants as ratiometric dual emission pH sensors. 1. Structural characterization and preliminary application. *Biochemistry.* 41:15477–15488. <http://dx.doi.org/10.1021/bi026609p>
- Iovannisci, D., B. Illek, and H. Fischer. 2010. Function of the HVCN1 proton channel in airway epithelia and a naturally occurring mutation, M91T. *J. Gen. Physiol.* 136:35–46. <http://dx.doi.org/10.1085/jgp.200910379>
- Ishida, I.G., G.E. Rangel-Yescas, J. Carrasco-Zanini, and L.D. Islas. 2015. Voltage-dependent gating and gating charge measurements in the Kv1.2 potassium channel. *J. Gen. Physiol.* 145:345–358. <http://dx.doi.org/10.1085/jgp.201411300>
- Kapus, A., R. Romanek, A.Y. Qu, O.D. Rotstein, and S. Grinstein. 1993. A pH-sensitive and voltage-dependent proton conductance in the plasma membrane of macrophages. *J. Gen. Physiol.* 102:729–760. <http://dx.doi.org/10.1085/jgp.102.4.729>
- Mutoh, H., W. Akemann, and T. Knöpfel. 2012. Genetically engineered fluorescent voltage reporters. *ACS Chem. Neurosci.* 3:585–592. <http://dx.doi.org/10.1021/cn300041b>
- Nagai, T., K. Ibata, E.S. Park, M. Kubota, K. Mikoshiba, and A. Miyawaki. 2002. A variant of yellow fluorescent protein with fast and efficient maturation for cell-biological applications. *Nat. Biotechnol.* 20:87–90. <http://dx.doi.org/10.1038/nbt0102-87>
- Nunogaki, K., and M. Kasai. 1988. The H⁺/OH⁻ flux localizes around the channel mouth in buffered solution. *J. Theor. Biol.* 134:403–415. [http://dx.doi.org/10.1016/S0022-5193\(88\)80070-5](http://dx.doi.org/10.1016/S0022-5193(88)80070-5)
- Okamura, Y., Y. Fujiwara, and S. Sakata. 2015. Gating mechanisms of voltage-gated proton channels. *Annu. Rev. Biochem.* 84:685–709. <http://dx.doi.org/10.1146/annurev-biochem-060614-034307>
- Ramsey, I.S., M.M. Moran, J.A. Chong, and D.E. Clapham. 2006. A voltage-gated proton-selective channel lacking the pore domain. *Nature.* 440:1213–1216. <http://dx.doi.org/10.1038/nature04700>
- Sasaki, M., M. Takagi, and Y. Okamura. 2006. A voltage sensor-domain protein is a voltage-gated proton channel. *Science.* 312:589–592. <http://dx.doi.org/10.1126/science.1122352>
- Thomas, R.C., and R.W. Meech. 1982. Hydrogen ion currents and intracellular pH in depolarized voltage-clamped snail neurones. *Nature.* 299:826–828. <http://dx.doi.org/10.1038/299826a0>
- Wachter, R.M., M.A. Elsliger, K. Kallio, G.T. Hanson, and S.J. Remington. 1998. Structural basis of spectral shifts in the yellow-emission variants of green fluorescent protein. *Structure.* 6:1267–1277. [http://dx.doi.org/10.1016/S0969-2126\(98\)00127-0](http://dx.doi.org/10.1016/S0969-2126(98)00127-0)
- Wagner, J., and J. Keizer. 1994. Effects of rapid buffers on Ca²⁺ diffusion and Ca²⁺ oscillations. *Biophys. J.* 67:447–456. [http://dx.doi.org/10.1016/S0006-3495\(94\)80500-4](http://dx.doi.org/10.1016/S0006-3495(94)80500-4)
- Zimmerman, A.L., J.W. Karpen, and D.A. Baylor. 1988. Hindered diffusion in excised membrane patches from retinal rod outer segments. *Biophys. J.* 54:351–355. [http://dx.doi.org/10.1016/S0006-3495\(88\)82966-7](http://dx.doi.org/10.1016/S0006-3495(88)82966-7)